

# Selectivity in Hydrogenation of $\alpha,\beta$ -unsaturated Carbonyl Compounds on Model Palladium Catalysts

DISSERTATION

zur Erlangung des akademischen Grades

**doctor rerum naturalium**

(Dr. rer. nat.)

im Fach Chemie

eingereicht an der

Mathematisch-Naturwissenschaftlichen Fakultät

Humboldt-Universität zu Berlin

von

**Dipl.-Chem. Karl-Heinz Dostert**

Präsident der Humboldt-Universität zu Berlin:

Prof. Dr. Jan-Hendrik Olbertz

Dekan der Mathematisch-Naturwissenschaftlichen Fakultät:

Prof. Dr. Elmar Kulke

Gutachter:

1. Prof. Dr. Hans-Joachim Freund

2. Prof. Dr. Klaus Rademann

3. Prof. Dr. Hans-Peter Steinrück

**eingereicht am:** 29.09.2015

**Tag der mündlichen Prüfung:** 26.11.2015



## Abstract

The conversion of  $\alpha, \beta$ -unsaturated aldehydes and ketones with hydrogen over model palladium catalysts was investigated using molecular beam techniques combined with infrared reflection-absorption spectroscopy (IRAS), quadrupole mass spectrometry (QMS), and near-edge X-ray absorption fine structure (NEXAFS) studies under well-defined ultra-high vacuum conditions. The aim of this work was to gain atomistic-level understanding of structural factors governing the selectivity and activity of a Pd(111) single crystal and Fe<sub>3</sub>O<sub>4</sub>-supported Pd nanoparticles for C=C and C=O bond hydrogenation. The ketone *isophorone* and the aldehyde *acrolein* were chosen as prototypical  $\alpha, \beta$ -unsaturated carbonyl compounds.

NEXAFS studies showed that isophorone is adsorbed on Pd(111) in a flat-lying geometry at low coverages. With increasing coverage, both C=C and C=O bonds tilt with respect to the surface plane. The tilting is more pronounced for the C=C bond on pristine Pd(111), indicating a strong distortion of the conjugated  $\pi$  system upon interaction with Pd. Co-adsorbed hydrogen leads to higher tilting angles of both  $\pi$  bonds and a conservation of the in-plane geometry of the conjugated  $\pi$  system, pointing to a much weaker interaction of isophorone with Pd in the presence of hydrogen.

IRAS studies were combined with density functional theory calculations to obtain a detailed assignment of IR vibrational modes of normal isophorone, deuterium-labeled isophorone, and the saturated ketone 3,3,5-trimethylcyclohexanone (TMCH). In agreement to the NEXAFS studies, IRAS studies showed strongly distorted chemical bonds in isophorone at low coverages on pristine Pd(111) and a less perturbed molecular structure in the presence of hydrogen. In contrast, the saturated ketone TMCH is always adsorbed in a strongly tilted geometry interacting with the surface primarily through the C=O group. Similar results were obtained in IRAS studies on acrolein and the saturated aldehyde propanal adsorbed on Pd(111).

The selective partial hydrogenation over a Pd(111) surface and Fe<sub>3</sub>O<sub>4</sub>-supported Pd nanoparticles with different particle sizes was investigated using acrolein. Molecular beam techniques were combined with IRAS and QMS measurements in order to simultaneously monitor the evolution of surface species and the formation of the final gas-phase products. Over a Pd(111) single crystal, acrolein is hydrogenated at the C=O bond to form propenol with nearly 100% selectivity, while over Pd/Fe<sub>3</sub>O<sub>4</sub>, selective conversion of the C=C bond to propanal occurs.

The propenol formation rate on Pd(111) exhibits a clear temperature dependence with a maximum at 270 K. IRAS investigations on the surface turning over showed that a distinct modification of the Pd(111) surface with a dense overlayer of an oxopropyl species is required for propenol formation. This layer is formed out of the first monolayer of acrolein deposited on the pristine Pd crystal under reaction conditions, most effectively at 270 K. Subsequently deposited acrolein is adsorbed via the C=O bond forming a half-hydrogenated reaction intermediate with a saturated C–O bond. The propenol formation rate detected in the gas-phase clearly follows the surface concentration of the reaction intermediate. Under identical reaction conditions on Pd/Fe<sub>3</sub>O<sub>4</sub>, decarbonylation of acrolein occurs, inhibiting the surface modification required for propenol formation.

Finally, our studies showed that particle size and temperature have a significant effect on the surface chemistry during acrolein conversion on Pd/Fe<sub>3</sub>O<sub>4</sub> model catalysts. In general, propanal production appears at rather low temperatures, while decarbonylation of acrolein dominates at higher temperatures. However, IRAS and QMS studies on the largest Pd particles with a diameter of 12 nm indicated that C=O bond hydrogenation might also be possible on Pd particles. This final observation constitutes the base for future attempts to control the selectivity of the partial hydrogenation of unsaturated aldehydes and ketones over oxide-supported Pd particles.

## Zusammenfassung

Die Umsetzung von  $\alpha,\beta$ -ungesättigten Aldehyden und Ketonen mit Wasserstoff über Pd-Modellkatalysatoren wurde anhand von Molekularstrahlmethoden, kombiniert mit Infrarot-Reflexions-Absorptions-Spektroskopie (IRAS), Quadrupol-Massenspektrometrie (QMS) und Röntgen-Nahkanten-Absorptions-Spektroskopie (NEXAFS), unter wohldefinierten Ultrahochvakuumbedingungen untersucht. Das Ziel dieser Arbeit war es, ein atomistisches Verständnis der strukturellen Faktoren zu gewinnen, die die Aktivität und Selektivität eines Pd(111)-Einkristalls und  $\text{Fe}_3\text{O}_4$ -geträgerter Pd-Nanopartikel für die Hydrierung der C=C- und C=O-Bindungen bestimmen. Exemplarisch für diese Art von Kohlenwasserstoffen wurden das Aldehyd *Acrolein* und das Keton *Isophoron* gewählt.

Die NEXAFS-Studien zeigten, dass Isophoron bei niedrigen Bedeckungen auf Pd(111) in einer flachliegenden Geometrie adsorbiert wird. Die Neigungswinkel der C=C- und C=O-Bindungen in Bezug auf die Pd(111)-Ebene nehmen mit zunehmender Oberflächenbedeckung zu. Auf reinem Pd(111) ist die Neigung der C=C-Bindung stärker ausgeprägt, was auf eine Verzerrung des konjugierten  $\pi$ -Systems hindeutet. Co-adsorbierter Wasserstoff führt zu einem höheren Neigungswinkel beider  $\pi$ -Bindungen, dabei bleibt die planare Geometrie des konjugierten  $\pi$ -Systems erhalten. Diese Beobachtung deutet auf eine deutliche schwächere Bindung von Isophoron an Pd bei Anwesenheit von Wasserstoff.

IRAS wurde mit Dichtefunktionaltheorie-Rechnungen kombiniert, um eine detaillierte Zuordnung der IR-Vibrationsmoden von normalem Isophoron, deuteriummarkiertem Isophoron und dem gesättigten Keton 3,3,5-Trimethylcyclohexanon (TMCH) zu erhalten. In Übereinstimmung mit den NEXAFS-Daten zeigten die IRAS-Untersuchungen stark verzerrte chemische Bindungen bei niedrigen Isophoron-Konzentrationen auf reinem Pd(111) und weniger gestörte Strukturen bei höheren Bedeckungen. Im Gegensatz dazu wird das gesättigte Keton TMCH immer in einer stark geneigten Geometrie über die C=O-Gruppe adsorbiert. Ähnliche Ergebnisse wurden in den IRAS-Studien zu Acrolein und Propanal auf Pd(111) erhalten.

Die selektive partielle Hydrierung über einer Pd(111)-Oberfläche und  $\text{Fe}_3\text{O}_4$ -geträgerten Pd-Nanopartikeln unterschiedlicher Größen wurde unter Verwendung von Acrolein untersucht. Molekularstrahlmethoden wurden mit IRAS- und QMS-Messungen kombiniert, um gleichzeitig die Bildung von Adsorbaten auf der Oberfläche und die der Produkte in der Gasphase verfolgen zu können. Über einem Pd(111)-Kristall wird Propenol mit nahezu 100% Selektivität durch Hydrierung der C=O-Gruppe gebildet, während über Pd/ $\text{Fe}_3\text{O}_4$  Propanal durch selektive Hydrierung der C=C-Gruppe erzeugt wird.

Die Bildungsrate von Propenol auf Pd(111) zeigt eine klare Temperaturabhängigkeit mit einem deutlichen Maximum bei 270 K. IRAS-Untersuchungen unter Reaktionsbedingungen zeigten, dass die Propenol-Bildung eine Modifikation der Pd(111)-Oberfläche mit einer dichten Monolage einer Oxopropyl-Species voraussetzt. Dieses Adsorbat wird aus der ersten aufgetragenen Acrolein-Monolage auf dem Pd(111)-Kristall unter Reaktionsbedingungen gebildet, am effektivsten bei 270 K. Die darauffolgend adsorbierten Acrolein-Moleküle werden über die C=O-Gruppe adsorbiert und bilden ein halb-hydriertes Reaktions-Intermediat mit einer gesättigten C–O-Bindung. Der Verlauf der in der Gasphase gemessenen Propanal-Bildungsrate folgt klar dem der Oberflächenkonzentration des Intermediates. Auf Pd/ $\text{Fe}_3\text{O}_4$  tritt unter identischen Reaktionsbedingungen eine Decarbonylierungsreaktion auf, die die für die Propenolbildung notwendige Oberflächenmodifizierung verhindert.

Abschließend zeigen unsere Studien, dass die Partikelgröße und die Temperatur einen großen Einfluss auf die Reaktionen auf der Pd/ $\text{Fe}_3\text{O}_4$ -Oberfläche haben. Allgemein tritt die Propanal-Bildung bei eher niedrigen Temperaturen auf, während bei höheren Temperaturen die Decarbonylierung von Acrolein dominiert. Darüber hinaus deuteten IRAS und QMS-Untersuchungen an den größten Pd-Partikeln mit einem Durchmesser von 12 nm an, dass eine C=O-Hydrierung auch auf Partikeln möglich ist. Die zuletzt genannte Beobachtung bildet eine vielversprechende Basis für zukünftige

ge Versuche, die Selektivität der partiellen Hydrierung ungesättigter Aldehyde und Ketone auf oxidgeträgerten Pd-Partikeln zu kontrollieren.



# Contents

<b>1</b>	<b>Introduction</b>	<b>1</b>
<b>2</b>	<b>Theoretical Background</b>	<b>9</b>
2.1	Kinetics at Gas-Surface Interfaces . . . . .	9
2.1.1	Basic Kinetics on Surfaces . . . . .	9
2.1.2	Kinetic Effects on Model Catalysts . . . . .	13
2.2	Experimental Methods . . . . .	15
2.2.1	Molecular Beams . . . . .	15
2.2.2	Infrared Spectroscopy . . . . .	20
2.2.3	Quadrupole Mass Spectrometry . . . . .	24
2.2.4	Near Edge X-Ray Absorption Fine Structure . . . . .	26
<b>3</b>	<b>Pd/Fe<sub>3</sub>O<sub>4</sub> Model Catalysts</b>	<b>29</b>
3.1	Fe <sub>3</sub> O <sub>4</sub> film on Pt(111) . . . . .	30
3.2	Pd particles on Fe <sub>3</sub> O <sub>4</sub> /Pt(111) . . . . .	31
3.2.1	CO adsorption on Pd . . . . .	33
<b>4</b>	<b>Selectivity in Hydrogenation of <math>\alpha,\beta</math>-unsaturated Carbonyl Compounds on Pd - an Overview</b>	<b>35</b>
4.1	Adsorption of Isophorone and Acrolein . . . . .	35
4.2	Hydrogenation of Acrolein over Pd(111) and Pd/Fe <sub>3</sub> O <sub>4</sub> . . . . .	42
<b>5</b>	<b>Conclusions and Outlook</b>	<b>53</b>
<b>6</b>	<b>Interaction of Isophorone with Pd(111): A Combination of Infrared Reflection- Absorption Spectroscopy, Near-Edge X-ray Absorption Fine Structure, and Den- sity Functional Theory Studies</b>	<b>55</b>
6.1	Introduction . . . . .	57
6.2	Experimental Details and Methods . . . . .	58
6.3	Results and Discussion . . . . .	59
6.3.1	Unsaturated C=C and C=O Bonds/Pd(111) . . . . .	60
6.3.2	Effect of Hydrogen on the Geometry of C=C and C=O Bonds . . . . .	70
6.4	Conclusions . . . . .	72
<b>7</b>	<b>Adsorption of Isophorone and Trimethyl-Cyclohexanone on Pd(111): A Combi- nation of Infrared Reflection-Absorption Spectroscopy and Density Functional Theory Studies</b>	<b>75</b>
7.1	Introduction . . . . .	77
7.2	Experimental Details and Methods . . . . .	78

7.3	Results and Discussion . . . . .	79
7.3.1	IR Vibrations in Isophorone Multilayers . . . . .	80
7.3.2	Isophorone at sub-monolayer coverage . . . . .	92
7.3.3	IR Vibrations and Adsorption of TMCH . . . . .	95
7.4	Conclusions . . . . .	104
7.5	Acknowledgements . . . . .	106
<b>8</b>	<b>Adsorption of Acrolein, Propanal, and Allyl Alcohol on Pd(111): A combination of Infrared Reflection-Absorption Spectroscopy and Temperature Programmed Desorption Studies</b>	<b>107</b>
8.1	Introduction . . . . .	109
8.2	Experimental Details . . . . .	109
8.3	Results . . . . .	110
8.3.1	Adsorption of Acrolein . . . . .	111
8.3.2	Adsorption of Propanal . . . . .	115
8.3.3	Adsorption of Allyl Alcohol . . . . .	119
8.4	Discussion . . . . .	122
8.5	Conclusions . . . . .	125
<b>9</b>	<b>Spectators control Selectivity in Surface Chemistry: Acrolein partial Hydrogenation over Pd</b>	<b>127</b>
9.1	Introduction . . . . .	129
9.2	Experimental . . . . .	130
9.3	Results and Discussion . . . . .	131
9.4	Conclusions . . . . .	138
9.5	Supporting Information . . . . .	140
<b>10</b>	<b>Selective partial Hydrogenation of Acrolein on Pd: a mechanistic Study</b>	<b>143</b>
10.1	Introduction . . . . .	145
10.2	Experimental Details . . . . .	146
10.3	Results and Discussion . . . . .	147
10.3.1	Acrolein Conversion at 270 K . . . . .	150
10.3.2	Acrolein Conversion at lower Temperatures . . . . .	155
10.3.3	Acrolein Conversion at higher Temperatures . . . . .	158
10.3.4	Selectivity on Pd(111) and Pd/Fe <sub>3</sub> O <sub>4</sub> at 270 K . . . . .	161
10.4	Conclusions . . . . .	162
10.5	Supporting Information . . . . .	164
<b>11</b>	<b>Selective Hydrogenation of Acrolein over Pd Model Catalysts: Temperature and Particle Size Effects</b>	<b>167</b>
11.1	Introduction . . . . .	169
11.2	Experimental . . . . .	170
11.3	Results and Discussion . . . . .	171
11.3.1	Influence of Temperature and Particle Size on Gas-Phase Products of Acrolein Hydrogenation . . . . .	171
11.3.2	Comparison of Pd(111) and Pd/Fe <sub>3</sub> O <sub>4</sub> at 270 K . . . . .	171

11.3.3 Influence of Sample Temperature on Pd Nanoparticle Surface Chem- istry . . . . .	175
11.3.4 Particle Size Effects . . . . .	178
11.4 Discussion . . . . .	179
11.5 Conclusions . . . . .	180
<b>12 Insights into the Origin of Selectivity in Acrolein Conversion over Pd/Fe<sub>3</sub>O<sub>4</sub></b>	<b>181</b>
12.1 Introduction . . . . .	183
12.2 Experimental Details . . . . .	184
12.3 Results and Discussion . . . . .	184
12.3.1 Acrolein on Fe <sub>3</sub> O <sub>4</sub> . . . . .	184
12.3.2 Acrolein on Pd/Fe <sub>3</sub> O <sub>4</sub> . . . . .	188
12.4 Conclusion . . . . .	191



# 1 Introduction

Catalytic reactions at interfaces constitute the basis for a large number of chemical processes in industry, such as chemical synthesis, environmental technologies, energy storage and conversion, and food production. During the last decades, new applications of heterogeneous catalysts emerged from the growing attempt to protect the natural environment. The focus of catalysis changed from pure acceleration to improved selectivity of chemical reactions. Catalysts control the rate as well as the selectivity of a chemical reaction. High reaction rates under mild conditions combined with high selectivity towards the desired product is economically and environmentally beneficial [1–4].

Heterogeneous catalysts are typically based on a thermally stable support, often a metal oxide, on which the active phase, a metal or metal oxide, is dispersed as small particles. These systems exhibit a large number of non-equivalent sites, which may critically control the kinetics of the catalyzed reaction. Particles are typically terminated by distinct facets as well as by edge, corner, and defect sites. The support exhibits regular oxide areas as well as defect sites. Moreover, sites can be modified, *e.g.* by promoters or poisons. It has been found that the particle size, size distribution, the morphology as well as the oxidation state can drastically influence the performance of the supported catalyst. In addition, the support itself and particle–support interactions can strongly affect the catalytic behavior. Finally, it has to be taken into account that the catalyst may restructure under reaction conditions. Due to the high complexity of these systems, a rational design of new catalysts has not been achieved yet and new catalysts are still found mainly by empirical methods. Therefore, a microscopic understanding requires detailed knowledge of the interaction between the adsorbates and the catalyst [1, 5–11].

There are two principally different approaches in catalysis research. Either the reaction is studied on an applied catalyst under realistic conditions and the global kinetics is modeled as function of the reaction parameters; or the reaction is studied on simplified model systems under well-defined conditions, which allows a microscopic understanding of elementary processes.

In the first approach, structural parameters of the catalyst are varied over a wide range and subsequent changes of the global kinetics are detected. The advantage of this method is that the results give macroscopic information that are directly relevant for applications. Nevertheless, it is often difficult to vary just one structural parameter and a detailed understanding of microscopic processes is not possible from this macroscopic view.

In the microscopic approach, the structural and chemical complexity is reduced to have a very well-defined system that is accessible by surface science methods. In the most sim-

ple case, surface processes are studied on a metal single crystal under ultra-high vacuum (UHV) conditions. The goal is a detailed description of the kinetics of all elementary steps, such as adsorption, diffusion, reaction, and desorption. In fact, such detailed models are hardly available. Nevertheless, a combination of surface science studies and kinetic investigations provide increasingly detailed insights into chemical reactions on surfaces. First, the surface chemistry on single crystal surfaces was investigated [11] until in the last two decades several groups developed a model catalysts approach [10, 12–19]. Model catalysts mimic some important structural properties of applied catalysts, while the full complexity is avoided. These catalysts are fully accessible by surface science methods, which allows an atomic-level characterization of their geometric and electronic structures. A variety of model systems has been developed, such as metal nanoparticles dispersed on a metal oxide support, which is employed in this work.

When trying to use results from the microscopic approach to understand reaction kinetics of an applied catalyst, two basic difficulties appear, which are illustrated in Figure 1.1. The first one arises from the reduced structural complexity of model systems. However, structural complexity can critically affect the reaction kinetics. The discrepancy in complexity of an applied catalyst and a system available for surface science methods is called *material gap*. An attempt to overcome the material gap is the use of well-defined model supported catalysts instead of single crystals.

The second difficulty is the large degree of chemical complexity which originates from the interaction between multiple adsorbed gases under high pressure conditions while surface science studies are typically performed under UHV. The term *pressure gap* refers to the latter issue. The pressure gap can be approached to a certain extent by crossing multiple molecular beams (MB) on the catalyst. Molecular beams provide a well-defined directed flux of molecules with pressures from  $10^{-10}$  mbar to  $10^{-5}$  mbar at the sample surface, while the background pressures stays several orders of magnitude lower. Hence, some degree of chemical complexity is created on the catalyst’s surface in an otherwise UHV environment. MB techniques are a well-established tool for studying dynamics and kinetics of surface reactions [9, 20–25].

This study is aiming at an atomistic understanding of the selective hydrogenation of multi-unsaturated hydrocarbons. Particularly, we studied the kinetics of the hydrogenation of  $\alpha,\beta$ -unsaturated carbonyl compounds. As prototypical hydrocarbons acrolein, which is the most simple unsaturated aldehyde, and isophorone, a pro-chiral ketone, were chosen.

For molecules with unsaturated C=C and C=O bonds, such as acrolein and isophorone, hydrogenation can occur either on one of the bonds or on both of them. Conversion of the C=C group gives the saturated aldehyde or ketone, hydrogenation of the C=O group will yield an unsaturated alcohol, and conversion of both bonds will give a saturated alcohol.

The selective hydrogenation of the C=O bond in the presence of a C=C bond is of special interest for industrial applications, such as in the fields of fine chemicals or pharmaceuticals [27–30]. Thermodynamics, however, favors the hydrogenation of the C=C bond [28]. Hence, conversion of the C=O group requires manipulation of the kinetics by

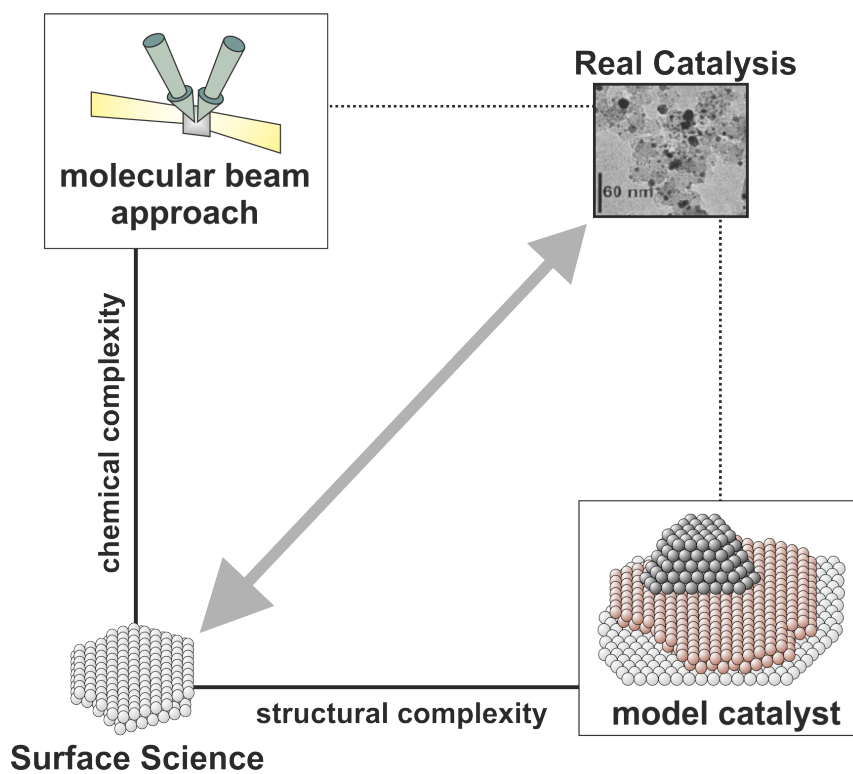


Figure 1.1: Schematic representation of the reduced chemical and structural complexity of systems in surface science as compared to applied catalysts. Model catalysts are used to mimic structural properties of applied catalysts and molecular beam methods introduce some degree of chemical complexity (TEM image from [26])

## 1 Introduction

means of an adequate catalyst.

It has been noted that acrolein is the most difficult  $\alpha,\beta$ -unsaturated aldehyde to selectively hydrogenate at the carbonyl group, while higher selectivities towards C=O bond hydrogenation have been found for homologous compounds such as cinnamaldehyde or prenal. In the latter cases, the hydrogenation of the C=C group is suppressed by large substituents that prevent the attack of the catalyst at the C=C group and thus increase the chance of C=O conversion [31, 32].

A considerable number of studies have been performed to trigger the selectivity in favor of C=O bond hydrogenation over powdered catalyst at ambient or higher pressures. For instance, silver or gold were employed instead of conventional hydrogenation catalysts like palladium or platinum. Silver [33–35] and gold [36–39] are the only monometallic catalysts that are known to hydrogenate the C=O bond in  $\alpha,\beta$ -unsaturated aldehydes and ketones with selectivities up to approximately 50%. The selectivity, however, depends on a number of factors, such as the particle size, reactant pressures, and the support material.

The effect of reactant pressures on the selectivity in acrolein hydrogenation over oxide-supported Ag catalysts was investigated by several groups. All of these studies point to higher selectivities towards C=O bond hydrogenation at higher pressures of acrolein and hydrogen [34, 35, 40]. Wei *et al.* observed an increasing selectivity to allyl alcohol formation from 1 bar to 5 bar total pressure [40]. Bron *et al.* found a minimum total pressure of about 100 mbar for allyl alcohol formation. The pressure-dependent selectivity was explained by two different adsorption modes of acrolein on Ag: a flat-lying geometry at lower pressures and a tilted orientation with the C=O group attached to the surface at higher pressures [34].

The particle size dependence of the selectivity and activity is closely related to the role of the different surface sites in activating the unsaturated chemical bonds. The large majority of studies report increasing selectivities towards the unsaturated alcohol with increasing particle size for a large variety of transition metals [27, 38–42]. Bron *et al.*, in contrast, obtained contradictory results for Ag particles [34, 35]. In the latter studies, the authors concluded that mainly low-coordinated sites are responsible for the C=O group activation. In the former group of studies, Schimpf *et al.* [38], Wei *et al.* [40], and Englisch *et al.* [41] concluded that most likely the (111) facets of Pt, Ag, and Au activate the C=O group. However, it should be noted that over Pt the selectivity to C=O bond hydrogenation was always very low, even though TiO<sub>2</sub> and ZrO<sub>2</sub> supports were used, which were found to activate the C=O bond, as will be discussed below. Mohr *et al.* found higher selectivities towards alcohol formation over larger Au particles, however, the authors identified the edges of particles to be responsible for C=O bond hydrogenation [43].

In the majority of studies on the partial selective hydrogenation of  $\alpha,\beta$ -unsaturated carbonyl compounds in the last five decades, the activity and selectivity of Pt-group based catalysts were modified with promoters, such as a second metal or metal oxide (*e.g.* [27, 30, 44–51]). For instance, increasing selectivities to C=O bond hydrogenation over Pt catalysts were found by promotion with Fe [46, 48, 49, 51] or Sn [49–51]. In most

of these studies unsaturated aldehydes with bulky substituents at the C=C group, *e.g.* crotonaldehyde or cinnamaldehyde, were used. Marinelli and Ponec, however, investigated the hydrogenation of acrolein over Sn-modified Pt powdered catalysts [51]. An increase in selectivity to allyl alcohol from near 0% over Pt/SiO<sub>2</sub> to approximately 10-20% over SnPt/SiO<sub>2</sub> was observed. Nevertheless, the major product in both systems was propanal.

Furthermore, also the support material was found to be able to act as a promoter for C=O bond conversion. In general, higher selectivities towards C=O bond hydrogenation were observed over catalysts with partially reducible supports. There are two possible ways how the support may activate the carbonyl group. On the one hand, the hydrocarbon can be adsorbed and thus activated by the support in the vicinity of the metal particles. On the other hand, *strong metal-support interactions* (SMSI) can create reduced support material on the active metal which interacts with the reactant.

In acrolein conversion over Au particles, the selectivity to C=O hydrogenation was found to increase from about 20% to 40% when ZrO<sub>2</sub> is used as support instead of SiO<sub>2</sub>. The promoting effect of the support was explained by adsorption of the hydrocarbon on Au with the oxygen atom of the C=O group attached to a Zr<sup>4+</sup> site at the ZrO<sub>2</sub>-Au interface [37]. Kennedy, Baker, and Somorjai spectroscopically investigated the hydrogenation of crotonaldehyde over Pt/SiO<sub>2</sub> and Pt/TiO<sub>2</sub> catalysts. They found that crotonaldehyde is adsorbed via the C=O group at O vacancies of the TiO<sub>2</sub> support and react with spillover hydrogen from Pt forming an unsaturated alcohol while SiO<sub>2</sub> has no active role in the reaction [52]. Englisch, Jentys, and Lercher, however, obtained rather similar activity and selectivity of Pt/SiO<sub>2</sub> and Pt/TiO<sub>2</sub> in crotonaldehyde hydrogenation. Nevertheless, the selectivity towards C=O bond conversion was found to increase on TiO<sub>x</sub> decorated Pt particles (SMSI state) obtained by high-temperature reduction of the Pt/TiO<sub>2</sub> catalyst [41]. The results from Lercher's group agree well to earlier studies by Vennice *et al.* showing an increase in activity for hydrogenation of the C=O group of crotonaldehyde over Pt/TiO<sub>2</sub> by one order of magnitude after an SMSI state has been created [53, 54]. The group of Iwasawa studied the kinetics and the mechanism of acrolein hydrogenation over Ir/Nb<sub>2</sub>O<sub>5</sub> catalyst in normal and SMSI state with the help of isotopic labeling. The main hydrogenation product was always propanal. However, allyl alcohol was observed over both catalysts, but a higher selectivity towards allyl alcohol was found on the SMSI system. According to investigations of the reaction kinetics, the activation energy for allyl alcohol formation decreased for the SMSI catalyst, while that for propanal increased. The authors concluded that hydrogen is dissociatively adsorbed on bare metal sites, while the addition of hydrogen to acrolein happens in the vicinity of NbO<sub>x</sub> islands on the Ir metal [55, 56].

Despite the large variety of attempts to control the selectivity in hydrogenation of  $\alpha,\beta$ -unsaturated aldehydes and ketones over powdered catalyst, selective production of unsaturated alcohols remains challenging. Especially when using acrolein, the main product in partial hydrogenation is essentially always the saturated aldehyde propanal. The only possibility to produce allyl alcohol with near 50% selectivity is to use Au or Ag particles supported on a reducible oxide like TiO<sub>2</sub>. However, the drawback of using Ag or Au is their weak interaction with hydrogen as compared to conventional hydrogenation catalysts

## 1 Introduction

like Pt or Pd. The dissociation of hydrogen on Ag and Au was shown to be an endothermic process and Ag surfaces at ambient temperatures were found to not dissociate  $\text{H}_2$  molecules [57–59].

While a large number of studies on the hydrogenation of  $\alpha,\beta$ -unsaturated carbonyl compounds over powdered catalyst under realistic conditions were conducted over several decades, surface science studies on the reaction of hydrogen with molecules containing both C=C and C=O bonds under well-defined conditions became more numerous only in recent years.

The adsorption of acrolein on Pt(111) was investigated by sum-frequency generation vibrational spectroscopy (SFG-VS) and kinetic measurements by Kliewer *et al.* [60] and by density functional theory (DFT) calculations from Loffreda *et al.* [61]. Both studies showed that a mixture of different adsorption modes containing  $\eta_2$  (di- $\sigma$ -C–C, *cis* and *trans*),  $\eta_3$  (*trans*), and  $\eta_4$  (*trans*) configurations of acrolein on the surface. However, the SFG-VS results did not indicate any products from acrolein hydrogenation during heating up to 415 K in the presence of hydrogen. For crotonaldehyde and prenal, in contrast, the experimental data points to the formation of saturated aldehydes and unsaturated alcohols.

The geometries of the unsaturated C=C and C=O bonds with respect to metal single crystal surfaces were determined under well-defined conditions by the group of Lambert. In a study by Brandt *et al.*, the adsorption and hydrogenation of acrolein on a Ag(111) surface was investigated by synchrotron X-ray photoelectron spectroscopy (XPS), near-edge X-ray absorption fine structure (NEXAFS), and temperature programmed reaction (TPR) [62]. The TPR study showed an increasing selectivity towards allyl alcohol formation with increasing acrolein coverage. By NEXAFS, both unsaturated bonds C=C and C=O were found almost parallel to the Ag surface at low acrolein coverage. However, a stronger tilting of the C=C bond was observed at high coverages. The authors concluded that the inclined C=C bond at high acrolein concentrations is less likely to react with hydrogen, increasing the change for C=O hydrogenation.

In order to study the enantioselective hydrogenation of isophorone over a Pd(111) single crystal surface, Beaumont *et al.* investigated the tilting of the unsaturated bonds in isophorone with respect to the surface plane by NEXAFS studies [63]. A strong tilting of the C=C–C=O framework was found at sub-monolayer isophorone coverage. However, it was not possible to discriminate between the geometries of the C=C and C=O bonds.

Murillo *et al.* studied the effects 0.5 ML of Ni, Co, and Cu on the selectivity towards C=C or C=O bond hydrogenation of acrolein on a Pt(111) crystal by temperature programmed desorption (TPD), high-resolution electron energy loss spectroscopy (HREELS) and DFT studies [64]. The TPD studies showed the highest hydrogenation activity and the highest selectivity towards C=O bond hydrogenation, which was 17%, when Ni was dissolved in the Pt(111) subsurface (Pt-Ni-Pt(111)). HREELS studies indicated a di- $\sigma$ -C–O adsorption mode on the Pt-Ni-Pt(111) surface. The authors concluded that a di- $\sigma$ -C–O adsorption mode facilitates C=O bond hydrogenation while configurations involving the interaction of the C=C group with the surface will mainly result in C=C bond conversion.

Hydrogenation reactions over palladium were established to not necessarily be pure surface processes. Palladium has a unique ability to dissolve large amounts of hydrogen and carbon. While carbonaceous species on the surface are responsible for poisoning of the catalyst [65, 66], subsurface carbon was found to promote hydrogen diffusion into the palladium subsurface and bulk [67–70]. Hydrogen in the subsurface region, which is more weakly bound than hydrogen on the surface, may critically affect the kinetics of an alkene conversion [57, 69–74]. Additionally, it is well known that during hydrocarbon conversion under realistic conditions, the catalyst surface can be covered with a large variety of carbonaceous species. In most previous surface science studies, however, rather clean metal surfaces were investigated and the effects related to the presence of hydrocarbons remained largely unexplored. For a true microscopic understanding the effects of co-adsorbed species need to be taken into account.

The aim of this work is to gain an atomistic-level understanding of structural factors governing the selectivity and activity of partial selective hydrogenation of  $\alpha, \beta$ -unsaturated carbonyl compounds over palladium catalysts. We start with a detailed investigation of the adsorption process on a Pd(111) single crystal. The molecular structure of the adsorbed hydrocarbons is investigated with special emphasis on the geometries of the C=C and C=O bonds with respect to the metal surface. We particularly focus on the coverage-dependent changes of the inclination angles as well as on the effect of co-adsorbed hydrogen. In the second part, the selectivity to C=C and C=O bond hydrogenation over Pd catalysts with different structures is investigated by molecular beam experiments under isothermal conditions. The evolution of surface species, such as intermediate products and spectators, is studied under reaction conditions. Especially the role of spectators on the catalyst’s surface is discussed in detail. We chose the ketone *isophorone* and the aldehyde *acrolein* as two prototypical  $\alpha, \beta$ -unsaturated compounds. The hydrogenation reactions are studied on a Pd(111) single crystal and on well-defined Pd/Fe<sub>3</sub>O<sub>4</sub>/Pt(111) model catalysts with different Pd particle sizes.

Adsorption properties are studied mainly for isophorone on a Pd(111) single crystal by a combination of infrared reflection-absorption spectroscopy (IRAS) and near-edge X-ray absorption fine structure (NEXAFS) measurements under UHV conditions. On the one hand, IRAS and NEXAFS are employed to determine the coverage-dependent inclination angles of the C=C and C=O bonds on pristine and hydrogen-precovered Pd(111). On the other hand, detailed assignment of the IR vibrations of isophorone allows us to study the molecular structure of the whole molecule, including the C–H and C–C bonds.

Acrolein is mainly employed to study the selectivity and activity of the different Pd catalysts. The kinetics of the partial hydrogenation is investigated by isothermal molecular beam experiments over a Pd(111) single crystal and Pd/Fe<sub>3</sub>O<sub>4</sub>/Pt(111) model catalysts with different Pd particle sizes. We focus on the influence of the catalysts structure on the selectivity to C=C or C=O bond conversion. Quadrupole mass spectrometry (QMS) is employed to study the gas-phase composition while IRAS is used to monitor the formation of adsorbates on the surface during acrolein conversion. Simultaneous monitoring of

## 1 Introduction

gas-phase molecules by QMS and surface species by IRAS opens up the opportunity to distinguish between different adsorbates, such as spectators and intermediate products. With these studies, not only the structure of the intermediate product is determined, also the role of different spectators on the selectivity and activity of the Pd catalysts becomes clear.

In the following chapter, the theoretical background of this thesis is presented. In the first part of Chapter 2, basic kinetic processes are summarized before the experimental techniques are described. In Chapter 3, the preparation method as well as the structural properties of Pd/Fe<sub>3</sub>O<sub>4</sub> model catalysts are briefly reviewed.

Chapter 4 outlines the general content of the research articles presented in Chapters 6 to 12 and provides an overview on the most important results. First, NEXAFS and IRAS studies on the adsorption of isophorone with a special focus on the geometries of the C=C and C=O bond with respect to the Pd(111) surface are discussed in detail. Next, IRAS studies on the structure of the saturated ketone 3,3,5-trimethylcyclohexanone (TMCH) on Pd(111) are presented and compared to the structure of isophorone on Pd(111). Moreover, IRAS studies on the adsorption of acrolein and propanal will be briefly described. In the second part of Chapter 4, the key results on acrolein hydrogenation over a Pd(111) single crystal and over Pd/Fe<sub>3</sub>O<sub>4</sub> model catalysts are summarized. Special emphasis is put on the relation between the structure of the Pd catalyst and the selectivity to C=C or C=O bond conversion. Conclusions and a future outlook are presented in Chapter 5.

In Chapter 6, a publication on NEXAFS and IRAS studies is presented that mainly focuses on the adsorption geometries of the C=C and C=O bonds in isophorone on pristine and hydrogen-precovered Pd(111) single crystals. In the article in Chapter 7 IR vibrations of isophorone and TMCH are assigned in detail and the molecular structure of both compounds on Pd(111) is discussed. IR studies on acrolein, propanal, and allyl alcohol on Pd(111) are the topic of Chapter 8. In Chapter 9, a mechanistic study on the selective hydrogenation of acrolein on Pd(111) compared to the conversion on Pd/Fe<sub>3</sub>O<sub>4</sub> model catalysts is presented. More detailed studies on acrolein conversion on a Pd(111) single crystal can be found in Chapter 10 and on Pd/Fe<sub>3</sub>O<sub>4</sub> model catalysts in Chapter 11. Finally, Chapter 12 shows a combination of IRAS and TPD studies for more detailed information on the origin of the selective C=C bond hydrogenation over Pd/Fe<sub>3</sub>O<sub>4</sub> model catalyst.

## 2 Theoretical Background

### 2.1 Kinetics at Gas-Surface Interfaces

#### 2.1.1 Basic Kinetics on Surfaces

Understanding the kinetics of a catalytic conversion requires atomistic-level insights into the dynamics of the fundamental gas-surface interactions. Catalytic reactions at surfaces often involve several elementary reaction steps that might exhibit different dynamics and result in overall complex kinetic behavior. In this section, we will focus on basic processes that can occur in a very simple reaction on a surface with a single facet. More complex systems will be discussed in section 2.1.2. Figure 2.1 illustrates the most important elementary processes. In a collision between a molecule and a surface translational and/or internal energy is exchanged. Subsequently, the molecule might scatter back into the vacuum, or it might not escape the potential well and become adsorbed. In the latter case, the species might be trapped in a physisorbed precursor state first, diffuse at the surface and finally chemisorb. The adsorbed molecule may undergo a chemical reaction and desorb, if it gains sufficient thermal energy.

#### Scattering

Atoms or molecules can be scattered from a surface elastically or inelastically. In elastic scattering, the kinetic energy of the species is conserved and the angle of incidence is equal to the angle of scattering [75]. In inelastic scattering, molecules that impinge on the surface gain or lose perpendicular momentum but the parallel momentum is conserved. The angular distribution of inelastically scattered molecules is broader than that for elastic scattering. For instance, molecules with masses like CO, O<sub>2</sub>, or heavier will exchange perpendicular momentum with the surface and thus heat or cool the surface [21].

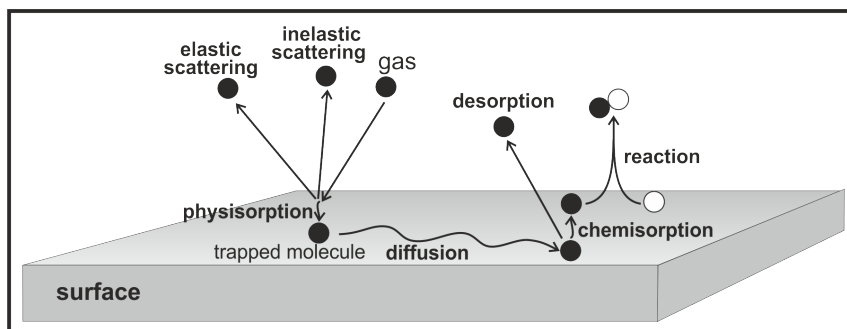


Figure 2.1: Schematic representation of basic processes in gas-surface interactions

### Chemisorption and Physisorption

The adsorption of a molecule is a complex process that usually can be divided into two stages. First there is physisorption, a relatively weak and long-range dipolar interaction between the adsorbate and the surface. Van der Waals interactions cause attractive potentials between the surface and the adsorbate at large distances. Closer to the surface, electronic repulsion becomes dominant, which leads to an increase of the potential energy and defines a *potential well*, in which the molecule can be trapped. Secondly, chemisorption occurs when a chemical bond is formed between the adsorbate and the surface. In this case, the potential of the system decreases along the reaction coordinate until the chemical bond is formed. Often chemisorption follows an initially formed physisorbed precursor state [76].

**Trapping** Trapping describes the adsorption of a species from the gas phase into a gas-surface potential well. The adsorbate thermally equilibrates to the surface. It is mostly associated with non-activated, non-dissociative physisorption [20, 21]. In order to be trapped, the incident species must lose sufficient momentum along the surface normal, for instance through coupling to its momentum parallel to the surface or to surface phonons. Hence, the trapping probability will decrease with increasing energy of the impinging species. However, the trapping probability depends on numerous further parameters such as surface temperature, mass, and chemical structure of the adsorbate [20, 77, 78]. Trapping might be followed by desorption, this process is called *trapping-desorption*. The intensity of the desorbing signal is a cosine distribution around the surface normal and the kinetic energy corresponds to a Maxwell-Boltzmann velocity distribution characteristic for the surface temperature [20, 21, 75].

**Precursor States** A species that has been trapped on a surface might be in a precursor state. The lifetime of a precursor state is short compared to the lifetime of the strongly adsorbed state. Precursor states can exist over sites that are available for chemisorption (intrinsic precursor), but it can also exist over surface sites that are occupied by chemisorbed species (extrinsic precursor). Extrinsic precursor states ensure high sticking probabilities of adsorbates up to high surface coverages, since impinging molecules get trapped and can diffuse along the surface until they find a site available for chemisorption. Physisorption can also be followed by desorption, which then corresponds to the phenomenon of trapping-desorption, which has been discussed before 2.1.1. Figure 2.2 illustrates the different precursor states and the possible pathways of their conversion [20, 76, 77].

**Sticking** Sticking refers to the formation of a chemisorbed species. Often it is formed from a weaker bonded physisorbed precursor state. The fraction of the impinging gas phase molecules that stick to a surface is the sticking coefficient  $S$ , which is generally a function of the coverage  $\Theta$ . Langmuir assumed that molecules impinging on a site occupied by a chemisorbed species will scatter back while species arriving at empty sited will stick with a probability  $S_0$ . According to this model, the sticking probability  $S_L(\Theta)$  decreases

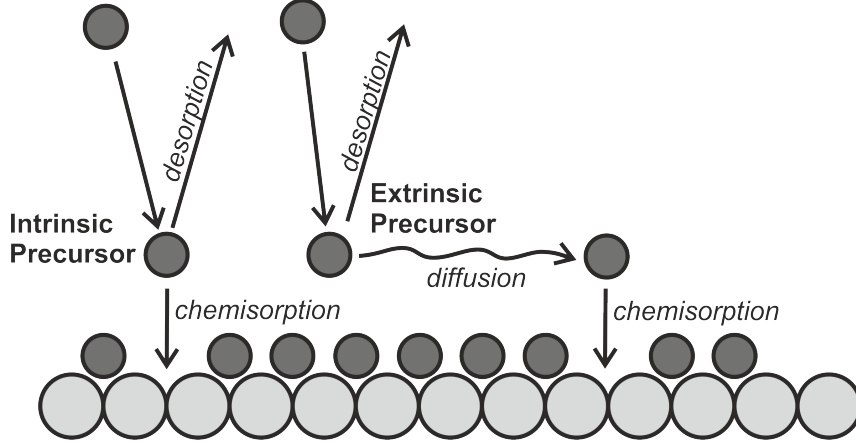


Figure 2.2: Illustration of the adsorption into a precursor state over an empty site (intrinsic precursor) and over a site occupied by a chemisorbed species (extrinsic precursor). The formation of the intrinsic precursor state can be directly followed by chemisorption. During the lifetime of the extrinsic precursor, the adsorbate can diffuse along the surface to find a site available for chemisorption.

linearly with the density of empty sites and thus with the surface coverage  $\Theta$ .

$$S_L(\Theta) = S_0 \left(1 - \frac{\Theta}{\Theta_{sat}}\right)^n \quad (2.1)$$

$\Theta_{sat}$  is the saturation coverage and  $n$  is the order of the adsorption process.

However, in many studies the sticking probability was found to stay high up to high coverages, caused by a *precursor-mediated sticking*. In this process, adsorbates can first be trapped in an extrinsic precursor state that enables them to diffuse along the covered surface to find sites available for chemisorption. Thus, the rate of this precursor-mediated sticking depends on the rate of diffusion of the extrinsic precursor to sites which are available for chemisorption and on the rate of chemisorption from these intrinsic precursor state. This coverage-dependent sticking probability  $S(\Theta)$  was described by Kisliuk as follows:

$$S(\Theta) = S_0 \left(1 + \frac{K_P \Theta}{1 - \Theta}\right)^{-1} \quad (2.2)$$

$S_0$  is the sticking probability on the pristine surface. The *precursor state parameter*  $K_P$  is a measure for the effect of the precursor on the sticking probability. If  $K_P=1$ , the precursor plays no role in the chemisorption process and the sticking probability decreases linearly with increasing coverage, which corresponds to the Langmuir model. Assuming a nearly random distribution of empty and filled sites, which is most likely true for  $\Theta \approx 0$  and  $\Theta \approx 1$ ,  $K_P$  is given by the ratio between the probabilities of desorption from the extrinsic precursor state  $P_{de}$  and adsorption from the intrinsic precursor state  $P_{ai}$ :

$$K_P = \frac{S_0 P_{de}}{P_{ai}} \quad (2.3)$$

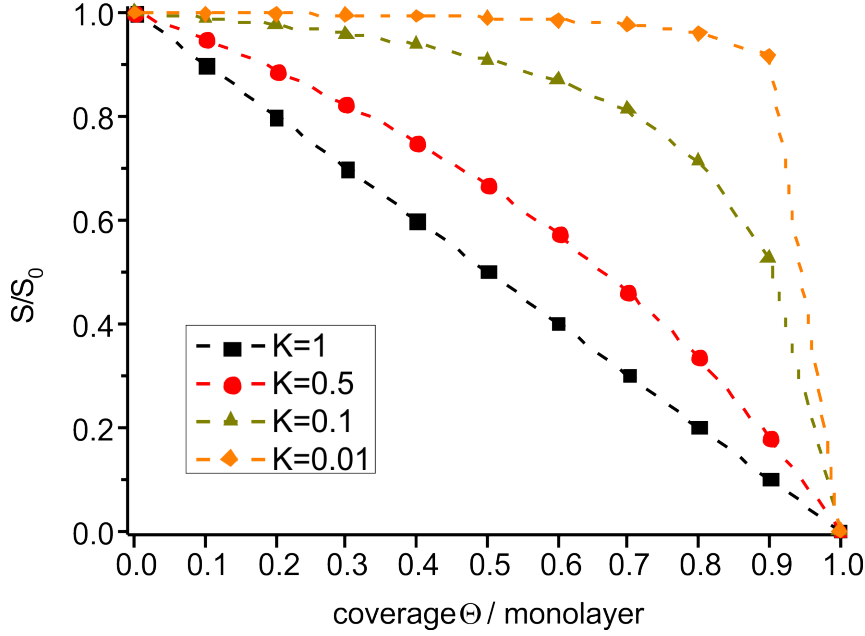


Figure 2.3: The effect of the precursor state parameter on the coverage-dependent sticking probability  $S$  relative to the initial sticking probability ( $S_0$ ).  $K=1$  corresponds to no effect of the precursor states (Langmuir model).  $K=0.01$  corresponds to a strong precursor effect on the chemisorption rate, such as for large organic molecules.

Qualitatively, the precursor states lead to increased sticking when the desorption probability from the extrinsic precursor state is low and the adsorption probability from the intrinsic precursor state is high [79]. Figure 2.3 illustrates the effect of changing precursor state parameters on the coverage dependent sticking probability. The studies in this thesis show that for relatively large molecules such as organic compounds with masses higher than 50 amu, the sticking probability is high until high surface coverages indicating a low desorption rate from the extrinsic precursor states and a high adsorption rate from intrinsic precursor.

### Diffusion and Desorption

After an adsorbed species has entered the potential well of a surface, it can diffuse across the surface or desorb into the gas phase. For diffusion on the energetically corrugated surface, the adsorbate has to overcome the energetic barrier to hop from one potential well to the next one. The activation barrier for diffusion is generally lower than the activation barrier for desorption. As both processes are driven by thermal fluctuations, the surface temperature critically governs the rates of diffusion and desorption.

The root mean square distance  $\langle x^2 \rangle^{1/2}$  that an adsorbate diffuses within its residence time  $t$  on a uniform two-dimensional surface is given by

$$\langle x^2 \rangle^{1/2} = \sqrt{4Dt} \quad (2.4)$$

with  $D$  representing the diffusion coefficient. The diffusion constant is described by an Arrhenius equation with the pre-exponential factor  $D_0$  and the activation energy for diffusion  $E_{diff}$ .

$$D = D_0 \exp\left(\frac{-E_{diff}}{k_B T}\right) \quad (2.5)$$

The rate of desorption  $\frac{-d\Theta}{dt}$  is given by

$$\frac{-d\Theta}{dt} = \Theta^n k_0^{des} \exp\left(\frac{-E_{des}}{k_B T}\right) \quad (2.6)$$

with  $\Theta$  the coverage,  $n$  the desorption order,  $k_0$  the pre-exponential factor for desorption, and  $E_{des}$  the activation barrier for desorption.[20, 75]

### Bimolecular Reactions on Surfaces

Figure 2.4 illustrates two principle ways of bimolecular reactions on surfaces, Langmuir-Hinshelwood (LH) and Eley-Rideal (ER). Most reactions proceed by the LH mechanism, in which both reactants are fully accommodated on the surface before they react. The adsorption process of both reactants might follow the steps that are described above: Physisorption in a precursor state, diffusion between different sites, and chemisorption with and without dissociation. Finally, the adsorbates can react and desorb into the gas phase. The formation rate of the product AB  $\left(\frac{d\Theta_{AB}}{dt}\right)$  out of the reactants A and B in an elementary reaction step is given by:

$$\frac{d\Theta_{AB}}{dt} = k_0^{LH} \exp\left(\frac{-E_{act}^{LH}}{k_B T}\right) \Theta_A \Theta_B \quad (2.7)$$

with  $\Theta_A$  and  $\Theta_B$  representing the surface coverages of species A and B,  $E_{act}^{LH}$  is the activation energy for the reaction, and  $k_0^{LH}$  is the pre-exponential factor.

The ER mechanism describes a far rare type of bimolecular reactions. Here, the reaction occurs between an adsorbate and an incident species, which has not equilibrated to the surface. Evidence for LH or ER mechanisms can be found by molecular beam studies [20, 21].

#### 2.1.2 Kinetic Effects on Model Catalysts

In this thesis reactions are studied on single crystal surfaces as well as on model supported catalysts. A typical model catalyst is based on a thermally stable metal oxide, which supports well-dispersed nanoparticles of a catalytically active metal [9, 12–14, 80]. An example for such a system is Pd nanoparticles supported by an  $\text{Fe}_3\text{O}_4$  film, which will be discussed in more detail in chapter 3.

The global kinetics of reactions on surfaces depend on the kinetics of the elementary processes, which have been described before. However, the kinetics of the elementary

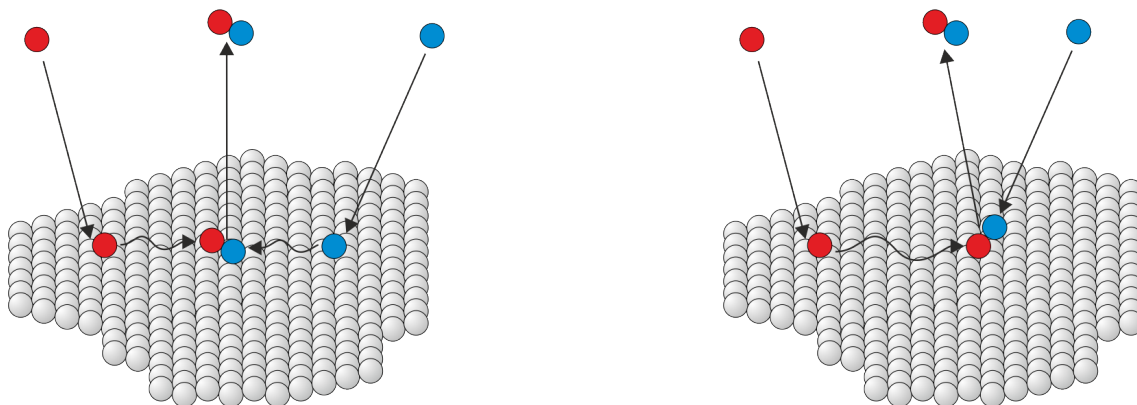


Figure 2.4: Schematics of Langmuir-Hinselwood (LH) (left) and Eley-Rideal (ER) (right) mechanism. In the LH mechanism both reactants are fully accommodated on the surface. In the Eley-Rideal the reaction occurs directly at the point of impact between an incident and an adsorbed species.

steps on a supported model catalyst become complicated due to a large number of non-equivalent sites of the support and the particles. For instance, the support may exhibit regular oxide areas as well as defect sites and chemically modified oxide structures such as hydroxyl groups. Moreover, the particles are terminated by a variety of facets as well as by edge, corner, and defect sites. Additionally, particles and support can be modified by adsorbates that poison or promote a chemical reaction [9].

The kinetic effects on supported catalysts can critically depend on the inherent properties of the supported system. They can tentatively be divided into two groups: On the one hand, phenomena that arise from specific local properties of individual adsorption and reaction sites, involving the interplay with neighboring sites, such as electronic effects; and on the other hand, effects which evolve from the complexity of the whole system, such as diffusion between different sites [9].

### Local Kinetic Effects

*Support Effects.* It was recognized that the support does not only stabilize the dispersion of metal particles, but it can also be directly involved in a catalytic conversion (*e.g.* reduction of NO [81–83]).

Adsorption of reactants on the support might be coupled to chemical reactions on the metal by diffusion between binding sites. Reactants can be trapped on the support and when their mean path is long enough they can reach a particle. The area around a particle which provides additional reactants is called *capture zone* [84, 85]. Moreover, adsorbates can be formed on particles by an activated process and diffuse onto the support (*spillover*) or vice versa (*reverse-spillover*) [86, 87]. Additionally, interactions between the support and the particles can modify the adsorption and reaction properties of the metal. Such an example is the phenomenon of *strong metal-support interactions (SMSI)* for metals on reducible oxide supports [88].

*Electronic Effects.* The electronic structure of a small particle might be different from that of an extended metal due to electron confinement, or interactions with the support might influence the electronic properties. Moreover, interface sites between metal and support as well as adsorbed promoters or poisons can cause local electronic effects [89].

*Geometric Effects.* An inherent property of particles is their termination by different facets and specific sites, such as edges and corners, which are not present on single crystal surfaces. Different sites may have different reactivity in specific steps of the chemical conversion. [9, 10].

### Kinetic Effects resulting from overall Complexity of Model Catalyst System

*Communication Effects.* Surface areas with different adsorption and reaction properties can be coupled by fast diffusion. Spillover or capture zone effects are specific cases of communication effects. Coupling between different sites can drastically influence the global reaction kinetics. The observed kinetics can be very different from pure superposition of the kinetics of the individual surface sites [90, 91].

*Confinement Phenomena.* The mobility of an adsorbate can be limited to one particle. This might result in coverage fluctuations along the surface. Moreover, diffusion into the bulk is restricted by the limited size of the particles. Both effects can change reaction kinetics as compared to an extended single crystal [92–94].

*Restructuring Effects.* Adsorbates might induce restructuring or refaceting, such as changes of the particles equilibrium shape or bulk phase transformation (*e.g.* oxidation) [95]. Especially on small particles, restructuring is expected to appear frequently, with large impact on the reaction equilibrium [9].

## 2.2 Experimental Methods

### 2.2.1 Molecular Beams

Molecular beam (MB) techniques are a well established tool in various kinds of research on chemical dynamics. General overviews on MB techniques [96–99] and more specific summaries of MB applications to study kinetics of surface reactions [9, 20, 21, 89, 100–103] can be found elsewhere. Here, we will focus on the application of molecular beams to study reaction kinetics.

**Principle of Molecular Beams** A molecular beam is a spatially well-defined, directed and collision-free flow of molecules. A molecular beam source is schematically illustrated in Figure 2.5. It is produced by expansion of a gas from a so-called stagnation stage into vacuum. An aperture or skimmer cuts a small solid angle to form a directed beam, which can be further modified in various ways. To separate the beam from background molecules, several pumping stages are usually implemented. A temporal structure can be

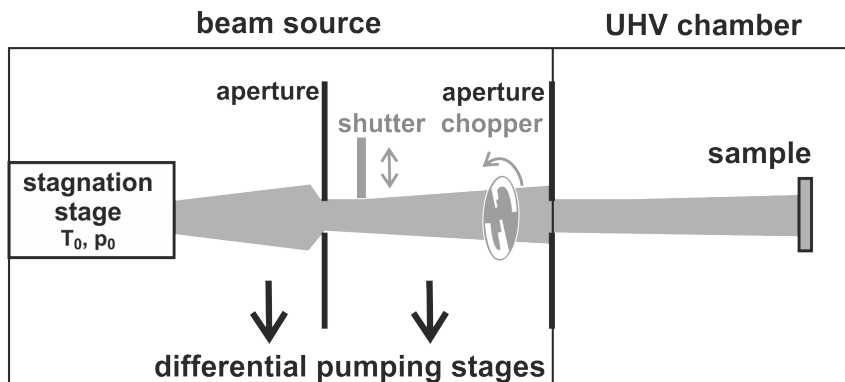


Figure 2.5: Schematic illustration of a molecular beam source for gas-surface experiments.

prepared by using a chopper or a shutter and the external and internal degrees of freedom can be controlled via state-preparation techniques.

**Molecular Beams in Model Catalysis** In order to study chemical reactions over single crystals or model catalysts, the reactants can either be introduced via the background or by crossing of multiple molecular beams. The latter method is of advantage due to the larger degree of control and the lower background pressure during the experiment. UHV background pressure provides a collision-free environment for the molecules in the beam. While the background pressure is low, local pressures up to  $10^{-5}$  mbar can be obtained at the sample position. The main advantages of the molecular beam approach over simple traditional reactor studies arise from the fact that a molecular beam experiment is performed under *single collision conditions*. In other words, every molecule interacts exactly once with the sample in an otherwise collision-free environment. The experimental advantages can be summarized as follows:

- **Determination of absolute reaction probabilities:**  
Single collision conditions make it possible to exactly determine the number of surface events and thus the absolute probability of a surface process, *e.g.* adsorption or reaction. This ability is particularly interesting for studies on heterogeneous or nanostructured surfaces. The dependence of a reaction rate on the surface structure can give insights into coupling effects between surface areas via diffusion.
- **Fast flux modulation:**  
Temporal flux modulation in transient experiments gives information on micro-kinetic processes. Combined with mass spectrometry, the method is called *molecular beam relaxation spectroscopy* (MBRS).
- **Control over dynamic properties of incident molecules:**  
The collision-free environment ensures that the molecules approach the surface as prepared by the beam. A beam of molecules with a certain kinetic or internal energy can be prepared by using distinct state-preparation techniques to study dynamics of gas-surface interactions and the potential energy surface.

- Detection of scattered and desorbed molecules:  
The collision-free environment ensures that the molecules approach a detector with the same kinetic energy, internal energy distribution and angular distribution as they left the sample surface. Thereby, details on the potential energy surface, which determines processes like desorption, reaction, or scattering, can be obtained.
- Chemical complexity available for surface science methods:  
The pressure of the reactants at the sample position is several orders of magnitude higher than the UHV background. Thus, a chemically complex situation is made available for surface science techniques.

Molecular beam sources can be divided into two categories: *effusive sources* and *supersonic sources*. The two types can be distinguished by the expansion conditions, resulting in specific energy distributions of the molecules in the beam. The conditions of the expansion are classified by the *Knudsen number*  $Kn$ :

$$Kn = \frac{\lambda}{d} \quad (2.8)$$

where  $\lambda$  is the mean free path of the gas molecules and  $d$  the source aperture dimension.

**Effusive beam sources** Effusive beam sources operate at large Knudsen numbers. Physically this means that the pressure  $p_0$  in the stagnation state is kept sufficiently low to maintain molecular flow during the expansion. Under such conditions, the number of intermolecular collisions is kept low and the energy distribution in all degrees of freedom is described by the temperature of the gas in the stagnation stage  $T_0$ . The velocity  $v$  of the gas molecules with mass  $M$  follows a Maxwell-Boltzmann distribution:

$$I = Nv^3 \exp\left(-\frac{Mv^2}{2kT_0}\right) \quad (2.9)$$

There are several possibilities to realize an effusive expansion. The simplest design is a thin-walled orifice, which produces a cosine angular flux distribution (Figure 2.6a). To produce a beam, a small solid angle is extracted and the rest of the gas is removed by differential pumping. The available pumping speed in the expansion chamber is typically the limiting factor for the maximum beam intensity. A more collimated flux and thus larger beam intensities can be achieved by using a capillary array instead of an orifice. In the absence of intermolecular collisions, only the molecules flying parallel to the center line can path the channels (Figure 2.6b).

The angular distribution of the beam is a function of the ratio of length ( $L$ ) to the radius ( $r$ ) of the channels. The collimation can be described by the *peaking factor*  $\kappa$ , which equals the ratio of the center-line intensity of the actual distribution  $I(0)$  and the center-line intensity of the cosine distribution at identical total flux  $\dot{N}$ . At low pressure and sufficiently long channels,  $\kappa$  can be approximated as follows [104]:

$$I = \frac{\pi}{\dot{N}I(0)} = \frac{3L}{8r} \quad (2.10)$$

## 2 Theoretical Background

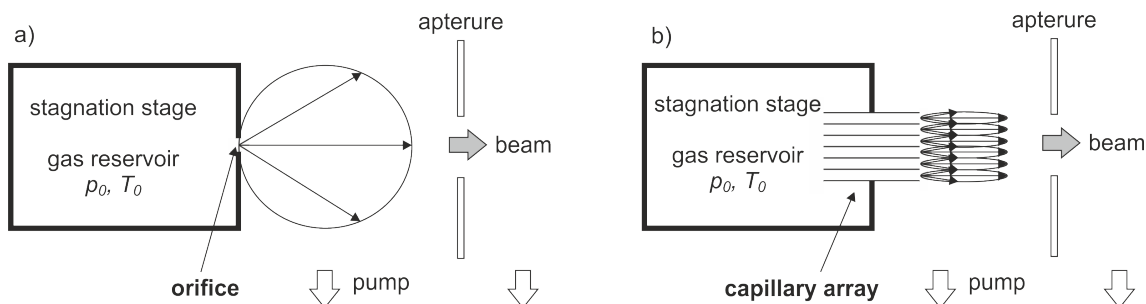


Figure 2.6: a) Schematic illustration of an effusive beam source based on a thin-walled orifice with cosine angular distribution. b) Illustration of the focusing effect of a capillary array. Smaller amounts of gas have to be removed and pumped with the capillary array as compared to the orifice.

A typical  $L/r$  value of 40 gives a peaking factor  $\kappa$  of about 15. For comparison,  $\kappa$  for supersonic beam sources is in the range of 1.1 to 2.0 only. With increasing stagnation pressure, the mean free path of the molecules approaches the channel length. Intermolecule collisions lead to a broadening of the angular distribution and thus to a deviation from the Maxwell-Boltzmann velocity distribution. This pressure limit is higher for channels with smaller overall dimensions; however, the total flux of molecules through small channels is low. The problem is solved by using a large number of parallel arrays of small channels. Such multi-channel arrays (MCA) are capable of providing a collimation effect at high stagnation pressure and thus at high total flux. The high flux through MCA is of advantage for studies in surface kinetics, where a high maximum intensity is required, while the energy distribution is of minor importance. Further advantages of MCA can be summarized as i) variable beam flux over several orders of magnitude without changes of the beam properties, ii) high maximum intensity at reduced pumping requirements, iii) low stagnation stage pressures for reactants with low vapor pressure and iv) low gas consumption.

**Supersonic Beam Source** Supersonic beams operate at low Knudsen numbers ( $Kn \ll 1$ ). This corresponds to an expansion from a high pressure stagnation stage, where collisions between molecules are frequent, through a nozzle. A supersonic beam source is schematically illustrated in Figure 2.7a. The gas in the reservoir (Mach number  $M \ll 1$ ) is accelerated by the pressure drop in the nozzle. The flow may reach sonic speed ( $M = 1$ ) at the exit of the nozzle and supersonic speed ( $M > 1$ ) in further expansion. A skimmer extracts a small solid angle of the beam. It can be further collimated by apertures and modified by a shutter or a shutter.

Inside the nozzle, frequent collisions between the molecules lead to an equilibration of their kinetic energies and to a narrow velocity distribution in the direction of the expansion as compared to the Maxwell-Boltzmann distribution. The velocity of the molecules rapidly approaches an asymptotic value and the translational temperature decreases until there is a transition to molecular flow (2.7b). The parallel velocity distribution for the flux

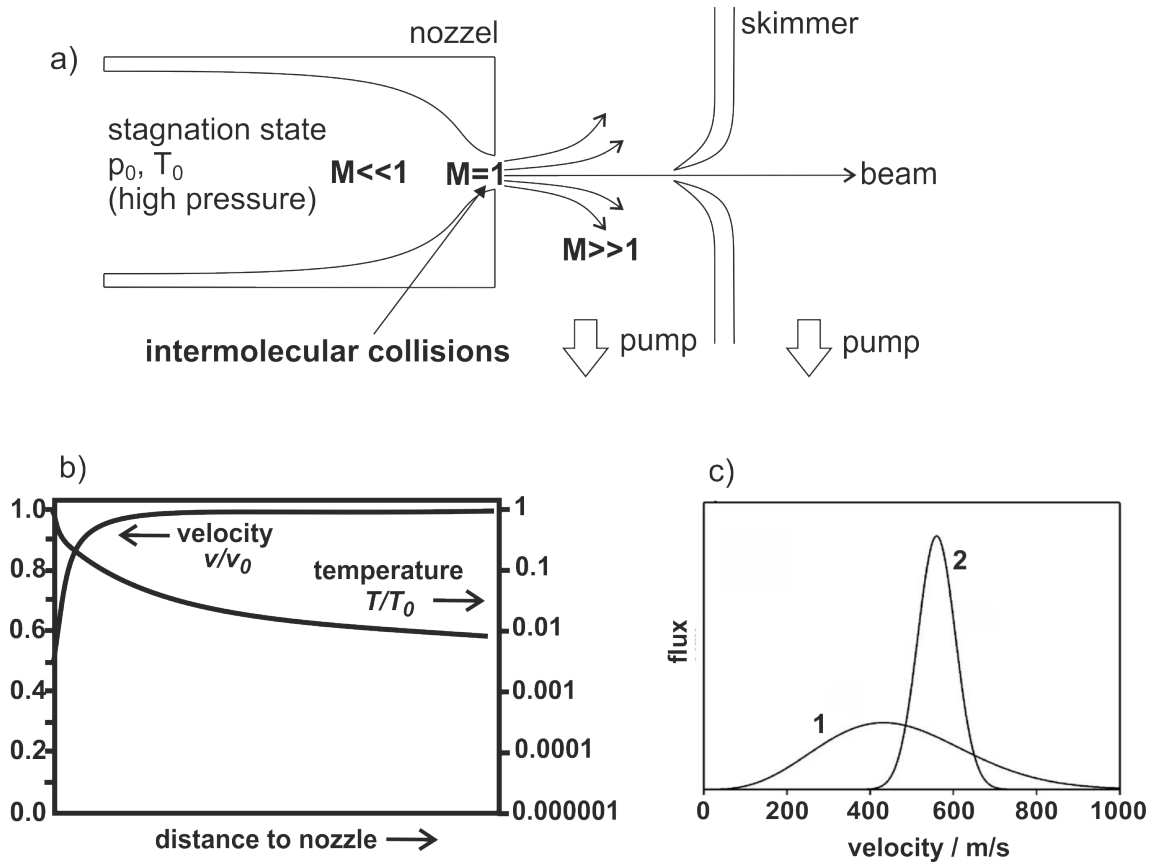


Figure 2.7: a) Schematic illustration of a supersonic molecular beam expansion; b) temperature and velocity of the beam as a function of the distance from the nozzle; c) velocity distribution before (1) and after (2) expansion (for Argon at 300 K) from [9]

## 2 Theoretical Background

$I_{\parallel}$  is generally modeled by a shifted Boltzmann distribution and is characterized by the translational temperature  $T_{\parallel}$  (Figure 2.7c).

$$I_{\parallel} \propto v^3 \exp \left( -\frac{M(v - v_{\parallel})^2}{2kT_{\parallel}} \right) \quad (2.11)$$

with  $v_{\parallel}$  denoting the parallel flow velocity and  $M$  the molecular mass of the molecules or atoms in the beam [9].

The relaxation of internal energies depends on the number of molecular collisions and the energy transfer between the degrees of freedom. In general, the cooling is efficient for rotational degrees of freedom and less efficient for vibrational degrees of freedom.

The main advantages of supersonic beam sources are i) the narrow velocity distribution, ii) the possibility to control the kinetic energy by state-preparation techniques and iii) the large degree of control over the internal energy. Therefore, supersonic beams are very suitable for studies of gas-surface dynamics, surface scattering, and fast transient kinetics.

### 2.2.2 Infrared Spectroscopy

Infrared (IR) spectroscopy is a powerful tool to study the interaction of molecules with surfaces. Molecular vibrations are excited by the absorption of IR light. The vibration frequency gives detailed information about chemical bonds and thus about the interaction of the molecule with the metal surface [105–109]. The vibration frequency of covalent bonds in some adsorbates, such as CO, does not only depend on the metal, but also on the specific site to which they are attached. Therefore, CO adsorption is frequently used to characterize the morphology of a surface (see chapter 3.2.1). This kind of information can also be obtained under reaction conditions, providing information which sites are populated during a chemical conversion. Moreover, in some cases reaction intermediates can be identified, which gives insights into the mechanisms of the reaction.

#### Molecular Vibrations

The excitation of molecular vibrations by IR light can be described as a pure time-dependent perturbation, since the electromagnetic field is approximately constant over the size of the excited dipole [110]. Thus, the Hamilton operator  $H^{(1)}$  of the perturbation can be described as

$$H^{(1)} = -\vec{\mu} \cdot \vec{E} \quad (2.12)$$

with  $\vec{\mu}$  the electric dipole moment of the molecule and  $\vec{E}$  the electric field vector of the electromagnetic radiation [111].

According to Fermi's Golden Rule, the probability for an excitation is given by

$$W \propto \left| \langle \psi_f | \vec{\mu} \cdot \vec{E} | \psi_i \rangle \right| \quad (2.13)$$

with  $\psi_f$  and  $\psi_i$  the eigenfunctions in the excited and the ground state. The Born-Oppenheimer approximation (BOA) allows to break the eigenfunctions into its electronic  $\epsilon$  and nuclear (vibrational)  $\nu_k$  compound.

$$\psi = \langle \epsilon, \nu'_k | \vec{\mu} | \epsilon, \nu_k \rangle \quad (2.14)$$

with  $\nu_k$  and  $\nu'_k$  representing the eigenfunction of the vibration before and after the excitation.

Within the BOA, both compounds can be treated separately. Thus, the probability for a vibrational excitation along the normal coordinate  $Q_k$  is given by

$$\langle \nu'_k | \vec{\mu} | \nu_k \rangle = \left\langle \nu'_k \left| \vec{\mu} + \sum_i \left( \frac{\partial \vec{\mu}}{\partial Q_i} \right)_0 Q_i + \dots \right| \nu_k \right\rangle = \left( \frac{\partial \vec{\mu}}{\partial Q_k} \right)_0 \langle \nu'_k | Q_k | \nu_k \rangle \quad (2.15)$$

Therefore, a vibration can only be IR-active, if it involves a dynamic dipole moment:

$$\frac{\partial \vec{\mu}}{\partial Q_k} \neq 0 \quad (2.16)$$

### Infrared Spectroscopy on Metal Surfaces

Vibrational spectra of molecules on metal surfaces can be obtained by *infrared reflection-absorption spectroscopy* (IRAS) in a reflection mode. In this case, the *metal surface selection rule* (MSSR) has to be taken into account [106, 112, 113]. According to the MSSR, only the components of the dynamic dipole moments perpendicular to the surface can be detected because dipoles parallel to the surface are compensated by a mirror dipole in the metal. Moreover, IR light with polarization parallel to the surface (s polarization) is reflected with a phase shift of  $180^\circ$  leading to almost complete vanishing of the s polarized field. In contrast, the effective field of the p polarized light is almost doubled at angles close to grazing incidence. Therefore, IRAS measurements are typically performed only with p polarized light. Taking the MSSR into account, adsorption geometries of molecules on metal surfaces can be deduced from characteristic intensity distributions of IR absorption peaks.

### IRAS of adsorbed Molecules

The vibration frequencies of adsorbed molecules can be significantly different from gas phase species, due to the interaction with the metal surface or inter-adsorbate interactions [105, 106, 113].

**Frequency shifts by metal-adsorbate interaction** There are four important effects, which are responsible for frequency shifts of an isolated adsorbate.

*Mechanical renormalization.* Adsorption of a diatomic molecule (*e.g.* CO) to a rigid surface will result in a purely mechanical shift of vibration frequencies (*e.g.* C–O stretch).

## 2 Theoretical Background

The shift can be estimated from a simple model of masses and springs. In case of the metal–C–O system, the C–O stretching shifts of  $50\text{ cm}^{-1}$  to higher wavenumbers as compared to the gas phase. In case of a vibrating substrate, additional renormalization appears [114].

The renormalization model predicts a frequency shift to higher wavenumbers; however, experimental results indicate mostly lower frequencies for adsorbed molecules. This indicates that this model alone is not sufficient to describe the experimental results.

*Chemical shifts.* Chemical shifts arise from chemical interaction between the molecule and the substrate. Chemical shifts were found to be responsible for the appearance of several IR vibrations of CO adsorbed on supported transition metals. A theoretical description of this phenomenon has been given by Blyholder [115, 116]. In this model, a chemical bond between CO and the metal is formed by charge transfer from the  $5\sigma$  orbital of CO into the metal ( $\sigma$  bonding) and from the metal d-bands into the unoccupied  $2\pi^*$  orbital of CO ( $\pi$  backbonding). The  $\sigma$  bonding increases the C=O bond strength while the  $\pi$  backdonation weakens the C=O bond. Since the  $\pi$  backdonation is dominant on transition metal surfaces, the C=O bond is weakened. Thus, the degree of backdonation into the antibonding  $2\pi^*$  is directly reflected by the lowering of the C=O stretch frequency.

*Self-image shifts.* The adsorbate can interact with its own image dipole in the metal. This effect tends to lower the vibration frequency in the case of adsorbed CO.

*Charge transfer.* Charge transfer between the substrate and the adsorbate results in electrostatic interaction and therefore causes a frequency shift. Theoretical calculations showed a shift of  $10\text{--}20\text{ cm}^{-1}$  for a single adsorbed non-polar molecule, such as CO [117].

The effects of the substrate–adsorbate interaction on vibrational frequencies is widely used in surface science to identify adsorption sites. For example, the C=O stretch frequency generally decreases with increasing coordination number. In this work, the Pd surface was saturated with CO in order to probe different surface sites.

**Frequency shifts by adsorbate–adsorbate interaction** While the vibrational frequency of an isolated molecule typically undergoes a shift to lower wavenumbers by means of the substrate–adsorbate interaction (redshift), an increase of the frequencies is typically observed with increasing surface coverage (blueshift). This blueshift arises from the lateral interaction between adsorbates. Here, we will summarize three major effects:

*Dynamic dipole–dipole coupling.* Vibrational coupling between adsorbates can appear as through-space dipole–dipole coupling [118]. As the distance between adsorbates decreases, this effect becomes increasingly important. The dynamic dipole–dipole interaction increases the vibration frequency.

*Chemical shifts.* Chemical shifts have been discussed as a phenomenon of the adsorbate–metal interaction before. However, with increasing coverage, adsorbates compete for d-electrons of the metal, which decreases the strength of the  $\pi$  backdonation.

*Static dipole–dipole interaction.* The vibrational frequency of an adsorbate is affected by an electric field, which is created by neighboring static dipoles. This effect is typical for co-adsorbed dipoles with significantly different vibration frequencies. The shift depends on the orientation of the two dipoles: parallel orientation results in a blueshift, while an antiparallel orientation leads to a redshift [119].

**Intensity changes** The intensity of the IR absorption of adsorbed molecules is not only influenced by the MSSR, but also by adsorbate–adsorbate interactions. In the low coverage limit, the intensity is proportional to the number of vibrating dipoles. With increasing coverage, the intensity is subject to the influence of the effects described above: static and dynamic dipole–dipole coupling and chemical effects. The impact of these effects on the IR absorption intensities is non-linear with increasing coverage.

One frequently observed effect is known as *intensity borrowing*. This effect can lead to difficulties in identification of species on a surface. If a surface is populated with two species with slightly different vibration frequencies, dipole–dipole coupling can result in intensity transfer from the IR adsorption at the lower frequency to the one at the higher frequency. This effect can result in strong changes in the intensity distribution between different species.

### Fourier-Transform Infrared Spectroscopy

Fourier-transform (FT) IR spectrometers [108, 109, 120] are the most commonly employed IR spectrometers. They have a number of advantages over dispersive spectrometers. In dispersive spectrometers, the sample is exposed to monochromatic light and the absorption is detected at each wavelength individually. In FT-IR spectrometers the sample is exposed to light from a wide spectral range. The absorption data in the whole spectral range is collected simultaneously. An FT-IR spectrometer consists of an IR source, a Michelson interferometer, an IR detector and a computer. The principle is illustrated in Figure 2.8.

In the interferometer, the radiation from the source is passed through a beam splitter, which reflects half of the light to a fixed mirror and passes the other half to a movable mirror. The two beams are reflected from the mirrors and interfere again at the beam splitter. The recombination will be constructively or destructively, depending on the path difference. The position of the movable mirror ( $x$ ) is altered and the detector collects the beam intensity as function of the mirror displacement  $I(x)$ , which is called *interferogram*. For monochromatic light, the detected intensity is a cosine function of the mirror displacement. For polychromatic light, the interferogram is the sum of all interferences of each wavelength. With path difference  $x = 0$ , constructive interference of all waves occurs, resulting in a maximum intensity of the interferogram. With increasing distance to  $x = 0$ , most waves undergo partial or total destructive interference, which leads to rapidly decaying oscillations on both sides of the center. The intensity of the light at frequency  $I(\nu)$  is obtained by Fourier transformation of  $I(x)$ .

$$I(\nu) = \int_{-\infty}^{\infty} I(x) \cos(2\pi\nu x) dx \quad (2.17)$$

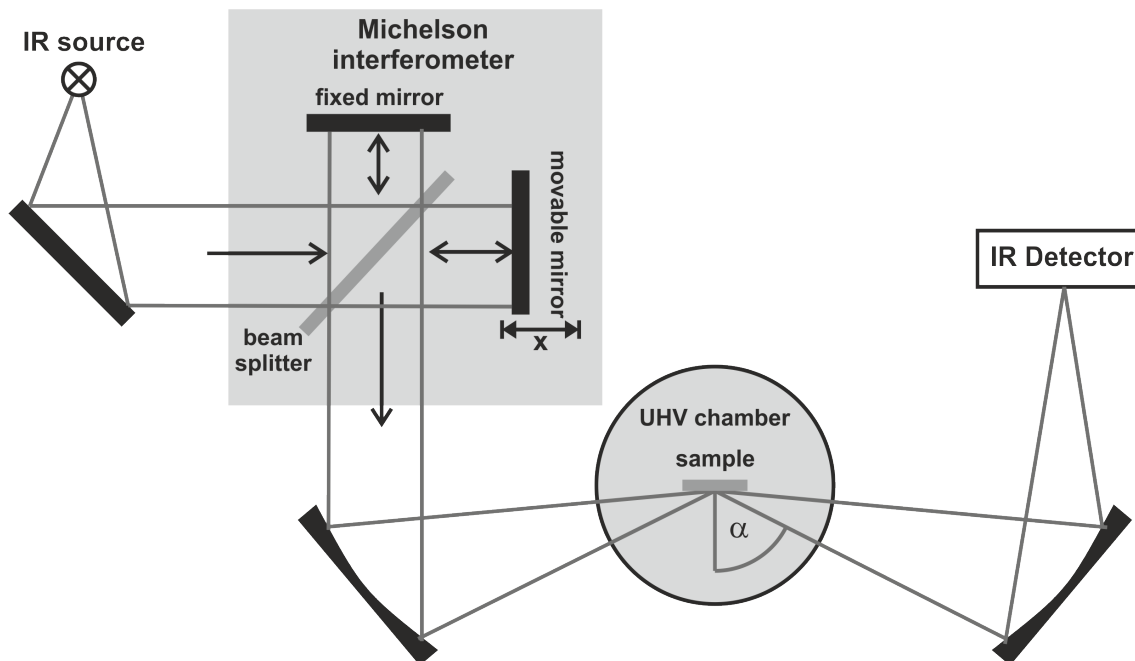


Figure 2.8: Schematic of an FT-IR spectrometer with Michelson interferometer.

### 2.2.3 Quadrupole Mass Spectrometry

Mass spectrometry is a well established technique for analyzing the chemical composition of a gas phase. Detailed introductions can be found in literature [121–123]. In this work, quadrupole mass spectrometry (QMS) was employed, which is a widely used technique in vacuum science. The principle of QMS is based on three steps: gas is ionized, the ions are selected by their mass to charge ratio ( $m/z$ ), and subsequently quantitatively detected by a channeltron electron multiplier. Hence, a QMS setup consists of an ionizer, a quadrupole mass filter, and a detector. The setup is schematically illustrated in Figure 2.9.

The mean free path of the ions should be long enough to allow collision-free travelling from the ion source to the detector. Therefore, typically gas pressures below  $10^{-4}$  mbar

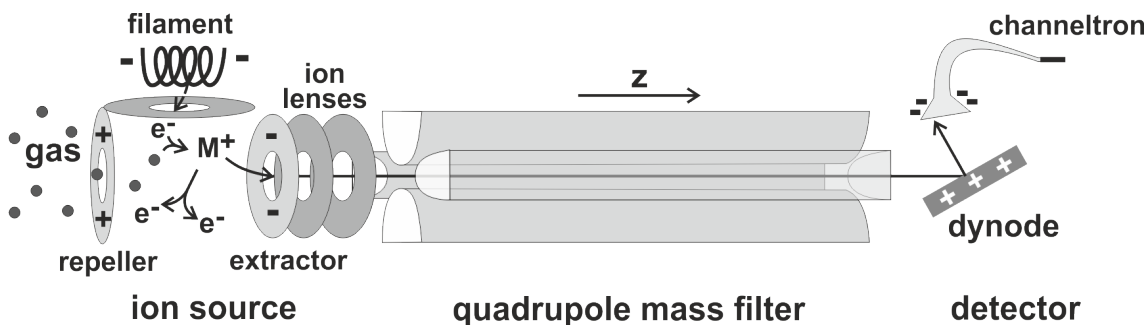


Figure 2.9: Illustration of the principle of a quadrupole mass spectrometer (QMS) with an ion source, a quadrupole mass filter and a channeltron detector.

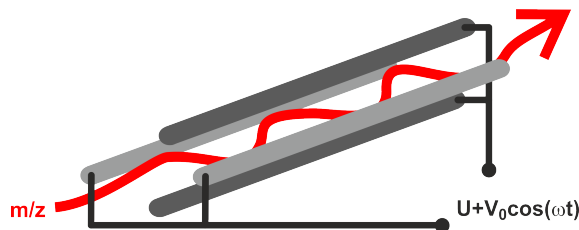


Figure 2.10: Schematic representation of a quadrupole mass filter

are required.

**Ionization** Neutral gas atoms or molecules can be ionized using different procedures. A common method for gas compound ionization, which was applied in this work, is the ionization by electron impact. In this case, the gas is bombarded by electrons accelerated from a filament. If the kinetic energy of the electrons is higher than the first ionization potential, the gas species  $M$  can be ionized:



Furthermore, if enough energy is transferred to the ion, fragmentation will occur.



At a typically applied acceleration voltage of 70 eV, a significant portion of the ions will undergo fragmentation, especially larger organic compounds. Large organic molecules will give characteristic fragmentation pattern. We took advantage of this effect to resolve two species with the same molecular mass, propanal and propenol.

**Quadrupole Mass Filter** Ions with different mass-to-charge ratios ( $m/z$ ) can be separated in a static or periodic electromagnetic field. In the present work, a quadrupole mass filter was used, which is schematically illustrated in Figure 2.10. In a quadrupole mass filter, the ions with different  $m/z$  ratio are separated in an oscillating field. It consists of four parallel metal rods, opposing rods are on the same potential. Between the two pairs of rods, a radio frequency voltage ( $V_0 \cos(\omega t)$ ) and a direct current voltage ( $U$ ) are superimposed. Ions propagate along the quadrupole in an oscillating motion, described by Mathieu's differential equation, which shows that there are stable and unstable pathways. For specific parameters  $U$  and  $V_0 \cos(\omega t)$ , only ions with certain  $m/z$  ratio pass the filter. Ions on an unstable path, gradually approach the electrodes until they collide with one of them.

**Detector** A common detector for ions is a channeltron electron multiplier (CEM), which was used in our setup. The main advantages are a high temporal resolution and a high signal-to-noise ratio. A CEM is based on a material, which emit secondary electrons when a cation with sufficiently high energy hits the surface. An electric field is applied along the length of the CEM to accelerate the electrons. On their travel towards the anode,

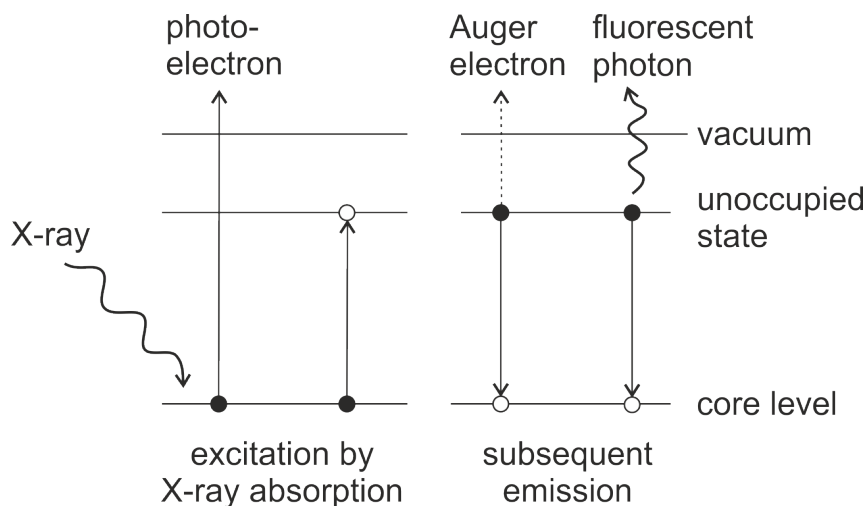


Figure 2.11: Energy diagram of the photoabsorption process by emission of a photoelectron or population of an unoccupied state and the subsequent filling of the core hole by emission of a photon or Auger electron.

their impact on electron emitting material creates an avalanche of secondary electrons, generating amplification factors up to  $10^8$ .

#### 2.2.4 Near Edge X-Ray Absorption Fine Structure

Near-edge X-ray absorption fine structure (NEXAFS) spectroscopy probes electronic transitions from a core level (*e.g.* from K-shell) to an unoccupied orbital or continuum state. Detailed information can be found in literature [124–128]. Typically, strong and distinctive transitions to unoccupied molecular orbitals (MO) appear in the energy region from just below to about 50 eV above the core level ionization edge (*e.g.* K-edge).

During the measurement, the sample is irradiated with monochromatic X-rays. The energy of the X-rays is varied in the desired range. The dominant process is absorption, which results in a core hole and an excited electron. The electron can either be excited to the vacuum (emission as photoelectron), or to an unoccupied MO. The hole is subsequently filled with an electron, either radiatively by emission of a fluorescent photon or non-radiatively by emission of an Auger electron. The emission of a photon or electron is a direct measure for the existence of a core hole and thus for the preceding X-ray absorption. A corresponding energy diagram is illustrated in Figure 2.11.

#### Information on electronic Structure

In NEXAFS studies, the dependence of the photoabsorption cross section on the energy of the incident X-ray beam is investigated. The spectra are dominated by a step function, which results from the excitation of a core electron to the vacuum. Near the step, resonant transitions to unoccupied MO are superimposed. Such excitations occur if the energy of the X-ray matches the energy difference between the initial state and an unoccupied MO.

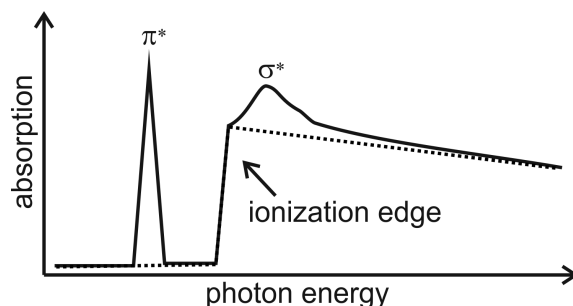


Figure 2.12: A schematic NEXAFS spectrum with ionization potential and resonant transitions to  $\pi^*$  and  $\sigma^*$  orbital (adapted from [124]).

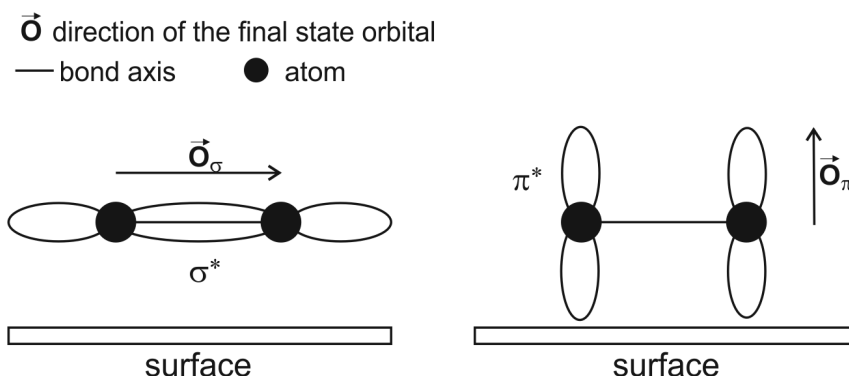


Figure 2.13: Illustration of the polarization dependence of transition resonances to  $\sigma^*$  and  $\pi^*$  MO. The maximum amplitude of a  $\sigma^*$  orbital is along the bond axis and the maximum amplitude of the  $\pi^*$  orbital is along the normal of the bond direction. The electric field vector has to match the polarization of the MO in order to excite the transition (adapted from [124]).

In unsaturated hydrocarbons, excitations to the first unoccupied  $\pi^*$  MO appear below the ionization step while excitations to  $\sigma^*$  MO have higher energy than the step edge. A schematic illustration of a NEXAFS spectrum is shown in Figure 2.12.

### Information on molecular Orientation

In addition to the information on the electronic states of molecules, NEXAFS can also provide information on their orientation. Molecular bonds and their MO are highly directional. Therefore, the transition intensity of a K-shell spectrum depends not only on the energy, but also on the orientation of the electric field vector relative to the orientation of the MO.  $\sigma$  orbitals have a maximum amplitude along the bond axis while  $\pi$  orbitals have a maximum amplitude perpendicular to the bond axis. The polarization dependence of NEXAFS transitions is illustrated in Figure 2.13. In contrast, the excitation of electrons to the vacuum is independent from the polarization. Therefore, the intensity of the step function can be used to normalize the spectra.

## 2 *Theoretical Background*

Measuring the dependence of the transition intensity on the polarization of the X-ray beam can be achieved in two ways. Either the geometry between the sample and the X-ray beam is varied with fixed beam polarization; or the beam is switched between s and p polarization while the sample–beam geometry is fixed at small incident angle. The latter method has two major advantages. On the one hand, exactly the same region of the surface is probed in both measurements, in contrast to angular-dependent investigations, where a large surface area is probed at small incident angles and a small are at large incident angles. On the other hand, the experiment are much less time-consuming. Typically, switching the polarization of the beam takes much less time than aligning the sample before each measurement.

### 3 Pd/Fe<sub>3</sub>O<sub>4</sub> Model Catalysts

Since several decades, surface science methods are successfully applied to study chemical reactions over single crystal surfaces, including stepped and defect-rich surfaces [11, 129, 130]. Studies on these systems give valuable information on the reactivity of different surface facets or specific sites. In this work, a Pd(111) single crystal was used to study the adsorption and intrinsic reactivity of hydrocarbons on (111)-facets. However, single crystals only poorly resemble industrial catalysts, which are highly complex materials with respect to their composition and structure. Generally, single crystals cannot reproduce the characteristic structural and electronic properties of supported catalysts, which are responsible for the kinetic effects that we discussed in chapter 2.1.2. To overcome this limitation, model supported catalysts have been developed two decades ago by several groups [10, 12–19, 131]. In model catalysts, distinct structural complexity is introduced in a well-defined manner to mimic properties of industrial catalysts. In contrast to industrial catalysts, model catalysts are fully accessible by surface science methods and their structure can be characterized in great detail.

A model catalyst is based on a well-defined thin metal oxide film that is grown onto a single crystal substrate. The oxide film acts as support for particles of the catalytically active metal. The underlying metal single crystal as a substrate ensures a macroscopically planar structure and good electric and thermal conductivity, which is required for many surface science techniques. There are two principle ways of preparing thin oxide films on top of a conducting substrate: either by oxidation of the single crystal substrate [132–135] or by deposition of the metal onto the substrate and subsequent oxidation [136, 137]. In this study, we used the latter method to grow an iron oxide film on a Pt(111) substrate. On the Fe<sub>3</sub>O<sub>4</sub> film, Pd particles are deposited as the active phase of the catalyst. The preparation of the Pd/Fe<sub>3</sub>O<sub>4</sub>/Pt(111) model catalysts is schematically illustrated in Figure 3.1. It will be discussed in more detail in the following part of this chapter.

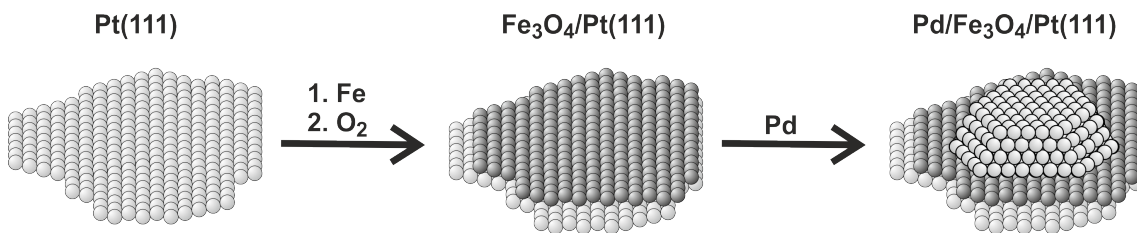


Figure 3.1: Preparation of the Pd/Fe<sub>3</sub>O<sub>4</sub>/Pt(111) model catalysts

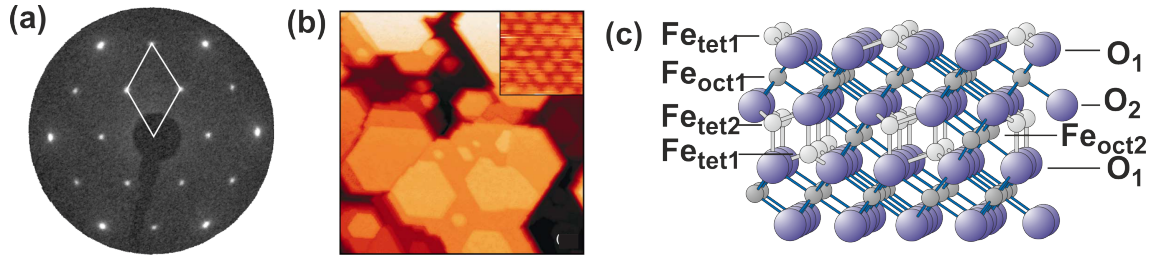


Figure 3.2: (a) LEED diffraction pattern and (b) STM image of an Fe<sub>3</sub>O<sub>4</sub> film; (c) model of the crystal structure of Fe<sub>3</sub>O<sub>4</sub> (from [142])

### 3.1 Fe<sub>3</sub>O<sub>4</sub> film on Pt(111)

The preparation and growth of iron oxide on a Pt(111) single crystal substrate have been described in detail in literature [138–143]. First, a monolayer of FeO is grown on a clean Pt(111) single crystal by physical vapor deposition of iron from an electron beam evaporator under UHV at 125 K and subsequent oxidation in  $1 \cdot 10^{-6}$  mbar O<sub>2</sub> at 990 K. To avoid sputtering damages to the surface, the same potential was applied to the sample as to the iron evaporant in the evaporator. Next, Fe<sub>3</sub>O<sub>4</sub> is prepared on top of the FeO by cycles of 4–6 ML Fe deposition under UHV at room temperature, followed by oxidation in  $1 \cdot 10^{-6}$  mbar O<sub>2</sub> at 900 K. After six cycles, an approximately 10 nm thick film is obtained.

The morphology of the first Fe layer strongly influences the structure of the subsequently formed Fe<sub>3</sub>O<sub>4</sub>(111) film. Fe deposition at low temperature is required to ensure a complete wetting of the Pt(111) surface and thus to form a 2D FeO(111) layer. Fe<sub>3</sub>O<sub>4</sub> grows on top of the FeO film first as three-dimensional islands. With increasing coverage, the islands grow and coalesce to form a closed and flat Fe<sub>3</sub>O<sub>4</sub> film. The sharp spots in the low-energy electron diffraction (LEED) pattern in Figure 3.2a show a well-ordered long-range structure. The scanning tunneling microscopy (STM) image in Figure 3.2b illustrates extended, atomically flat terraces, separated in height by steps of 5 Å or a multiple of that.

The Fe<sub>3</sub>O<sub>4</sub> film has been characterized in detail by many techniques, e.g. photoelectron spectroscopy (PES) [144, 145], Auger electron spectroscopy (AES) [144], STM [141, 142, 146, 147], X-ray photoelectron diffraction (XPD) [146, 148], LEED [140, 143, 144, 149], and thermal desorption spectroscopy (TDS) [142, 150]. It was shown that a thin Fe<sub>3</sub>O<sub>4</sub> film has the same crystal structure as the bulk phase of magnetite. This is an inverse spinel structure where the O<sup>2-</sup> ions are ordered in an fcc-grid. The tetrahedral vacancies are filled with Fe<sup>3+</sup> ions and the octahedral sites are occupied by Fe<sup>2+</sup> and Fe<sup>3+</sup> ions (see Figure 3.2c). Nevertheless, the surface termination is still under discussion. Based on dynamic LEED and STM studies combined with theoretical calculations, Ritter and Weiss suggested a termination by tetrahedrally coordinated Fe<sup>3+</sup> ions [149]. In contrast, Lemire *et al.* concluded from TDS and IRAS measurements of adsorbed CO, combined with HREELS (high resolution electron energy loss spectroscopy) studies a model with termination by octahedrally coordinated Fe<sup>2+</sup> ions [142].

Table 3.1: Growth parameters of Pd particles as determined by STM from [153]

nominal Pd coverage	0.3 Å	4.0 Å	7.0 Å
- in atome/cm <sup>-2</sup>	2.0 · 10 <sup>14</sup>	2.7 · 10 <sup>15</sup>	4.7 · 10 <sup>15</sup>
<i>after annealing at 600 K:</i>			
island density/cm <sup>-2</sup>	1.7 · 10 <sup>12</sup>	3.8 · 10 <sup>12</sup>	1.0 · 10 <sup>12</sup>
Pd atoms/island	≈ 100	≈ 700	≈ 4900
diameter/nm	≈ 2	≈ 4	≈ 8
<i>after stabilization:</i>			
island density/cm <sup>-2</sup>	4.8 · 10 <sup>11</sup>	8.4 · 10 <sup>11</sup>	6.0 · 10 <sup>11</sup>
Pd atoms/island	≈ 400	≈ 3300	≈ 8100
<b>diameter/nm</b>	<b>≈ 4</b>	<b>≈ 7</b>	<b>≈ 12</b>

### 3.2 Pd particles on Fe<sub>3</sub>O<sub>4</sub>/Pt(111)

The preparation, growth, structure and morphology of Pd particles on oxide supports have been studied in detail before [12, 13, 112, 151–153]. In this work, Pd was deposited onto a freshly prepared Fe<sub>3</sub>O<sub>4</sub> film by physical vapor deposition from an electron beam evaporator in UHV. To avoid sputtering damages to the oxide film by the deposited Pd, the same potential was applied to the sample as to the evaporator. The flux of Pd was  $4.5 \cdot 10^{12} \text{ atoms} \cdot \text{cm}^{-2} \cdot \text{s}^{-1}$  and the surface temperature was kept at 120 K. The freshly deposited Pd particles were heated in UHV to 600 K. We prepared Pd particles with different sizes. The nominal depositions, as well as structural and morphological parameters, are summarized in Tabel 3.1.

It has been shown that these Pd particles are not stable when they are heated in  $10^{-6}$  mbar oxygen to 500 K [152]. Therefore, the particles were stabilized before use by repeated cycles of oxidation by  $1 \cdot 10^{-6}$  mbar O<sub>2</sub> and reduction by  $1 \cdot 10^{-6}$  mbar CO at 500 K. This treatment leads to an oxygen-assisted sintering of the particles, resulting in significantly larger particles and lower island densities as listed in Table 3.1. All experiments in this work were conducted with stabilized particles.

The structure of stabilized Pd particles has previously been investigated by STM and IRAS [152]. From the STM image in Figure 3.3a it can be seen that the Pd particles exhibit a hexagonal crystalline shape. The aspect ratio (height to diameter) is  $\approx 1:3.5$ . The STM study shows that the particles are terminated on top by a (111)-facet and on the sides by three (100)- and three (111)-facets. Based on this investigation, it can be estimated that about 80% of the particle's surface exhibit (111)-facets and 20% are terminated by (100)-facets (Figure 3.3b). In the same study, the structure of the Pd particles was also investigated by IRAS measurements of adsorbed CO molecules. As discussed in chapter 2.2.2, the effects of the substrate-adsorbate interaction on vibrational frequencies can be widely used to identify adsorption sites.

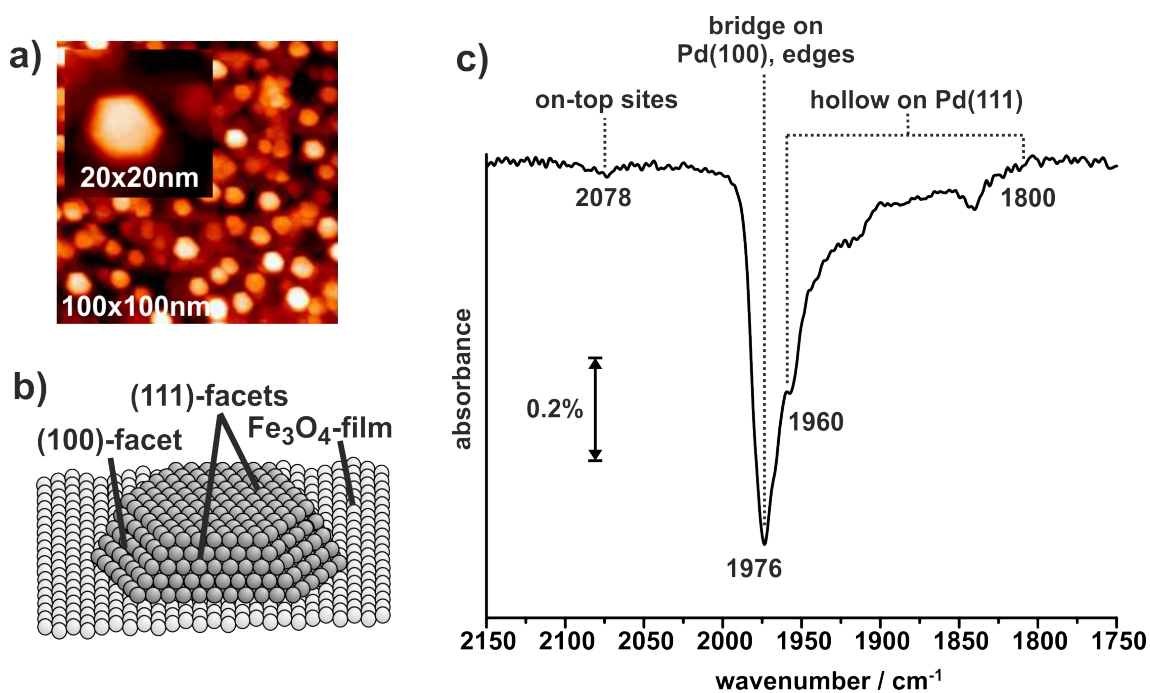


Figure 3.3: (a) STM image of stabilized 7 nm Pd particles on Fe<sub>3</sub>O<sub>4</sub>/Pt(111) and (b) schematic illustration of the a Pd particle (adapted from [152]); (c) IRAS of CO adsorbed at 300 K on stabilized 7 nm Pd particles on Fe<sub>3</sub>O<sub>4</sub>/Pt(111) measured at 120 K.

### 3.2.1 CO adsorption on Pd

IR studies on CO-covered Pd particles show a number of vibrational peaks, reflecting the variety of different adsorption sites, such as facets, edges, corners or defects. To some extent, the IR vibrations can be assigned on the basis of single crystal data.

#### CO on Pd(111)

CO forms a variety of adsorption structures on Pd(111) depending on the surface coverage [152]. At low coverage, CO adsorbs in hollow sites with an internal  $(\sqrt{3} \times \sqrt{3}) R30^\circ$  structure that grows until a closed layer is formed at a surface coverage of  $\Theta = 0.33$ . The C–O stretching vibration of this species appears near  $1840 \text{ cm}^{-1}$  [154–156]. Upon further increase of the CO coverage up to  $\Theta = 0.5$  at 300 K under UHV conditions, a  $c(4 \times 2)$ -2-CO-structure with stretching vibration at  $1936 \text{ cm}^{-1}$  is formed [154]. At this coverage, CO occupies *fcc* and *hcp* hollow sites as well as bridge sites [155, 157–159]. Under UHV conditions below 120 K a maximum coverage of  $\Theta = 0.75$  can be obtained. Under such conditions, CO is adsorbed in a  $c(2 \times 2)$ -3-CO structure with CO linearly adsorbed on top of Pd with stretching frequency near  $2100 \text{ cm}^{-1}$  and in *fcc* and *hcp*-hollow sites with stretching near  $1895 \text{ cm}^{-1}$  [155, 158, 160, 161].

#### CO on Pd(100)

CO occupies bridge sites of the Pd(100) surface from the low-coverage limit up to the saturation coverage of  $\Theta = 0.8$  at 300 K under UHV conditions. The stretching frequency shifts from  $1895 \text{ cm}^{-1}$  at low coverage to  $1997 \text{ cm}^{-1}$  at saturation coverage. Up to  $\Theta = 0.5$ , CO forms an ordered  $c(2\sqrt{2} \times \sqrt{2}) R45^\circ$  structure. At higher coverages, a compressed layer evolves [154, 162].

#### CO on Pd particles

IR vibrations of CO on Pd particles have been investigated in detail before [112, 161, 163–167]. The IR spectra exhibit a variety of vibrational peaks resulting from different adsorption sites, such as facets, edges, and defects. A typical spectrum after CO saturation of stabilized 7 nm Pd particles on Fe<sub>3</sub>O<sub>4</sub>, adsorbed at 300 K and measured at 120 K, is illustrated in Figure 3.3c. Based on CO-adsorption data on single crystals, the broad IR absorption feature  $\leq 1960 \text{ cm}^{-1}$  is assigned to CO mainly occupying hollow sites on regular (111) facets. The pronounced peak at  $1976 \text{ cm}^{-1}$  is related to CO attached to bridge sites on both (100) facets and edge sites. The weak signal near  $2078 \text{ cm}^{-1}$  is assigned to CO adsorbed on-top of Pd atoms; only a very small concentration of on-top CO is expected at 300 K.

It should be noted that the C–O stretching vibration on the strongly tilted Pd sites should be partially attenuated due to the metal surface selection rule (MSSR). In contrast, dipole coupling effects resulting in *intensity borrowing* (see 2.2.2) are expected to increase the IR absorption signal of CO in bridge sites at  $1976 \text{ cm}^{-1}$  at the expense of signals from CO adsorbed on regular (111) facets below  $1960 \text{ cm}^{-1}$ . Due to this effects, the

### *3 Pd/Fe<sub>3</sub>O<sub>4</sub> Model Catalysts*

intensity distribution of the different IR vibrational modes does not quantitatively reflect the concentration of the corresponding species [105].

## 4 Selectivity in Hydrogenation of $\alpha,\beta$ -unsaturated Carbonyl Compounds on Pd - an Overview

Understanding the kinetic effects that govern the selectivity and activity of partial selective hydrogenation of  $\alpha,\beta$ -unsaturated aldehydes and ketones on late transition metals is crucial for the rational design of new catalytic materials with the desired selectivity towards C=C or C=O bond conversion. Among the most useful target products in transformation of multi-unsaturated oxygenates are unsaturated alcohols produced by heterogeneous selective hydrogenation of the C=O bond in unsaturated aldehydes and ketones [27–30]. Generally, thermodynamics favors hydrogenation of the C=C bond in these compounds to form the saturated aldehyde or ketone [28]. Therefore, chemoselective hydrogenation of the C=O bond requires manipulation of the reaction kinetics by means of a suitable catalyst.

The surface chemistry of  $\alpha,\beta$ -unsaturated carbonyl compounds on Pd catalysts has been investigated using the prototypical molecules acrolein, an aldehyde, and isophorone, a ketone. The aim of this work was to identify microscopic factors that govern the selectivity and activity in acrolein and isophorone conversion with hydrogen on a Pd(111) single crystal and on Fe<sub>3</sub>O<sub>4</sub>-supported Pd particles with different sizes. This chapter provides an overview on the key results.

### 4.1 Adsorption of Isophorone and Acrolein

**Adsorption of Isophorone on Pd(111)** Infrared reflection-absorption spectroscopy (IR-AS) and near-edge X-ray absorption fine structure (NEXAFS) studies were combined to investigate the effects of isophorone coverage and hydrogen coadsorption on the orientations of the C=C and C=O  $\pi$  bonds with respect to the Pd(111) surface plane. NEXAFS has been demonstrated to be a powerful tool that provides electronic and structural information on adsorbed molecules. In the past two decades it was shown that the application of NEXAFS can be extended from small to large organic molecules [124, 125]. The determination of the orientation of large molecules by C 1s  $\rightarrow \pi^*$  resonances is employed to study the adsorption of organic molecules on metal surfaces [128, 168–170], Langmuir-Blodgett monolayers [127], self-assembly of long-chain alkanes [171], or aromatic molecules [169]. More recently high-resolution beamlines enabled spectroscopy with highly resolved additional fine structures, such as vibronic coupling and local vibronic excitations. NEXAFS data of organic molecules that show vibrational fine structure in superposition with the electronic excitation were obtained [172]. With regard to catalytic conversions, sev-

eral NEXAFS studies focus on the interaction of unsaturated hydrocarbons with metal surfaces. Attempts were made to correlate chemoselectivity in hydrogenation of multiple unsaturated compounds with the conformation of the adsorbates on the catalyst surface as determined by NEXAFS [63, 173].

We have investigated the adsorption of isophorone on a Pd(111) single crystal at temperatures between 100 K and 120 K under well-defined ultrahigh-vacuum (UHV) condition by NEXAFS and IRAS experiments. While NEXAFS probes electronic states with very high sensitivity to small adsorbate coverages, IR spectroscopy is a very established tool to study the vibrations of chemical bonds. Complementary density functional theory studies including van der Waals interaction (DFT+vdW) were performed by Wei Liu and Alexandre Tkatchenko to rationalize the experimental observations. This chapter summarizes the results published in [174, 175] (see Chapters 6 and 7).

IRAS studies have been performed on normal and deuterium-labeled ( $d_5$ -) isophorone. In the latter molecule, the five hydrogen atoms attached to the  $C_6$  ring are substituted by deuterium atoms. IR spectra of isophorone at multilayer coverages provide a reference for mainly unperturbed molecules. For unlabeled isophorone, three main spectral regions can be distinguished, which are characteristic for C–H stretching ( $2800$ – $3200\text{ cm}^{-1}$ ), C=C and C=O stretching ( $1550$ – $1850\text{ cm}^{-1}$ ), as well as C–H and C–C deformation vibrations ( $\leq 1500\text{ cm}^{-1}$ ). For  $d_5$ -isophorone, additionally C–D stretching vibrations appear at  $2000$ – $2300\text{ cm}^{-1}$  and C–D deformations in the region  $\leq 1500\text{ cm}^{-1}$ . The assignment of the C–H and C–C vibration modes is quite complicated and has been achieved with the help of DFT calculations carried out by Wei Liu and Alexandre Tkatchenko [175] (see Chapter 7). The vibrations of the C=O and C=C bonds, however, can be clearly identified. In unlabeled isophorone, the frequency range of the stretching vibration of the C=O bond near  $1665\text{ cm}^{-1}$  is strongly overlapping with that of the C=C bond near  $1655\text{ cm}^{-1}$ , making a distinction rather difficult. To overcome this problem, the ring-substituted  $d_5$ -isophorone has been used, where the C=C stretching appears at  $1620\text{ cm}^{-1}$  and thus shifted by  $35\text{ cm}^{-1}$  as compared to the non-substituted compound. The C=O bond vibration, however, appears to be hardly affected by the substitution and remains essentially at the same frequency.

The orientation of chemical bonds with respect to a metal surface has been deduced from their IR absorption intensities based on the metal surface selection rule (MSSR), which is described in Chapter 2.2.2. IR spectra have been obtained at different  $d_5$ -isophorone coverages, in order to determine the coverage-dependent orientation of the C=O and C=C bonds. A typical series is displayed in Figure 4.1a, for coverages ranging from 0.2 monolayers (ML) to 3 ML. At the lowest coverage of  $d_5$ -isophorone (0.2 ML), there are significant signals in the  $CH_x$  stretching and deformation regions, however, there is no signal for the  $\pi$  bonds. This intensity distribution is in sharp contrast to the situation found for isophorone ice (multilayers, *e.g.* 3 ML), where intense IR absorption features show C=O and C=C bond vibrations. The absence of C=O and C=C absorption bands indicates that these bonds are either oriented parallel to the metal surface or strongly perturbed (*e.g.* dissociated) by the interaction with Pd(111). With increasing  $d_5$ -isophorone coverage, the intensities of the  $CH_x$  stretching and deformation vibrations increase slightly, but the IR absorption intensities in the region of the C=C and C=O stretching vibrations

change strongly. After exposure of 0.5 ML  $d_5$ -isophorone, a pronounced C=C stretching vibration is observed near  $1620\text{ cm}^{-1}$ , while the CO vibration peak at  $1665\text{ cm}^{-1}$  is hardly visible. With increasing coverage, the intensity of the C=O stretching peak increases rapidly and becomes the most dominant peak. Near the full-monolayer coverage, the ratio of the C=O to C=C peak intensities amounts approximately  $I_{\text{C=O}}/I_{\text{C=C}} \approx 4$  and is thus roughly similar to the intensity ratio in isophorone ice ( $I_{\text{C=O}}/I_{\text{C=C}} \approx 6\text{-}8$ ).

In order to obtain quantitative information on the coverage-dependent adsorption geometries of the C=C and C=O bonds in isophorone on Pd(111), NEXAFS experiments have been performed under the same experimental conditions. C K-edge spectra have been measured for isophorone coverages of 0.2 ML, 0.4 ML, and 0.7 ML, each with horizontally and vertically polarized X-ray beam and incident angles of  $70^\circ$  and  $80^\circ$  with respect to the surface normal. A series of representative spectra obtained at incident angle of  $70^\circ$  is illustrated in Figure 4.1b. The two most important features in the spectra are the two pre-edge peaks that are assigned to the C  $1s \rightarrow \pi^*$  (C=C) resonance at 284.9 eV and the C  $1s \rightarrow \pi^*$  (C=O) resonance at 286.6 eV. The peaks can be clearly identified at low coverage, thus indicating that both  $\pi$  bonds are not dissociated upon interaction with Pd(111). At low coverage, a parallel orientation of the C=C and C=O bonds is evident by the strong dependence of the X-ray absorption coefficient on the polarization of the incident beam. While there is a strong resonance for both  $\pi$  bonds with vertically polarized light (black), almost no X-ray absorption is detectable with horizontally polarized beam (grey), suggesting a flat-lying adsorption geometry of the unsaturated bonds. With increasing coverage, the intensity of the  $\pi$  resonances with the horizontally polarized X-ray beam increases relative to that of the resonances with the vertically polarized light, indicating that the tilting of the C=C and C=O bonds increases. The coverage-dependent tilting angles of the  $\pi$  bonds have been calculated from the intensity ratio between their absorption of horizontally and vertically polarized light. The results point to a tentatively more upright position of the C=C bond than the C=O bond. At 0.4 ML, the inclination angles of the C=C and C=O bonds amount  $33^\circ (\pm 2^\circ)$  and  $28^\circ (\pm 2^\circ)$  and at 0.7 ML,  $41^\circ (\pm 2^\circ)$  is found for the C=C bond and  $37^\circ (\pm 2^\circ)$  for the C=O bond.

Both studies, IRAS and NEXAFS, show a coverage-dependent adsorption geometry of Pd(111)-adsorbed isophorone. The flat-lying geometry at low coverage results in a complete attenuation of the vibrational features characteristic for the C=C and C=O bonds, while the dynamic dipole moments of the C-H vibrations are at least partially inclined and therefore visible in IR spectra. As observed by NEXAFS, C=C and C=O bonds are present in a undissociated form, which rules out the hypothesis on scission of these bonds as a reason for missing IR absorption features at low isophorone coverage. The flat-lying geometry of the C=C and C=O bonds at 0.2 ML suggests that isophorone essentially preserves the in-plane configuration of the conjugated  $\pi$  system at low coverage. At intermediate coverage, however, strong distortion of the  $\pi$  system is indicated. With increasing coverage, the inclination of both C=C and C=O bonds increases, with the tilting of the C=C bond being considerably more pronounced than that of the C=O bond according to IRAS. In fact, at a coverage of 0.5 ML, the intensity of the C=C stretch vibration is already similar to the intensity of this IR band on an isophorone-saturated surface, while the intensity of the C=O stretch vibration is still close to zero. If both bonds would uniformly lift up, one would expect the intensity ratio  $I_{\text{C=O}}/I_{\text{C=C}}$  of the

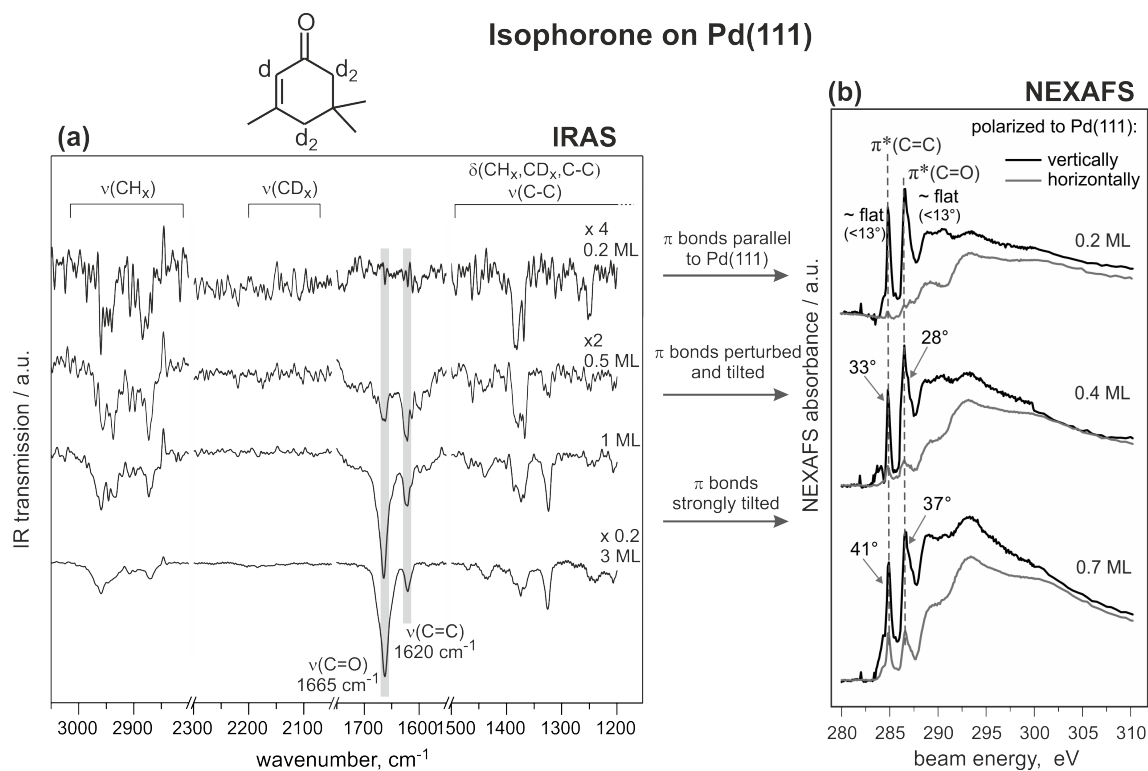


Figure 4.1: (a) IR spectra of  $d_5$ -isophorone adsorbed at 120 K on Pd(111) for different surface coverages. (b) NEXAFS spectra of isophorone on Pd(111) obtained at 100 K for different exposures. Both studies show a coverage-dependent tilting of the C=C and C=O bonds.

IR absorption to be close to the value observed at coverages in the multilayer regime ( $I_{C=O}/I_{C=C} \approx 6-8$ ). The intense C=C vibration in the absence of the C=O vibration in IRAS indicates that at intermediate coverages the C=O bond is still nearly lying flat on the surface, while the C=C bond lifts up, resulting in a strong distortion of the originally planar  $\pi$  system. The higher tilting angle of the C=C bond can also be observed in the NEXAFS data; however, this trend is somewhat less pronounced, probably because of an absolute difference in coverage. The strongly tilted geometry at high coverages most likely results from steric constraints on the surface. Note that IRAS data allow more reliable conclusions on the adsorption geometry since the relative orientation of the C-C and C-O axes with respect to the metal surface plane is determined. In NEXAFS, only the angle between the metal surface plane and the direction of the C 1s  $\rightarrow \pi^*$  transition dipole moments can be obtained.

**Adsorption of the saturated ketone TMCH** Furthermore, the adsorption of the saturated ketone 3,3,5-trimethylcyclohexanone (TMCH) on Pd(111) at 120 K has been studied at coverages ranging from 1/12 ML to the multilayer regime. The results can be found in reference [175] (see Chapter 7). IR spectra are illustrated in Figures 7.7 and 7.8. As discussed for isophorone, IR spectra at multilayer coverages mainly show vibrations of rather unperturbed molecules. Three spectral regions can be distinguished, which are typical for  $\text{CH}_x$  stretching ( $2800-3200 \text{ cm}^{-1}$ ), C=O stretching ( $1550-1850 \text{ cm}^{-1}$ ), and  $\text{CH}_x$  deformation as well as C-C stretching and deformation modes ( $\leq 1500 \text{ cm}^{-1}$ ). The most important observation is that there are different peaks in the C=O stretching region that likely result from different TMCH species. At the lowest TMCH exposure (1/12 ML), a sharp peak at  $1648 \text{ cm}^{-1}$  is detected. This peak grows slightly with increasing exposure and is saturated at 1/6 ML exposure. A small peak at  $1701 \text{ cm}^{-1}$  appears at 1/6 ML exposure and increases slightly in intensity up to 1/3 ML, but does not appear to grow further with increasing exposure. At 1/2 ML exposure, a peak at  $1713 \text{ cm}^{-1}$  appears and this peak continues to grow with increasing exposure.

The coverage-dependent IR spectra give valuable information about the interaction of TMCH with the Pd(111) substrate. First, there are several different peaks in the C=O stretching region that likely result from different TMCH species. The strong peak at  $1713 \text{ cm}^{-1}$ , which grows continuously with increasing exposure beyond 1/2 ML, is assigned to C=O stretching of TMCH molecules in the multilayer regime. The peak at  $1648 \text{ cm}^{-1}$ , which is observed at the lowest exposure (1/12 ML) and is saturated by 1/6 ML, is related to a C=O stretching vibration from sub-monolayer TMCH. The C=O stretching vibrations at  $1701 \text{ cm}^{-1}$  and  $1747 \text{ cm}^{-1}$  most likely relates to TMCH species in the intermediate coverage range between sub-monolayer and multilayer, probably the second layer. Finally, the strong intensity of the C=O vibration at  $1648 \text{ cm}^{-1}$  even at the lowest TMCH exposure (1/12 ML) indicates that the C=O bond in TMCH is strongly tilted with respect to the Pd(111) surface plane at low sub-monolayer coverages. These results indicate that at low coverage TMCH adsorbs roughly perpendicular to the Pd(111) plane through the C=O group, strongly perturbing the C=O stretching vibration. Second, the C-H stretching and the C-H deformation regions, which are not discussed in this summary, grow roughly monotonically with increasing TMCH exposure; there is no indication that these vibrational modes are strongly affected by the Pd(111) substrate.

Pronounced differences in the adsorbates' structure of TMCH and isophorone have been found, especially in the orientation of the  $\pi$  bonds with respect to the Pd(111) surface plane. In the low-coverage limit, TMCH adsorbs in a strongly tilted geometry, interacting with the surface primarily through to the C=O group, while isophorone adopts a flat-lying geometry with the C=O and C=C bonds parallel to the Pd(111) surface plane. The IR absorption features assigned to the C–H stretching and C–H deformation vibrations grow roughly monotonically with increasing coverage, pointing to a possibly less strict ordering of TMCH molecules on the surface.

**Effect of co-adsorbed hydrogen on isophorone** We have further investigated the effect of hydrogen on Pd(111)-adsorbed isophorone by IRAS and NEXAFS measurements under the same experimental conditions as described before. The results are published in [174, 175] (see Chapter 6 and 7). Prior to isophorone exposure, the Pd(111) surface was saturated with  $H_2$ . Two series of coverage-dependent IR spectra are illustrated in Figures 6.6 and 7.6. The IR absorption of the C=C and C=O bonds strongly changes when hydrogen is preadsorbed at coverages near 0.5 ML isophorone. At this coverage, the C=O stretching is clearly visible on  $H_2$ -precovered Pd(111), while the C=C vibration is absent. On the pristine Pd(111) surface, the situation is reversed – the most intense absorption feature corresponds to the C=C stretching, while the intensity of the C=O vibration is close to zero. At lower coverage, close to 0.2 ML, the region of the C=C and C=O stretching vibrations are essentially identical on both surfaces, pointing to a flat-lying geometry of both  $\pi$  bonds also on the  $H_2$ -precovered Pd(111). On  $H_2$ /Pd(111), however, the  $CH_3$  vibration frequencies and their intensity distribution appear similar to those at multilayer coverages, indicating considerably less perturbation of the  $CH_3$  groups as compared to molecules adsorbed on pristine Pd(111).

The IRAS results indicate that the interaction of isophorone with Pd is considerably affected by preadsorbed hydrogen. While at the lowest coverage isophorone adopts a flat lying geometry – similar to pristine Pd(111) – the interaction changes strongly at intermediate coverages. Particularly the ratio  $I_{C=O}/I_{C=C}$  becomes close to the multilayer value indicating that isophorone lifts up rather uniformly and that the conjugated  $\pi$  system preserves to a large extent its in-plane geometry. This behavior is in sharp contrast to the coverage dependence of the isophorone adsorption geometry on the pristine Pd(111) surface, where the C=C bond seems to be strongly tilted with respect to the flat-lying C=O bond and thus the conjugated  $\pi$  system to be significantly distorted. The diminished distortion of the molecule in the presence of hydrogen is attributed to a weaker interaction of isophorone with the hydrogen-saturated Pd surface.

NEXAFS studies have been performed to gain quantitative information on the changes in the tilting angles of the C=C and C=O bonds in the presence of preadsorbed hydrogen. Our results indicate that preadsorbed hydrogen slightly increases the inclination angle of the C=C bond (from  $41^\circ (\pm 2^\circ)$  to  $45^\circ (\pm 2^\circ)$ ) and the C=O bond (from  $37^\circ (\pm 2^\circ)$  to  $41^\circ (\pm 2^\circ)$ ) with respect to the Pd(111) surface plane. However, the isophorone coverage used in these experiments was 0.7 ML and thus at a value where IRAS data do not indicate any strong difference between the adsorption geometries on pristine and  $H_2$ -precovered Pd(111). NEXAFS data at lower coverages are not available. However, the NEXAFS

results are consistent with the observations in IRAS experiments showing generally higher inclination angles on hydrogen-precovered Pd(111).

**Adsorption of Acrolein, Propanal, and Allyl Alcohol** In addition to our studies on the Pd-adsorption of isophorone, the binding of acrolein and its partially hydrogenated products – propanal and allyl alcohol – to Pd(111), Fe<sub>3</sub>O<sub>4</sub>, and Pd/Fe<sub>3</sub>O<sub>4</sub> at 120 K has been investigated by IRAS and TPD experiments. The results are published in [176] and [177] (see Chapters 8 and 12). IRAS and TPD spectra of acrolein, propanal and allyl alcohol on Pd(111) are illustrated in Figures 8.1, 8.2, and 8.3. For all three molecules, mostly unperturbed molecular structures are found at multilayer coverages and significantly perturbed chemical bonds appear in the sub-monolayer regime on all surfaces. The most important results on the adsorption of acrolein and propanal at sub-monolayer coverages will be briefly summarized here.

On Pd(111), acrolein adopts a flat-lying geometry with the C=C, C–C, and C=O bonds parallel to the surface plane in the low-coverage limit, similar to isophorone. On Fe<sub>3</sub>O<sub>4</sub>, however, the molecule adsorbs in a strongly tilted geometry with the C=O group attached to the surface. The IR vibrations of the C=O, C–C, and CH<sub>2</sub> groups appear significantly shifted compared to acrolein ice, indicating a strong perturbation of the whole conjugated  $\pi$  system by the Fe<sub>3</sub>O<sub>4</sub> film. On Pd/Fe<sub>3</sub>O<sub>4</sub> model catalysts, a large fraction of the acrolein molecules is attached to the Fe<sub>3</sub>O<sub>4</sub> support with the same molecular perturbation as observed on the pure Fe<sub>3</sub>O<sub>4</sub> film. However, chemical conversion of all sub-monolayer species in TPD experiments points to a high mobility of acrolein on the Fe<sub>3</sub>O<sub>4</sub> support. It seems that during TPD experiments all acrolein molecules reach Pd islands by diffusion across the support.

While the geometries of the C=C and C=O bonds in the two unsaturated carbonyl compounds acrolein and isophorone on Pd(111) are similar, IR spectra point to rather different structures of the two saturated carbonyl species propanal and TMCH on Pd(111). While sub-monolayer TMCH on Pd(111) shows a pronounced IR absorption of the C=O bond, the C=O stretching cannot be identified with certainty in sub-monolayer TMCH on Pd(111). A vibrational feature more than 150 cm<sup>-1</sup> below the C=O stretching in propanal ice tentatively points to a strongly weakened C=O bond by the Pd surface. Several C–H stretching and deformation vibrations, however, are clearly assigned in the low-coverage limit indicating intact CH<sub>3</sub> and CH<sub>2</sub> groups. Nevertheless, their vibration frequencies appear shifted as compared to propanal ice pointing to a strong interaction of these groups with the Pd surface.

IRAS studies of acrolein adsorbed on Fe<sub>3</sub>O<sub>4</sub> point to a strongly inclined adsorption geometry with heavily perturbed chemical bonds. Especially the C=O bond appears significantly weakened in Fe<sub>3</sub>O<sub>4</sub>-adsorbed acrolein. Nevertheless, in TPD experiments, acrolein molecules stay intact on the Fe<sub>3</sub>O<sub>4</sub> film until desorption. On Pd/Fe<sub>3</sub>O<sub>4</sub>, however, decomposition as well as conversion to propanal occurs. Our results provide insights into the origin of the selectivity towards C=C bond hydrogenation over Pd/Fe<sub>3</sub>O<sub>4</sub> model catalysts. For a detailed description we refer to reference [177] and Chapter 12.

## 4.2 Hydrogenation of Acrolein over Pd(111) and Pd/Fe<sub>3</sub>O<sub>4</sub>

After having studied the adsorption of isophorone and acrolein by Pd and Fe<sub>3</sub>O<sub>4</sub>, the selective partial hydrogenation of acrolein on well-defined model Pd catalysts has been investigated in-situ under UHV conditions. Previously, acrolein was reported to be hydrogenated almost exclusively at the C=C bond forming propanal over powdered Pd catalysts [28]. The activity and selectivity of a large number of powdered supported metal catalysts in acrolein hydrogenation have been investigated. As key structural parameters controlling the chemoselectivity, a series of ideas conceiving the amount of steric hindrance to adsorption via the C=C bond [31, 32], presence of surface modifiers [178, 179] or alloying with other metals [47] have been put forward. Complementary, some theoretical work and model studies have been presented in order to understand the chemoselectivity of the underlying elementary processes [52, 60, 180–184]. Despite these efforts, a deep fundamental understanding of this reaction and the parameters governing its activity and selectivity is still missing. Particularly, it remains unclear how the C=O bond is activated on a transition metal surface and what are the structures of the surface intermediates formed under the reaction conditions. Information on the reaction intermediates formed on the surface would be particularly important for approaching a rational design of new catalytic materials for this class of reactions.

In this work, the selective partial hydrogenation of acrolein on two well-defined surfaces has been investigated in-situ under UHV conditions: (i) on a Pd(111) single crystal and (ii) on Fe<sub>3</sub>O<sub>4</sub>-supported Pd nanoparticles (Pd/Fe<sub>3</sub>O<sub>4</sub>) with particle sizes of 4 nm, 7 nm, and 12 nm. The catalytic activity of these surfaces has been probed using molecules beams (MB) under isothermal conditions. The formation of the gas-phase products has been detected by quadrupole mass spectrometry (QMS); simultaneously, the evolution of surface species has been monitored by in-situ IRAS. In all experiments, the surfaces have been pre-exposed to  $4.8 \cdot 10^{15}$  H<sub>2</sub>/(cm<sup>2</sup>s) for 300 s before the acrolein beam has additionally been switched on. The acrolein flux has been varied over a range from  $6 \cdot 10^{12}$  to  $4.5 \cdot 10^{13}$  molecules/(cm<sup>2</sup>s) and the beam has been operated in pulsed as well as in continuous modes. The results are published in [185–187] (see Chapters 9, 10, and 11).

Pd(111) and Pd/Fe<sub>3</sub>O<sub>4</sub> show very different selectivity in partial acrolein hydrogenation. Figure 4.2 illustrates the rates of propanal (upper row) and propenol (lower row) formation over 12 nm Pd particles (left) and a Pd(111) single crystal (right) in experiments using a pulsed acrolein beam and a continuous hydrogen beam. Over Pd particles of 7 nm and 12 nm, selective conversion of acrolein to propanal occurs. Over a Pd(111) single crystal, however, propenol is formed with near 100% selectivity. Note that it has not been possible to determine with certainty whether the propenol species is the allyl alcohol (1-propen-3-ol) or the enol (1-propen-1-ol). In the following part of this chapter, the most important observations on acrolein conversion over a Pd(111) single crystal will be summarized followed by the results on the hydrogenation on Pd/Fe<sub>3</sub>O<sub>4</sub>.

**Acrolein conversion over Pd(111)** Acrolein conversion over a Pd(111) single crystal has been investigated by IRAS and the gas-phase composition has been detected by QMS. In all experiments, hydrogen has been exposed continuously with a rate of  $4.8 \cdot 10^{15}$  molecules/(cm<sup>2</sup>s). The acrolein beam, in contrast, has been operated in pulsed or con-

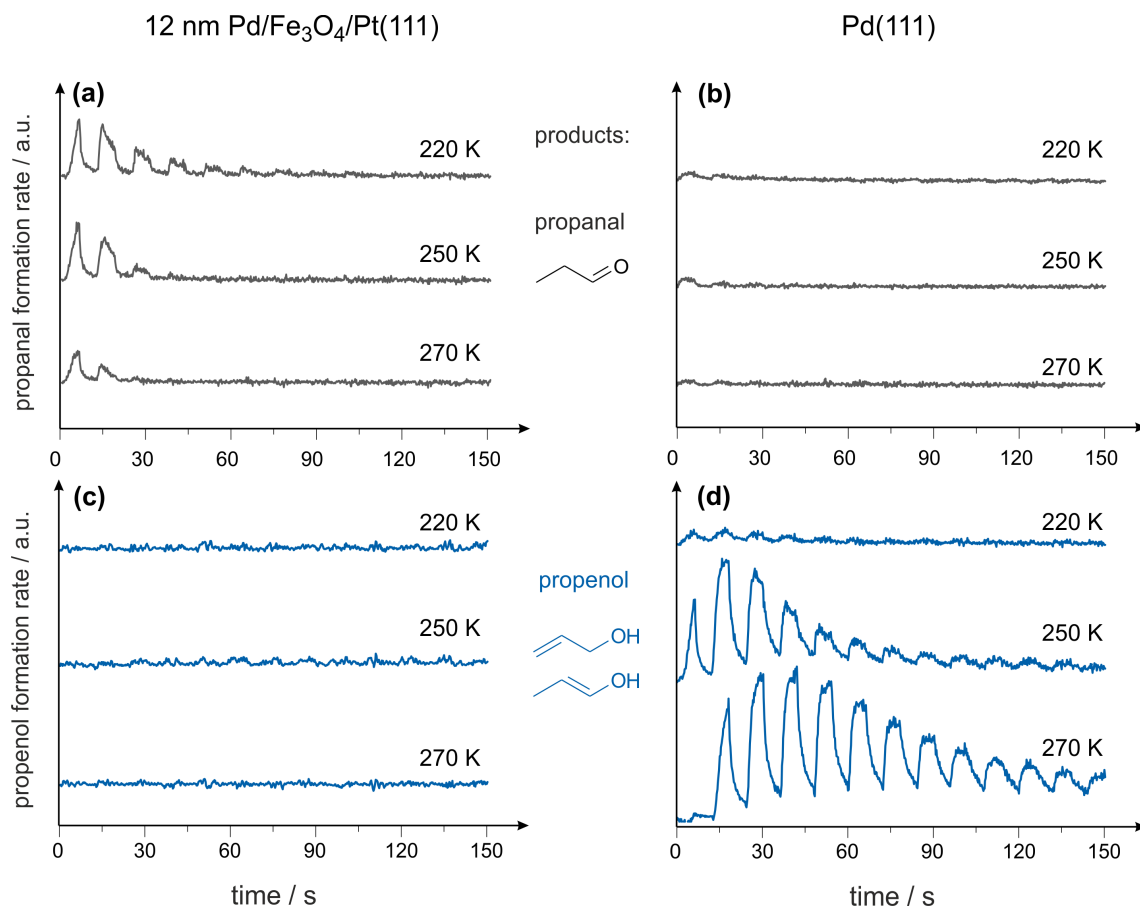


Figure 4.2: Propanal (top row) and propenol (bottom row) formation rates in acrolein hydrogenation over Fe<sub>3</sub>O<sub>4</sub>-supported 12 nm Pd particles (left column) and a Pd(111) single crystal (right column) during continuous H<sub>2</sub> exposure and pulsed acrolein dosing at different sample temperatures.

tinuous modes and the flux has been varied between  $6 \cdot 10^{12}$  and  $4.5 \cdot 10^{13}$  molecules/(cm<sup>2</sup>s).

The product formation in acrolein hydrogenation over a Pd(111) single crystal has been studied at temperatures ranging from 220 K to 350 K. The results obtained at 220 K, 270 K, and 320 K are illustrated in Figure 4.3. The rate of propenol formation exhibits a clear temperature dependence with a maximum at 270 K. The propanal formation rate, in contrast, is relatively low at all investigated temperatures with a minimum at 270 K.

At all temperatures between 220 K and 320 K, the propenol production starts after an induction period, passes through a maximum and then slowly decreases. At 270 K, the formation of propenol starts after irreversible adsorption of  $3.6 \cdot 10^{14}$  acrolein molecules/cm<sup>2</sup>, which corresponds approximately to one acrolein molecule per four Pd surface atoms. This observation is independent from the acrolein deposition rate. The following summary will be limited to acrolein conversion at 270 K. A detailed discussion of the product formation at other temperatures can be found in reference [186] (see Chapter 10).

Analysis of the IR spectra obtained on the Pd(111) surface under reaction conditions allow to determine the composition of the active surface turning over and the nature of the reactive intermediate resulting in formation of propenol. A time-resolved series of spectra obtained on the Pd(111) surface turning at 270 K is illustrated in Figure 4.4. Three major groups of IR bands characteristic for different surface species can be identified. First, the IR absorption at  $1755 \text{ cm}^{-1}$  corresponds to the stretching vibration of a C=O bond. While the C=O vibration of adsorbed intact acrolein appears near  $1660 \text{ cm}^{-1}$ , the frequency band at  $1755 \text{ cm}^{-1}$  is indicative of a surface species containing a C=O group, but not conjugated to a C=C bond anymore. The appearance of this IR vibration under reaction conditions points to the formation of an oxopropyl surface species, resulting from partial hydrogenation of acrolein with only one H atom at the C=C group. Our data do not allow to make a more precise conclusion on whether acrolein was hydrogenated on the  $\alpha$ - or  $\beta$ -C atom to form this species; both products would be consistent with IR vibration at  $1755 \text{ cm}^{-1}$ . Remarkably, this band appears at a very early stage of the reaction, grows in intensity and remains intense even after the reaction rate is recorded to decrease to zero. This observation strongly suggests that this species is not the reaction intermediate leading to the final gas phase product, but is merely a spectator. We refer to this species as spectator I (SI).

The second prominent band appears very intense at  $1120 \text{ cm}^{-1}$ . This IR absorption is present neither in adsorbed molecular acrolein on Pd nor in acrolein ice and therefore cannot be related to any distinctive vibration of intact acrolein molecules. Furthermore, this band appears only under the reaction conditions suitable for propenol formation. The most striking observation is that the evolution of this vibrational band shows strong correlation with the evolution of gas phase propenol. Indeed, this band starts to appear in the induction period and is growing in intensity while the propenol concentration in the gas phase is increasing. Consecutively, the intensity of this band strongly decreases accompanied by the strong decrease of the propenol formation rate observed in the gas phase and finally completely disappears. A few other IR bands in the region of the CH<sub>x</sub> stretching and bending vibrations can also be correlated to the production of propenol. The corresponding peaks are indicated in Figure 4.4.

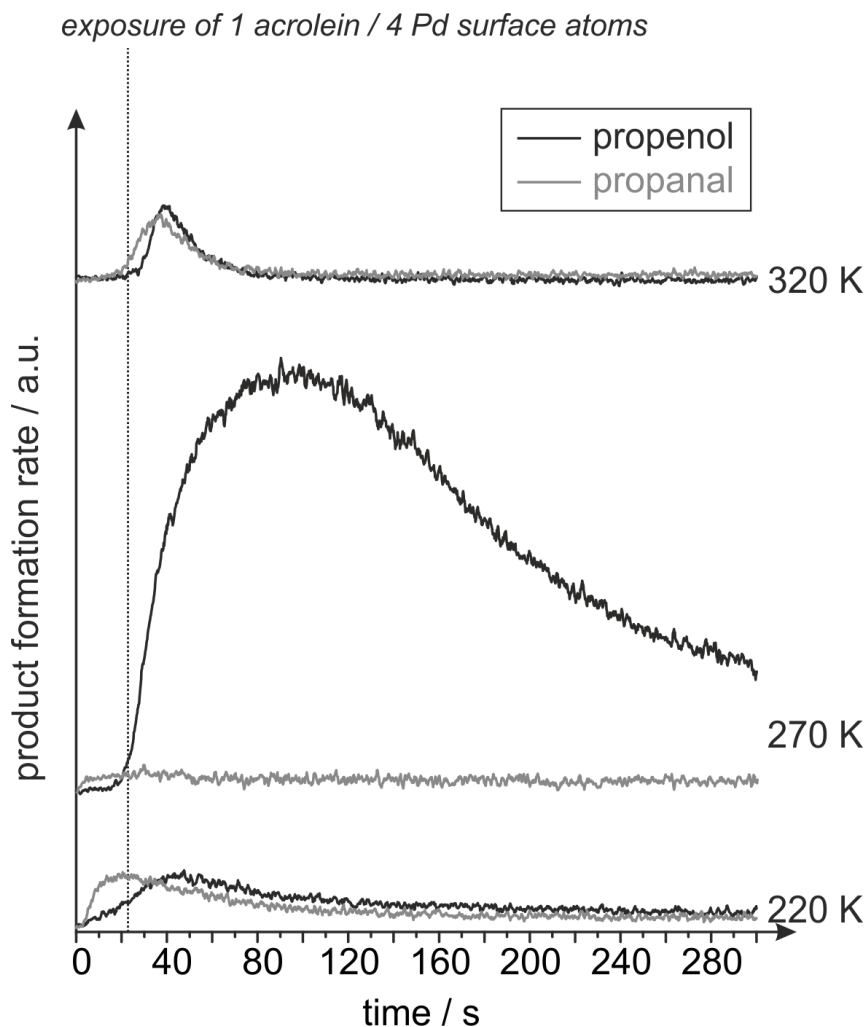


Figure 4.3: Formation rates of propenol (black) and propanal (grey) on Pd(111) during continuous exposure of acrolein and H<sub>2</sub> at 220 K, 270 K, and 320 K. Propenol formation exhibits a clear temperature dependence with a maximum at 270 K. In contrast, only rather small amounts of propanal are observed with a minimum at 270 K.

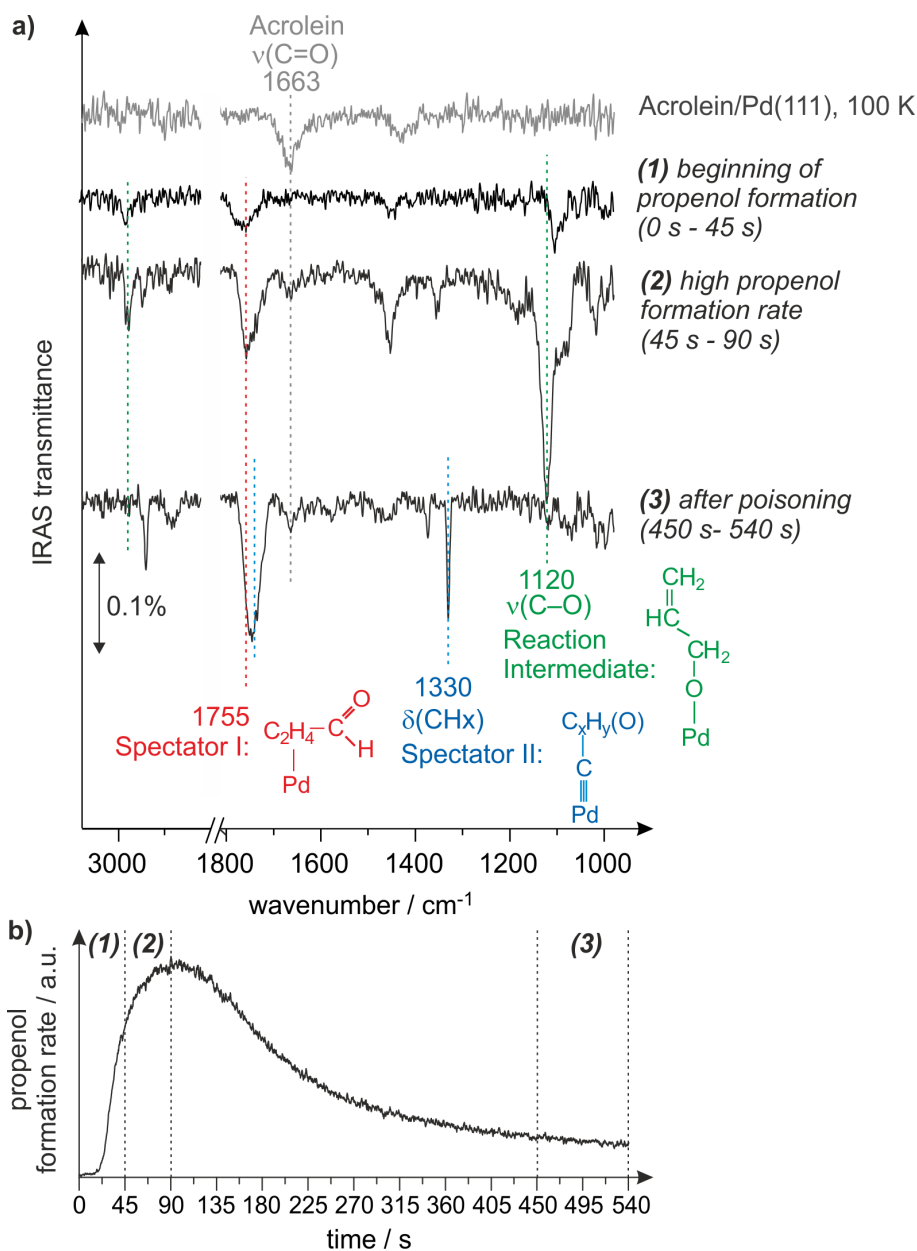


Figure 4.4: (a) IR spectra of a monolayer of acrolein on pristine Pd(111) at 100 K (grey line) and on Pd(111) turning over at 270 K during continuous exposure to acrolein and  $\text{H}_2$  (black lines). (b) The formation rate of propenol on Pd(111) at 270 K detected by QMS in the gas-phase.

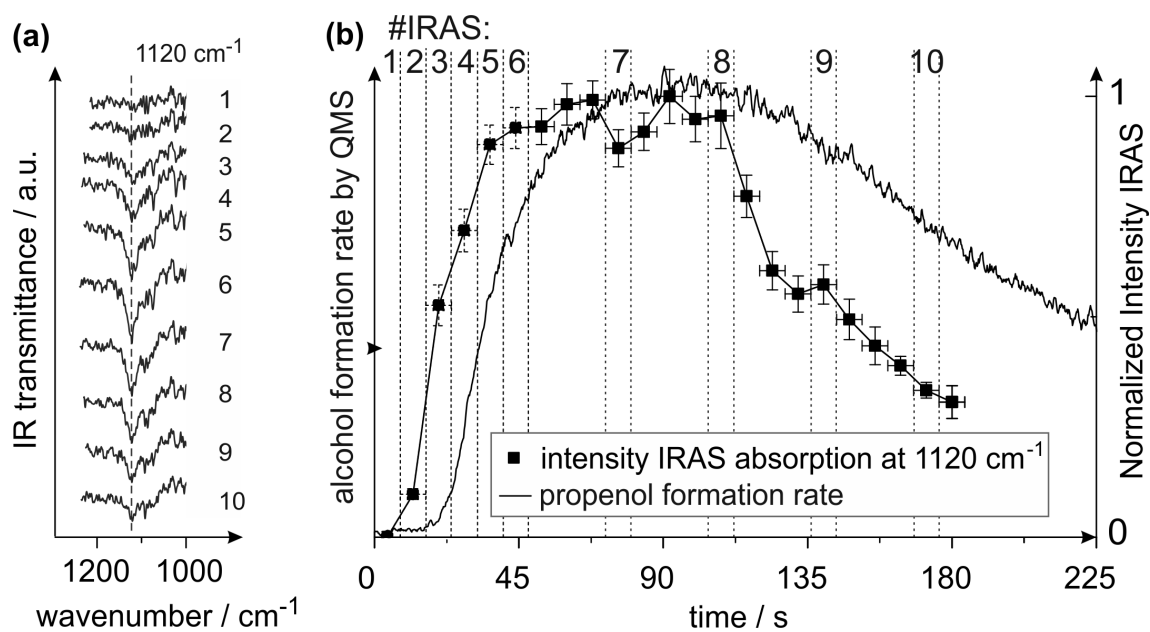


Figure 4.5: The formation of the reaction intermediate on the surface compared to the evolution of gas-phase propenol. (a) Series of IR spectra with high time resolution taken on the surface turning over. The integral of the peak at 1120 cm<sup>-1</sup>, which is assigned to the reaction intermediate, is plotted in (b) together with the propenol formation rate detected in the gas phase by QMS.

Figure 4.5a shows a series of IR spectra taken on the surface turning over with higher time resolution. In Figure 4.5b the integral of the peak at  $1120\text{ cm}^{-1}$  is plotted together with the formation rate of propenol in the gas phase. As can be clearly seen, the evolution of the product in the gas phase directly follows the intensity of the vibrational band at  $1120\text{ cm}^{-1}$  related to the proposed reaction intermediate. However, there is a slight delay between the the formation of the reaction intermediate on the surface and the propenol detection in the gas phase, which is discussed in reference [186] (see Chapter 10).

The observed strong correlation between the gas-phase formation of propenol and the evolution of the vibrational band at  $1120\text{ cm}^{-1}$  unambiguously shows that the corresponding surface species is the surface intermediate that is directly involved in the selective hydrogenation of acrolein to the propenol. To the best of our knowledge, this is the first direct experimental observation of a direct correlation between the evolution of a product in the gas phase and the formation of the corresponding reaction intermediate on the surface obtained under well-defined and isothermal conditions.

C–O vibrations in alkoxy-groups typical appear in the range from  $1050$  to  $1200\text{ cm}^{-1}$ . In our case, the most likely surface species related to the IR absorption at  $1120\text{ cm}^{-1}$  is a propenoxy-group, in which the C–O entity is attached to the Pd through the O atom ( $\text{CH}_2=\text{CH}-\text{CH}_2-\text{O}-\text{Pd}$ ). The high intensity of this band, exceeding even the most intense C=O vibrational band in acrolein and the oxopropyl species, additionally supports the formation of a C–O bond exhibiting a large dynamic dipole moment and, hence, explains the very high IR intensity. Furthermore, a IR vibration at  $2990\text{ cm}^{-1}$ , which also directly correlates with the formation of propenol, might indicate a C–H stretching vibration in which the C atom is part of a C=C bond suggesting that the reaction intermediate preserves a C=C group. The high intensity of the C–O stretching vibration indicates that the C–O–Pd entity is not lying flat on the surface according to the MSSR. This consideration implies that the C=C bond cannot be in very close proximity of the Pd surface and is most likely not directly involved into the interaction with the surface.

The most likely reaction intermediate contains a C=C bond and is attached to the Pd via the O atom forming a Pd–O–C group. This intermediate can be formed through adsorption of acrolein via the C=O group and addition of one H atom to a C atom. Only one additional step – the insertion of the second H atom into the Pd–O bond – is required to form propenol.

The third prominent band in the spectra in Figure 4.4 appears at  $1330\text{ cm}^{-1}$  during the period of high reactivity and steadily grows in intensity while the propenol formation rate decreases. This band indicates an ethylidyne or ethylidyne-like species. Since this species cannot be related to the reaction intermediate, it can be considered as a second spectator (SII).

It is important to note that the surface reaction intermediate is formed not on the pristine Pd(111) surface, but on the surface strongly modified with spectator I (oxopropyl species). Indeed, about one acrolein molecule per four Pd surface atoms is accumulated on Pd(111) to form the spectator prior to the onset of the propenol formation. Microscopically, this corresponds to a situation when every fourth Pd atom is covered by spectator I, forming a dense spectator overlayer structure. Most likely, such strong geometrical con-

finement of an adsorption site for acrolein on the spectator-I-covered surface prevents the competing pathway of C=C bond hydrogenation and allows acrolein to adsorb only via the O atom to activate the C=O group. Obviously, the clean Pd(111) surface is not capable of activating the C=O group towards selective hydrogenation and the strong modification of the surface by spectator I is required to trigger the desired selective chemistry. Formation of spectator II is correlated with the deactivation of the catalyst's surface. It might be speculated that it blocks the surface sites that are relevant for the formation of the reaction intermediate.

**Acrolein conversion over Pd/Fe<sub>3</sub>O<sub>4</sub>** In order to understand the absence of selective acrolein hydrogenation to propenol over Pd particles, identical spectroscopic investigations on the evolution of surface species during the reaction over Fe<sub>3</sub>O<sub>4</sub>-supported Pd model catalysts have been carried out. The experiments have been performed at 270 K, the optimal temperature for acrolein conversion to propenol on Pd(111). The results are illustrated in Figure 4.6. Under these conditions, selective formation of a relatively small amount of propanal occurs after a short induction period and the reaction rate decreases rapidly after passing a maximum. The evolution of surface species has been monitored by IRAS. A completely different surface composition is formed on the Pd/Fe<sub>3</sub>O<sub>4</sub> model catalysts. The spectra are dominated by features in the range of 1800-1960 cm<sup>-1</sup>, which can be clearly related to an accumulation of CO resulting from acrolein decarbonylation. The observation strongly suggests that acrolein decomposes on Pd/Fe<sub>3</sub>O<sub>4</sub> under this reaction conditions forming CO molecules that block surface sites and prevent the formation of a well-ordered spectator overlayer, which is required for acrolein conversion to propenol. We conclude that most likely low-coordinated surface sites and (100) facets of the Pd clusters are responsible for the facile acrolein decomposition and formation of CO.

Figure 4.7 summarizes the dominant pathways of acrolein conversion on a Pd(111) single crystal (a) and on Fe<sub>3</sub>O<sub>4</sub>-supported Pd particles (b).

The conversion of acrolein has been investigated in more detail on Fe<sub>3</sub>O<sub>4</sub>-supported Pd particles with diameters of 4 nm, 7 nm, and 12 nm. Our studies show that particle size and temperature have a significant effect on the surface chemistry during acrolein conversion on Pd/Fe<sub>3</sub>O<sub>4</sub> model catalysts. The results are discussed in detail in reference [187] (see Chapter 11). In brief summary, the rate of propanal formation on 7 nm and 12 nm particles exhibits a clear temperature dependence with a maximum at 220 K and thus at a lower temperature as the highest propenol production rate on Pd(111). With both particles sizes 7 nm and 12 nm, similar propanal production rates are observed, which passes through a maximum and then decreases to zero. On 4 nm particles, however, no significant production of any product appears. As mentioned before, IRAS studies during acrolein conversion at 270 K show fast accumulation of CO on the surface that rapidly covers the whole Pd facets. At 250 K and 220 K, however, significantly different surface chemistry occurs. The IR spectra collected during acrolein conversion over 7 nm and 12 nm particles at 220 K and 250 K mainly point to molecularly adsorbed acrolein and a small concentration of a spectator species. Finally, we briefly address the question whether propenol formation is possible on Pd/Fe<sub>3</sub>O<sub>4</sub> model catalyst. There are several aspects that

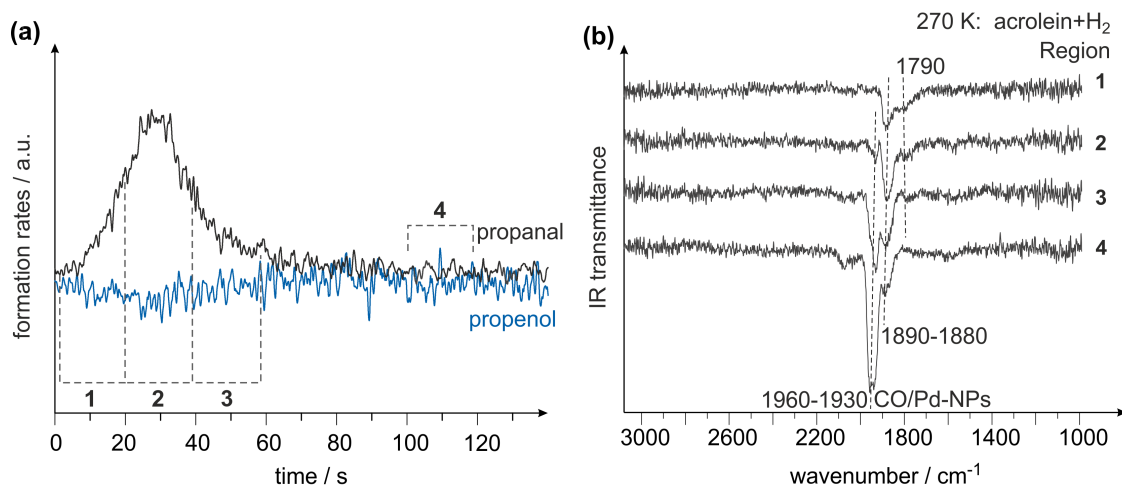


Figure 4.6: (a) Formation rates of propanal (black line) and propenol (blue line) on  $\text{Fe}_3\text{O}_4$ -supported Pd nanoparticles at 270 K under continuous exposure of  $\text{H}_2$  and acrolein. (b) IR spectra obtained on Pd/ $\text{Fe}_3\text{O}_4$  turning over. Spectra 1-4 correspond to the regions 1-4 indicated in (a).

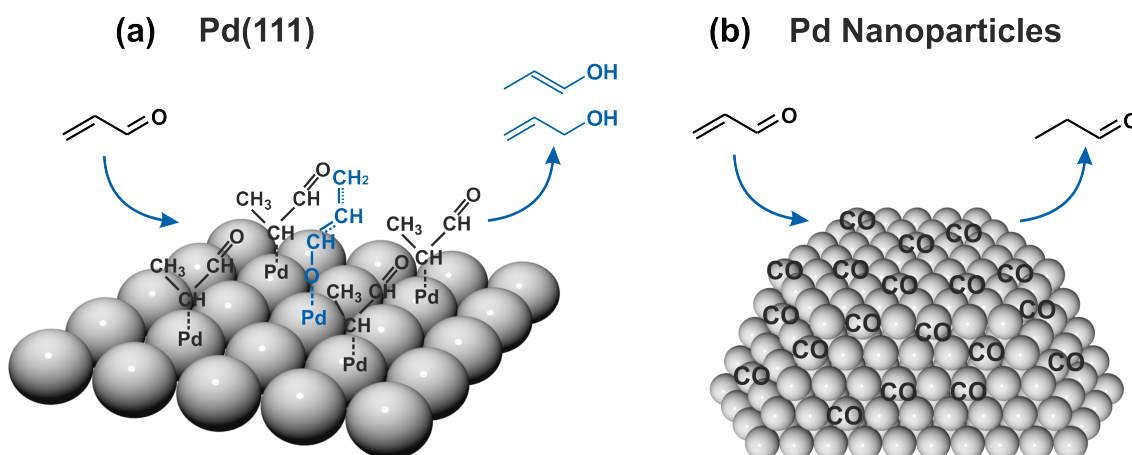


Figure 4.7: Summary of the dominant pathways of acrolein conversion on Pd(111) and Pd/ $\text{Fe}_3\text{O}_4$ : On Pd(111), an oxopropyl overlayer is formed during the initial stage of acrolein conversion. Subsequently acrolein is selectively converted to propenol. On Pd/ $\text{Fe}_3\text{O}_4$ , selective hydrogenation to propanal and decarbonylation to CO are the most likely reactions.

#### 4.2 Hydrogenation of Acrolein over Pd(111) and Pd/Fe<sub>3</sub>O<sub>4</sub>

need to be taken into account exceeding the scope of this summary.



## 5 Conclusions and Outlook

We have presented detailed investigations on mechanisms and kinetics of partial selective hydrogenation of  $\alpha,\beta$ -unsaturated aldehydes and ketones over well-defined Pd/Fe<sub>3</sub>O<sub>4</sub> model catalysts and Pd(111) single crystals. The conversion of this class of compounds has been investigated on two prototypical compounds, acrolein and isophorone. On the one hand, we have obtained detailed spectroscopic information on the chemical structure of the Pd-adsorbed hydrocarbons as well as on the effect of co-adsorbed hydrogen. On the other hand, we have obtained atomistic-level insights into mechanisms of acrolein partial hydrogenation over Pd and structural parameters controlling this surface reactions.

We have investigated the interaction of isophorone with Pd(111) in detail by NEXAFS and IRAS studies. In particular, the adsorption geometries of the C=C and C=O bonds on pristine and hydrogen-precovered Pd(111) as well as coverage-dependent effects on the adsorbates' structures have been studied. In the low-coverage limit, flat-lying C=C and C=O bonds indicating that the conjugated  $\pi$  system of the C=C and C=O bonds preserves its in-plane configuration, while dehydrogenation of a CH<sub>3</sub> to a CH<sub>2</sub> group appears to be possible. For intermediate sub-monolayer coverages, the structure of the conjugated  $\pi$  system seems to be strongly distorted with the C=C bond significantly tilted while the C=O bond is still oriented parallel to the Pd(111) facet. Close to the saturation coverage, both C=C and C=O bonds lift up, and the inclination angle of the entire  $\pi$  system (C=C–C=O) increases to about 40° with slightly stronger tilting of the C=C bond. In contrast to isophorone, the saturated ketone TMCH adsorbs in a strongly tilted geometry, interacting with the surface primarily through the C=O group from the low-coverage limit until saturation coverage. Furthermore, the coverage-dependent interaction of acrolein and propanal on Pd(111) has been investigated by IRAS. The adsorption geometries of the  $\pi$  bonds in acrolein and propanal at sub-monolayer coverages appear to be very similar to those in isophorone and TMCH.

IR studies show that the adsorption geometry of isophorone on Pd(111) is significantly affected by the presence of co-adsorbed hydrogen, in particular at intermediate coverages. On the hydrogen-precovered surface, the ratio of the IR absorption intensities of the C=O and C=C stretch vibration  $I_{C=O}/I_{C=C}$  indicates a rather unperturbed molecular structure that is similar to the gas-phase molecule. Higher tilting angles of both  $\pi$  bonds point to a weaker interaction of isophorone with hydrogen-precovered Pd and suggests the conservation of the in-plane geometry of the conjugated  $\pi$  system.

The mechanism of selective partial hydrogenation of acrolein over Pd(111) and Fe<sub>3</sub>O<sub>4</sub>-supported Pd nanoparticles has been investigated using a combination of molecular beam techniques with in-situ IRAS and QMS under well-defined UHV conditions. Acrolein is converted at the C=O bond with hydrogen to the unsaturated alcohol propenol over the

Pd(111) surface with nearly 100% selectivity, while C=C bond hydrogenation to the saturated aldehyde propanal occurs over supported Pd particles. The selectivity in propenol production critically depends on the presence of an overlayer of spectator species formed at an initial stage of Pd(111) exposure to acrolein and hydrogen. Most likely, a spectator, controlling the the surface chemoselectivity, results from addition of one H atom to the C=C bond of acrolein to form an oxopropyl species. After formation of a dense overlayer of this species, acrolein adsorbs on this modified surface via the C=O bond and converses to propenol. The nature of the corresponding surface reaction intermediate has been determined spectroscopically under reaction conditions. By monitoring the surface by IRAS in the course of acrolein conversion and simultaneously detecting the gas phase composition by QMS, we have been able for the first time to experimentally follow simultaneously the formation of the reaction intermediate on the surface and evolution of the product in the gas phase. With this approach, a direct assignment of one of the surface species to a reaction intermediate has been achieved, while the other surface species have been identified as spectators. On Fe<sub>3</sub>O<sub>4</sub>-supported Pd nanoparticles, formation of a spectator overlayer is prevented by strong acrolein decarbonylation and the surface is active essentially only for hydrogenation of the C=C bond.

The aim of the present study was to provide a comprehensive picture of the origin of selectivity and activity in partial hydrogenation of  $\alpha,\beta$ -unsaturated aldehydes and ketones over Pd catalysts. We have obtained detailed insights into the kinetics of acrolein and isophorone conversion over different Pd catalysts from different aspects. On the one hand, the coverage- and co-adsorbate-dependent changes in the molecular structures of isophorone and acrolein, particularly the adsorption geometry of the C=C and C=O bonds, are expected to have a decisive influence on the selectivity in hydrogenation reactions. In fact, our in-situ IRAS studies during acrolein hydrogenation unambiguously show that the change in selectivity from propanal to propenol formation is accompanied by a change in the adsorption geometry from a configuration with the C=C and C=O bonds lying flat on Pd(111) to a strongly tilted geometry with only the C=O group attached to the surface. On the other hand, the obtained atomistic-level insights into the chemoselective hydrogenation chemistry of acrolein highlights the exceptional importance of spectator species which are usually formed on the catalytically active surface under reaction conditions. Related effects are expected to generally play a key role in controlling the selectivity in hydrogenation of  $\alpha,\beta$ -unsaturated carbonyl compounds and thus hold a great potential for the development of new chemoselective practical catalysts, such as ligand-modified nanoparticles.

## 6 Interaction of Isophorone with Pd(111): A Combination of Infrared Reflection-Absorption Spectroscopy, Near-Edge X-ray Absorption Fine Structure, and Density Functional Theory Studies

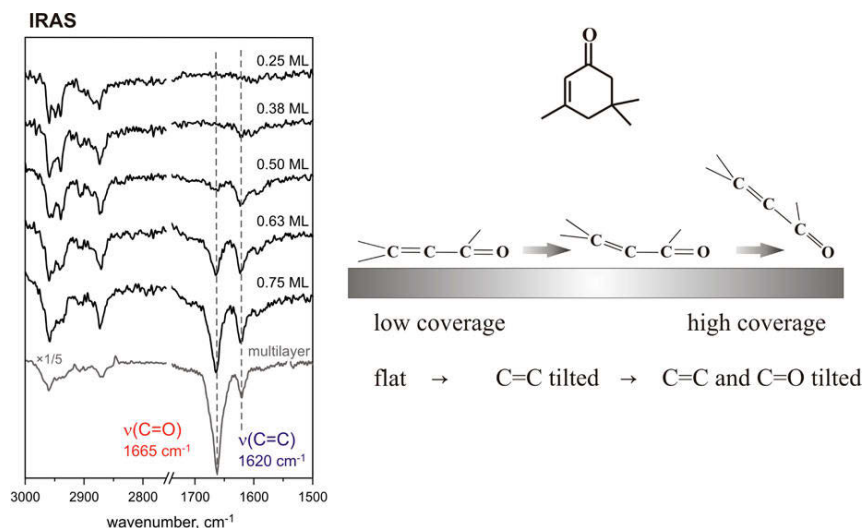
*Karl-Heinz Dostert<sup>1</sup>, Casey P. O'Brien<sup>1</sup>, Wiebke Riedel<sup>1</sup>, Aditya Savara<sup>1</sup>, Wei Liu<sup>1</sup>, Martin Oehzelt<sup>2</sup>, Alexandre Tkatchenko<sup>1</sup>, and Svetlana Schauermann<sup>1</sup>*

<sup>1</sup>Fritz-Haber-Institut der Max-Planck-Gesellschaft, Faradayweg 4-6, 14195 Berlin, Germany

<sup>2</sup>Helmholtz-Zentrum für Materialien und Energie, Albert-Einstein-Straße 15, 12489 Berlin, Germany

published in *J. Phys. Chem. C*, **2014**, *118* (48), 27833-27842

## Abstract



Atomistic level understanding of interaction of  $\alpha,\beta$ -unsaturated carbonyls with late transition metals is a key prerequisite for rational design of new catalytic materials with the desired selectivity toward C=C or C=O bond hydrogenation. The interaction of this class of compounds with transition metals was investigated on  $\alpha,\beta$ -unsaturated ketone isophorone on Pd(111) as a prototypical system. In this study, infrared reflection-absorption spectroscopy (IRAS), near-edge X-ray absorption fine structure (NEXAFS) experiments, and density functional theory calculations including van der Waals interactions (DFT+vdW) were combined to obtain detailed information on the binding of isophorone to palladium at different coverages and on the effect of pre-adsorbed hydrogen on the binding and adsorption geometry. According to these experimental observations and the results of theoretical calculations, isophorone adsorbs on Pd(111) in a flatlying geometry at low coverages. With increasing coverage, both C=C and C=O bonds of isophorone tilt with respect to the surface plane. The tilting is considerably more pronounced for the C=C bond on the pristine Pd(111) surface, indicating a prominent perturbation and structural distortion of the conjugated  $\pi$  system upon interaction with Pd. Pre-adsorbed hydrogen leads to higher tilting angles of both  $\pi$  bonds, which points to much weaker interaction of isophorone with hydrogen-precovered Pd and suggests the conservation of the in-plane geometry of the conjugated  $\pi$  system. The results of the DFT+vdW calculations provide further insights into the perturbation of the molecular structure of isophorone on Pd(111).

## 6.1 Introduction

Chemo- and enantioselectivity in hydrogenation of  $\alpha,\beta$ -unsaturated carbonyls on transition metals is a topic of ongoing research in the field of heterogeneous catalysis. Particularly important is the possibility to tune surface chemistry of multiunsaturated hydrocarbons, such as  $\alpha,\beta$ -unsaturated ketones and aldehydes, and their derivatives since they represent a broad class of valuable intermediates for practically important processes [188–190]. For molecules containing both a C=C and a C=O  $\pi$ -bond, such as, *e.g.*, the  $\alpha,\beta$ -unsaturated ketone isophorone, hydrogenation can yield either a saturated ketone (3,3,5-trimethylcyclohexanone), an unsaturated alcohol (isophorol), or a saturated alcohol (trimethylcyclohexanol). To avoid the formation of undesired products and thereby an often difficult and cost-intense separation of the different products, a high selectivity in hydrogenating either the C=C or the C=O bond is desirable. Over Pd catalysts, the hydrogenation of the C=C double bond of isophorone is strongly favored, yielding the saturated ketone in high selectivity (100%) and essentially no alcohols [191–193]. The origin of this chemoselectivity is, however, not fully understood. Not only a high chemoselectivity but even high enantioselectivities in hydrogenation reactions can be achieved over heterogeneous catalysts using a chiral modifier [194–196] that renders the surface asymmetric. Compared to homogeneous catalysts traditionally applied in enantioselective synthesis, the use of heterogeneous catalysts has operational, economical, and often environmental advantages. A number of different modifiers have been tested for the enantioselective hydrogenation of isophorone, which is a benchmark test molecule for enantioselective hydrogenation reactions of enones [194, 197–204]. Even though the exact origin of the enantioselectivity during hydrogenation of isophorone is not well understood so far, the specific adsorption geometry of isophorone, particularly the tilting angles of the unsaturated C=C and C=O bonds with respect to the surface plane, in combination with the adsorption geometry of the chiral modifier are usually discussed to play a decisive role in rendering the surface chemistry chiral [202, 203]. The effects of isophorone coverage and presence of hydrogen on the isophorone adsorption geometry have not been thoroughly investigated so far.

In this work, we investigate the adsorption of isophorone on Pd(111). Infrared reflection absorption spectroscopy (IRAS) and near-edge X-ray absorption fine structure (NEXAFS) studies were combined to investigate the effects of isophorone coverage and hydrogen coadsorption on the orientations of the C=C and C=O  $\pi$  bonds with respect to the Pd(111) surface plane. NEXAFS has been demonstrated to be a powerful tool that provides electronic and structural information on adsorbed molecules. In the past two decades it was shown that the application of NEXAFS can be extended from small to large organic molecules [124, 125]. The determination of the orientation of large molecules by C 1s  $\rightarrow$   $\pi^*$  resonances is employed to study the adsorption of organic molecules on metal surfaces [128, 168–170], Langmuir-Blodgett monolayers [127], self-assembly of long-chain alkanes [171], or aromatic molecules [169]. More recently high-resolution beamlines enabled spectroscopy with highly resolved additional fine structures, such as vibronic coupling and local vibronic excitations. NEXAFS data of organic molecules that show vibrational fine structure in superposition with the electronic excitation were obtained [172]. With regard to catalytic conversions, several NEXAFS studies focus on the interaction of unsaturated

hydrocarbons with metal surfaces. Attempts were made to correlate chemoselectivity in hydrogenation of multiple unsaturated compounds with the conformation of the adsorbates on the catalyst surface as determined by NEXAFS [63, 173]. In this study, infrared spectroscopy is used to complement NEXAFS in determining the adsorbate molecular structure as well as to provide additional information on the geometry of chemical bonds with respect to the substrate. While NEXAFS probes electronic states with very high sensitivity to small adsorbate coverages, IR spectroscopy is a very established tool to study the vibrations of chemical bonds. Complementary density functional theory studies including van der Waals interaction (DFT+vdW) were performed to rationalize the experimental observations.

We show that isophorone adsorbs on Pd(111) in a flat-lying geometry at low coverages preserving the in-plane geometry of the conjugated  $\pi$  system. The tilting angle of both double bonds changes with increasing coverage, however, to a different extent. Pre-adsorbed hydrogen leads to high tilting angles of both  $\pi$  bonds, which points to the conservation of the in-plane geometry of the conjugated  $\pi$  system and weaker interaction with Pd. DFT+vdW calculations confirm the flat-lying adsorption geometry of isophorone at low coverages. Both experimental and computational results suggest that the C=C bond of isophorone is significantly perturbed by the interaction with Pd, in terms of both the electronic and geometric structure, while the carbonyl bond appears to be hardly affected by the interaction with the metal.

## 6.2 Experimental Details and Methods

IRAS experiments were performed at the Fritz-Haber-Institut, Berlin, in an UHV apparatus that has been described in detail before [100]. In brief, either normal or deuterium-labeled isophorone ( $d_5$ -isophorone) was dosed onto the sample cooled to 100 K through a doubly differentially pumped multichannel array molecular beam controlled by valves and shutters. The source was operated at room temperature, and the beam diameter was chosen to exceed the sample size. The Pd(111) single crystal was cleaned prior to use by repeated cycles of  $\text{Ar}^+$  ion bombardment at room temperature, annealing at 1000 K, and oxidation in  $1 \cdot 10^{-6}$  mbar  $\text{O}_2$  at 750 K to remove residual carbon. The final cleaning cycle was stopped after annealing. The flatness and cleanliness of the Pd(111) single-crystal surface were checked by low-energy electron diffraction (LEED) and IRAS of adsorbed CO. IRAS data were acquired using a vacuum Fourier-Transform infrared (FT-IR) spectrometer (Bruker IFS 66v/S) with a spectral resolution of  $2 \text{ cm}^{-1}$  and using a mid-infrared (MIR) polarizer and p-polarized IR light. The surface was precovered with hydrogen by dosing 100 L of  $\text{H}_2$ . Isophorone (Acros Organics, 98%) or  $d_5$ -isophorone (Quotient Bioresearch (Radiochemicals) Limited, 90%) were purified prior to the experiments by repeated freeze-pump-thaw cycles. The stated coverages for IRAS experiments are given in fractions of a monolayer (ML) that were determined by TPD experiments (1 ML is defined as the surface coverage where the multilayer desorption feature begins to appear in the temperature-programmed desorption of isophorone from Pd(111)). The upper limit of a monolayer of isophorone is estimated to approximately  $7 \cdot 10^{14}$  molecules/ $\text{cm}^2$ .

NEXAFS experiments were performed at the undulator beamline UE52-PGM at the

BESSY-II synchrotron facility in Berlin. The Pd(111) single crystal was cleaned as described above by repeated sputtering-annealing-oxidizing cycles. Isophorone was purified by freeze-pump-thaw cycles prior to the exposure. Isophorone was deposited onto the Pd(111) at 100 K by placing the crystal in front of the gas doser. The monolayer coverage of isophorone was determined by the position of the C 1s peak in X-ray photoelectron spectroscopy that was found to change at the onset of a multilayer formation (data not shown) in agreement with literature data [63]. To deposit any defined submonolayer coverage of isophorone, correspondingly lower exposure times were used. Following deposition of isophorone onto the Pd(111) crystal, the sample was transferred to a separate analysis chamber for NEXAFS spectra collection. The analysis chamber was equipped with a channeltron detector with a retarding field of 150 V for partial electron yield NEXAFS measurements. The energy of the incident X-ray beam was scanned from 250 to 350 eV with a resolution of 0.1 eV in the range of 280-300 eV and 0.5 eV elsewhere. Spectra were taken at incident beam angles of 70° and 80° with respect to the sample normal, both with horizontal and vertical polarization with respect to the Pd(111) surface. The spectra were normalized by their C K edge. The pre-edge peaks were fitted by Gaussian functions. The absorption edge was fitted by a Gaussian onset and a linear decrease toward high energies [124, 127]. The orientations of the molecular orbitals were calculated from the ratio of the corresponding peak areas in the spectra measured with horizontally and vertically polarized light (the upper estimate of accuracy is  $\pm 5^\circ$ ) [124].

The DFT calculations were carried out using the recently developed PBE+vdW<sup>surf</sup> method [205], as implemented in the FHI-aims all-electron code [206]. The PBE+vdW<sup>surf</sup> method extends pairwise vdW approaches to modeling of adsorbates on surfaces by a synergetic combination of the PBE+vdW method [207] for intermolecular interactions with the Lifshitz-Zaremba-Kohn theory [208, 209] for the nonlocal Coulomb screening within the bulk. We employed the *tight* settings for integration grids and standard numerical atom-centered orbitals basis sets in FHI-aims code. We used the FHI-aims *tier2* basis set for light elements (H, C, and O) and *tier1* for Pd. The scaled zeroth-order regular approximation (ZORA) [210] was used to treat relativistic effects for Pd atoms. We built up four-layer Pd slabs with a  $(4 \times 4)$  unit cell, and each slab was separated by a 20 Å vacuum. The bottom two metal layers were constrained, whereas the uppermost two metal layers and the adsorbate were allowed to fully relax during geometry relaxations. For slab calculations, we used a  $3 \times 3 \times 1$  k-points mesh. On the basis of the most stable geometries, infrared vibrational spectra were calculated by a second derivative of the energy from the numerical change of the forces arising from small finite displacements. Six finite displacements were applied to each of the atoms with a value of 0.005 Å.

## 6.3 Results and Discussion

The adsorption of isophorone on Pd(111) at 100 K was experimentally studied under well-defined UHV conditions by IRAS and NEXAFS experiments. DFT+vdW simulations of the vibration modes of isophorone were employed to help the interpretation of the IR spectra. In this section, we discuss the adsorption geometry of isophorone, specifically focusing on tilting angles of both unsaturated bonds – C=C and C=O – with respect to

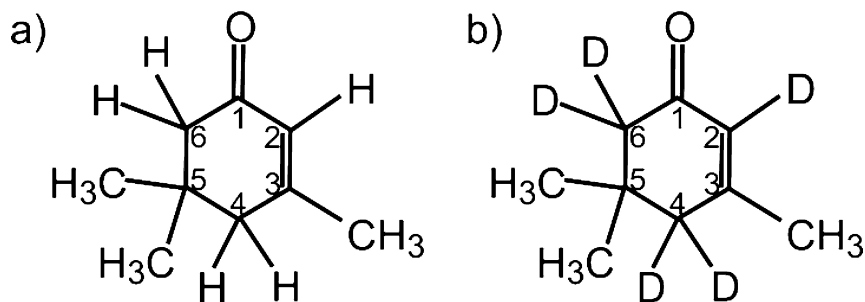


Figure 6.1: Molecular structure of isophorone (a) and  $d_5$ -isophorone (b)

the Pd(111) surface. The adsorption geometry of isophorone was investigated as a function of coverage on both pristine and hydrogen-precovered Pd(111).

### 6.3.1 Unsaturated C=C and C=O Bonds/Pd(111)

The structural formulas of normal and deuterium-substituted ( $d_5$ -) isophorone are shown in Figure 6.1. In the latter molecule, all five hydrogen atoms directly attached to the C<sub>6</sub> ring were substituted by five deuterium atoms. The IR spectra of isophorone ice, providing a reference for a nonperturbed molecular structure, are displayed in Figure 6.2 for normal and  $d_5$ -isophorone. For both molecules, three main spectral regions can be distinguished, which are characteristic of C–H stretching vibrations (2800–3200 cm<sup>−1</sup>), C=C and C=O stretching (1550–1850 cm<sup>−1</sup>), as well as for C–H, C–D, and C–C deformation vibrations (≤1500 cm<sup>−1</sup>). While the exact assignment of the stretching and deformation vibrations of C–H, C–D, and C–C bonds is rather complex and will be the subject of a forthcoming publication, the vibrational features corresponding to the C=C and C=O bonds can be clearly identified. In the normal isophorone molecule, the most intense vibration is the C=O stretching mode at 1665 cm<sup>−1</sup>, which lies very close to the vibrational frequency 1655 cm<sup>−1</sup> characteristic for the C=C stretching vibration. As can be clearly seen from the spectrum, these vibrational features strongly overlap making the distinction of both bonds rather difficult. In order to overcome this problem, the ring-substituted  $d_5$ -isophorone can be used, where the C=C vibrational feature appears at 1620 cm<sup>−1</sup>, showing a shift by 35 cm<sup>−1</sup> as compared to its nonsubstituted counterpart. The C=O bond in the  $d_5$ -isophorone appears to be hardly affected by the substitution in the ring and remains essentially at the same position as in the nonsubstituted isophorone.

The adsorption geometry of molecular species adsorbed on the metal surface can be deduced from their IRAS spectra based on the metal surface selection rule (MSSR) [106, 113]. According to the MSSR, only vibrations having a projection of the dynamic dipole moment perpendicular to the surface are visible in IRA spectra, while the vibrations parallel to the surface are strongly attenuated due to formation of an image dipole moment in the underlying metal substrate. To determine the orientation of isophorone, particularly the C=C and C=O bonds, a series of IR spectra were obtained at different isophorone coverages spanning the range from 0.25 ML up to 2.40 ML.

Figure 6.3a shows the IR spectra of  $d_5$ -isophorone adsorbed on Pd(111) at 100 K at dif-

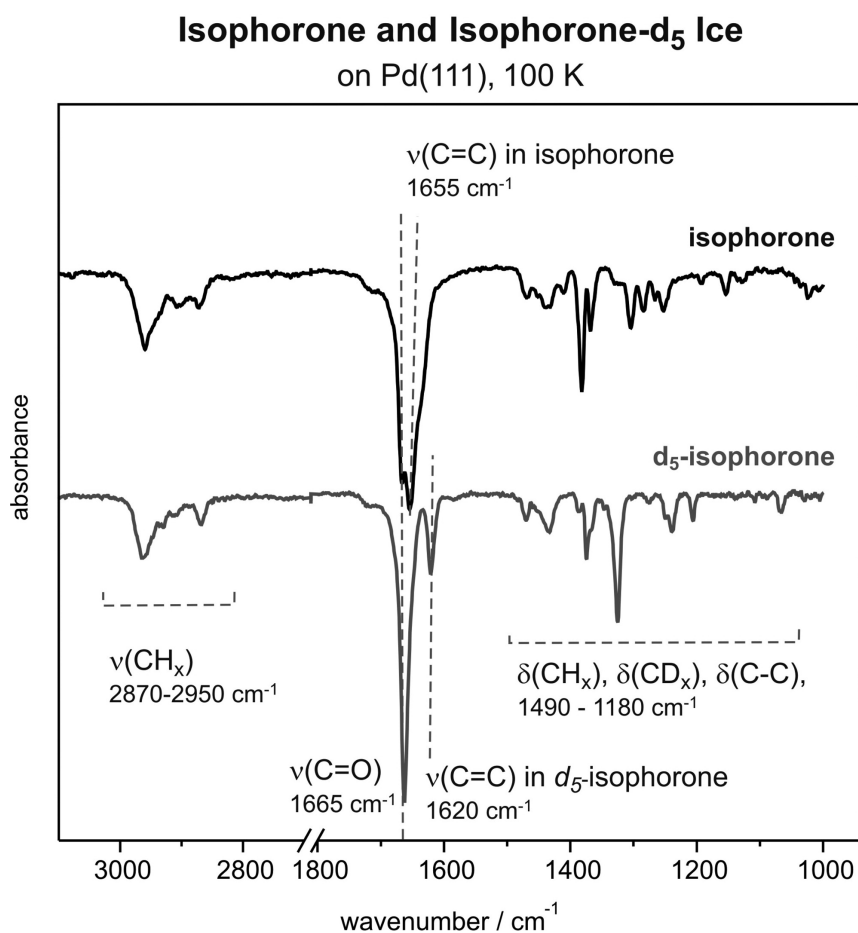


Figure 6.2: IR spectra of isophorone ice for the regular (upper trace) and  $d_5$ -substituted (lower trace) forms formed at 100 K on Pd(111). Three main spectral regions can be distinguished characteristic for C–H stretching (2800–3200 cm<sup>-1</sup>), C=C and C=O stretching (1550–1850 cm<sup>-1</sup>), and C–H, C–D, and C–C deformation vibrations ( $\leq 1500$  cm<sup>-1</sup>).

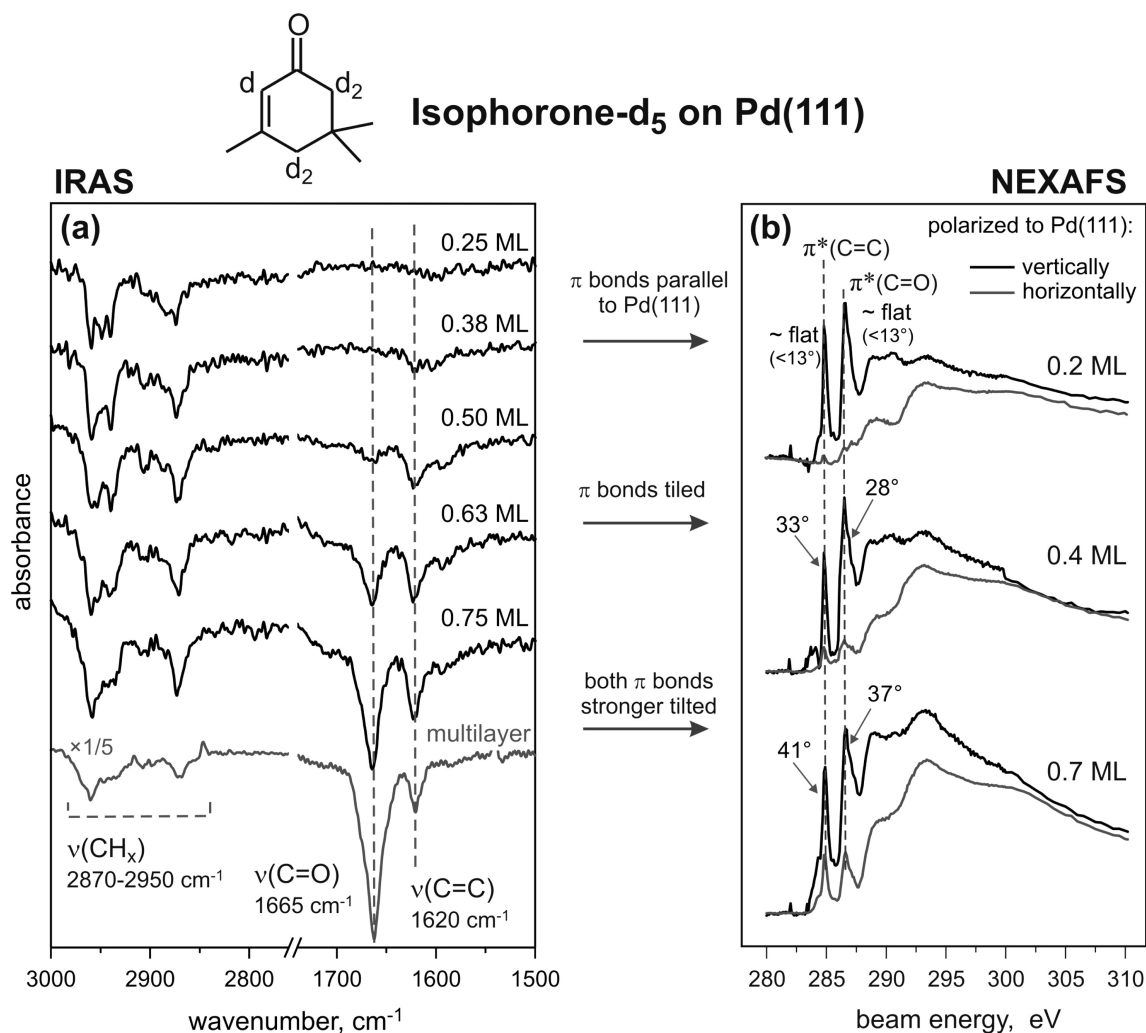


Figure 6.3: (a) IR spectra of  $d_5$ -isophorone adsorbed at 100 K on pristine Pd(111) for different exposures displayed for two main vibration regions: from 3000 to 2750  $\text{cm}^{-1}$  (C–H stretching vibrations) and from 1750 to 1500  $\text{cm}^{-1}$  (C=O and C=C stretching vibrations). (b) NEXAFS spectra of isophorone/Pd(111) obtained at 100 K show coverage-dependent orientations of both  $\pi$  bonds.

ferent coverages and the spectrum of isophorone ice for comparison with an unperturbed molecule. In these spectra, two vibrational regions are displayed for simplicity: the region of the C–H stretching vibrations (2800–3000  $\text{cm}^{-1}$ ) and the region of the C=O and C=C stretching vibrations (1665–1620  $\text{cm}^{-1}$ ). At the lowest coverage of  $d_5$ -isophorone (0.25 ML), there is a significant signal in the C–H stretching region; however, there is essentially no signal for the double bonds: neither for the C=O stretching mode nor for the C=C stretching mode. This intensity distribution is in a sharp contrast to the situation found for isophorone ice (see Figure 6.2 and the last spectrum shown in this series), where the most intense vibrations are that of the C=O and C=C bonds. The absence of absorption bands in the C=C and C=O stretching region indicates that these bonds are either oriented parallel to the surface and therefore cannot be seen because of MSSR or strongly perturbed (*e.g.*, dissociated to form bidentate species) by the interaction with Pd(111). With increasing  $d_5$ -isophorone coverage (0.38–0.75 ML), the intensity of the C–H stretching region increases only slightly, but the intensity of the absorption features in the region characteristic for C=C and C=O stretching vibrations changes very strongly. For an exposure of 0.5 ML  $d_5$ -isophorone, a pronounced C=C stretching signal centered around 1620  $\text{cm}^{-1}$  is observed, while the C=O stretching peak around 1665  $\text{cm}^{-1}$  is hardly visible. With increasing  $d_5$ -isophorone coverage, the intensity of the C=O stretching signal at 1665  $\text{cm}^{-1}$  increases rapidly and becomes the most intense peak in the spectra from 0.75 ML and higher. The ratio of the C=O to C=C peak intensities at 0.75 ML amounts to approximately  $I_{\text{C=O}}/I_{\text{C=C}} \approx 4$  and is roughly similar to the intensity ratio in the isophorone multilayer (*e.g.*, at 2.4 ML)  $I_{\text{C=O}}/I_{\text{C=C}} \approx 6$ –8. The intensities  $I_{\text{C=O}}$  and  $I_{\text{C=C}}$  are determined by integration of the IRAS peak areas. §§

NEXAFS experiments were performed under the same experimental conditions to obtain quantitative information on the coverage-dependent adsorption geometry of the C=C and C=O bonds in isophorone on Pd(111). In the present experiments, two different ways of determining the molecular tilting angles were used. The first method is based on the use of vertically polarized light; the NEXAFS spectra were obtained as a function of the incidence angle of the photon beam [126]. In the second method the incidence angle of the X-ray beam was kept constant, and the polarization was changed from vertically to horizontally polarized light [211]. The second method has the advantage that the sample geometry remains unchanged, and therefore the spectra become less susceptible to experimental uncertainties (*e.g.*, the illuminated area of the sample is the same). Both methods were applied, and the results showed very good qualitative agreement; however, the spread of the experimental data was considerably larger for the method one. For this reason, we will discuss only the results of the experiments based on the changing polarization while keeping the sample geometry constant.

Figure 6.4 shows two example NEXAFS curves in horizontal and vertical polarization corresponding to 0.7 ML of isophorone on Pd(111) with the fitted C K-edge and indication of the most pronounced excitations around the edge.

The pre-edge peak 1 around 284.9 eV and peak 2 around 286.6 eV appear much sharper than the postedge transitions. According to previous studies, peaks 1 and 2 are assigned to C 1s  $\rightarrow \pi^*$  (C=C) and C 1s  $\rightarrow \pi^*$  (C=O) excitations [63, 128, 170, 212, 213]. It should be noted that what permits the differentiation between the C=O and C=C resonances is not the final state (LUMO) but the initial state, *i.e.*, the C 1s states of the C=O carbon

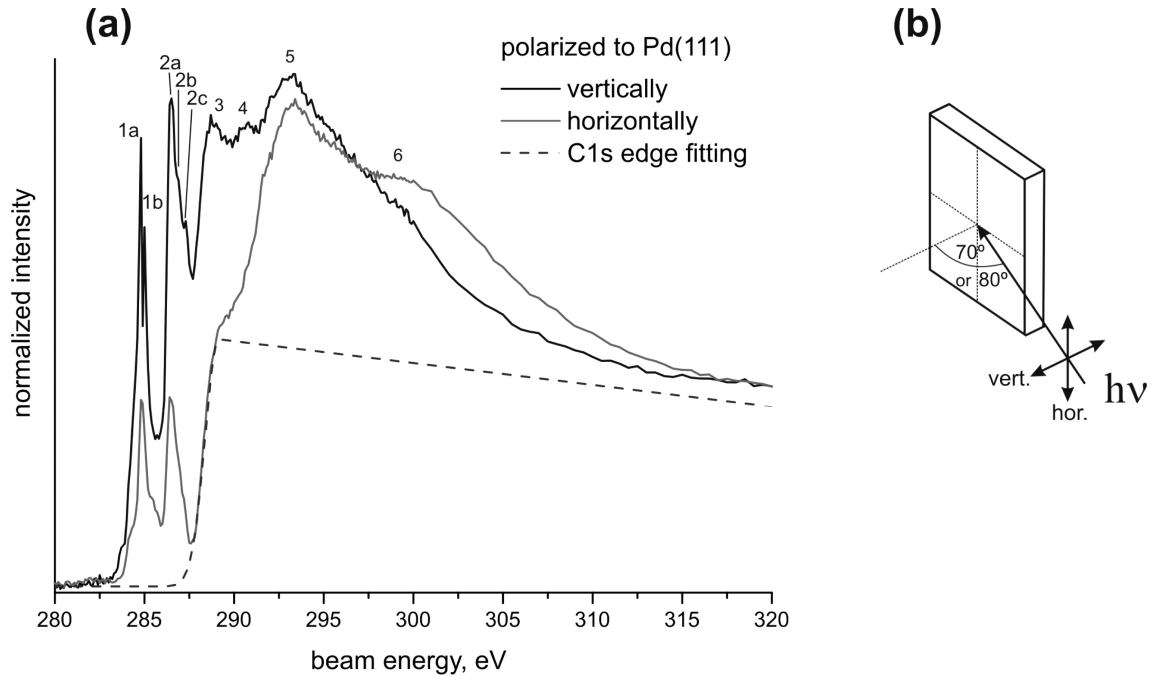


Figure 6.4: (a) C K-edge NEXAFS of 0.7 ML isophorone/Pd(111) at 100 K in vertical and horizontal polarization. The spectra are normalized to the C K-edge, which was fitted and is indicated with the dashed line. The most pronounced transitions around the edge are indicated with numbers 1 to 6. The assignment is given in Table 6.1. (b) Schematic representation of the NEXAFS experimental geometry.

Table 6.1: Assignment of NEXAFS peaks of isophorone

peak	energy/eV	excitation	reference
1 (1a, 1b)	284.9 (284.8, 285.0)	C $1s \rightarrow \pi^*$ (C=C)	[63, 128, 170, 212, 213]
2a (2b, 2c)	286.6 (286.9, 287.2)	C $1s \rightarrow \pi^*$ (C=O)	[63, 212, 213]
3	288.8	C $1s \rightarrow \pi_2^*$ (C=C)	[63, 128, 213]
4	290.7	C $1s \rightarrow \pi_2^*$ (C=O)	[63]
5	293.1	C $1s \rightarrow \sigma^*$	[63]
6	299	C $1s \rightarrow \sigma^*$	[63, 128, 213]

and the C=C carbons having different binding energies due to different chemical shifts. As long as the chemical nature of the molecule is preserved, i.e., both C=C and C=O bonds are not dissociated as in the case of this study, both resonances  $C\ 1s \rightarrow \pi^*$  (C=C) and  $C\ 1s \rightarrow \pi^*$  (C=O) can be observed as separate peaks.

In more detail, peak 1 consists of two features at 284.8 and 285.0 eV, which we correlate to excitations of C 1s electrons located at the two different C atoms of the C=C bond. However, they cannot be resolved as two peaks in every measurement and might appear as one feature located around 284.9 eV ( $\pm 0.1$  eV). Peak 2 has its maximum at 286.6 eV ( $\pm 0.1$  eV); in every recorded spectrum two shoulders appear around 286.9 eV ( $\pm 0.1$  eV) and 287.2 eV ( $\pm 0.1$  eV). The energy difference between the three features amounts to approximately 0.3 eV ( $\pm 0.2$  eV), which we tentatively assign to coupled excitations of  $C\ 1s \rightarrow \pi^*$  (C=O) electronic transitions and C=O vibronic excitations. Previously such coupled electronic and vibronic excitations have been observed for various organic molecules [172]. From IRAS the energy of the C=O bond vibration is calculated to be 0.21 eV. However, the resolution limit of the NEXAFS experiments was 0.1 eV, which is not ideal to determine vibration frequencies. According to previous assignments, the broad features 3 and 4 around 288.8 and 290.7 eV are assigned to  $1s \rightarrow \pi_2^*$  (C=C) and  $1s \rightarrow \pi_2^*$  (C=O) transitions [63, 213]. Both features show identical dependence on the polarization of the incident beam as the corresponding  $C\ 1s \rightarrow \pi^*$  (C=C) and  $C\ 1s \rightarrow \pi^*$  (C=O). The very broad excitation features 5 and 6 around 293.1 and 299 eV are to a large extent independent of the polarization and can be attributed mainly to several  $C\ 1s \rightarrow \sigma^*$  transitions, as reported elsewhere [63, 213].

C K-edge NEXAFS was measured for isophorone coverages of 0.2, 0.4, and 0.7 ML, each with horizontally and vertically polarized X-ray beam and incident angles of 70° and 80° with respect to the surface normal. A series of representative coverage-dependent, step-edge normalized C K-edge NEXAFS spectra with incident angle of 70° are shown in Figure 6.3b. The two most important features in the spectra are the pre-edge peaks that are assigned to the  $C\ 1s \rightarrow \pi^*$  (C=C) resonance at 284.9 eV and the  $C\ 1s \rightarrow \pi^*$  (C=O) resonance at 286.6 eV. These peaks can be already clearly seen at the lowest coverages of isophorone (0.2 ML), indicating thus that both C=C and C=O bonds are not dissociated upon interaction with Pd(111). At the lowest coverage (0.2 ML), a flat-lying geometry of the  $\pi$ (C=C) and the  $\pi$ (C=O) bond is evident by the strong dependence of the intensity of both pre-edge peaks on the polarization of the incident beam. While there is a strong resonance of both  $\pi$  bonds with vertically polarized light (black), almost no absorption is detectable with horizontally polarized light (gray) suggesting a flat-lying adsorption geometry of isophorone. With increasing coverage, the intensity of both  $\pi$  resonance peaks with horizontally polarized light increases relative to the resonance with vertically polarized light, indicating that the tilting of isophorone increases. The coverage-dependent angles of the C=C and C=O bonds with respect to the Pd(111) crystal plane were calculated and are summarized in Table 6.2. It should be pointed out that in a general case the directions of specific bonds are not accessible with NEXAFS. Only the angle between the substrate surface normal and the direction of the transition dipole moments of the respective  $C\ 1s \rightarrow \pi^*$  transitions can be determined. In this study, we make an assumption that the geometry of the  $\pi^*$  orbital with respect to the corresponding double bond remains fairly constant upon adsorption, an assumption that is supported

Table 6.2: Inclination angles of the unsaturated bonds in isophorone with respect to the Pd(111) surface for different coverages of isophorone and for 0.7 ML isophorone with co-adsorbed hydrogen.

isophorone coverage/ML	tilting C=C bond/°	tilting C=O bond/°
0.2	$\leq 13$ ( $\pm 6$ )	$\leq 13$ ( $\pm 6$ )
0.4	$33$ ( $\pm 2$ )	$28$ ( $\pm 2$ )
0.7	$41$ ( $\pm 2$ )	$37$ ( $\pm 2$ )
H/Pd(111)+0.7	$45$ ( $\pm 2$ )	$40$ ( $\pm 2$ )

by theoretical calculations. Therefore, we assume that the changes of the C 1s  $\rightarrow \pi^*$  transitions corresponding to the C=C and C=O double bonds reflect the tilting of the conjugated fraction of the molecule. An excellent agreement between the NEXAFS results and IRAS data as well as the results of theoretical calculations, which will be discussed in the following, support a good validity of this assumption.

The strong polarization dependence of the pre-edge peaks at a coverage of 0.2 ML allows us to conclude that isophorone adopts essentially a flat adsorption geometry on Pd(111) at low coverages. Since NEXAFS becomes relatively inaccurate at very small tilting angles of the  $\pi$  bonds, the formally determined tilting angle of  $13^\circ$  with respect to the Pd(111) should be rather considered as an upper limit of the inclination angle. The possible source of the error can also be the uncertainty of the experimental alignment, *e.g.*, difficulty of setting the sample surface precisely parallel to the horizontal electric vector or the polarization factor of the incident X-ray. At an intermediate coverage (0.4 ML), the C=C bond ( $33^\circ \pm 2^\circ$ ) is slightly more tilted than the C=O bond ( $28^\circ \pm 2^\circ$ ). At high coverage (0.7 ML) both unsaturated bonds are strongly inclined. Still, the C=C bond ( $41^\circ \pm 2^\circ$ ) takes a tentatively more upright position than the C=O bond ( $37^\circ \pm 2^\circ$ ). The inclination angles obtained for the highest isophorone coverages are in a good agreement with the recent NEXAFS results from Lambert *et al.*, where the C=C–C=O framework in isophorone was found to be tilted by  $42^\circ$  with respect to the surface at high isophorone coverages [63].

The IRAS and NEXAFS results for the coverage-dependent adsorption geometry of isophorone on clean Pd(111) are in qualitative agreement. At low coverages isophorone lays flat on the Pd(111) surface, which results in a complete attenuation of the vibrational features characteristic for C=O and C=C bonds, while the dynamic dipole moments of C–H stretching vibrations are at least partly inclined and therefore the corresponding bond vibrations visible. As observed by NEXAFS, both C=C and C=O bonds are present in a nondissociated form, which rules out the hypothesis on scission of these bonds as a reason for the missing IR bands at the lowest isophorone coverages. The estimated upper limit for the inclination angle of both  $\pi$  bonds ( $13^\circ$ ) is in a good agreement with the flat adsorption geometry of the conjugated C=C and C=O bonds deduced from the IRAS data. This observation suggests that isophorone essentially preserves the in-plane configuration of the conjugated  $\pi$  system in the low coverage limit.

With increasing coverage, the inclination angles of both the C=C and C=O bonds increase, with the tilting of the C=C bond being considerably more pronounced than that of the C=O bond according to IRAS. In fact, at the coverage of 0.5 ML the intensity of

the IRAS absorption of the C=C bond is already comparable with the intensity of this bond on the isophorone-saturated surface, while the intensity of C=O vibration is still very close to zero. This observation indicates that the conjugated  $\pi$  system of C=C and C=O bonds is very strongly distorted. In a gas-phase molecule, these two bonds are lying in the same plane. If the molecule would uniformly lift up, one would expect identical tilting angles and, hence, the ratio of the absorptions in IRAS  $I_{\text{C=O}}/I_{\text{C=C}}$  close to the ice value ( $I_{\text{C=O}}/I_{\text{C=C}} \approx 6-8$ ). The observation of the intense C=C vibration and the absence of the C=O vibration in IRAS indicate that at intermediate coverages the C=O bond is still nearly lying flat on the surface, while the C=C bond lifts up resulting in a strong distortion of the original in-plane molecular structure of isophorone. The higher tilting of isophorone at intermediate coverages can also be observed in the NEXAFS data; however, this trend is somewhat less pronounced, probably because of an absolute difference in coverage. The pronouncedly tilted adsorption geometry at high coverages most likely originates from steric constraints on the surface. Since the intensity ratio in IRAS  $I_{\text{C=O}}/I_{\text{C=C}} \approx 4$  at this coverage becomes closer to the ice value of 6-8, diminishing distortion of the isophorone molecular structure can be concluded for the high coverage limit. Note that the IRAS data allow more reliable conclusions on the adsorption geometry of both double bonds since the relative orientation of the C-C and C-O axes with respect to the metal surface plane is determined. In NEXAFS, only the angle between the metal surface plane and the direction of the transition dipole moments of the respective  $1s \rightarrow \pi^*$  transitions can be obtained; possible rotation of the  $\pi$  bonds with respect to the C-C or C-O axes might complicate the interpretation of the NEXAFS spectra.

The experimental results pointing to the flat-lying adsorption geometry of isophorone at the lowest coverage were corroborated by the theoretical calculations. In this study, the DFT+vdW<sup>surf</sup> method with the Perdew-Burke-Ernzerhof (PBE) functional [214] was applied to computationally investigate the details of the electronic structure of isophorone adsorbed on Pd. The PBE+vdW<sup>surf</sup> method is an accurate and efficient vdW-inclusive approach that allows quantitative treatment of both weakly and strongly adsorbed molecules on metal surfaces [205, 215–217].

Figure 6.5a illustrates the most stable adsorption structure found in vdW<sup>surf</sup> geometry relaxations for isophorone. In agreement with the experimental observations by IRAS and NEXAFS, isophorone was computed to adsorb in a flat-lying adsorption geometry with the C=C and C=O bonds oriented parallel to the substrate surface plane [218]. The O-Pd and C-Pd distances for the C=O and C=C bonds are in the range of 2.14-2.29 Å, close to typical covalent bond lengths. In contrast, carbon atoms in the three methyl groups attached to the ring, which are highly affected by the vdW forces, are lifted above the surface by 2.87-4.98 Å. The C=C bond in the adsorbed isophorone was found to be elongated by 0.1 Å as compared to the isolated molecule (from 1.35 to 1.45 Å), suggesting a change of the effective bond order of the C=C bond. The carbonyl bond is less elongated than the C=C bond (from 1.23 to 1.29 Å).

To examine the feasibility of the calculated adsorption structure, the isophorone IR spectra were calculated both for gas-phase and adsorbed on Pd(111) molecules using the harmonic approximation (Figure 6.5b, two lowest curves). The calculated spectra were found to reproduce the most essential features of the experimentally measured IR spectra. The most intense vibrational features for the isophorone gas-phase molecule were

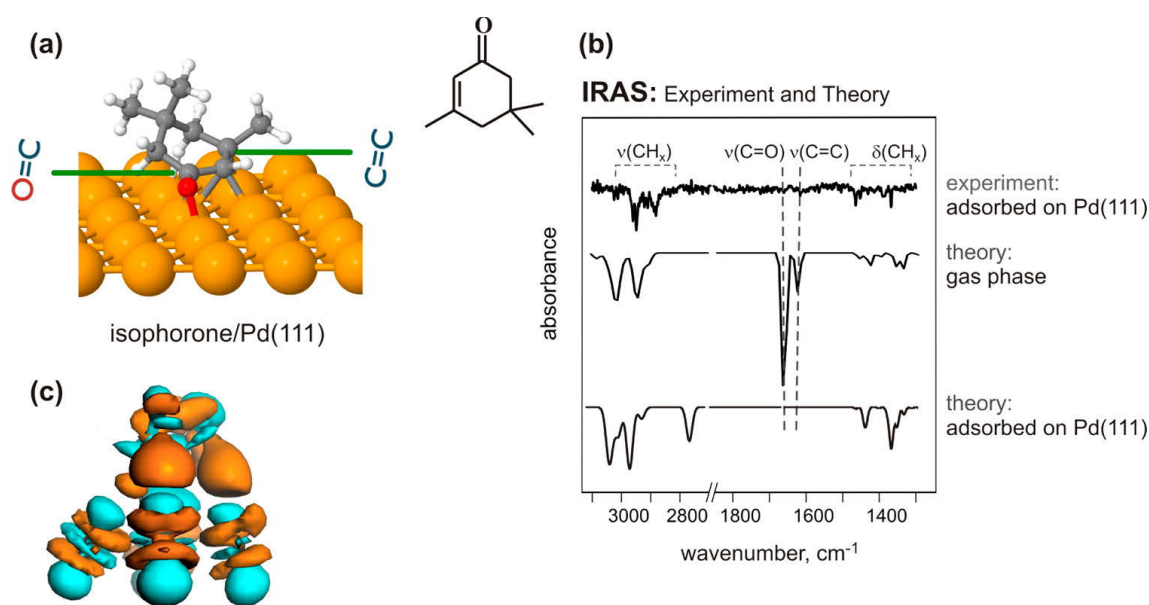


Figure 6.5: (a) Calculated structures of isophorone adsorbed on the Pd(111) surface. (b) Experimental and theoretical IR spectra of gas-phase and surface-adsorbed isophorone on Pd(111); the uppermost trace is the experimental spectrum measured at 100 K; the intermediate and the lowest traces are the calculated harmonic IR spectra for the gas-phase and the adsorbed molecules, correspondingly. The peak at 2753 cm<sup>-1</sup> does not appear in the experimental spectrum due to substantial broadening of this vibrational band because of a very short lifetime of the C–H–Pd bond. (c) A side view of the electron density difference upon isophorone adsorption on Pd(111) at its equilibrium adsorption structure, using the value of the isosurface of 0.25 Å<sup>-3</sup>. Cyan and orange indicate electron depletion and accumulation, respectively.

computed in the range of C=O and C=C vibrations, which are in good agreement with the experimental observations obtained for isophorone ice (Figure 6.2) that can be considered as a proxy for a nonperturbed molecular form of isophorone. For the adsorbed molecule, a vanishing of C=O and C=C stretching modes was computed as expected for a flat-lying molecule. This observation is in excellent agreement with the experimental IR spectra at the lowest measured isophorone coverage (the upper curve in Figure 6.5b and Figure 6.3a). For the high frequency region of C–H stretching vibrations ( $2200\text{--}2900\text{ cm}^{-1}$ ), there is good qualitative agreement between the calculated and the measured spectra of adsorbed isophorone. The only visible difference appears for the calculated isophorone spectrum at  $2573\text{ cm}^{-1}$ , which is the stretch mode of the C–H–Pd vibration. This discrepancy arises from substantial broadening of this vibrational band due to a very short lifetime of the C–H–Pd bond precluding its experimental observation. To check the latter possibility, an *ab initio* molecular dynamics simulation was carried out at 130 K, and the anharmonic IR spectra for isophorone/Pd(111) through the Fourier transform of the dipole autocorrelation function were calculated [219]. The explicit inclusion of anharmonic effects through dipole–dipole autocorrelation function leads to the disappearance of the peak at  $2573\text{ cm}^{-1}$  in the PBE+vdW IR spectra, in very good agreement with experimental spectra. Further details will be presented in an upcoming publication.

The vdW forces were found to significantly contribute to the adsorption of isophorone. The standard PBE functional predicts 0.58 eV binding energy for isophorone, while the inclusion of the vdW interaction increases the binding energy to 1.80 eV. It should be noted that the most stable configuration (the flat-lying molecule) could not be located by PBE calculations when starting from a random isophorone configuration, while it was readily obtained using PBE+vdW. The large contribution of the vdW interaction to the final binding energy can be traced back to the fact that the methyl groups and the ring of isophorone lie very close to Pd(111). Having obtained the adsorption geometries correctly reproducing the experimental observations from IRAS and NEXAFS, we performed an analysis of its electronic structure and the degree of its perturbation by the interaction with the metal surface. Figure 6.5c shows the side view of the electron density difference for isophorone on the Pd(111) surface, which serves to visualize the electron density redistribution upon adsorption. Cyan and orange colors indicate electron depletion and accumulation, respectively. The observed strong charge redistributions clearly indicate a substantial charge transfer between the adsorbate and the substrate.

As a next step, the electron density redistribution between the molecule and the substrate was analyzed by projection of the density of states (DOS) of the full adsorption system onto selected molecular orbitals of the free molecule.<sup>49</sup> The full details of this analysis will be discussed in a forthcoming publication; here, we will only briefly discuss the main results. Three particular molecular orbitals of isophorone were found to be mostly perturbed by the interaction with the metal: the former  $\text{HOMO}^{-1}$ , former HOMO, and former LUMO. While former HOMO and  $\text{HOMO}^{-1}$  of isophorone were computed to be rather localized orbitals in the full adsorption system (mainly located on the C=O and C=C bonds, respectively) the former LUMO is distributed over the entire  $\pi$  system. The former LUMO of isophorone was found to be partially filled with 0.656 electrons and largely shifted below the Fermi level. The occupancy of the former  $\text{HOMO}^{-1}$ , mainly located on the C=C bond, is reduced from 2 to 1.57. In contrast, the occupation number

of the former HOMO, located on the C=O bond, remains hardly changed. In total, in the scope of this analysis about 1.27 electrons are donated from the molecule (HOMO and below) to the empty band of the metal, and 1.08 electrons are back-donated from metal to the empty bands of the molecule (LUMO and above). Combining these observations, we conclude that the electronic structure of isophorone is strongly perturbed by interaction with Pd(111), with notably larger charge transfer from the C=C bond than from the C=O bond.

In the next section, we investigate the effect of pre-adsorbed hydrogen.

### 6.3.2 Effect of Hydrogen on the Geometry of C=C and C=O Bonds

The effect of pre-adsorbed H was investigated by IRAS and NEXAFS measurements that were conducted at 100 K on Pd(111). Prior to the isophorone exposure, Pd(111) was exposed to 100 L of H<sub>2</sub>. At this exposure, hydrogen forms a saturated layer of surface-adsorbed H species with a formal stoichiometry H:Pd 1:1 [220]. The corresponding IR spectra for isophorone exposures ranging from 0.25 to 0.75 ML are depicted in Figure 6.6a (black traces). For comparison, the IR spectra of isophorone adsorbed on clean Pd(111) are also displayed (gray traces).

The total intensities of the C–H stretching features (2800–3000 cm<sup>−1</sup>) were found to be similar on both clean and hydrogen-precovered Pd(111) at different isophorone exposures. This observation might be considered as an indication that similar isophorone coverages are formed on both surfaces. In contrast, IR absorption due to C=C and the C=O vibrations strongly changes when hydrogen was pre-adsorbed and is most pronounced around the coverage of 0.5 ML. At the coverage of 0.5 ML, the C=O vibration is clearly visible on Hprecovered Pd(111), while the C=C vibration cannot be identified yet. On the pristine Pd(111) surface, the situation was found to be reverse – the most intense vibrational feature corresponds to the C=C bond, while the C=O bond vibration is hardly visible. At 0.75 ML, the ratio of the C=O to the C=C vibration peak intensities ( $I_{\text{C=O}}/I_{\text{C=C}} \approx 5$ ) is similar to that of multilayer isophorone on clean Pd(111) ( $I_{\text{C=O}}/I_{\text{C=C}} \approx 6 - 8$ ). At the lowest coverage of 0.25 ML the spectra are essentially identical on both surfaces pointing to the flat-lying adsorption geometry of isophorone also on the hydrogen-precovered surface.

The observed coverage dependence indicates that the interaction of isophorone with Pd is considerably affected by pre-adsorbed hydrogen. While at the lowest coverage isophorone adopts – similarly to the pristine Pd surface – a flat adsorption geometry, the interaction changes at the intermediate surface coverages. Particularly, the ratio  $I_{\text{C=O}}/I_{\text{C=C}}$  becomes close to the ice (or gas-phase) value, indicating that isophorone lifts up rather uniformly and that the conjugated  $\pi$  system of two double bonds preserves to a large extent its inplane geometry characteristic for ice or the gas-phase molecule. This behavior is in sharp contrast for the coverage dependence of isophorone adsorption geometry obtained on the pristine Pd(111) surface, where the C=C bond was concluded to be strongly tilted with respect to the flat-lying C=O bond and the total conjugated  $\pi$  system is significantly geometrically distorted. The diminished distortion of the molecule in the presence of hydrogen most likely originates from the weaker interaction of isophorone with the hydrogen-containing Pd surface, a phenomenon which was discussed also for other hydrocarbon–metal systems.

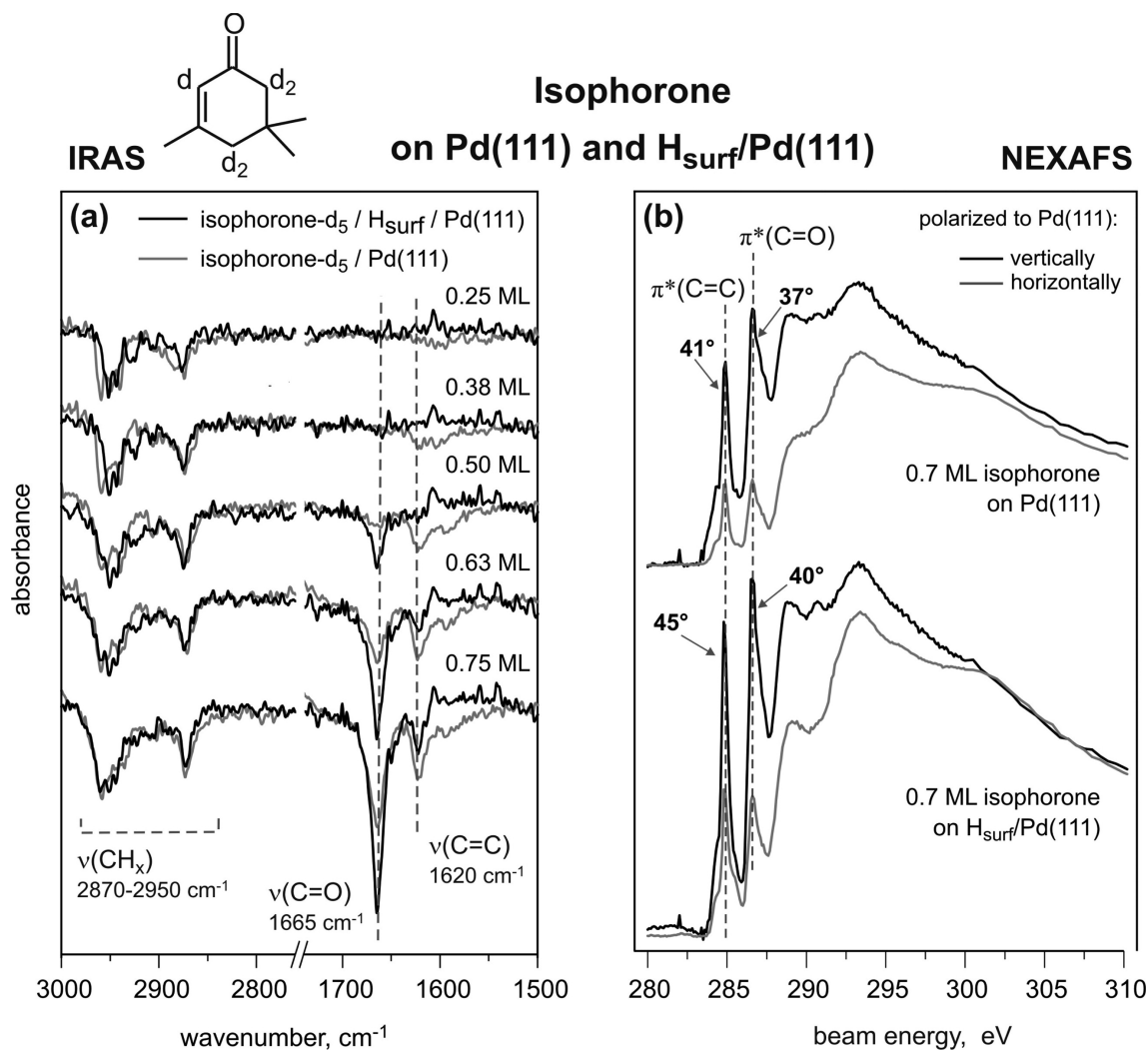


Figure 6.6: (a) IR spectra of *d*<sub>5</sub>-isophorone adsorbed at 100 K on hydrogen-precovered (black traces) and pristine (gray traces) Pd(111) for different exposures. Displayed are two main vibration regions: from 3000 to 2750 cm<sup>-1</sup> (C–H stretching vibrations) and from 1750 to 1500 cm<sup>-1</sup> (C=O and C=C stretching vibrations). (b) NEXAFS spectra obtained at 100 K for 0.7 ML isophorone coverage on pristine Pd(111) (upper traces) and H-precovered Pd(111) (lower traces).

NEXAFS studies were performed to gain quantitative information on the changes in tilting angle of the two unsaturated C=C and C=O bonds in the presence of pre-adsorbed hydrogen. In Figure 6.6b, representative C K-edge normalized NEXAFS spectra of 0.7 ML isophorone adsorbed on clean Pd(111) (top) and on hydrogen-precovered Pd(111) (bottom) are displayed. The angles of the C=C and the C=O bonds relative to the Pd(111) substrate were calculated and are given in Table 6.2. Our results indicate that coadsorbed hydrogen slightly increases the inclination angle of the C=C bond (from  $41^\circ \pm 2^\circ$  to  $45^\circ \pm 2^\circ$ ) and the C=O bond (from  $37^\circ \pm 2^\circ$  to  $41^\circ \pm 2^\circ$ ) with respect to Pd(111). It should be noted that the isophorone coverages used in these experiments are close to the saturation, where the IRAS data do not indicate any strong differences between the adsorption geometries of isophorone. NEXAFS data at lower coverage, where IRAS point to a stronger influence of hydrogen precovering on the adsorption of isophorone, are not available. However, the NEXAFS data are consistent with the observations of the IRAS experiments showing in general higher inclination angles of unsaturated bonds on the hydrogen-precovered Pd(111).

It should be noted that under the reaction conditions some of the isophorone molecules might undergo chemical transformations, *e.g.*, partial dissociation, resulting in different surface species with presumably different adsorption geometries. Whether these eventual species could be produced and be involved in the reactive pathway is a question that needs to be answered in future studies. At the present time, we cannot exclude that higher variety of surface species might be present on Pd during isophorone partial hydrogenation.

## 6.4 Conclusions

Interaction of isophorone with Pd was investigated experimentally by the combination of NEXAFS and IRAS and theoretically with DFT+vdW. Particularly, the adsorption geometry of the two unsaturated bonds (C=C and C=O) in isophorone on pristine and hydrogen-precovered Pd(111) surfaces as well as the coverage dependence of the adsorbate structures were determined. At low coverages, both NEXAFS and IRAS data point to a flat-lying adsorption geometry of isophorone on Pd(111) with the C–C and C–O bonds being oriented parallel to the surface plane. This observation suggests that isophorone preserves the in-plane configuration of the conjugated  $\pi$ -system in the low coverage limit. For intermediate coverages, the structure of isophorone adsorbed on pristine Pd(111) was observed to be strongly distorted. The C=C bond becomes noticeably tilted with respect to the surface plane, while the C=O bond is still oriented flat on the surface. Close to saturation, both the C=O and the C=C bonds lift up, and the inclination angles of the entire conjugated  $\pi$  system increase to around  $40^\circ$  with slightly more pronounced tilting of the C=C bond. High tilting angles of the entire molecule at higher coverages most likely originate from steric constraints on the surface.

DFT+vdW calculations confirmed the flat-lying adsorption geometry of isophorone at low coverages and provided further microscopic insights into interaction of isophorone with Pd. It was found that the C=C bond of isophorone is significantly perturbed by the interaction with Pd, in terms of both the electronic and geometric structure, showing a strong elongation of the bond and a large extent of the electron density redistribution.

In contrast, the carbonyl bond in isophorone was found to be hardly affected by the interaction with the metal. The computed IR spectra are in good agreement with the experimentally measured ones.

The IR spectra show that the adsorption of isophorone is significantly affected by the presence of coadsorbed hydrogen, particularly pronounced at the intermediate coverage. While at the lowest coverages isophorone exhibits a flat-lying geometry, similarly to pristine Pd(111), both unsaturated bonds strongly tilt already at intermediate coverages. In this case, the intensity ratio  $I_{\text{C=O}}/I_{\text{C=C}}$  of the main vibrational peaks on hydrogen-precovered Pd(111) indicates a rather unperturbed molecular structure of adsorbed isophorone that is similar to the gas-phase molecule. Higher tilting angles of both  $\pi$  bonds point to much weaker interaction of isophorone with hydrogen-precovered Pd and suggest the conservation of the in-plane geometry of the conjugated  $\pi$  system.

With respect to the gas-phase structure, the molecules appear to be more perturbed on the clean Pd(111) surface and considerably less on the hydrogen-precovered surface. These coverage- and coadsorbate-dependent changes in the adsorption geometry of the C=C and/or the C=O bond are expected to have a decisive influence on the selectivity in hydrogenation reactions.

## Acknowledgements

The authors thank Matthias Peter, Sergey Adamovski, Jose Manuel Flores Camacho, Helmut Kuhlenbeck, and the technical staff of BESSY-II for the scientific and technical support during the beam time. A.T. acknowledges support from the European Research Council (ERC Starting Grant VDWCMAT). S.S. acknowledges support from the Fonds der Chemischen Industrie for the Chemiedozentenstipendium and the European Research Council (ERC Starting Grant 335205-ENREMOS).



# 7 Adsorption of Isophorone and Trimethyl-Cyclohexanone on Pd(111): A Combination of Infrared Reflection-Absorption Spectroscopy and Density Functional Theory Studies

*Karl-Heinz Dostert<sup>1</sup>, Casey P. O'Brien<sup>1</sup>, Wei Liu<sup>1,3</sup>, Wiebke Riedel<sup>1</sup>, Aditya Savara<sup>1</sup>, Alexandre Tkatchenko<sup>1</sup>, Svetlana Schauermann<sup>1,2</sup>, and Hans-Joachim Freund<sup>1</sup>*

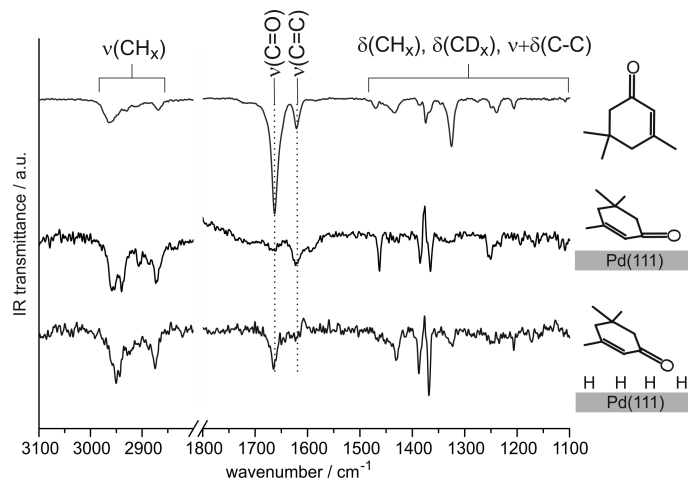
<sup>1</sup>Fritz-Haber-Institut der Max-Planck-Gesellschaft, Faradayweg 4-6, 14195 Berlin, Germany

<sup>2</sup>Institut für Physikalische Chemie, Christian-Albrechts-Universität zu Kiel, Max-Eyth-Str. 1, 24118 Kiel, Germany

<sup>3</sup>Nano Structural Materials Center, School of Materials Science and Engineering, Nanjing University of Science and Technology, Nanjing 210094, Jiangsu, China

submitted to *Surf. Sci.*

## Abstract



Understanding the interaction of  $\alpha,\beta$ -unsaturated carbonyl compounds with late transition metals is a key prerequisite for rational design of new catalysts with desired selectivity towards C=C or C=O bond hydrogenation. The interaction of the  $\alpha,\beta$ -unsaturated ketone isophorone and the saturated ketone TMCH (3,3,5-trimethylcyclohexanone) with Pd(111) was investigated in this study as a prototypical system. Infrared reflection-absorption spectroscopy (IRAS) and density functional theory calculations including van der Waals interactions (DFT+vdW<sup>surf</sup>) were combined to form detailed assignments of IR vibrational modes in the range from 3000 cm<sup>-1</sup> to 1000 cm<sup>-1</sup> in order to obtain information on the binding of isophorone and TMCH to Pd(111) as well as to study the effect of co-adsorbed hydrogen. IRAS measurements were performed with deuterium-labeled (*d*<sub>5</sub>-) isophorone, in addition to unlabeled isophorone and unlabeled TMCH. Experimentally observed IR absorption features and calculated vibrational frequencies indicate that isophorone and TMCH molecules in multilayers have a mostly unperturbed structure with random orientation. At sub-monolayer coverages, strong perturbation and preferred orientations of the adsorbates were found. At low coverage, isophorone interacts strongly with Pd(111) and adsorbs in a flat-lying geometry with the C=C and C=O bonds parallel, and a CH<sub>3</sub> group perpendicular, to the surface. At intermediate sub-monolayer coverage, the C=C bond is strongly tilted, while C=O remains flat lying, which indicates a prominent perturbation of the conjugated  $\pi$  system. Pre-adsorbed hydrogen leads to significant changes in the adsorption geometry of isophorone, which suggests a weakening of its binding to Pd(111). At low coverage, the structure of the CH<sub>3</sub> groups seems to be mostly unperturbed on the hydrogen pre-covered surface. With increasing coverage, a conservation of the in-plane geometry of the conjugated  $\pi$  system was observed in the presence of hydrogen. In contrast to isophorone, TMCH adsorbs in a strongly tilted geometry independent of the surface coverage. At low coverage, an adsorbate with a strongly distorted C=O bond is formed; with increasing exposure, species with a less perturbed C=O group appear.

## 7.1 Introduction

Chemo- and enantioselectivity in hydrogenation of  $\alpha,\beta$ -unsaturated carbonyls on transition metals is a widely discussed topic in the field of heterogeneous catalysis. Particularly important is the possibility to tune the selectivity of multiple unsaturated hydrocarbons, such as  $\alpha,\beta$ -unsaturated ketones and aldehydes, which represent a broad class of valuable intermediates for practically important processes [188–190]. For molecules containing both a C=C and a C=O  $\pi$  bond, such as the  $\alpha,\beta$ -unsaturated ketone isophorone (3,5,5-trimethylcyclohex-2-enone), hydrogenation can yield either a saturated ketone, an unsaturated alcohol or a saturated alcohol. To avoid the formation of undesired products and thereby an often difficult and costly separation of the different products, a high selectivity towards hydrogenating of either the C=C or C=O bonds is desirable. Over Pd catalysts, the hydrogenation of the C=C double bond of isophorone is strongly favored yielding the saturated ketone TMCH (3,3,5-trimethylcyclohexanone) in high selectivity ( $\approx 100\%$ ) and almost no alcohols [191–193]. The origin of this chemoselectivity is, however, not fully understood.

Not only a high chemoselectivity, but even high enantioselectivity in hydrogenation reactions can be achieved over heterogeneous catalysts using chiral modifiers [194–196, 221]. Compared to homogeneous catalysts traditionally applied for enantioselective reactions, the use of heterogeneous catalysts has operational, economical and often environmental advantages, so that heterogeneously catalyzed enantioselective hydrogenation was quickly recognized to be a promising field of research. A number of different modifiers have been tested also for the enantioselective hydrogenation of isophorone which is a benchmark test molecule for enantioselective hydrogenation reactions of enones [194, 197–204]. Although the origin of the enantioselectivity during hydrogenation of isophorone is not well understood, Lambert *et al.* [63, 222] have proposed a mechanism in which the stereochemistry of the chiral modifier and the adsorption geometry of isophorone on the Pd catalyst play a decisive role. More specifically, strong tilting of the unsaturated bonds on Pd was put forward to explain the enantioselective interaction of isophorone with the chiral modifier. To the best of our knowledge, the effects of isophorone coverage and co-adsorbed hydrogen on the isophorone adsorption geometry have not been investigated so far in surface science studies.

In our previous work we found that at low coverage isophorone adsorbs in a flat-lying geometry with the C=C and C=O bonds parallel to the Pd(111) surface [174, 218]. Coverage dependent NEXAFS studies showed increasing tilting angles for both unsaturated bonds with increasing isophorone coverage. The tilting is considerably more pronounced for the C=C bond, indicating a perturbation and strong structural distortion of the conjugated  $\pi$  system [174].

In this work, infrared reflection-absorption spectroscopy (IRAS) and density functional theory studies including van der Waals interactions (DFT+vdW<sup>surf</sup> [205]) are used to assign vibrational modes of isophorone, *d*<sub>5</sub>-isophorone, and TMCH as well as to study the effects of hydrogen co-adsorption. IRAS is a powerful tool not only for determining the vibrational frequencies of chemical bonds, but also – making use of the metal surface

selection rule [106, 112, 113] – for probing their orientation with respect to the metal surface. Thus, the combination of IRAS studies at sub-monolayer coverages with DFT hold great potential to provide detailed insights into the interaction of isophorone and TMCH with Pd(111).

Our results show that IR absorption features of molecules at multilayer coverages agree well with the calculated vibration frequencies for unperturbed molecules. At sub-monolayer coverages, isophorone was found to be strongly perturbed by interaction with the Pd(111) surface and to prefer a flat-lying adsorption geometry with C=C and C=O bonds parallel to the surface and a distinct orientation of the CH<sub>3</sub> groups pointing away from the surface. Strong perturbations of the isophorone molecule are very pronounced on pristine Pd(111), however, this effect is reduced by pre-adsorbing hydrogen on Pd(111). TMCH was found to form a very different adsorption structure by attaching to Pd(111) substrate via a strongly tilted and perturbed C=O group.

## 7.2 Experimental Details and Methods

IRAS experiments were performed at the Fritz-Haber-Institut, Berlin, in a UHV apparatus that has been described in detail before [100]. Isophorone, *d*<sub>5</sub>-isophorone, or TMCH were dosed onto the sample cooled to 120 K through a doubly differentially pumped multi-channel array sources controlled by valves and shutters. The surface was precovered with hydrogen by dosing 100 L of H<sub>2</sub> through a second doubly differentially pumped multi-channel array source controlled by valves and shutters. The sources were operated at room temperature, and the beam diameter was chosen to exceed the sample size. The Pd(111) single crystal was cleaned prior to use by repeated cycles of Ar<sup>+</sup> ion bombardment at room temperature, annealing at 1000 K and oxidation in  $1 \cdot 10^{-6}$  mbar O<sub>2</sub> at 750 K to remove residual carbon. The final cleaning cycle was stopped after annealing. The flatness and cleanliness of the Pd(111) single crystal surface was checked by low energy electron diffraction (LEED) and infrared reflection-absorption spectroscopy (IRAS) of adsorbed CO. IRAS data were acquired using a vacuum Fourier-Transform infrared (FT-IR) spectrometer (Bruker IFS 66v/S) with a spectral resolution of 2 cm<sup>-1</sup> and using a mid-infrared (MIR) polarizer and p-polarized IR light. Isophorone (Acros Organics, 98%), *d*<sub>5</sub>-Isophorone (Quotient Bioresearch (Radiochemicals) Limited, 90%) and TMCH (Aldrich, 98%) were purified prior to the experiments by repeated freeze-pump-thaw cycles. The stated exposures for IRAS experiments are given in fractions of a monolayer (ML) that were determined by TPD experiments.

The DFT calculations were carried out using the PBE+vdW<sup>surf</sup> method [205], as implemented in the FHI-aims all-electron code [206]. The PBE+vdW<sup>surf</sup> method, which accurately and effectively include the vdW interactions and dielectric screening within the bulk, has been demonstrate to perform very well for both strongly and weakly bound adsorption systems [216, 223, 224]. The *tight* settings were employed for integration grids and standard numerical atom-centered orbitals basis sets in FHI-aims code. The scaled zeroth-order regular approximation [210] was used to treat relativistic effects for Pd atoms. We built up four-layer Pd slabs with a (4×4) unit cell, and each slab was separated by a 20 Å vacuum. The bottom two metal layers were constrained, whereas the uppermost two

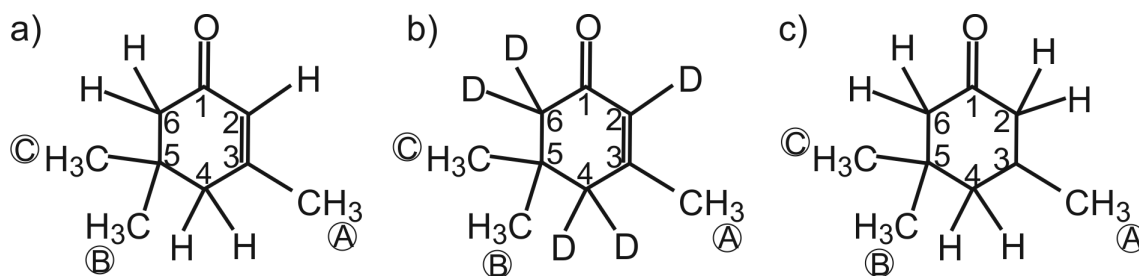


Figure 7.1: Structures of the isophorone (a),  $d_5$ -isophorone (b), and TMCH (c)

metal layers and the adsorbate were allowed to fully relax during geometry relaxations. For slab calculations, we used a  $3 \times 3 \times 1$  k-points mesh. Based on the most stable geometries, infrared vibrational spectra were calculated by a second derivative of the energy from the numerical change of the forces arising from small finite displacements. Six finite displacements were applied to each of the atoms with a value of  $0.005 \text{ \AA}$ .

### 7.3 Results and Discussion

The adsorption of the unsaturated ketone isophorone (3,5,5-trimethylcyclohex-2-enon) and deuterium substituted ( $d_5$ -) isophorone as well as the saturated ketone TMCH (3,5,5-trimethylcyclohexanone) on Pd(111) at 120 K was studied under well-defined UHV conditions by infrared reflection-absorption spectroscopy (IRAS). IR vibration frequencies were calculated by the DFT+vdW<sup>surf</sup> method. The structural formulae of normal and  $d_5$ -isophorone are shown in Figure 7.1a and b. In  $d_5$ -isophorone, the five hydrogen atoms attached to the C<sub>6</sub> ring are substituted by deuterium atoms, while the hydrogen atoms on the CH<sub>3</sub> groups remained unlabeled. The structure of TMCH is shown in Figure 7.1c. Molecular vibrations will be discussed according to the labeling of the ring positions and methyl groups as illustrated in Figure 7.1. Ring positions are labeled with numbers 1 to 6, methyl groups are labeled with A, B, and C.

To the best of our knowledge, no detailed assignment of IR vibrations of isophorone or TMCH is available in literature. Therefore, we will compare our experimental and theoretical assignments of IR vibrations to vibrations of the same functional groups in other molecules. Among a large number of IR studies on hydrocarbons with identical groups, we chose some of the most fundamental investigations [225–242] for comparison. Here, we will only shortly summarize the most relevant results. An overview of typical vibrational frequencies of hydrocarbons can be found in a textbook by Colthup, Daly, and Wiberley [109]. In very early studies, Fox and Martin investigated CH<sub>3</sub>, CH<sub>2</sub>, and CH stretching vibration modes from an experimental and theoretical point of view. The authors achieved a clear assignment of vibrational frequencies to CH<sub>3</sub>, CH<sub>2</sub>, and CH stretching modes in a large number of molecules. For instance, strong CH<sub>3</sub> vibrations have been identified in several compounds near  $2962 \text{ cm}^{-1}$  and  $2872 \text{ cm}^{-1}$ , CH<sub>2</sub> stretching modes were typically observed near  $2926 \text{ cm}^{-1}$  and  $2853 \text{ cm}^{-1}$ , and the CH vibration in olefins was assigned close to  $3019 \text{ cm}^{-1}$ , while the CH vibration in saturated compounds was observed at

2890  $\text{cm}^{-1}$  [225, 226]. By using partially deuterium-labeled molecules, MacPhail *et. al.* could distinguish  $\text{CH}_3$  from  $\text{CH}_2$  stretching vibrations in *n*-alkyl chains [229]. Studies on stretching vibrations of deuterium-labeled  $\text{CD}_2$  groups are relatively rare. Nolin and Jones studied the IR absorption of normal and deuterium-substituted diethyl ketone. The authors assign  $\text{CH}_3$  and  $\text{CH}_2$  stretching and deformation vibrations as well as  $\text{CD}_3$ ,  $\text{CD}_2$  and  $\text{C=O}$  stretching modes.  $\text{CH}_3$  asymmetric stretching appeared at 2977  $\text{cm}^{-1}$  and 2936  $\text{cm}^{-1}$ , while the symmetric stretching was observed at 2883  $\text{cm}^{-1}$ . A  $\text{CH}_2$  stretching vibration was identified at 2902  $\text{cm}^{-1}$  and  $\text{CD}_2$  stretching at 2173  $\text{cm}^{-1}$ . Moreover, the carbonyl ( $\text{C=O}$ ) stretching was observed at 1720  $\text{cm}^{-1}$ .  $\text{CH}_3$  asymmetric bending modes were assigned at 1461  $\text{cm}^{-1}$  and 1454  $\text{cm}^{-1}$  and the symmetric bending at 1379  $\text{cm}^{-1}$ . The scissor vibration of the  $\text{CH}_2$  group was identified at 1414  $\text{cm}^{-1}$  and thus, at relatively low frequency. This is of particular interest for our study, since in both cases the  $\text{CH}_2$  groups are located next to a  $\text{C=O}$  group [236]. More general, Snyder and Schachtschneider presented very extensive interpretations of IR spectra of *n*-alkanes at 3000-2800  $\text{cm}^{-1}$  and 1500-700  $\text{cm}^{-1}$  in an experimental [231] and a theoretical [230] study. Lavalley and Sheppard investigated IR absorption features in the C-H stretching region, which result from Fermi resonance between  $\text{CH}_3$  asymmetric deformation overtones and  $\text{CH}_3$  symmetric stretching fundamentals [227]. A detailed study on the vibrations of linear and branched aliphatic hydrocarbons in the range below 1500  $\text{cm}^{-1}$  was published by Sheppard *et. al.*. Some characteristic features were observed for non-linear molecules, such as a splitting of the  $\text{CH}_3$  symmetric deformation into two peaks for two  $\text{CH}_3$  groups attached to the same saturated C atom [228]. Colthup found that this splitting is the result of an interaction force between two or three neighboring  $\text{CH}_3$  groups. The same study shows that the exact wavenumber of  $\text{CH}_3$ ,  $\text{CH}_2$ , and  $\text{CH}$  deformation vibrations is in general determined by the electron density at the respective C atom [232]. These references, along with DFT calculations from this work, form the basis for our assignment of infrared vibrations of isophorone and TMCH adsorbed on Pd(111).

In the following sections, we will first discuss the IR spectra of molecules in multilayers before we will focus on coverage-dependent IR vibrations from multilayer to sub-monolayer coverage, where the interaction with the underlying palladium substrate becomes more important. Finally, the sub-monolayer structures of isophorone and TMCH will be compared. The comparison of the binding properties of isophorone and TMCH is of particular interest for catalysis, since hydrogenation of the  $\text{C=C}$  bond in isophorone yields TMCH.

### 7.3.1 IR Vibrations in Isophorone Multilayers

In this section, we discuss the multilayer IR spectra of normal and  $d_5$ -isophorone. Multilayer spectra are dominated by molecules organized in an ice structure, providing a reference for mainly non-perturbed molecules. DFT+vdW<sup>surf</sup> calculations were performed for non-perturbed molecules in the gas-phase. Figure 7.2 displays the IR spectra of 3 ML of isophorone and  $d_5$ -isophorone on Pd(111) at 120 K. For both molecules, three main spectral regions can be distinguished: C-H stretching vibrations (3200-2800  $\text{cm}^{-1}$ ),  $\text{C=C}$  and  $\text{C=O}$  stretching (1850-1550  $\text{cm}^{-1}$ ), as well as for C-H, C-D and C-C deformation ( $\leq 1500$   $\text{cm}^{-1}$ ). C-D stretching vibrations (2300-2000  $\text{cm}^{-1}$ ) in  $d_5$ -isophorone are not shown in Figure 7.2.

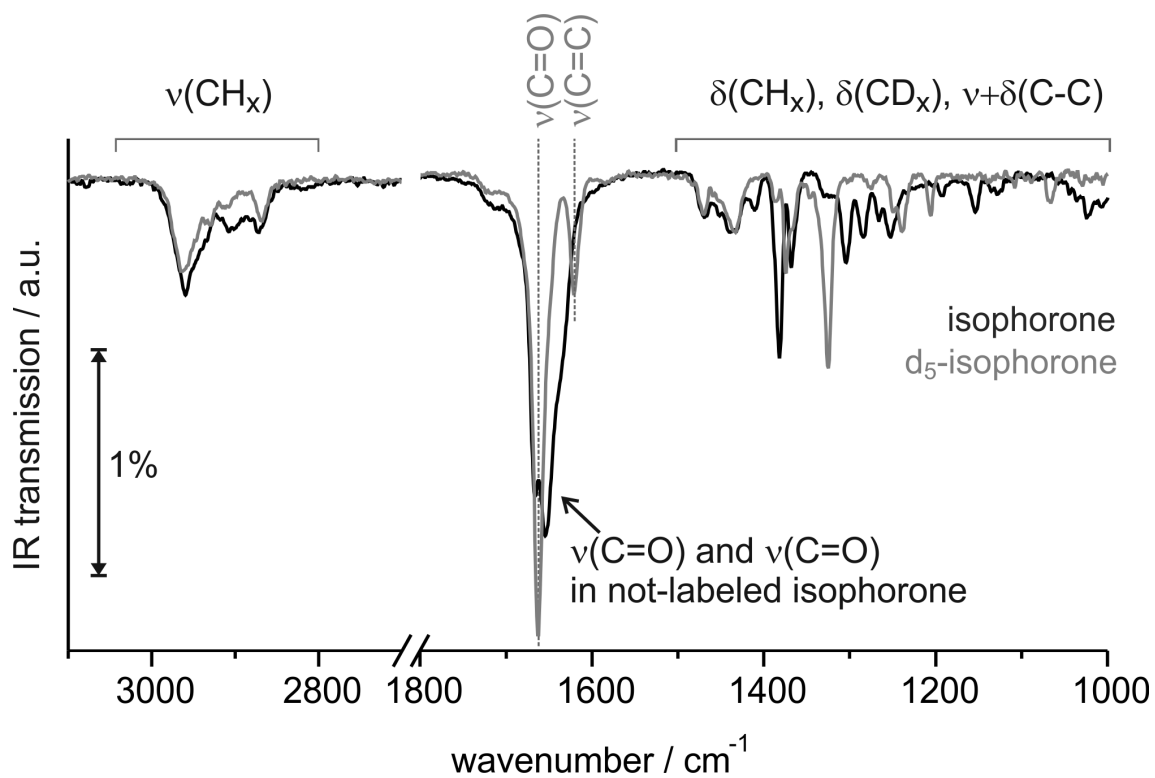


Figure 7.2: IR spectra of 3 ML isophorone (black) and  $d_5$ -isophorone (green) at 120 K on Pd(111). The region characteristic for C–H stretching vibrations (3100–2800  $\text{cm}^{-1}$ ), C=O and C=C stretching vibrations (1800–1600  $\text{cm}^{-1}$ ), and C–H and C–D deformation and C–C deformation and stretching vibrations (1500–1000  $\text{cm}^{-1}$ ).

We observed that DFT results coincide well with experimental data at the C=O stretching frequency, but a compression of the DFT spectrum by a factor of 0.945 with origin at  $1661\text{ cm}^{-1}$  is required to fit all simulated vibration frequencies from  $3100\text{ cm}^{-1}$  to  $1000\text{ cm}^{-1}$  approximately to the experimentally observed IR absorptions. It has been observed before that calculated harmonic vibrational frequencies systematically deviate from experimental results, since effects of anharmonicity of the interaction potential are not taken into account and frequency scaling factors of  $\approx 0.9$  to  $0.95$  are typical [243]. For simplicity, we will give only the scaled DFT results in the text. The unscaled calculated DFT values are listed in Table 7.1 and Table 7.2. The stretching modes are labeled with A1 to A15 and the deformation vibrations with B1 to B20. We will refer to the respective labels in the following discussion, in the tables, as well as in the IR spectra.

### Stretching Vibrations

The stretching vibrations of the C=O and the C=C bonds show very pronounced bands in the spectra displayed in Figure 7.2. In normal isophorone, the most intense vibration is the C=O stretching mode at  $1665\text{ cm}^{-1}$ , which is strongly overlapping with the C=C stretching mode at  $1655\text{ cm}^{-1}$ . In order to clearly identify both vibrations, the ring-substituted  $d_5$ -isophorone was used, in which the C=C stretching vibration appears at  $1620\text{ cm}^{-1}$ , exhibiting a shift by  $35\text{ cm}^{-1}$  as compared to the unsubstituted molecule. The C=O stretching mode appears to be hardly affected by the substitution and remains essentially at the same frequency of  $1665\text{ cm}^{-1}$ . The DFT study indicates the C=O stretching vibration at  $1661\text{ cm}^{-1}$  for both molecules, while the C=C stretching is predicted to shift from  $1624\text{ cm}^{-1}$  in normal isophorone to  $1608\text{ cm}^{-1}$  in  $d_5$ -isophorone. Previously it has been reported that the C=O and C=C stretching vibrations in  $\alpha,\beta$ -unsaturated ketones are strongly overlapping if the two bonds have *trans* orientation, such as in isophorone. The vibrational frequencies found in gas-phase studies of unlabeled molecules agree well with our results; C=O vibrations have been observed in the range of  $1690\text{--}1655\text{ cm}^{-1}$  and C=C stretching modes were observed in the  $1649\text{--}1618\text{ cm}^{-1}$  range.[109, 240, 241]. Furthermore, the lower C=C stretching frequency in  $d_5$ -isophorone agrees well with previous studies, which found that the C=C stretching vibration is lowered by  $10\text{--}20\text{ cm}^{-1}$  for each substituted H atom at the C=C bond [242].

Table 7.1: Assignment of IR vibration frequencies from DFT calculations and IRAS experiments of normal isophorone and  $d_5$ -isophorone in the range of C=O, C=C, and C-H stretching vibrations ( $3100\text{--}1600\text{ cm}^{-1}$ ). Vibration modes that strongly change when switching from normal to  $d$ -labeled isophorone are printed in bold. Vibration modes that are mostly independent from deuterium-labeling are printed with normal intensity.

	mode	vibrations isophorone / $\text{cm}^{-1}$			vibrations $d_5$ -isophorone / $\text{cm}^{-1}$		
		DFT	DFT scaled	IRAS	DFT	DFT scaled	IRAS
	$\nu(\text{C=O})$	1661	1661	1665	1661	1661	1665
	$\nu(\text{C=C})$	<b>1624</b>	<b>1626</b>	<b>1655</b>	<b>1608</b>	<b>1610</b>	<b>1620</b>
A1	$\nu(\text{CH})$	3085	3006		2287	2253	
A2	$\nu_a(\text{CH}_3)(\text{A})$	3046	2970		2287	2253	
A3	$\nu_a(\text{CH}_3)(\text{C})$	3032	2957		3034	2958	
				2975-2930		2975-2930	

	mode	vibrations isophorone / $\text{cm}^{-1}$			vibrations $d_5$ -isophorone / $\text{cm}^{-1}$		
		DFT	DFT scaled	IRAS	DFT	DFT scaled	IRAS
A4	$\nu_a(\text{CH}_3)(\text{B})$	3021	2946		3024	2949	
A5	$\nu_a(\text{CH}_3)(\text{B,C})$	3016	2941		3021	2946	
A6	$\nu_a(\text{CH}_3)(\text{B,C})$ * + $\nu_a(\text{CH}_2)(6)$	3011*	2937*		3015	2941	
A7	$\nu_a(\text{CH}_3)(\text{A})$	2990	2917	2910	2990	2917	2910
A8	$2\delta(\text{CH}_3)$			2920-2890			2920-2890
<b>A9</b>	<b><math>\nu_a(\text{CH}_2)(6)</math></b> * + <b><math>\nu_a(\text{CH}_3)(\text{B,C})</math></b>	<b>3008*</b>	<b>2934*</b>	<b><math>\approx 2940</math></b>	<b>2229</b>	<b>2198</b>	<b>2202</b>
<b>A10</b>	<b><math>\nu_a(\text{CH}_2)(4)</math></b>	<b>1955</b>	<b>2884</b>	<b><math>\approx 2885</math></b>	<b>2187</b>	<b>2158</b>	<b>2184</b>
A11	$\nu_s(\text{CH}_3)(\text{B,C})$ (in phase)	2949	2878		2957	2886	
A12	$\nu_s(\text{CH}_3)(\text{B,C})$ (out of phase)	2945	2874	2874-2865	2948	2877	2874-2865
A13	$\nu_s(\text{CH}_3)(\text{A})$	2942	2872		2945	2874	
A14	$\nu_s(\text{CH}_2)(6)$	2928	2858		2130	2104	
A15	$\nu_s(\text{CH}_2)(4)$	2908	2839	$\approx 2820$	2124	2098	2087-2079

$\nu$ : stretching,  $\nu_a$ : asymmetric stretching,  $\nu_s$ : symmetric stretching  
DFT scaling factor: 0.945

The C–H and C–D stretching modes show multiple peaks and their assignment is more complex due to strongly overlapping vibrations and weak dynamic dipole moments. Our DFT study predicts six asymmetric and three symmetric stretching modes for the three  $\text{CH}_3$  groups, one asymmetric and one symmetric stretching vibration for each  $\text{CH}_2$  or  $\text{CD}_2$  groups, as well as a stretching mode for the CH or CD group. The computed frequencies of the C–H and C–D stretching vibrations are summarized in Table 7.1. Figure 7.3 illustrates the IR spectra of normal isophorone and  $d_5$ -isophorone in the range of the C–H and C–D stretching vibrations.

The DFT and IRAS results indicate that the stretching vibrations of the  $\text{CH}_3$  groups are mostly unaffected by the deuterium-substitution of the ring H atoms. The scaled DFT results show asymmetric stretching vibrations of  $\text{CH}_3$  group A in normal isophorone at  $2970 \text{ cm}^{-1}$  and  $2917 \text{ cm}^{-1}$ , which are well isolated from other vibrations [A1, A7]. Isolated asymmetric stretching vibrations of  $\text{CH}_3$  groups C and B are observed at  $2957 \text{ cm}^{-1}$  and  $2946 \text{ cm}^{-1}$  [A3, A4] and simultaneous excitations of B and C is found at  $2941 \text{ cm}^{-1}$  and  $2937 \text{ cm}^{-1}$  [A5, A6]. The later vibration is strongly overlapping with the asymmetric stretching of the ring-related  $\text{CH}_2$  group 6 at  $2934 \text{ cm}^{-1}$ . In  $d_5$ -isophorone, the same vibration modes are almost at identical frequencies. Asymmetric stretching of group A is found at  $2971 \text{ cm}^{-1}$  and  $2917 \text{ cm}^{-1}$  [A1, A7], and the vibrations of groups B and C are observed at  $2958 \text{ cm}^{-1}$ ,  $2949 \text{ cm}^{-1}$ ,  $2946 \text{ cm}^{-1}$ , and  $2941 \text{ cm}^{-1}$  [A3-A6]. Experimentally, a broad and strong IR absorption feature is observed in the range from  $2975$ - $2930 \text{ cm}^{-1}$  with its maximum at  $2960 \text{ cm}^{-1}$  for both molecules. Weaker IR absorption appears near  $2910 \text{ cm}^{-1}$  for the  $d_5$ -substituted isophorone. The broad IR absorption most likely contains all  $\text{CH}_3$  asymmetric stretching vibrations, which were indicated by DFT between  $2970 \text{ cm}^{-1}$  and  $2937 \text{ cm}^{-1}$  in normal isophorone and between  $2971 \text{ cm}^{-1}$  and  $2941 \text{ cm}^{-1}$  in  $d_5$ -isophorone [A2-A6]. The IR absorption near  $2910 \text{ cm}^{-1}$  might correspond to the asym-

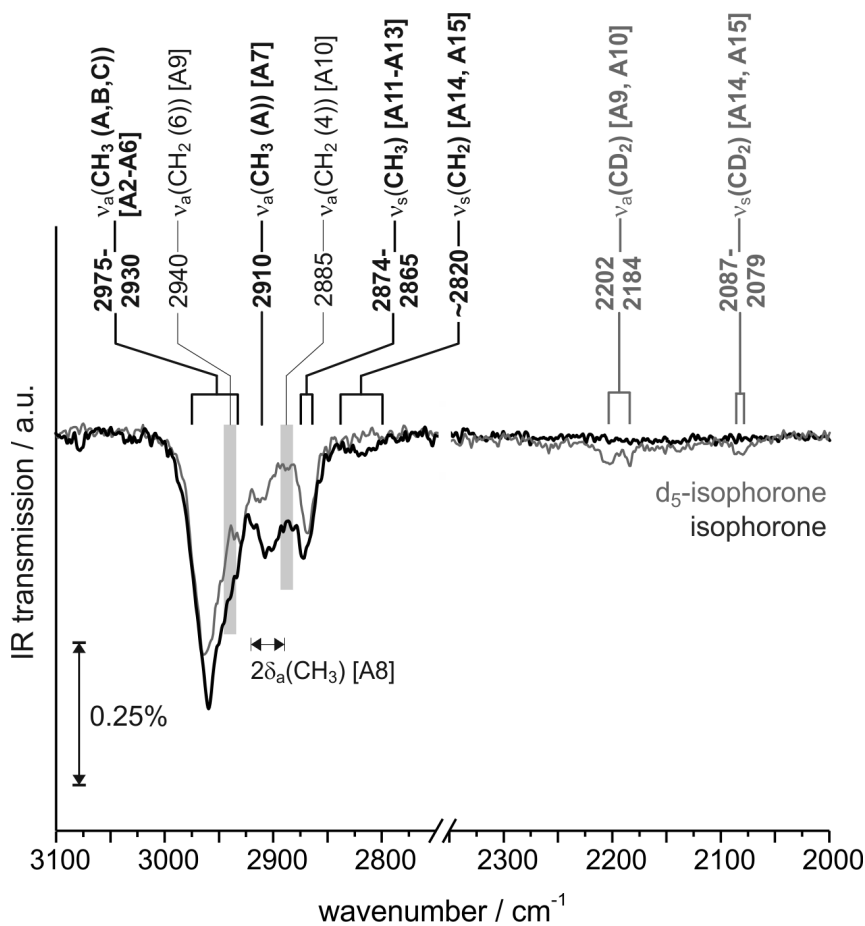


Figure 7.3: IR spectra of 3 ML of normal and  $d_5$ -isophorone adsorbed at 120 K on Pd(111) from 3100-2750  $\text{cm}^{-1}$  (C–H stretching) and 2400-2000  $\text{cm}^{-1}$  (C–D stretching). Clearly assigned vibrations are indicated with bold printed labels, more tentative assignments are labeled with normal thickness.

metric stretching mode of group A, which is observed at  $2917\text{ cm}^{-1}$  in DFT and thus, separated by about  $20\text{ cm}^{-1}$  from the other  $\text{CH}_3$  asymmetric stretching vibrations [A7]. The frequencies of the  $\text{CH}_3$  asymmetric stretching vibrations agree with previously reported values for aliphatic compounds, which have been reported near  $2960\text{ cm}^{-1}$  ( $\pm 10\text{ cm}^{-1}$ ) [109, 226, 229, 231, 236]. IR absorption near  $2925\text{ cm}^{-1}$  and thus at similar frequency as the vibration of group A, was observed in 2,3-dimethyl-2-butene, where all the  $\text{CH}_3$  groups are next to the unsaturated  $\text{C}=\text{C}$  bond [244].

The symmetric stretching frequencies of the  $\text{CH}_3$  groups observed experimentally between  $2874\text{ cm}^{-1}$  and  $2865\text{ cm}^{-1}$  are clearly separated by more than  $60\text{ cm}^{-1}$  from the asymmetric vibrations. DFT results show in-phase and out-of-phase  $\text{CH}_3$  symmetric stretching of groups B and C at  $2878\text{ cm}^{-1}$  and  $2874\text{ cm}^{-1}$  and symmetric stretching of group A at  $2872\text{ cm}^{-1}$  in normal isophorone. In  $d_5$ -isophorone, the same vibrations are observed at  $2886\text{ cm}^{-1}$ ,  $2877\text{ cm}^{-1}$ , and  $2874\text{ cm}^{-1}$  [A11-A13]. In literature,  $\text{CH}_3$  symmetric stretching vibrations have been assigned near  $2870\text{ cm}^{-1}$  [109, 226, 230, 231].

Additional IR absorption might appear in the range of  $2920\text{--}2890\text{ cm}^{-1}$  originating from Fermi resonance between  $\text{CH}_3$  deformation overtones and  $\text{CH}_3$  symmetric stretching fundamentals [A8]. In literature, this feature has been observed near  $2900\text{ cm}^{-1}$  [227, 229].

Vibrations of the deuterium-substituted  $\text{CD}_2$  groups are found at much lower frequencies than those of the  $\text{CH}_2$  groups. By DFT, the asymmetric stretching of  $\text{CH}_2$  groups 6 and 4 are identified at  $2934\text{ cm}^{-1}$  and  $2884\text{ cm}^{-1}$ . The vibration at  $2934\text{ cm}^{-1}$  is coupled with asymmetric stretches of  $\text{CH}_3$  groups B and C. In the deuterium-labeled molecule, the  $\text{CD}_2$  asymmetric stretching vibrations of groups 6 and 4 are observed at  $2198\text{ cm}^{-1}$  and  $2158\text{ cm}^{-1}$  [A9, A10]. Experimentally, the  $\text{CH}_2$  asymmetric stretching vibrations were hard to identify, since they are strongly overlapping with  $\text{CH}_3$  vibrations. Moreover, it is known that  $\text{CH}_2$  vibrations typically have two or three times less intensity per group than  $\text{CH}_3$  vibrations [109]. However, the stronger IR absorption around  $2940\text{ cm}^{-1}$  and  $2885\text{ cm}^{-1}$  in normal isophorone as compared to  $d_5$ -isophorone strongly point to a contribution from the ring-related  $\text{CH}_2$  groups to the total IR absorption at these frequencies. The  $\text{CH}_2$  vibration at  $2940\text{ cm}^{-1}$  is in the range of typical values found in literature, which have been observed in the range from  $2950\text{ cm}^{-1}$  to  $2915\text{ cm}^{-1}$  for aliphatic hydrocarbons [109, 225, 226, 230, 231]. The IR absorption at  $2885\text{ cm}^{-1}$  is at a lower wavenumber than expected. The reason for this low vibration frequency, however, remains unclear to us. The  $\text{CD}_2$  asymmetric stretching vibrations appear well-isolated from all other vibrations at  $2202\text{ cm}^{-1}$  and  $2184\text{ cm}^{-1}$ . Previously, a  $\text{CD}_2$  stretching vibration has been observed in diethyl ketone at  $2173\text{ cm}^{-1}$  and thus close to our experimentally observed IR absorption at  $2184\text{ cm}^{-1}$  [236].

DFT results show the symmetric stretching vibrations of  $\text{CH}_2$  groups 6 and 4 at  $2858\text{ cm}^{-1}$  and  $2839\text{ cm}^{-1}$  and the respective  $\text{CD}_2$  symmetric stretching vibrations at  $2104\text{ cm}^{-1}$  and  $2098\text{ cm}^{-1}$  [A14, A15]. Experimentally, we identified a weak and broad IR absorption near  $2820\text{ cm}^{-1}$  in normal isophorone, which we tentatively correlate with the symmetric stretching of both  $\text{CH}_2$  groups. In  $d_5$ -isophorone the  $\text{CD}_2$  symmetric stretching vibrations

are assigned to a somewhat more pronounced IR absorption at 2087-2079  $\text{cm}^{-1}$ . Previously,  $\text{CH}_2$  symmetric stretching vibrations in alkanes have typically been observed near 2850  $\text{cm}^{-1}$  [109, 225, 226, 230, 231] and thus at slightly higher wavenumbers.

The CH stretching vibration is predicted at 3006  $\text{cm}^{-1}$  and the CD stretching at 2253  $\text{cm}^{-1}$  [A1]. Both vibrations cannot be identified experimentally, probably due to weak dipole moments.

Combination of DFT and IRAS studies allow us to assign  $\text{CH}_3$  as well as  $\text{CH}_2$  and  $\text{CD}_2$  stretching vibrations in some detail. The comparison between the spectra of normal and  $d_5$ -isophorone is of advantage in two aspects. First, it allows to discriminate between C=O and C=C vibrations. Second, it enabled us to differentiate between  $\text{CH}_2$  and  $\text{CH}_3$  stretching vibrations. We found strongly overlapping IR absorption features from  $\text{CH}_3$  and  $\text{CH}_2$  stretching modes, with strong contribution from  $\text{CH}_3$  groups and weak IR absorption from  $\text{CH}_2$  groups. The vibrations of the ring-related  $\text{CD}_2$  groups appear well-separated from all other vibrations. IR absorption of the CH and CD group is most likely too weak to be detected.

### Region of C–H Deformation Vibrations ( $\leq 1500 \text{ cm}^{-1}$ )

Table 7.2: Assignment of IR vibration frequencies from DFT calculations and IRAS experiments of normal isophorone and  $d_5$ -isophorone in the C–H, C–D, and C–C deformation and C–C stretching vibrations (1500-1000  $\text{cm}^{-1}$ ). Vibration frequencies that strongly change when switching from normal to  $d$ -labeled isophorone are printed in bold. Vibration modes that are mostly independent from deuterium-labeling are printed with normal intensity.

	mode	vibrations isophorone / $\text{cm}^{-1}$			vibrations $d_5$ -isophorone / $\text{cm}^{-1}$		
		DFT	DFT scaled	IRAS	DFT	DFT scaled	IRAS
B1	$\delta_a(\text{CH}_3)(\text{B,C})$	1458 1453	1469 1464	1475-1445	1457 1455	1468 1466	1475-1445
B2	$\delta_a(\text{CH}_3)(\text{B,C})$ * + $\delta_a(\text{CH}_2)(4,6)$	1440* 1432*	1452 1445		1432 1429	1445 1442	
B3	$\delta_a(\text{CH}_3)(\text{A})^1$	1427 1423	1440 1436	1440-1430	1421 1419	1434 1432	1440-1430
<b>B4</b>	<b><math>\delta(\text{CH}_2)(4,6)</math> (in phase)</b> * + $\delta_a(\text{CH}_3)(\text{B,C})$	<b>1409*</b>	<b>1423*</b>	1418-1408	<b>1044</b>	<b>1078</b>	1067
B5	<b><math>\delta(\text{CH}_2)(4,6)</math> (out of phase)</b>	<b>1397</b>	<b>1412</b>		<b>1035</b>	<b>1069</b>	
B6	$\delta_s(\text{CH}_3)(\text{B,C})$ (open-open)	1368	1384	1382,1368	1365	1381	1385
B7	$\delta_s(\text{CH}_3)(\text{A})$	1355	1372		1351	1368	1372
B8	$\delta_s(\text{CH}_3)(\text{B,C})$	1347	1364		1344	1361	1368
B9	$\nu(\text{C6-C1-C2})$ $\nu(\text{C3-C4-C5})$				1290	1312	1325(?)
B10	$\omega(\text{CH}_2)(4)$ $\delta(\text{C-H})$ $\nu(\text{C3-C4})$	1334	1352				
B11	$\omega(\text{CH}_2)(4,6)$ $\delta(\text{C-H})$ $\nu(\text{C1-C2})$	1297	1317	1304			
B12	$\tau(\text{CH}_2)(4)$ $\nu(\text{C6-C1-C2})$	1271	1292	1283			
<b>B13</b>	<b><math>\nu(\text{C-C})</math> in ring</b> <b><math>a + \omega(\text{CH}_2)(4)</math></b>	<b>1251<sup>a</sup></b> <b>1234<sup>a,b,c</sup></b>	<b>1274<sup>a</sup></b> <b>1257<sup>a,b,c</sup></b>	<b>1266</b> <b>1253</b>	<b>1223</b> <b>1214</b>	<b>1247</b> <b>1239</b>	<b>1250</b> <b>1239</b>

	mode	vibrations isophorone / $\text{cm}^{-1}$			vibrations $d_5$ -isophorone / $\text{cm}^{-1}$		
		DFT	DFT scaled	IRAS	DFT	DFT scaled	IRAS
	$b + \omega(\text{CH}_2)(4)$ $c + \delta(\text{CH})$ $d + \tau(\text{CH}_2)(4)$ $d + \tau(\text{CH}_2)(6)$	<b>1221</b> <sup>c,d,e</sup>	<b>1245</b> <sup>c,d,e</sup>		<b>1200</b>	<b>1225</b>	
B14	$\nu(\text{C6-C1-C2})$ $\nu(\text{C5-CH}_3(\text{C}))$				1178	1205	1205
B15	$\nu(\text{C5-CH}_3(\text{B}))$ $\delta(\text{C-C})$ $\tau(\text{CH}_2)(4)$	1170	1197	1192			
B16	$\tau(\text{CH}_2)(4,6)$	1131	1159	1154			
B17	$\delta(\text{C-C})$ all bonds	1113	1143				
B18	$\tau(\text{CH}_2)(6)$	1101	1131	1133-1123	889 774	931 822	
B19	$\tau(\text{CH}_2)(4)$				832 821	878 867	
B20	$\rho(\text{CH}_3)(\text{A,B,C})$	1016 1002 988 972 929 920	1051 1038 1025 1010 969 961		1024 1011 989 933 920 909	1059 1047 1026 973 661 950	

$\nu$ : stretching,  $\delta$ : bending,  $\delta_a$ : asymmetric bending,  $\delta_s$ : symmetric bending,

$\omega$ : wag,  $\tau$ : twist,  $\rho$ : rock

DFT scaling factor = 0.945

<sup>1</sup>note that this band strongly shifts in the saturated ketone TMCH in which the immediate environment of  $\text{CH}_3(\text{A})$  is changed.

IR spectra in the range of the deformation vibrations are illustrated in Figure 7.4. The vibrational modes are summarized in Table 7.2. DFT results point to simultaneous excitations of  $\text{CH}_3$  asymmetric bending modes of groups B and C and – at lower frequencies – two isolated modes of group A. In detail, DFT predicts simultaneous excitation of the  $\text{CH}_3$  asymmetric bending of groups B and C in normal isophorone at  $1469 \text{ cm}^{-1}$ ,  $1464 \text{ cm}^{-1}$ ,  $1452 \text{ cm}^{-1}$ , and  $1445 \text{ cm}^{-1}$ . The latter two vibrations are mixed with  $\text{CH}_2$  scissor deformations. In  $d_5$ -isophorone the same modes of groups B and C are observed at  $1468 \text{ cm}^{-1}$ ,  $1466 \text{ cm}^{-1}$ ,  $1445 \text{ cm}^{-1}$ , and  $1442 \text{ cm}^{-1}$ , they are not mixed with any other vibration [B1, B2]. By DFT, pure asymmetric bending vibrations of group A are found at  $1440 \text{ cm}^{-1}$  and  $1436 \text{ cm}^{-1}$  in normal isophorone and at  $1434 \text{ cm}^{-1}$  and  $1432 \text{ cm}^{-1}$  in  $d_5$ -isophorone [B3]. Experimentally we observe a broad IR absorption at  $1475\text{--}1445 \text{ cm}^{-1}$  for both molecules, which we assign to the four asymmetric bending modes of groups B and C. The IR absorption in the range of  $1440\text{--}1430 \text{ cm}^{-1}$  is assigned to group A. In fact, our IRAS study on the saturated ketone TMCH confirms the lowering of the  $\text{CH}_3$  asymmetric bend frequencies of group A when the  $\text{C}=\text{C}$  bond is unsaturated. Previously,  $\text{CH}_3$  asymmetric bending was observed in the range of  $1470\text{--}1440 \text{ cm}^{-1}$  [109, 228, 230–232, 236]. The vibrational frequencies of groups B and C agree very well with the previously observed values; however, the vibrations of group A appear at slightly lower frequencies.

The DFT study predicts two simultaneous excitations of  $\text{CH}_3$  symmetric bending vibrations (umbrella) of groups B and C at  $1384 \text{ cm}^{-1}$  and  $1364 \text{ cm}^{-1}$  for normal isophorone and at  $1381 \text{ cm}^{-1}$  and  $1361 \text{ cm}^{-1}$  for  $d_5$ -isophorone [B6, B8]. The two modes are associated with both  $\text{CH}_3$  groups opening and closing in-phase (open-open) and out-of-phase

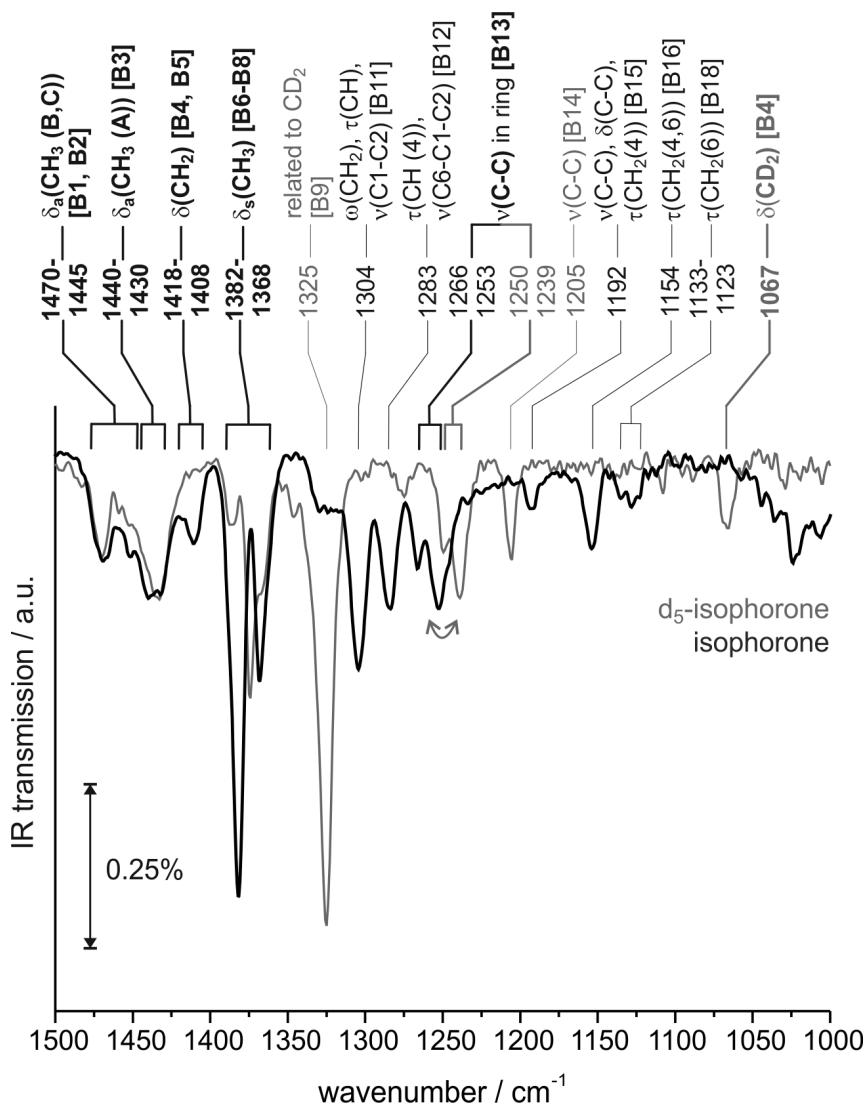


Figure 7.4: IR spectra of 3 ML of normal and  $d_5$ -isophorone adsorbed at 120 K on Pd(111) from 1500-1000  $\text{cm}^{-1}$ . Clearly assigned vibrations are indicated with bold printed labels, more tentative assignments are labeled with normal thickness.

(open-close), respectively. The umbrella vibration of group A is found at  $1372\text{ cm}^{-1}$  for normal isophorone and at  $1368\text{ cm}^{-1}$  for  $d_5$ -isophorone [B7], and thus for both molecules in the same ranges as the umbrella modes of B and C. Experimentally, a very strong IR absorption at  $1382\text{ cm}^{-1}$  and a second strong peak at  $1368\text{ cm}^{-1}$  are observed. In  $d_5$ -isophorone three weaker peaks appear at  $1385\text{ cm}^{-1}$ ,  $1372\text{ cm}^{-1}$ , and  $1368\text{ cm}^{-1}$ . The very strong intensity of the peak at  $1382\text{ cm}^{-1}$  in normal isophorone might indicate that two vibration modes contribute here. In previous studies, the  $\text{CH}_3$  symmetric deformation was observed in the range of  $1395\text{--}1365\text{ cm}^{-1}$  [109, 228, 230–232, 236]. The splitting of  $\text{CH}_3$  symmetric deformation of two  $\text{CH}_3$  groups attached to the same C atom was previously described in the literature [228, 232].

For the two ring-related  $\text{CH}_2$  groups, two simultaneously excited bending (scissor) modes are predicted by DFT. In-phase opening and closing of the  $\text{CH}_2$  scissor bending is predicted at  $1423\text{ cm}^{-1}$  and out-of-phase bending at  $1412\text{ cm}^{-1}$ . The calculations point to additional excitation of asymmetric bending of groups B and C at the higher frequency. In  $d_5$ -isophorone, the  $\text{CD}_2$  scissor modes have been found at  $1078\text{ cm}^{-1}$  and  $1069\text{ cm}^{-1}$ , well-isolated from other vibrations [B4, B5]. Experimentally, the  $\text{CH}_2$  and  $\text{CD}_2$  scissor vibrations have been clearly identified by comparison of the IR spectra of normal and labeled isophorone.  $\text{CH}_2$  vibrations are observed at  $1418\text{--}1408\text{ cm}^{-1}$  and  $\text{CD}_2$  scissor vibrations are assigned to the IR absorption at  $1067\text{ cm}^{-1}$ . In literature, scissor deformations of aliphatic  $\text{CH}_2$  groups have been described in a broad frequency range [109, 231, 235]. IR absorption of  $\text{CH}_2$  groups next to unsaturated  $\text{C}=\text{C}$  and  $\text{C}=\text{O}$  groups have been observed at  $1455\text{--}1435\text{ cm}^{-1}$  and at  $1445\text{--}1405\text{ cm}^{-1}$ , which is at tentatively higher frequency as compared to our results [232, 236, 237]. Previous studies assigned the  $\text{CD}_2$  scissor vibrations near  $1080\text{ cm}^{-1}$  and thus close to our assignment [233, 234].

In the IR spectrum of  $d_5$ -isophorone a strong peak at  $1325\text{ cm}^{-1}$  is observed which we cannot certainly assign. The calculations show a C–C stretching vibrations at  $1312\text{ cm}^{-1}$ , but the very strong intensity of the IR absorption points to a strong dynamic dipole moment, which is rather unlikely for a C–C vibration. However, C–C stretching cannot be excluded. Further investigations are necessary to clarify the origin of this IR absorption [B9].

Assignment of IR vibrations between  $1350\text{ cm}^{-1}$  and  $1100\text{ cm}^{-1}$  is more difficult, especially in normal isophorone. Multiple vibrational modes are excited simultaneously, such as C–C stretching and deformation, as well as different C–H deformation modes. However, stretching modes of saturated C–C bonds in the ring are observed in DFT calculations at  $1274\text{ cm}^{-1}$ ,  $1257\text{ cm}^{-1}$ , and  $1245\text{ cm}^{-1}$  for normal isophorone and at  $1247\text{ cm}^{-1}$ ,  $1239\text{ cm}^{-1}$ , and  $1225\text{ cm}^{-1}$  for  $d_5$ -isophorone [B13]. The vibrations in normal isophorone are mixed with  $\text{CH}_2$  wag and twist and CH bend vibrations in ring positions, as indicated in more detail in Table 7.2, line B13. The vibrations in  $d_5$ -isophorone only involve C–C bonds. We assign those vibrations to the relatively broad absorption with a double peak at  $1266\text{ cm}^{-1}$  and  $1253\text{ cm}^{-1}$  in normal isophorone, which slightly shifts to  $1250\text{ cm}^{-1}$  and  $1239\text{ cm}^{-1}$  in  $d_5$ -isophorone. Note, although multiple vibrations are excited in normal isophorone, we can attribute the IR absorption mainly to excitations of the C–C bonds,

since similar IR absorption appears in  $d_5$ -isophorone [B13].

Furthermore, some vibrations are detected only in normal isophorone. Simultaneous excitations of  $\text{CH}_2(4)$  wagging, CH bending, and C3–C4 stretching at  $1352\text{ cm}^{-1}$  are observed in DFT, but cannot be identified in our IR spectra [B10]. Wagging vibration of  $\text{CH}_2$  groups 4 and 6, mixed with CH bend and C1–C2 stretching is found at  $1317\text{ cm}^{-1}$  and  $\text{CH}_2(4)$  twist mixed with C6–C1–C2 stretching is seen at  $1292\text{ cm}^{-1}$  in the DFT calculation [B11, B12]. We tentatively assign these vibrations to the IR absorption peaks at  $1304\text{ cm}^{-1}$  and  $1283\text{ cm}^{-1}$ . Moreover, the calculations point to a C5– $\text{CH}_3(\text{B})$  stretching vibration, mixed with several C–C deformations and  $\text{CH}_2(4)$  twist at  $1197\text{ cm}^{-1}$ , which we assign to the experimentally observed IR absorption at  $1192\text{ cm}^{-1}$  [B15]. DFT shows twist of  $\text{CH}_2(6)$  at  $1159\text{ cm}^{-1}$  and deformation of all saturated C–C bonds at  $1143\text{ cm}^{-1}$  [B17, B18]. We tentatively assign the former one to the IR absorption at  $1154\text{ cm}^{-1}$ . For  $d_5$ -isophorone, DFT shows excitations of C6–C1–C2 and C5– $\text{CH}_3(\text{C})$  stretching at  $1205\text{ cm}^{-1}$ , which we assign to the experimentally observed vibration at the same wavenumber. Twist of  $\text{CH}_2$  group 6 is observed at  $1131\text{ cm}^{-1}$  by DFT and is assigned to the IR absorption at  $1333\text{--}1123\text{ cm}^{-1}$  [B18]. DFT shows the same mode in the deuterium-labeled molecule at  $931\text{ cm}^{-1}$  and  $882\text{ cm}^{-1}$ . Moreover, twisting vibrations of  $\text{CD}_2(4)$  in  $d_5$ -isophorone are found at  $878\text{ cm}^{-1}$  and  $867\text{ cm}^{-1}$  in DFT. We did not study vibrations below  $1000\text{ cm}^{-1}$  experimentally. It is well-known from previous studies, that in the range of  $1300\text{--}1000\text{ cm}^{-1}$  C–C stretching and several C–H deformation vibrations occur. Both  $\text{CH}_2$  wag and twist vibrations were found to spread over a region between  $1350\text{ cm}^{-1}$  and  $1180\text{ cm}^{-1}$ . The number of bands depends on the number of  $\text{CH}_2$  groups [109, 230, 231, 238, 239].

Our calculations show six  $\text{CH}_3$  rocking vibrations near  $1000\text{ cm}^{-1}$ , which we have not been able to study experimentally due to technical restrictions of our experimental setup. In normal isophorone, these vibrations are found at  $1051\text{ cm}^{-1}$ ,  $1038\text{ cm}^{-1}$ ,  $1025\text{ cm}^{-1}$ ,  $1010\text{ cm}^{-1}$ ,  $969\text{ cm}^{-1}$ , and  $961\text{ cm}^{-1}$ . In  $d_5$ -isophorone,  $\text{CH}_3$  rocking is calculated at  $1059\text{ cm}^{-1}$ ,  $1047\text{ cm}^{-1}$ ,  $1026\text{ cm}^{-1}$ ,  $973\text{ cm}^{-1}$ ,  $961\text{ cm}^{-1}$ , and  $950\text{ cm}^{-1}$  [B20].

In summary, the combination of DFT and IRAS studies on normal and  $d_5$ -isophorone opened up the opportunity to clearly discriminate between  $\text{CH}_3$  and  $\text{CH}_2$  bending vibrations. Moreover, the comparison of the spectra of the two compounds helped to identify C–C stretching from  $\text{CH}_2$  wag and twist and CH bending vibrations in the range from  $1350\text{--}1100\text{ cm}^{-1}$ . Nevertheless, a clear assignment of the vibrations modes of isophorone in this range is very difficult. The spectrum of  $d_5$ -isophorone, in contrast, is less complicated, since only C–C vibrations appear well-isolated from vibrations of other groups. Thus, similar IR absorption features in normal and  $d_5$ -isophorone point to predominant excitation of C–C bond vibrations. In contrast, vibrations that are unique for normal isophorone strongly point to predominant excitation of ring-related  $\text{CH}_2$  or CH groups.

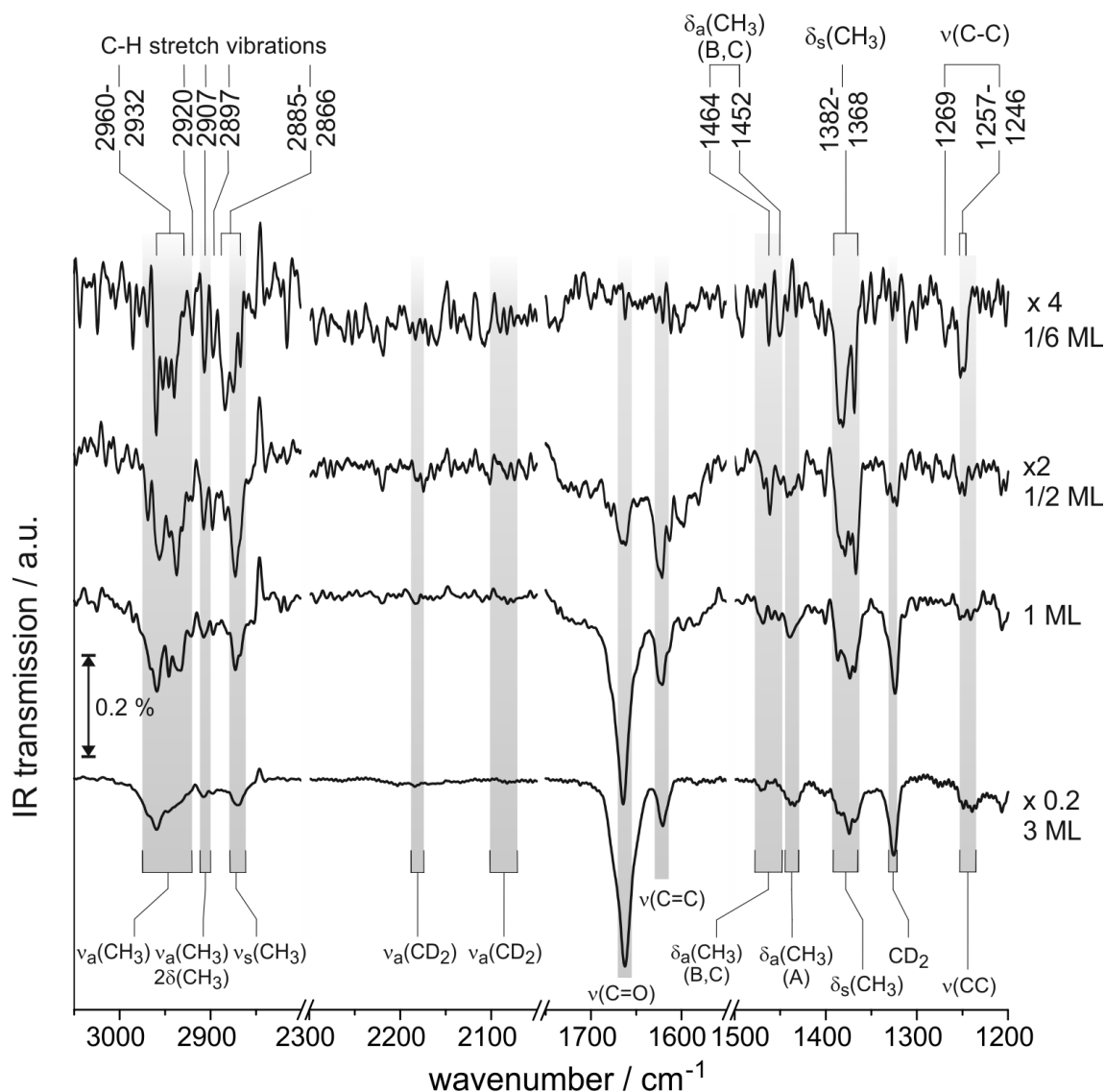


Figure 7.5: IR spectra  $d_5$ -isophorone adsorbed at 120 K on Pd(111) from 3050-2800  $\text{cm}^{-1}$  (C-H stretching), 2300-2050  $\text{cm}^{-1}$  (C-D stretching), 1800-1600  $\text{cm}^{-1}$  (C=C and C=O stretching), and 1500-1000  $\text{cm}^{-1}$  (C-H, C-D, C-C deformation and C-C stretching) at different coverages. Vibrations in isophorone ice are indicated below close to 3 ML spectrum (lowest trace). The wavenumbers of the IR vibrations at the lowest coverage (1/6 ML) (topmost trace) are given on top.

### 7.3.2 Isophorone at sub-monolayer coverage

#### Isophorone on pristine Pd(111)

Figure 7.5 displays IR spectra of  $d_5$ -isophorone adsorbed on Pd(111) at 120 K at coverages ranging from the multilayer to the sub-monolayer regime. While the IR spectra of isophorone at multilayer coverages are dominated by molecules in isophorone ice, the sub-monolayer spectra show the vibrations of isophorone molecules directly interacting with the Pd surface. The adsorption geometry of molecules on metal surfaces can be deduced from their IR spectra based on the metal surface selection rule (MSSR) [106, 113]. According to the MSSR, only the component of a dynamic dipole moment perpendicular to the metal surface can be detected, while vibrations parallel to the surface are strongly attenuated by an image dipole in the metal substrate. Changes of the intensity distribution between C=C, C=O and C-H vibrations with decreasing isophorone coverage indicate the transition from a more random orientation in multilayers to a favored geometry of molecules attached to Pd(111).

At the lowest coverage of  $d_5$ -isophorone on Pd(111) (1/6 ML), there are significant signals in the C-H stretching and deformation regions; however, there is no signal for the C=O or C=C stretching vibrations. This intensity distribution is in sharp contrast to the observation at multilayer coverage, where the most intense vibration is the C=O stretching mode. The absence of IR absorption in the C=O and C=C stretching region indicates that these bonds are either orientated parallel to the metal surface and cannot be seen in IRAS because of the MSSR or strongly perturbed by the interaction with the Pd(111) surface. The orientation of the unsaturated C=C and C=O bonds has been studied in more detail by previous NEXAFS and IRAS experiments [174]. NEXAFS experiments confirmed that the C=C and C=O bonds stay intact, but are oriented parallel to the Pd(111) surface plane at a coverage of 0.2 ML. With increasing coverage, the intensities of the IR bands assigned to the C=O and C=C stretching vibrations strongly increase. For a coverage of 1/2 ML, the C=C stretching peak at  $1620\text{ cm}^{-1}$  is more pronounced than the C=O stretching signal around  $1665\text{ cm}^{-1}$ . With further increasing coverage, the C=O stretching peak increases rapidly and becomes the most intense peak at full monolayer coverage and higher. The ratio of the C=O to C=C stretching vibration at multilayer coverage amounts to  $I_{\text{C=O}}/I_{\text{C=C}} \approx 6 - 8$ . The strong C=C band and an absent C=O band at 1/2 ML points to a strongly tilted C=C bond, while the orientation of C=O bond remains nearly parallel to the surface – this observation is in excellent agreement with our earlier NEXAFS study.

At sub-monolayer coverage, pronounced IR absorption is observed at  $2960\text{--}2932\text{ cm}^{-1}$  and at  $2885\text{--}2866\text{ cm}^{-1}$  and thus in the range of the  $\text{CH}_3$  (and  $\text{CH}_2$ ) asymmetric and symmetric stretching modes. IR absorption has not been observed at  $2885\text{--}2874\text{ cm}^{-1}$  in multilayer isophorone. Further IR absorption features can be recognized at  $2920\text{ cm}^{-1}$ ,  $2907\text{ cm}^{-1}$ , and  $2897\text{ cm}^{-1}$ . The absorption at  $2907\text{ cm}^{-1}$  is most likely related to an overtone of a  $\text{CH}_3$  asymmetric bend mode and will be discussed further in the section on isophorone on hydrogen precovered Pd(111). Among the  $\text{CH}_3$  bend vibrations, symmetric modes are strongly absorbing at  $1382\text{--}1368\text{ cm}^{-1}$ , while the asymmetric modes are

hardly visible as two weak peaks at  $1464\text{ cm}^{-1}$  and  $1452\text{ cm}^{-1}$ . This intensity distribution between vibrations of the same functional group points to a strongly favored adsorption geometry, with some  $\text{CH}_3$  dynamic dipole moments parallel to the metal surface and others strongly inclined with respect to the surface plane. In fact, a strong dynamic dipole perpendicular to the surface for the symmetric bending and parallel dipole moment for the asymmetric bending strongly points to a  $\text{CH}_3$  group which is facing away from the surface and is strongly inclined with respect to the  $\text{C}=\text{C}-\text{C}=\text{O}$  plane of isophorone. IR vibrations near  $2885\text{--}2874\text{ cm}^{-1}$ , which is unique for low coverage, could either point to a shifted  $\text{CH}_3$  symmetric stretching frequency and thus to a perturbation of a  $\text{CH}_3$  group; or to  $\text{CH}_2$  asymmetric stretching and thus to dehydrogenation of a  $\text{CH}_3$  group. Note that intact  $d_5$ -isophorone molecules do not have unlabeled  $\text{CH}_2$  groups.

In conclusion, our study on the coverage dependent IR absorption gives insights into the geometries of the  $\text{C}=\text{C}$  and  $\text{C}=\text{O}$  bond as well as of the  $\text{CH}_3$  groups. In line with the previous NEXAFS study we found that the  $\text{C}=\text{O}$  and  $\text{C}=\text{C}$  bonds prefer a parallel geometry to the surface plane at low isophorone coverage. Consequently, we expect the whole  $\text{H}_2\text{C}-(\text{CO})-\text{C}=\text{C}(\text{CH}_3(\text{A}))-\text{CH}_2$  unit to be mostly flat lying on the  $\text{Pd}(111)$  surface. Therefore, we assign the observed  $\text{CH}_3$  symmetric bending rather to the twin groups B and C than to group A. In a flat lying  $\text{C}-\text{CH}_3(\text{A})$  group, the symmetric  $\text{CH}_3$  bending has a dynamic dipole moment parallel to the surface, which cannot be detected by IRAS. Since we cannot observe any characteristic vibration of  $\text{CH}_3$  group A, it might either be strongly distorted or decomposed. The IR absorption near  $2885\text{--}2874\text{ cm}^{-1}$  may indicate a dehydrogenated  $\text{CH}_3$  group.

### Isophorone on $\text{H}_2$ pre-covered $\text{Pd}(111)$

Figure 7.6 shows IR spectra of  $d_5$ -isophorone adsorbed on pristine  $\text{Pd}(111)$  (black traces) and on  $\text{H}_2$  saturated  $\text{Pd}(111)$  (red traces) at 120 K at coverages ranging from  $1/8\text{ ML}$  to  $1/2\text{ ML}$ . While the spectra of  $d_5$ -isophorone multilayers on pristine and  $\text{H}_2$  precovered  $\text{Pd}(111)$  are very similar, significant differences are observed at sub-monolayer coverages. Black labels indicate IR absorption peaks that are more pronounced on the clean  $\text{Pd}(111)$  surface, red labels mark peaks having higher intensity on  $\text{H}_2$  pre-covered  $\text{Pd}(111)$  in the low coverage limit.

At the lowest coverages, clearly different  $\text{C}-\text{H}$  vibration modes appear on pristine and  $\text{H}_2$  precovered  $\text{Pd}(111)$ . Stronger IR absorption of isophorone on  $\text{H}_2$  precovered  $\text{Pd}(111)$  is observed at the frequencies  $2955\text{ cm}^{-1}$  and  $2927\text{ cm}^{-1}$  ( $\text{CH}_3$  asymmetric stretching modes) and at  $1430\text{ cm}^{-1}$  (the  $\text{CH}_3$  asymmetric bend of group A). In contrast, on pristine  $\text{Pd}(111)$  pronounced peaks appear in the  $\text{C}-\text{H}$  stretching region at  $2907\text{ cm}^{-1}$  and  $2885\text{ cm}^{-1}$ . The vibration at  $2907\text{ cm}^{-1}$  most likely shows the overtone of the  $\text{CH}_3$  asymmetric bend at  $1464\text{ cm}^{-1}$ , which is also unique for molecules on pristine  $\text{Pd}(111)$ . Moreover, the  $\text{C}-\text{C}$  stretching vibration modes near  $1251\text{ cm}^{-1}$  are more pronounced on the clean surface, while the mode at  $1205\text{ cm}^{-1}$  is more intense on the  $\text{H}$ -precovered surface.

According to the MSSR we conclude that the different distribution of IR absorption intensities on pristine and  $\text{H}_2$  precovered  $\text{Pd}(111)$  point to different adsorption geome-

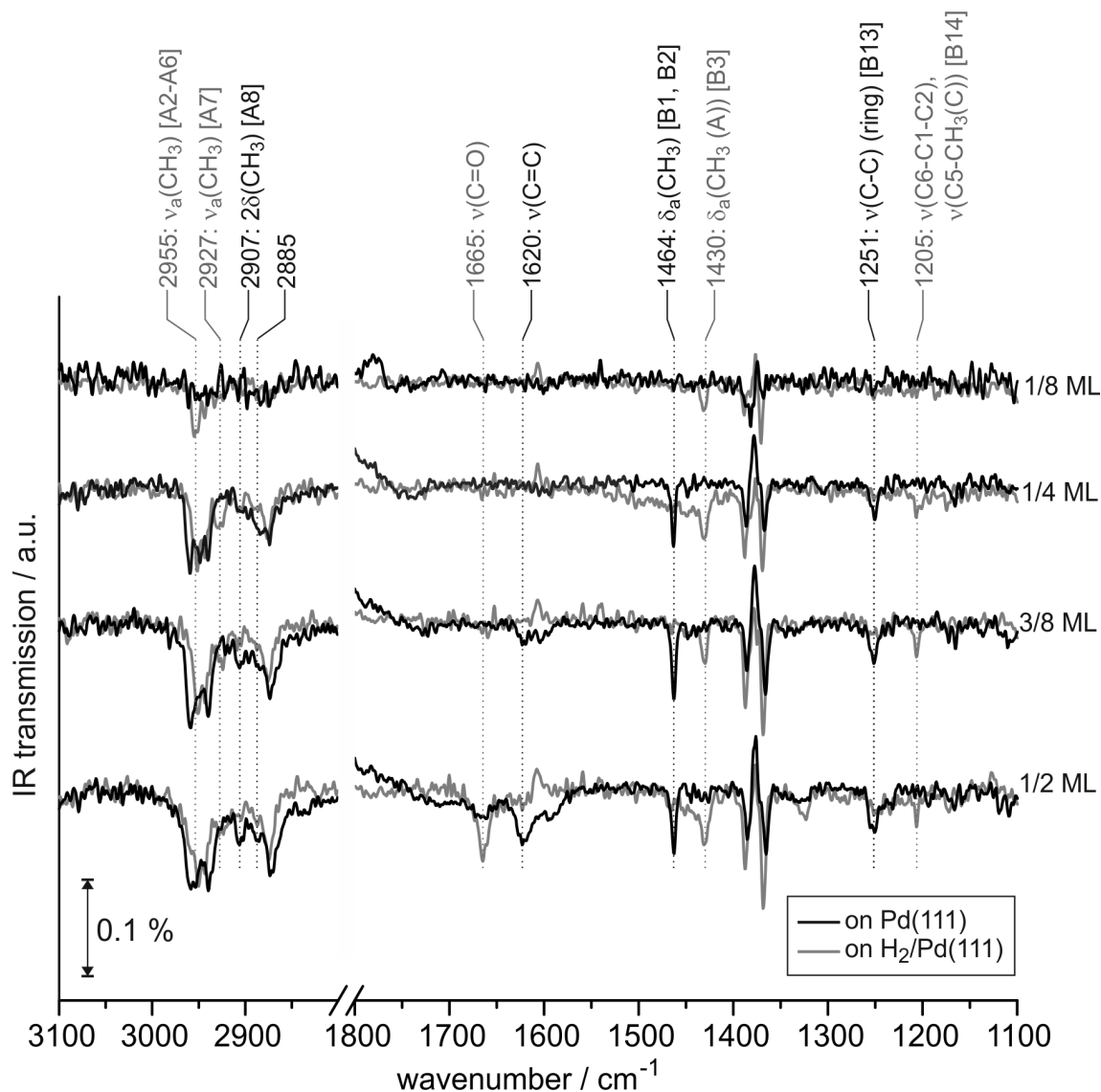


Figure 7.6: IR spectra  $d_5$ -isophorone adsorbed at 120 K on Pd(111) (black traces) and on  $H_2$  precovered Pd(111) (red traces) in the frequency range 3100-2800  $\text{cm}^{-1}$  (C-H stretching) and 1800-1600  $\text{cm}^{-1}$  (C=C and C=O stretching), 1500-1100  $\text{cm}^{-1}$  (C-H, C-D, C-C deformation and C-C stretching at sub-monolayer coverages). Vibrations that are more pronounced in isophorone on pristine Pd(111) are indicated with back labels, vibrations that are more pronounced on  $H_2$  precovered Pd(111) are indicated with red labels.

tries of isophorone on both surfaces. Especially the characteristic C–H vibrations indicate significant changes in the orientation of the CH<sub>3</sub> groups with respect to the surface in the presence of hydrogen. Furthermore, not only geometric effects, but also perturbation and/or chemical transformation of isophorone could yield different spectroscopic signatures on each surface. The IR absorption near 2885 cm<sup>-1</sup>, which is unique for isophorone on pristine Pd(111) at low coverage, might point to conversion of a CH<sub>3</sub> to a CH<sub>2</sub> group. This pathway seems to be suppressed in the presence of H<sub>2</sub>.

Our IR studies show a strong influence of pre-adsorbed hydrogen on the structure of isophorone on Pd(111). From the lowest coverage on, we observed rather unperturbed CH<sub>3</sub> groups with different orientation as compared to the pristine surface. With increasing coverage, the strong influence of hydrogen on the unsaturated C=C and C=O bond becomes even more pronounced. At intermediate coverage, the intensity ratio of the C=C and C=O stretching vibration becomes closer to that of isophorone in ice, which indicates conservation of the in-plane geometry and thus a more unperturbed  $\pi$  system as compared to pristine Pd(111). Previously, we discussed the effect of co-adsorbed hydrogen on the geometry of the C=C and C=O bonds in more detail [174].

### 7.3.3 IR Vibrations and Adsorption of TMCH

The product in C=C bond hydrogenation in isophorone is the saturated ketone 3,3,5-trimethylcyclohexanone (TMCH). In this section, we will assign the IR vibrations of TMCH and compare them to the vibrations of isophorone. After that, the major differences in the adsorption of both molecules on the Pd(111) surface will be discussed.

#### Assignment of Vibrations in TMCH multilayers

As discussed above, scaling of the DFT results is necessary to fit the calculated values to the experimentally observed IR vibrations. In the following discussion, DFT results will be compressed by the factor 0.954 around 1630 cm<sup>-1</sup>. The unscaled values can be found in Table 7.3 and Table 7.4. Stretching vibrations of TMCH are labeled with C1 to C15 and deformation modes with D1 to D28. We will refer to the respective labels in the following discussion, in the tables, as well as in the IR spectra. The IR spectra in Figure 7.7 compare the molecular vibrations in TMCH and isophorone. Most importantly, there are two different peaks in the C=O stretching region that likely result from different TMCH species. We can assign the strong peak at 1713 cm<sup>-1</sup> to C=O stretching in TMCH ice since it continuously grows in intensity with increasing exposure, and the peak at 1648 cm<sup>-1</sup> to a C=O stretching vibration from sub-monolayer TMCH. These peaks will be discussed in more detail in the following section.

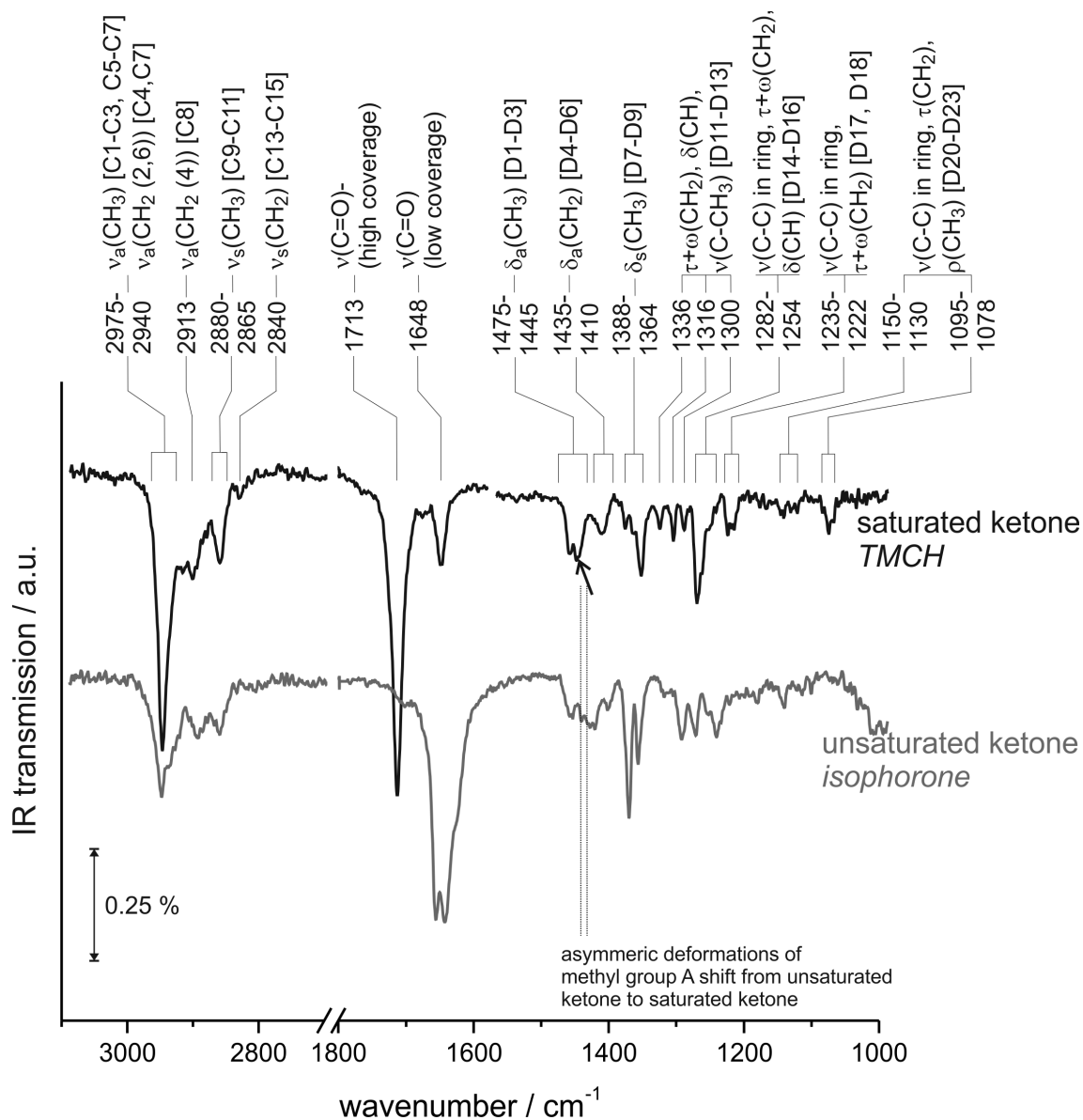


Figure 7.7: IR spectra of 1.5 ML of TMCH and  $d_5$ -isophorone adsorbed at 120 K on Pd(111) in the frequency range 3100-2700  $\text{cm}^{-1}$  (C-H stretching), 1800-1600  $\text{cm}^{-1}$  (C=C and C=O stretching), and 1500-1000  $\text{cm}^{-1}$  (C-H and C-C deformation and C-C stretching).

Table 7.3: Assignment of IR vibrations of TMCH from DFT and IRAS studies in the range of the C=C, C=O, and C-H stretching vibrations (3100-1600  $\text{cm}^{-1}$ ).

	mode	vibrations TMCH / $\text{cm}^{-1}$		
		DFT	DFT scaled	IRAS
	$\nu(\text{C=O})$	1693	1690	1713
	$\nu(\text{C=O})$			1648
C1	$\nu_a(\text{CH}_3)(\text{B})$	3026	2962	
C2	$\nu_a(\text{CH}_3)(\text{A})$	3023	2959	
C3	$\nu_a(\text{CH}_3)(\text{B})$	3021	2957	
	$\nu_a(\text{CH}_3)(\text{C})$			
	$\nu_a(\text{CH}_2)(6)$			
C4	$\nu_a(\text{CH}_2)(2)$	3018	2954	
	$\nu_a(\text{CH}_3)(\text{A,C})$			
	$\nu(\text{CH})(3)$			
C5	$\nu_a(\text{CH}_3)(\text{B})$	3016	2952	2975-2940
	$\nu_a(\text{CH}_3)(\text{C})$			
	$\nu_a(\text{CH}_2)(2,6)$			
C6	$\nu_a(\text{CH}_3)(\text{C})$	3013	2949	
	$\nu_a(\text{CH}_3)(\text{B})$			
	$\nu_a(\text{CH}_2)(6)$			
C7	$\nu_a(\text{CH}_3)(\text{A})$	3012	2948	
	$\nu_a(\text{CH}_2)(6)$			
	$\nu_a(\text{CH}_3)(\text{C})$			
	$\nu_a(\text{CH})(3)$			
	$\nu_a(\text{CH}_2)(2)$			
C8	$\nu_a(\text{CH}_2)(4)$	2967	2905	2913
	$\nu(\text{CH})(3)$			
C9	$\nu_s(\text{CH}_3)(\text{B})$	2953	2892	
C10	$\nu_s(\text{CH}_3)(\text{B})$	2946	2885	2880-2865
	$\nu(\text{CH})(3)$			
C11	$\nu_s(\text{CH}_3)(\text{C})$	2943	2883	
C12	$\nu(\text{CH})(3)$	2936	2876	
	$\nu_s(\text{CH}_2)(2,4,6)$	2931	2871	
C13	$\nu_s(\text{CH}_2)(6)$	2931	2871	
C14	$\nu_s(\text{CH}_2)(2)$	2916	2857	
	$\nu_s(\text{CH}_2)(4)$			
	$\nu(\text{CH})(3)$			
C15	$\nu_s(\text{CH}_2)(4)$	2912	2853	$\approx 2840$
	$\nu(\text{CH})(3)$			
	$\nu_s(\text{CH}_2)(2)$			

$\nu$ : stretching,  $\nu_a$ : asymmetric stretching,  $\nu_s$ : symmetric stretching  
DFT scaling factor: 0.945

Table 7.4: Assignment of IR vibration modes of TMCH in the range from 1500  $\text{cm}^{-1}$  to 1000  $\text{cm}^{-1}$ 

	mode	vibrations TMCH / $\text{cm}^{-1}$		
		DFT	DFT scaled	IRAS
D1	$\delta_a(\text{CH}_3)(\text{B,C})$	1457	1465	
	$\delta_a(\text{CH}_3)(\text{A})$	1452	1459	
D2	$\delta_a(\text{CH}_3)(\text{A})$	1446	1455	
				1475-1445

7 Adsorption of Isophorone and Trimethyl-Cyclohexanone on Pd(111): IRAS and DFT

	mode	vibrations TMCH / cm <sup>-1</sup>		
		DFT	DFT scaled	IRAS
D3	$\delta_a(\text{CH}_3)(\text{B,C})$	1445	1454	
	$\delta_a(\text{CH}_3)(\text{B,C})$	1441	1450	
	$\delta_a(\text{CH}_3)(\text{B,C})$	1433	1442	
	$\delta(\text{CH}_2)(4,6)$			
D4	$\delta(\text{CH}_2)(4)$	1426	1435	
	$\delta(\text{CH}_2)(2,6)$			
	$\delta_A(\text{CH}_3)(\text{B,C})$			
D5	$\delta(\text{CH}_2)(2,6)$	1410	14535	1435-1410
	(in-phase)			
	$\delta(\text{CH}_2)(4)$ (out-of-phase)			
D6	$\delta(\text{CH}_2)(2,6)$ out-of-phase	1403	1413	
D7	$\delta_s(\text{CH}_3)(\text{B,C})$ (open-open)	1369	1381	1388
D8	$\delta_s(\text{CH}_3)(\text{A})$	1359	1371	1376
D9	$\delta_s(\text{CH}_3)(\text{B,C})$ (open-closed)	1348	1361	1364
D10	$\delta(\text{CH})(3)$	1333	1347	
	$\omega(\text{CH}_2)(2,4)$			
D11	$\delta(\text{CH})(3)$	1314	1329	1336
	$\tau(\text{CH}_2)(2,4)$			
D12	$\nu(\text{C5-CH}_3(\text{C}))$	1289	1305	1316
	$\omega(\text{CH}_2)(4,6)$			
	$\delta(\text{CH})(3)$			
D13	$\nu(\text{C5-CH}_3(\text{B}))$	1274	1290	1300
	$\tau(\text{CH}_2)(2,4,6)$			
	$\delta(\text{CH})(3)$			
D14	$\nu_s(\text{C6-C1-C2})$	1259	1276	
	$\omega(\text{CH}_2)(2,4,6)$			
	$\delta(\text{CH})(3)$			
D15	$\nu_a(\text{C6-C1-C2})$	1242	1260	1282-1254
	$\omega(\text{CH}_2)(2,4,6)$			
D16	$\nu(\text{C-C})+\delta(\text{C-C})$	1233	1251	
	$\tau(\text{CH}_2)(2,4,6)$			
D17	$\nu(\text{C-C})$ in ring	1207	1226	
	$\tau(\text{CH}_2)(2,4,6)$			
D18	$\nu(\text{C4-C5-C5})$	1197	1217	1235-1222
	$\omega(\text{CH}_2)(2,4,6)$			
D19	$\nu(\text{C5-CH}_3(\text{B}))$	1154	1177	
	$\rho(\text{CH}_3)(\text{A,B,C})$			
	$\omega(\text{CH}_2)(6)$			
D20	$\nu(\text{C3-C4})$	1134	1157	
	$\tau(\text{CH}_2)(2,4,6)$			
	$\rho(\text{CH}_3)(\text{A})$			
D21	$\nu(\text{C2-C3-C4})$	1117	1141	1150-1130
	$\rho(\text{CH}_3)(\text{A})$			
D22	$\nu(\text{C5-C6-C1-C2})$	1061	1087	
	$\tau(\text{CH}_2)(2,4,6)$			
	$\rho(\text{CH}_3)(\text{A,C})$			
D23	$\nu(\text{C3-CH}_3(\text{A}))$	1050	1077	1095-1078
	$\rho(\text{CH}_3)(\text{A,B,C})$			

	mode	vibrations TMCH / $\text{cm}^{-1}$		
		DFT	DFT scaled	IRAS
D24	$\rho(\text{CH}_3)(\text{A,C})$ $\delta(\text{C-C})+\nu(\text{C-C})$ $\tau(\text{CH}_2)(2,6)$	1018	1046	
D25	$\rho(\text{CH}_3)(\text{B,C})$	988	1018	
D26	$\rho(\text{CH}_3)(\text{A})$	962	993	
	$\rho(\text{CH}_3)(\text{B,C})$	943	975	
D27	$\rho(\text{CH}_3)(\text{B,C})$	917	950	
	$\rho(\text{CH}_3)(\text{A})$	909	942	
D28	$\rho(\text{CH}_3)(\text{A,B,C})$ $\nu(\text{C3-C4})$	887	921	

$\nu$ : stretching,  $\delta$ : bend,  $\delta_a$ : asymmetric bend,  $\delta_s$ : symmetric bend,  
 $\omega$ : wag,  $\tau$ : twist,  $\rho$ : rock  
DFT scaling factor = 0.954

Our DFT study predicts strongly overlapping excitations of multiple stretching vibration modes of  $\text{CH}_3$ ,  $\text{CH}_2$  and  $\text{CH}$  groups. In our discussion, we will focus on the main excitation frequency for each vibration mode. A more detailed overview of all calculated vibrations and experimentally measured values is given in Table 7.3. The IR spectrum of multilayer TMCH on Pd(111) is plotted together with the IR spectrum of the same coverage of isophorone in Figure 7.7. This Figure also shows the assignment of selected vibrational modes.

Our DFT study shows all  $\text{CH}_3$  asymmetric stretching vibrations in a relatively narrow frequency range. The main vibrations of group A are predicted at  $2959 \text{ cm}^{-1}$  and  $2948 \text{ cm}^{-1}$  [C1, C7], those of the twin-groups B and C are observed at  $2962 \text{ cm}^{-1}$ ,  $2957 \text{ cm}^{-1}$ ,  $2952 \text{ cm}^{-1}$ , and  $2949 \text{ cm}^{-1}$  [C1, C3, C5, C6]. In the same frequency range,  $\text{CH}_2$  asymmetric stretching vibrations of the two groups which are adjacent to the  $\text{C=O}$  group have been found.  $\text{CH}_2(2)$  is excited at  $2954 \text{ cm}^{-1}$  and  $\text{CH}_2(6)$  mainly vibrates at  $2948 \text{ cm}^{-1}$  [C4, C7]. The asymmetric stretching of  $\text{CH}_2(4)$  is observed at  $2905 \text{ cm}^{-1}$  and thus more than  $40 \text{ cm}^{-1}$  shifted to lower wavenumbers [C8]. Experimentally, we assign the broad and strong IR absorption feature from  $2975 \text{ cm}^{-1}$  to  $2940 \text{ cm}^{-1}$  to asymmetric stretching modes of all  $\text{CH}_3$  groups and  $\text{CH}_2$  groups 2 and 6. The asymmetric stretching of  $\text{CH}_2$  group 4 is assigned to the IR absorption at  $2913 \text{ cm}^{-1}$ . The  $\text{CH}_3$  and  $\text{CH}_2$  asymmetric stretching frequencies are found in a similar range as observed for isophorone. In isophorone, however, the lower frequency vibration of group A was found to be isolated from all other  $\text{CH}_3$  asymmetric stretching vibrations at lower frequency, which is not the case for TMCH.

DFT results show  $\text{CH}_3$  symmetric stretching of groups B, A, and C at  $2892 \text{ cm}^{-1}$ ,  $2885 \text{ cm}^{-1}$ , and  $2883 \text{ cm}^{-1}$  [C9-C11]. The  $\text{CH}_2$  symmetric stretching modes of groups 6, 2, and 4 are observed at  $2871 \text{ cm}^{-1}$ ,  $2857 \text{ cm}^{-1}$ , and  $2853 \text{ cm}^{-1}$  [C13-C15]. In addition, DFT predicts the stretching vibration of the  $\text{CH}$  group at  $2876 \text{ cm}^{-1}$  and thus very close to the symmetric stretching modes of all  $\text{CH}_3$  and  $\text{CH}_2$  groups [C12]. We assign the experimentally observed IR absorption from  $2880 \text{ cm}^{-1}$  to  $2865 \text{ cm}^{-1}$  to the  $\text{CH}_3$  symmetric

stretching vibration. The weak IR absorption feature near  $2840\text{ cm}^{-1}$  coincides best with the symmetric stretching of  $\text{CH}_2$  group 4. The CH stretching cannot be identified in our spectra. The  $\text{CH}_3$  and  $\text{CH}_2$  vibrations are observed at almost the same frequencies as compared to isophorone. In contrast to the asymmetric stretching, the unsaturated  $\text{C}=\text{C}$  bond present in isophorone seems to not significantly influence the symmetric stretching frequency of group A.

The DFT study predicts  $\text{CH}_3$  asymmetric bending vibrations of groups B and C at  $1465\text{ cm}^{-1}$ ,  $1459\text{ cm}^{-1}$ ,  $1450\text{ cm}^{-1}$ , and  $1442\text{ cm}^{-1}$  [D1, D3], and those of group A at  $1455\text{ cm}^{-1}$  and  $1454\text{ cm}^{-1}$  [D2]. Strongly overlapping  $\text{CH}_2$  bending (scissor) modes are found at  $1435\text{ cm}^{-1}$ ,  $1420\text{ cm}^{-1}$ , and  $1413\text{ cm}^{-1}$  [D4-D6]. For the  $\text{CH}_3$  symmetric (umbrella) bending, DFT points to three modes: in-phase opening of the two groups B and C at  $1381\text{ cm}^{-1}$ , and out-of-phase opening at  $1361\text{ cm}^{-1}$  [D7, D9], as well as the bending of group A at  $1371\text{ cm}^{-1}$  [D8]. Experimentally, we observe well-isolated IR absorption features at  $1475\text{--}1445\text{ cm}^{-1}$ ,  $1435\text{--}1410\text{ cm}^{-1}$ , as well as at  $1388\text{--}1364\text{ cm}^{-1}$ . The first one is assigned to the  $\text{CH}_3$  asymmetric bending modes, the second to the  $\text{CH}_2$  scissor vibrations and the third to the  $\text{CH}_3$  umbrella bending. In contrast to isophorone, the asymmetric bending modes of  $\text{CH}_3$  group A is no longer shifted to lower wavenumbers as compared to those groups B and C. The  $\text{CH}_2$  scissor bending as well as the  $\text{CH}_3$  symmetric bending modes appear at very similar frequencies as in isophorone.

In the range from about  $1350\text{ cm}^{-1}$  to  $1100\text{ cm}^{-1}$ , DFT shows strongly overlapping excitations of different deformation modes of  $\text{CH}_2$ , CH and C–C groups. Mixed vibrations of  $\text{CH}_2$  wag and twist, CH bending, and C– $\text{CH}_3$  stretching modes appear at  $1347\text{ cm}^{-1}$ ,  $1329\text{ cm}^{-1}$ ,  $1305\text{ cm}^{-1}$ , and  $1290\text{ cm}^{-1}$  [D10-D13]. We assign these vibrations to the experimentally observed IR absorptions at  $1336\text{ cm}^{-1}$ ,  $1316\text{ cm}^{-1}$ , and  $1300\text{ cm}^{-1}$ . In this frequency range, TMCH gives a larger number of IR absorption peaks as compared to isophorone. We explain this observation with the additional  $\text{CH}_2$  group in TMCH, which contributes with twist and wag vibrations to the IR absorption.

Towards lower frequencies, further  $\text{CH}_2$  wag and twist as well as CH bend deformation modes, mixed with C–C stretching in ring positions are indicated by DFT. Vibrations are found at  $1276\text{ cm}^{-1}$ ,  $1260\text{ cm}^{-1}$ , and  $1251\text{ cm}^{-1}$  [D14-D16], as well as at  $1226\text{ cm}^{-1}$  and  $1217\text{ cm}^{-1}$  [D17-18]. Experimentally, we observe two broad IR absorption features at  $1282\text{--}1254\text{ cm}^{-1}$  and at  $1235\text{--}1222\text{ cm}^{-1}$ . The IR absorption peaks appear somewhat different in intensities and positions as compared to isophorone; however, C–C stretching vibrations in ring positions mixed with  $\text{CH}_2$  wag and twist and CH bending was observed in normal and  $d_5$ -isophorone in the same frequency range. The fact, that all three molecules show similar IR absorption, strongly indicates that primarily C–C bond vibrations are excited.

DFT indicates further C–C stretching in ring positions, mixed with  $\text{CH}_2$  twist and  $\text{CH}_3$  rock vibrations at  $1157\text{ cm}^{-1}$  and  $1141\text{ cm}^{-1}$  [D20, D21], as well as at  $1087\text{ cm}^{-1}$  and  $1077\text{ cm}^{-1}$  [D23]. In IRAS experiments, we identified vibrations at  $1150\text{--}1130\text{ cm}^{-1}$  and  $1095\text{--}1078\text{ cm}^{-1}$ . At lower frequencies, DFT shows  $\text{CH}_3$  rock vibrations at  $1046\text{ cm}^{-1}$ ,  $1018\text{ cm}^{-1}$ ,  $993\text{ cm}^{-1}$ ,  $975\text{ cm}^{-1}$ ,  $950\text{ cm}^{-1}$ ,  $942\text{ cm}^{-1}$ , and  $921\text{ cm}^{-1}$  [D24-28]. We did

not investigate these vibrations experimentally due to technical limitations of our experimental setup.

From the previously discussed differences in the IR spectra of TMCH and isophorone, we can draw some more general conclusions. The saturation of the C=C bond was found to significantly change vibration frequencies of the adjacent CH<sub>3</sub> group (A). Only in isophorone, one of the asymmetric stretching vibrations and both asymmetric bend modes of group A are isolated from the same vibrations of groups B and C. In contrast, no significant shift of the symmetric stretching and the symmetric bend frequencies is observed when switching from isophorone to TMCH. On the one hand, the impact of the chemical environment on vibration frequencies can have multiple reasons. In literature, such frequency shifts have been explained by differences in the steric repulsion and with electronic effects [232]. On the other hand, strongly overlapping vibration modes of CH<sub>3</sub> and CH<sub>2</sub> groups in TMCH make the interpretation of the C-H bond vibrations more complicated than for isophorone. Moreover, the additional saturated C-C bond makes the spectra more complex in the region below 1350 cm<sup>-1</sup>, where strong coupling between C-C stretching and C-H deformation vibrations appears.

### TMCH at sub-monolayer coverage

Figure 7.8 shows IR spectra of TMCH on Pd(111) at 120 K from 1800 cm<sup>-1</sup> to 1200 cm<sup>-1</sup> at different coverages. The coverage-dependent evolution of IR absorption features gives detailed insights into the binding and the geometry of TMCH on Pd(111). According to the MSSR, only the projection of the dynamic dipole moment perpendicular to the surface can be measured by IRAS.

The IR absorption intensities in the C-H stretching (not shown here) and the C-H deformation regions grow roughly monotonically with increasing TMCH exposure. In the C=O stretching region, however, there are non-trivial changes in the peaks observed with increasing TMCH exposure. At the lowest TMCH exposure (1/12 ML), a sharp peak at 1648 cm<sup>-1</sup> is detected and a smaller, broad band at 1747 cm<sup>-1</sup>. The peak at 1648 cm<sup>-1</sup> grows slightly with increasing exposure and is saturated at 1/6 ML exposure. The peak at 1747 cm<sup>-1</sup> does not change intensity up to 1/3 ML, and then disappears at coverages greater than 1/3 ML. A small peak at 1701 cm<sup>-1</sup> appears at 1/6 ML exposure and increases slightly in intensity up to 1/3 ML, but does not appear to grow further with increasing exposure. At 1/2 ML exposure, a peak at 1713 cm<sup>-1</sup> appears and this peak continues to grow with increasing exposure.

The IRAS series shown in Figure 7.8 gives valuable information about the interaction of TMCH with the Pd(111) substrate. First, there are several different peaks in the C=O stretching region that likely result from different TMCH species. We can assign the strong peak at 1713 cm<sup>-1</sup>, which grows continuously with increasing exposure beyond 1/2 ML, to C=O stretching in TMCH ice. We assign the peak at 1648 cm<sup>-1</sup>, which is observed at the lowest exposure (1/12 ML) and is saturated by 1/6 ML, to a C=O stretching vibration from sub-monolayer TMCH. The C=O stretching vibrations at 1701 cm<sup>-1</sup> and 1747 cm<sup>-1</sup> are most likely related to TMCH species in the intermediate coverage range between sub-

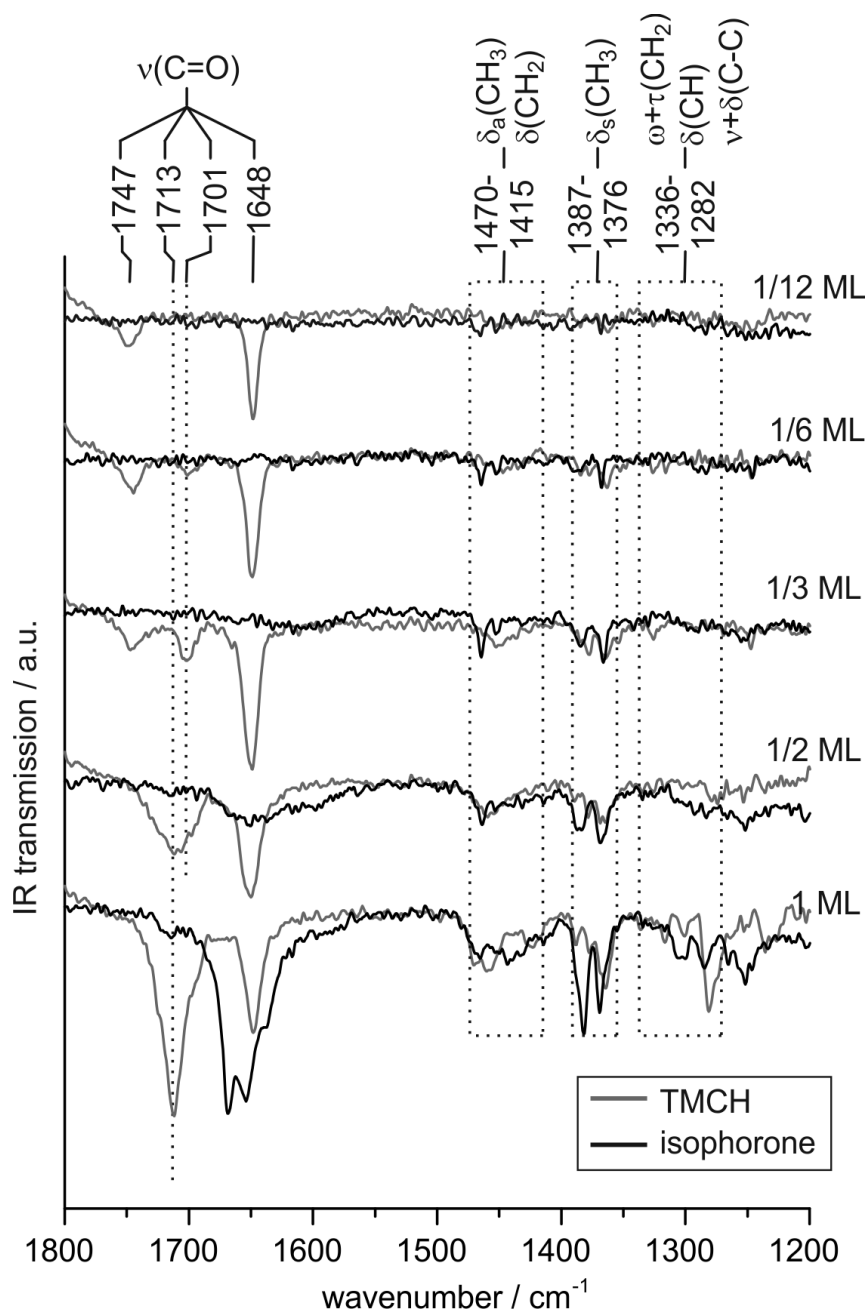


Figure 7.8: IR spectra of TMCH and  $d_5$ -isophorone adsorbed at 120 K on Pd(111) at 1800-1600  $\text{cm}^{-1}$  (C=C and C=O stretching) and 1500-1000  $\text{cm}^{-1}$  (C-H, C-D, C-C deformation and C-C stretching) at coverages from 1/12 ML (topmost trace) to 1 ML (lowest trace).

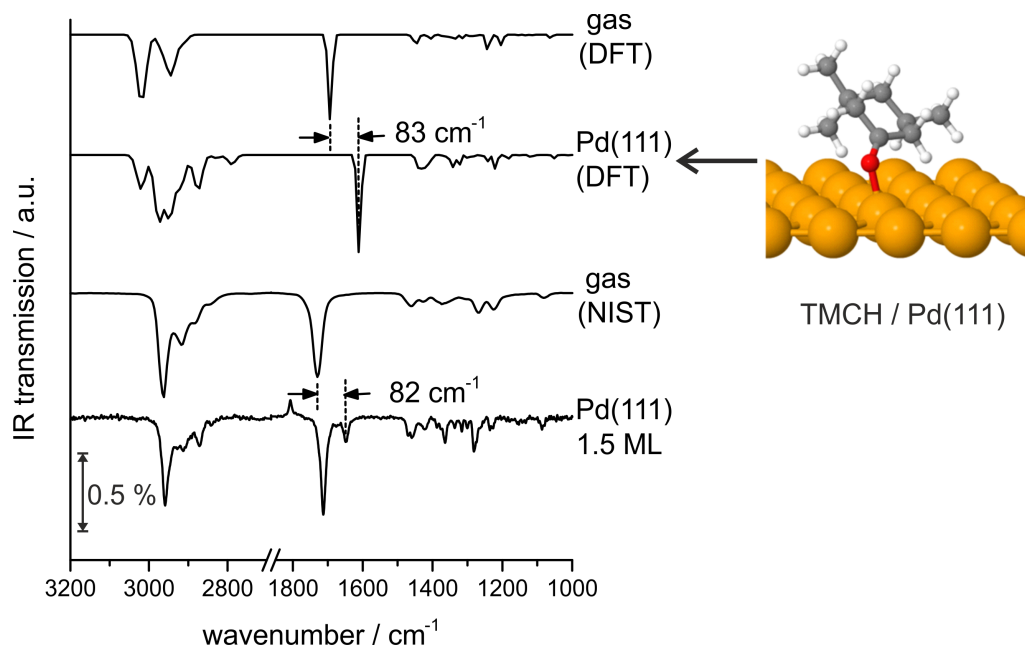


Figure 7.9: Comparison of C=O stretching vibration in TMCH in different states (from top down): calculated by DFT in gas phase and adsorbed on Pd(111), gas phase spectrum according to NIST [244], and IRAS measurement on multilayer coverage of TMCH on Pd(111) at 120 K.

monolayer and multilayer ice, probably the second layer. Finally, the strong intensity of the C=O vibration at  $1648\text{ cm}^{-1}$  even at the lowest TMCH exposure ( $1/12\text{ ML}$ ) indicates that the C=O bond in TMCH is strongly tilted with respect to the Pd(111) surface plane at sub-monolayer coverage. These results indicate that at low coverage TMCH adsorbs close to perpendicularly to Pd(111) plane through the C=O group, strongly perturbing the C=O stretching vibration. With increasing TMCH coverage, several more TMCH species are formed, giving rise to new C=O vibrational peaks. Second, the C–H stretching and the C–H deformation regions grow roughly monotonically with increasing TMCH exposure, and there is no indication that these vibrational modes are strongly affected by the Pd(111) substrate.

Below  $1500\text{ cm}^{-1}$ , all IR absorption features of TMCH become weaker with decreasing coverage. In contrast to isophorone, a selective disappearance of only some vibrations modes is not observed; the decrease in intensity is evenly distributed through all IR absorption features.

To better understand the influence of the Pd(111) substrate on the C=O stretching modes of TMCH, we have performed DFT calculations of the IR spectra of TMCH in the gas phase and of an isolated TMCH molecule adsorbed on Pd(111), which are shown in Figure 7.9. The position of the calculated C=O stretching mode of gas-phase TMCH ( $1694\text{ cm}^{-1}$ ) is  $83\text{ cm}^{-1}$  higher in wavenumber than that of TMCH adsorbed on Pd(111)

( $1611\text{ cm}^{-1}$ ), indicating a strong perturbation of the C=O vibrational mode of TMCH by interaction with the Pd(111) surface. Also shown in Figure 7.9 are the IR spectra of gas-phase TMCH from the NIST Chemistry WebBook [244] and TMCH (1.5 ML exposure at 120 K) adsorbed on Pd(111). The position of the calculated C=O vibrational peak in gas-phase TMCH ( $1694\text{ cm}^{-1}$ ) is not the same as that of gas-phase TMCH from the NIST database ( $1730\text{ cm}^{-1}$ ). Also, the position of the calculated C=O stretching vibration for an isolated TMCH molecule adsorbed on Pd(111) ( $1611\text{ cm}^{-1}$ ) is not the same as the C=O stretching vibration from sub-monolayer TMCH on Pd(111) that we measured ( $1648\text{ cm}^{-1}$ ). However, the difference in the position of the calculated C=O stretching vibration in gas-phase TMCH to the calculated C=O stretching vibration of an isolated TMCH molecule on Pd(111) ( $83\text{ cm}^{-1}$ ) is almost exactly the same as the difference in the position of the C=O stretching vibration in gas-phase TMCH from the NIST database and sub-monolayer TMCH on Pd(111) from this work ( $82\text{ cm}^{-1}$ ).

Combining the experimental IRAS results and DFT calculations, a clearer picture of the interaction between TMCH and Pd(111) emerges, which is very different from that of isophorone. The C–H stretching and C–H deformation regions grow roughly monotonically with increasing coverage, pointing to a possibly less strict ordering of molecules on the surface. TMCH interacts with the Pd(111) surface primarily through the C=O group. At low coverage, TMCH adsorbs roughly perpendicular to Pd(111) through the strongly perturbed C=O group, giving rise to a C=O vibrational peak that is strongly shifted by  $\approx 82\text{ cm}^{-1}$  to lower wavenumber relative to that of gas-phase TMCH. At intermediate coverage between sub-monolayer and multilayer ice, two new C=O vibrational peaks appear at  $1747\text{ cm}^{-1}$  and  $1701\text{ cm}^{-1}$ . The origin of these peaks is not fully clear, however, they may arise from the second layer of TMCH molecules. A C=O vibrational peak from multilayer TMCH ice appears at  $1713\text{ cm}^{-1}$ , which is by  $17\text{ cm}^{-1}$  lower than the C=O stretching vibration of gas-phase TMCH, and continues to grow with further increasing coverage.

## 7.4 Conclusions

The adsorption of the unsaturated ketone isophorone and its hydrogenation product, the saturated ketone TMCH, on Pd(111) were investigated. IR vibration modes of isophorone, deuterium-labeled ( $d_5$ -) isophorone and TMCH were studied in the range from  $3000\text{ cm}^{-1}$  to  $1000\text{ cm}^{-1}$  by IRAS and DFT studies. Detailed assignment of IR vibrations was achieved for the first time for normal and  $d_5$ -isophorone as well as TMCH at multilayers coverages.

Investigation of normal and  $d_5$ -isophorone was found to lead to three main advantages for assignment of the vibrational bands:

- C=C and C=O stretching vibrations appear well-separated in  $d_5$ -isophorone, but are strongly overlapping in normal isophorone,
- CH<sub>2</sub> stretching and bending vibrations can be distinguished from CH<sub>3</sub> stretching and bending vibrations, and

- C–C stretching vibrations are separated from CH<sub>2</sub> wag, CH<sub>2</sub> twist, and CH bend modes.

Vibration frequencies of isolated isophorone and TMCH molecules from DFT+vdW calculations agree well to the experimentally observed IR absorption features at multilayer coverages. A detailed assignment of vibrational modes between 3000 cm<sup>-1</sup> and 1000 cm<sup>-1</sup> was presented for the three molecules.

The coverage-dependent evolution of IR vibrational bands provides deep insights into the structure of isophorone on Pd(111):

- At the lowest isophorone coverage, we observed a flat-lying adsorption geometry with the C=C and C=O bonds being oriented parallel to the surface plane and at least one CH<sub>3</sub> group facing away from the Pd. This observation suggests that isophorone preserves the in-plane configuration of the conjugated  $\pi$  system in the low coverage limit. However, dehydrogenation of a CH<sub>3</sub> group to CH<sub>2</sub> appears to be possible.
- For intermediate sub-monolayer coverages, the in-plane structure of the isophorone ring adsorbed on pristine Pd(111) was observed to be strongly distorted. The C=C bond becomes noticeably tilted with respect to the surface plane, while the C=O bond remains still oriented flat on the surface.

The IR spectra indicate that the adsorption of isophorone is significantly affected by the presence of pre-adsorbed hydrogen:

- At intermediate isophorone coverages, the intensity ratio of C=O to C=C stretching vibrational peaks on hydrogen pre-covered Pd(111) indicates a rather unperturbed molecular structure similar to gas-phase isophorone.
- At low coverage of isophorone, the intensity ratio of the C–H vibrations strongly points to different orientation of the –CH<sub>3</sub> groups as compared to pristine Pd(111). The molecules appear to be more perturbed on the clean Pd(111) surface and considerably less on the hydrogen-precovered surface.
- This co-adsorbate induced change of the adsorbates geometry, especially of the orientation of the unsaturated bonds, is expected to have a decisive influence on the selectivity in hydrogenation reactions.

We found pronounced differences in the adsorbates' structures of the saturated ketone TMCH and the unsaturated ketone isophorone:

- TMCH adsorbs in a strongly tilted geometry with respect to the Pd(111) surface plane, interacting with the surface primarily through the C=O group.
- At the lowest TMCH coverage, the species give rise to a C=O vibrational peak that points to a considerable weakening of the C=O bond.
- At intermediate TMCH coverage, species with less strongly perturbed C=O bonds also appear.

- The C–H vibrational peaks grow roughly monotonically with increasing coverage, which might point to less perturbed C–H bonds and a less strict ordering of molecules on the surface.
- The strong changes of the adsorbates' structure going from the unsaturated to the saturated ketone (isophorone to TMCH) is expected to play a crucial role in the selectivity of C=C vs. C=O bond hydrogenation in  $\alpha,\beta$ -unsaturated carbonyl compounds.

## 7.5 Acknowledgements

S.S. acknowledges support from the Fonds der Chemischen Industrie for the Chemiedozentenstipendium and the European Research Council (ERC Starting Grant 335205 - ENREMOS). A.T. acknowledges support from the European Research Council (ERC Starting Grant VDW-CMAT).

## 8 Adsorption of Acrolein, Propanal, and Allyl Alcohol on Pd(111): A combination of Infrared Reflection-Absorption Spectroscopy and Temperature Programmed Desorption Studies

*Karl-Heinz Dostert<sup>1</sup>, Casey P. O'Brien<sup>1</sup>, Francesca Mirabella<sup>1</sup>, Francisco Ivars-Barceló<sup>1</sup>, Svetlana Schauermann<sup>1,2</sup>, and Hans-Joachim Freund<sup>1</sup>*

<sup>1</sup>Fritz-Haber-Institut der Max-Planck-Gesellschaft, Faradayweg 4-6, 14195 Berlin, Germany

<sup>2</sup>Institut für Physikalische Chemie, Christian-Albrechts-Universität zu Kiel, Max-Eyth-Str. 1, 24118 Kiel, Germany

*to be submitted*

## Abstract

Understanding the interaction of  $\alpha,\beta$ -unsaturated aldehydes with late transition metals is of fundamental importance for the rational design of new catalytic materials with desired selectivity towards C=C or C=O bond hydrogenation. The interaction of this group of molecules with transition metals has been investigated on acrolein, propanal, and allyl alcohol on Pd(111) as a prototypical system. In this study, infrared reflection-absorption spectroscopy (IRAS) and temperature programmed desorption (TPD) experiments have been applied under ultrahigh vacuum (UHV) conditions to obtain detailed information on the molecular structures and geometries of acrolein, propanal, and allyl alcohol at different coverages. IRAS experiments at multilayer coverages show rather unperturbed molecules, while the studies at sub-monolayer coverages indicate adsorbates with strongly distorted chemical bonds. Coverage-dependent IR spectra of acrolein on Pd(111) point to the formation of four different surface species: A, B, C, and D. The studies on propanal and allyl alcohol give similar results. Acrolein species A, B, and C are assigned to the first monolayer and species D is assigned to molecules in multilayers. Species A and B have their molecular plane parallel to the metal surface, adsorbates of type C appear significantly tilted with a perturbed C=O bond. TPD studies show complete decomposition of species A, B, and C. The different adsorbates are mainly characterized by their C=O stretching, CH<sub>2</sub> scissor, and HC=CH<sub>2</sub> trans-wag vibrational modes. For propanal, we have found characteristic C=O stretching frequencies as well as CH<sub>3</sub> asymmetric stretching, symmetric bend and rock vibration frequencies for low, intermediate, and high coverage species. For allyl alcohol, the assignment has been more difficult, due to weak IR absorption features. However, coverage-dependent C-H vibration frequencies have been identified.

## 8.1 Introduction

The catalytic hydrogenation of  $\alpha,\beta$ -unsaturated aldehydes is of broad interest for fundamental understanding as well as for industrial applications [30]. The primary hydrogenation product is either a saturated aldehyde or an unsaturated alcohol. To avoid the formation of undesired products and thereby an often difficult and cost-intensive separation process, a high selectivity in C=C or C=O bond hydrogenation is desirable.

It is generally believed that the adsorption geometry of the reactant on the catalyst surface is an important factor governing the selectivity of the hydrogenation reaction [34, 35, 40, 62, 181, 245]. On the one hand, the adsorption geometry of an  $\alpha,\beta$ -unsaturated aldehyde or ketone can be manipulated in favor of C=O bond hydrogenation by adding bulk substituents to the C=C functional group [27, 30, 245]. Acrolein, however, is the most difficult  $\alpha,\beta$ -unsaturated carbonyl compound to selectively hydrogenate the C=O bond because the C=C group is sterically not hindered by any substituent. On the other hand, the structure of the catalyst also influences the adsorption geometry of the reactant and thus may have a decisive influence on the selectivity of the conversion. Nevertheless, the effect of the catalyst structure is much less understood than the effects of the molecular structure on the adsorption geometry.

Our recent work on acrolein hydrogenation over a Pd(111) surface under well-defined ultrahigh vacuum (UHV) conditions provided new insight into the relationship between catalyst structure and selectivity in partial hydrogenation of acrolein. For the first time we showed that a near 100% selectivity towards hydrogenation of C=O in acrolein is possible [185]. This was a particularly unexpected result, since Pd has previously shown near 100% selectivity towards C=C bond conversion in  $\alpha,\beta$ -unsaturated carbonyl compounds [246, 247].

In the present work, we have investigated the adsorption of acrolein, propanal, and allyl alcohol on a Pd(111) single crystal. Infrared reflection-absorption spectroscopy (IRAS) has been employed to investigate the molecular structures and geometries of the adsorbates at different coverages. IR spectroscopy is a very established tool to study orientations, structures, and adsorbate-substrate interactions of hydrocarbon compounds on metal surfaces [106, 113]. The desorption and decomposition of the adsorbates on Pd(111) has been monitored by temperature programmed desorption (TPD) experiments.

## 8.2 Experimental Details

All experiments have been performed at the Fritz-Haber-Institut, Berlin, in a UHV apparatus that was described in detail previously [100]. In brief, acrolein, propanal, and allyl alcohol have been dosed onto the sample through a doubly differentially pumped multi-channel array source controlled by valves and shutters. The source has been operated at room temperature, and the beam diameter has been chosen to exceed the sample size. The Pd(111) single crystal has been cleaned prior to use by repeated cycles of Ar<sup>+</sup> ion bombardment at room temperature, annealing at 1000 K and oxidation in  $1 \cdot 10^{-6}$  mbar

O<sub>2</sub> at 750 K to remove residual carbon. The final cleaning cycle has been stopped after annealing. The flatness and cleanliness of the Pd(111) single crystal surface has been checked by low energy electron diffraction (LEED) and IRAS measurements of adsorbed CO.

IRAS data have been acquired using a vacuum Fourier-Transform infrared (FT-IR) spectrometer (Bruker IFS 66v/S) with a spectral resolution of 2 cm<sup>-1</sup> and a mid-infrared (MIR) polarizer and p polarized IR light. TPD experiments have been carried out in the same vacuum system and by using an automated quadrupole mass spectrometer (QMS) system (Hiden Analytics). The following atomic masses have been detected in TPD experiments: 2, 31, 56, 57, 58, and 60.

Shortly before each experiment the sample has been flash annealed to 600 K before cooling to 120 K. Acrolein (Fluka, 95% purity), propanal (Acros Organics, >99% purity), and allyl alcohol (Aldrich, >99% purity) have been purified prior to their exposure by repeated freeze-pump-thaw cycles.

### 8.3 Results

IR vibrations of acrolein, propanal, allyl alcohol, and molecules with similar functional groups were assigned in several studies before. We shortly summarize a few of them here and refer again to them later in our discussion. A general overview of typical vibration frequencies can be found in a textbook by Colthup, Daly, and Wiberley [109]. Hamada *et al.* assigned IR absorption features of gas-phase acrolein to calculated vibration frequencies in the range from 4000 cm<sup>-1</sup> to 400 cm<sup>-1</sup> [248]. Puzzarini *et al.* studied the gas-phase structures of acrolein and their IR vibration frequencies theoretically and compared them to experimental results. Several IR absorption features were found to significantly change from *trans*- to *cis*-acrolein [249]. However, Puzzari assigned IR absorption features of vinyl- and aldehyde-C-H bend modes reversed as compared to Hamdada [248]15, Fujii [250], and Akita [251]. Fujii *et al.* [250] and Akita *et al.* [251] investigated the structures of acrolein after adsorption on silver and gold films under UHV conditions. In both studies, IR vibrational modes were assigned in the range from 1800 cm<sup>-1</sup> to about 800 cm<sup>-1</sup>. Particularly, a strong intensity of the CH<sub>2</sub> wag vibration peak for adsorbates with molecular plane parallel to the metal surface was observed. Osaka *et al.* investigated the adsorption of 1,3-butadiene on Au(111) and Ag(111) surfaces [252]. In our study, comparison of the IR spectra of acrolein to those of 1,3-butadiene has helped to identify vibrations of the HC=CH<sub>2</sub> unit of acrolein. Loffreda *et al.* studied the adsorption of acrolein on Pt(111) by total energy and frequency calculations combined with high resolution electron energy loss spectroscopy (HREELS) experiments [61]. Several C-H deformation vibrations described in this study coincide well with our observed IR absorption features. C-H stretching modes of surface species during hydrogenation of acrolein and other  $\alpha,\beta$ -unsaturated aldehydes were studied by sum-frequency generation spectroscopy by Kliewer *et al.* [60].

Thorough experimental and theoretical studies on the vibrational modes of propanal were published by Guirgis *et al.* [253] and Frankiss *et al.* [254], which agree very well to our data. Guirgis studied the conformational stability and assigned vibrational modes in liquid xenon at wavenumbers up to 3500 cm<sup>-1</sup> and Frankiss investigated the vibrational modes of normal and deuterium-labeled propanal in the gas phase. In an earlier study,

vibrations of liquid and crystalline propanal were assigned experimentally by Sbrana [255]. In a more general investigation, Byrne *et al.* studied carbonyl vibration frequencies and C–H vibrations of saturated aliphatic aldehydes [256]. Guirgis, Frankiss, Sbrana, and Byrne pointed out two typical features in the C–H stretching region, which result from Fermi resonance between the CH bend overtone and the CH stretching fundamental at 2700–2770  $\text{cm}^{-1}$  and 2800–2870  $\text{cm}^{-1}$ . This characteristic IR absorption of the aldehyde-CH group was studied in more detail by Pinchas [257] and Eggers *et al.* [258].

A very detailed assignment of the vibrational modes of normal and isotopically labeled allyl alcohol in the gaseous, liquid, and glassy states as well as in argon and nitrogen matrices in the range from 4000  $\text{cm}^{-1}$  to 200  $\text{cm}^{-1}$  was performed by Silvi and Perchard. In this study, *cis* and *gauche* conformers have been identified by their IR vibration frequencies [259]. In a more recent study, Durig *et al.* assigned vibrational frequencies from theoretical calculations as well as from IR and Raman experiments for the four allyl alcohol conformers *gauche-trans*, *gauche-gauche*, *cis-trans*, and *cis-gauche* [260].

We have studied the adsorption of acrolein, propanal, and allyl alcohol on Pd(111) at 120 K under well-defined UHV conditions by IRAS experiments. The molecular structure and the adsorption geometry of the adsorbates have been investigated as a function of coverage. The IR spectra from molecules at multilayer coverages provide a reference for mainly unperturbed molecules while the IR vibrations at sub-monolayer coverages give insights into the perturbation of chemical bonds by the Pd(111) surface.

The adsorption geometry of molecular species adsorbed on metal surfaces can be deduced from their IR spectra based on the metal surface selection rule (MSSR) [106, 113]. According to the MSSR, only the component of the dynamic dipole moment perpendicular to the metal surface can be detected, while vibrations parallel to the surface are strongly attenuated by an image dipole in the substrate. Hence, characteristic intensity distributions between IR absorption peaks at low coverage indicate the favored adsorption geometry.

Three main spectral regions can be distinguished for all molecules, which are characteristic for C–H stretching vibrations (3100–2700  $\text{cm}^{-1}$ ), C=O and C=C stretching vibrations (1800–1600  $\text{cm}^{-1}$ ) as well as C–H deformation and C–C stretching vibrations ( $\leq 1500 \text{ cm}^{-1}$ ). The exact assignment of the IR vibration peaks for each compound will be discussed in the following sections.

### 8.3.1 Adsorption of Acrolein

Figure 8.1(a) illustrates the coverage-dependent evolution of IR spectra of acrolein on Pd(111) from the sub-monolayer to the multilayer regime. We have identified the appearance of different surface species, to which we refer to as types A, B, C, and D. Coverages up to  $2.7 \cdot 10^{14} \text{ molecules/cm}^2$ , at which the most strongly perturbed species A and B appear, are assigned to the sub-monolayer regime. The surface coverage of  $3.6 \cdot 10^{14} \text{ molecules/cm}^2$  ( $\approx 1$  acrolein molecule per 4 Pd surface atoms), at which species C is observed, is related to the full monolayer coverage. Finally, the multilayer regime is indicated

Table 8.1: Assignment of IR vibrational modes of acrolein on Pd(111) at 120 K.

mode	IRAS vibrations / $\text{cm}^{-1}$				references / $\text{cm}^{-1}$
	species A	species B	species C	species D	
$\nu(\text{CH})_v$					3069 [248] 3092-3077 [109]
$\nu_a(\text{CH}_2)$				2857	3103 [248] 3092-3077 [109]
$2\delta(\text{CH})_{CO}$				2766 <sup>b</sup>	2772 [257], 2800 [248] 2830-2810 [109] 2867-2818 [253]
$\nu(\text{CH})_{CO}$				2705 <sup>b</sup>	2718 [259], 2716 [254] 2774-2719 [253] 2720-2695 [109]
$\nu(\text{C}=\text{O})$			1663-1650	1699-1690	1672-1670 (on Ag) [251] 1684-1670 (on Ag) [250] 1724 (gas) [248]
$\nu(\text{C}=\text{C})$				1618	1618-1603 [250] 1625 [248] 1644-1617 [109]
$\delta(\text{CH}_2)$	1400	1425	1425	1425	1425 [251] 1420 [61, 248, 249] 1431-1425 [250]
$\delta(\text{CH})_{CO}$				1365	1365 [251], 1360 [248] 1365-1360 [250] 1275 [249]
$\delta(\text{CH})_{CC}$				1281	1281 [251], 1284 [250] 1275 [248], 1360 [249]
$\nu(\text{C}-\text{C})$				1164	1169-1159 [250] 1158 [248, 249] 1165-1159 [251]
$\omega_T(\text{HC}=\text{CH}_2)$	(975)	(975)	(990)	990	1018-841 [250] 1020-950 [251] 1022-1002 <sup>c</sup> [252] 995-985 [109] 993 [248]

$\nu$ : stretching,  $\nu_a$ : asymmetric stretching,  $\nu_s$ : symmetric stretching,  $\delta$ : bending,  $\omega_T$ : *trans*-wag vibration, C=O: aldehyde group, C=C: vinyl group, <sup>b</sup>: Fermi resonance, <sup>c</sup>vibration in 1,3-butadiene

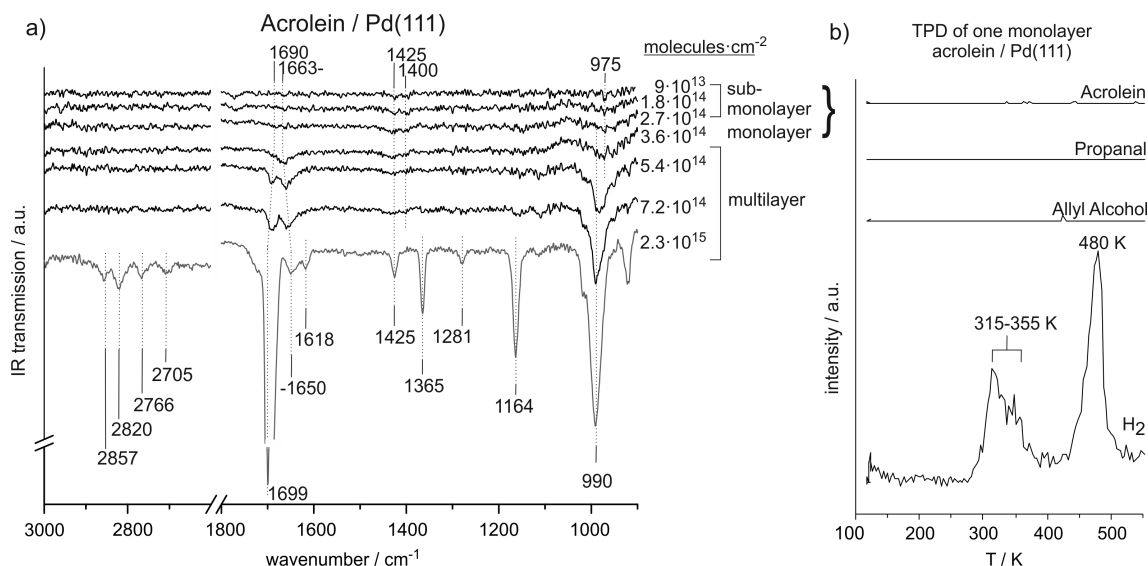


Figure 8.1: a) IR spectra of acrolein on Pd(111) from sub-monolayer to multilayer coverage recorded at 120 K. b) TPD study after adsorption of a monolayer of acrolein on Pd(111).

by the rather unperturbed species D, which is observed starting at the exposure of  $5.4 \cdot 10^{14}$  molecules/cm<sup>2</sup>. Saturation of the latter species is not found. Table 8.1 summarizes the assignment of vibrational modes to the observed IR absorption features of the different acrolein species on the Pd(111) surface.

### acrolein – type A and B

In the sub-monolayer regime, IR vibrations are detected at 1425 cm<sup>-1</sup>, 1400 cm<sup>-1</sup>, and 975 cm<sup>-1</sup>. All of these IR absorption peaks are assigned to deformation modes of the CH<sub>2</sub> group. We assign the vibrations at 1425 cm<sup>-1</sup> and 1400 cm<sup>-1</sup> to CH<sub>2</sub> scissor bend vibrations and the intense IR absorption at 975 cm<sup>-1</sup> to a deformation of the HC=CH<sub>2</sub> unit, possibly a *trans-wag* mode, which is a =CH<sub>2</sub> twist coupled with an H-C= out-of-plane bend vibration.

Previously, the CH<sub>2</sub> scissor deformation in acrolein was reported near 1425 cm<sup>-1</sup> [248, 249, 251]. The strong IR absorption near 975-990 cm<sup>-1</sup> was related to the HC=CH<sub>2</sub> unit; however, previous publications assigned these features to different modes, such as CH bend [250, 251] CH<sub>2</sub> wag [251] or CH<sub>2</sub> twist [252] vibrations. Colthup *et al.* referred to this intense IR absorption as HC=CH<sub>2</sub> *trans-wag* mode [109].

The vibration at 1400 cm<sup>-1</sup> appears at relatively low wavenumber as compared to typical CH<sub>2</sub> scissor frequencies reported in literature and thus points to a perturbed CH<sub>2</sub> group. We refer to this species as type A. The IR absorption at 1425 cm<sup>-1</sup>, however, indicates a second surface species with more unperturbed CH<sub>2</sub> group to which we refer as species B. The IR absorption at 975 cm<sup>-1</sup> cannot clearly be assigned to species A or B, it

might appear in both of them.

### acrolein – type C

Near the full monolayer coverage, a prominent peak appears and saturates at  $1663\text{ cm}^{-1}$  and thus in the typical range for a C=O stretching vibration. It shifts to  $1650\text{ cm}^{-1}$  with increasing coverage. The vibration is located about  $60\text{--}70\text{ cm}^{-1}$  to lower wavenumbers as compared to the C=O stretching frequency determined in previous studies on acrolein in the gas phase (near  $1720\text{ cm}^{-1}$ ) [244].

Furthermore, we observe the CH<sub>2</sub> scissor vibration at  $1425\text{ cm}^{-1}$  and thus at the same frequency as for type B. The HC=CH<sub>2</sub> *trans-wag* mode seems to shift to slightly higher frequencies, close to  $990\text{ cm}^{-1}$ . However, the absorption at  $990\text{ cm}^{-1}$  might also arise from species D.

### acrolein – type D

Several additional IR absorption features appear in the multilayer regime. In the C–H stretching region, IR vibrations are observed at  $2857\text{ cm}^{-1}$ ,  $2820\text{ cm}^{-1}$ ,  $2766\text{ cm}^{-1}$ , and  $2705\text{ cm}^{-1}$ . We assign the two higher wavenumber peaks to CH<sub>2</sub> asymmetric and symmetric stretching modes. Previously, the two CH<sub>2</sub> stretching modes were observed near  $3000\text{ cm}^{-1}$  and  $3100\text{ cm}^{-1}$  and thus at higher frequencies [109, 248]. The two features at  $2766\text{ cm}^{-1}$  and  $2705\text{ cm}^{-1}$  are assigned to the first overtone of the aldehyde-C–H bend and the aldehyde-C–H stretching fundamental vibrations. The appearance of the two peaks is known to typically appear in aldehydes and was previously explained by strong Fermi resonance [109, 253, 257].

In the C=C and C=O stretching region, a very pronounced IR vibration is observed at  $1690\text{--}1699\text{ cm}^{-1}$  and a weaker one at  $1618\text{ cm}^{-1}$ . The peaks are assigned to the C=O and C=C stretching modes. The C=O vibration wavenumber increases with coverage from  $1690\text{ cm}^{-1}$  at  $5.4 \cdot 10^{14}$  molecules/cm<sup>2</sup> to  $1699\text{ cm}^{-1}$  at  $2.3 \cdot 10^{15}$  molecules/cm<sup>2</sup>. Hence, it shifts closer to the previously reported gas phase value of  $1724\text{ cm}^{-1}$  [248]. The C=C stretching vibration at  $1618\text{ cm}^{-1}$  appears in the frequency range reported in literature [249, 250].

In the region below  $1500\text{ cm}^{-1}$ , well-separated IR absorption features appear at  $1425\text{ cm}^{-1}$ ,  $1365\text{ cm}^{-1}$ ,  $1281\text{ cm}^{-1}$ ,  $1164\text{ cm}^{-1}$ , and  $990\text{ cm}^{-1}$ . The vibration at  $1425\text{ cm}^{-1}$  is observed at identical frequency in types B and C and is assigned to the CH<sub>2</sub> scissor mode. We assign the IR absorption at  $990\text{ cm}^{-1}$  to the HC=CH<sub>2</sub> *trans-wag* mode which has been observed at  $975\text{ cm}^{-1}$  for molecules in the sub-monolayer regime. The vibration at  $1164\text{ cm}^{-1}$  is correlated with the C–C stretching vibration. In literature, the C–C stretching was observed at  $1169\text{--}1158\text{ cm}^{-1}$  [248–251]. Moreover, the IR absorption peaks at  $1365\text{ cm}^{-1}$  and  $1281\text{ cm}^{-1}$  strongly reveal bending of the aldehyde and vinyl C–H bonds. Previously, most studies related the higher wavenumber peak to the aldehyde C–H group and the

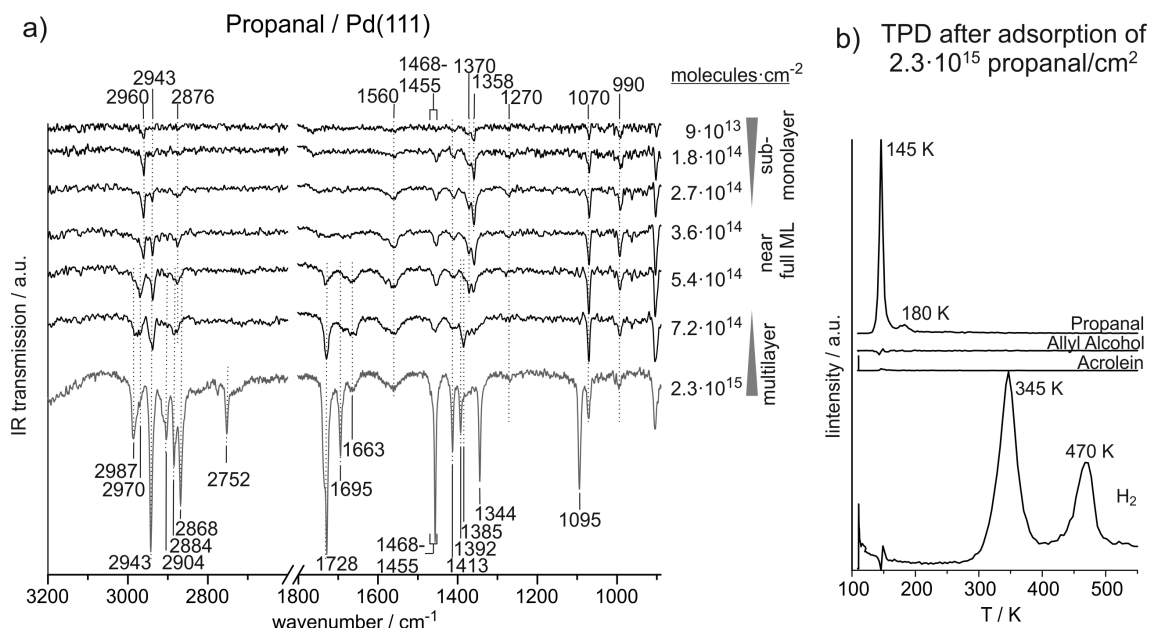


Figure 8.2: a) IR spectra of propanal on Pd(111) from the sub-monolayer to multilayer regime recorded at 120 K. b) TPD after deposition of about six layers of propanal on Pd(111).

lower frequency peak to the vinyl C–H group [61, 109, 248, 251]; however, we also found the reversed assignment [249].

### TPD of the acrolein monolayer

Figure 8.1(b) illustrates a temperature programmed desorption (TPD) experiment of 1 ML acrolein on Pd(111), which corresponds to the surface species A, B, and C. The desorption of acrolein, allyl alcohol, propanal, and hydrogen are illustrated. No acrolein, allyl alcohol or propanal are detected in the gas phase; however, hydrogen appears at 315–355 K and at 480 K. The peak at lower temperature indicates a desorption-limited process and the second peak shows C–H decomposition-limited desorption.

### 8.3.2 Adsorption of Propanal

Figure 8.2(a) illustrates the coverage dependent evolution of IR spectra of propanal on Pd(111) from the sub-monolayer to the multilayer regime at 120 K. Coverage-dependent changes of IR absorption features suggest three coverage regimes. The sub-monolayer range indicates up to  $2.7 \cdot 10^{14}$  propanal molecules per  $\text{cm}^2$ , the formation of a complete monolayer seems to require approximately an exposure of  $3.6 \cdot 10^{14}$  to  $5.4 \cdot 10^{14}$  molecules per  $\text{cm}^2$ , and the multilayer regime is observed when the surface coverage exceeds  $5.4 \cdot 10^{14}$  molecules per  $\text{cm}^2$ . Table 8.2 gives an overview on all IR vibrational peaks at low, intermediate, and high propanal coverages and compares them to values reported in literature.

Table 8.2: Assignment of IR vibrational modes of propanal on Pd(111) at 120 K.

mode	IRAS vibrations / $\text{cm}^{-1}$			references / $\text{cm}^{-1}$
	sub-monolayer	near monolayer	multilayer	
$\nu_a(\text{CH}_3)$	2960	2970	2987	2992-2985 [253] 2982-2985 [255] 2980 [254]
$\nu_a(\text{CH}_2)$	2943	2943	2943	2954-2941 [253] 2941-2939 [255]
$\nu_s(\text{CH}_2)$			2904	2914-2901 [253] 2899 [255]
$\nu_s(\text{CH}_3)$	2876		2884	2905-2883 [253] 2880 [254]
$\nu(\text{CH})$			2868 <sup>b</sup>	2867-2818+2774-2712 [253] 2700+2800 [254]
$2\delta(\text{CH})$			2752 <sup>b</sup>	2850-2700 [256] 2718+2772 [257]
$\nu(\text{C=O})$	1560	1663	1728/1695	1569 <sup>c</sup> [261], 1580 [262] 1595, 1562 [263] 1565 [264], 1750 [254] 1740-1720 [109] 1754-1729 [253]
$\delta_a(\text{CH}_3)$	1455-1468	1455-1468	1455-1468	1475-1450 [109] 1467-1451 [253] 1460,1451 [254]
$\delta(\text{CH}_2)$	1413	1413	1413	1425 [256], 1420 [254] 1423-1413 [253]
$\delta(\text{CH})$	1370	1370	1392	1395 [254], 1385 [258] 1381-1374 [253] 1410-1380 [109]
$\delta_s(\text{CH}_3)$	1358	1385		1342-1338 [255] 1383-1377 [109] 1395-1392 [253] 1380 [254]
$\omega(\text{CH}_2)$			1344	1340 [254]
$\tau(\text{CH}_2)$	1270			1261-1250 [253] 1250 [254], 1260 [255]
$\rho(\text{CH}_3)$	1070	1070	1095	1098-1093 [253]
$\nu_a(\text{CCC})$	990			1001-993 [253]

$\nu$ : stretching,  $\nu_a$ : asymmetric stretching,  $\nu_s$ : symmetric stretching,  $\delta$ : bending,  $\delta_s$ : bending,  $\omega$ : wagging, <sup>b</sup>: Fermi resonance, <sup>c</sup>in HREELS measurement

### propanal at low coverage

A variety of IR absorption features are identified at low propanal concentration on the Pd(111) surface. At surface coverages ranging from  $9 \cdot 10^{13}$  to  $2.7 \cdot 10^{14}$  molecules/cm<sup>2</sup>, pronounced IR absorption peaks are observed in the region of the C–H stretching vibrations. The IR vibrations at 2960 cm<sup>-1</sup>, 2943 cm<sup>-1</sup>, and 2876 cm<sup>-1</sup> are assigned to CH<sub>3</sub> asymmetric stretching, CH<sub>2</sub> asymmetric stretching, and CH<sub>3</sub> symmetric stretching modes. Previously, CH<sub>3</sub> asymmetric and symmetric stretching vibrations in propanal were observed at 2992–2980 cm<sup>-1</sup> [253–255] and 2905–2880 cm<sup>-1</sup> [253, 254]. The CH<sub>2</sub> asymmetric stretching was found at 2914–2899 cm<sup>-1</sup> [253, 255]. However, none of the literature data refers to propanal on a metal surface.

In the region of typical C=O stretching vibrations, no IR absorption features can be identified. At 1560 cm<sup>-1</sup>, however, an IR vibration is observed, which is present neither in propanal nor in other aldehydes and can therefore not be related to any prominent vibration of intact propanal molecules. Nevertheless, similar vibration frequencies have been observed before. Murillo *et al.* observed a vibration at 1569 cm<sup>-1</sup> in HREELS experiments on acrolein adsorbed on Pt-Ni-Pt(111) and Pt-Co-Pt(111) surfaces and assigned it to a C–O stretching vibration of acrolein adsorbed in a di- $\sigma$ -C–O configuration [261]. Furthermore, the COO-asymmetric stretching vibration of a propionate species on oxide surfaces were found at 1595 cm<sup>-1</sup> [263] and 1565 cm<sup>-1</sup> [264], and the C=O stretching frequencies of  $\beta$ -diketone complexes with Cu were reported to appear down to 1524 cm<sup>-1</sup> [262]. Hence, this IR absorption feature could point to a severe weakening of the carbonyl group because of the tendency of the oxygen to attract electrons  $\text{C}=\text{O} \leftrightarrow \text{C}^+-\text{O}^-$ . The polarized form could gain in importance, if the charge is stabilized by the Pd surface. However, a di- $\sigma$  configuration as observed by Murillo *et al.* for acrolein on Pt-Ni-Pt(111) and Pt-Co-Pt(111), seems unlikely here since a di- $\sigma$ -bonded C–O group would be parallel to the Pd surface and thus not detectable by IRAS.

In the region below 1500 cm<sup>-1</sup>, several pronounced vibrations are detected at sub-monolayer coverages. IR absorption features at 1468–1455 cm<sup>-1</sup> and 1413 cm<sup>-1</sup> are assigned to CH<sub>3</sub> asymmetric bend and CH<sub>2</sub> scissor vibrations. Previously, CH<sub>3</sub> asymmetric bending modes were found in the ranges from 1475–1451 cm<sup>-1</sup> and CH<sub>2</sub> scissor deformation vibrations were detected at 1425–1413 cm<sup>-1</sup> [109, 253, 254]. The vibrations at 1370 cm<sup>-1</sup> and 1358 cm<sup>-1</sup> strongly indicate CH bending or CH<sub>3</sub> umbrella bending modes; a clear assignment to one of them is difficult. In literature, CH bending and CH<sub>3</sub> symmetric bending modes were reported in overlapping frequency ranges at 1410–1374 cm<sup>-1</sup> [109, 253, 254, 258] and 1395–1338 cm<sup>-1</sup> [109, 253–255]. With higher certainty, we relate the peaks at 1270 cm<sup>-1</sup>, 1070 cm<sup>-1</sup>, and 990 cm<sup>-1</sup> to CH<sub>2</sub> twist, CH<sub>3</sub> rock, and CCC antisymmetric stretching modes. Previously, CH<sub>2</sub> twist vibrations were observed at 1261–1250 cm<sup>-1</sup>, CH<sub>3</sub> rocking was found at 1098–1093 cm<sup>-1</sup>, and CCC antisymmetric stretching modes were reported at 1001–993 cm<sup>-1</sup> [253].

**propanal at intermediate coverage**

Pronounced changes of IR vibration frequencies are observed at intermediate surface coverages ranging from  $3.6 \cdot 10^{14}$  to  $5.4 \cdot 10^{14}$  molecules/cm<sup>2</sup>. The CH<sub>3</sub> asymmetric stretching is observed at 2970 cm<sup>-1</sup>, which is slightly higher than at low coverage and closer to the literature values for non-adsorbed molecule. The same trend is observed for the more tentatively assigned CH<sub>3</sub> symmetric bending, which appears at 1385 cm<sup>-1</sup>. The vibrations of the CH<sub>2</sub> and CH groups as well as the CH<sub>3</sub> asymmetric bending appear at identical wavenumbers as observed at lower coverages.

In the C=O stretching region a clearly observable peak saturates at 1663 cm<sup>-1</sup>. Previous studies on rather unperturbed propanal molecules showed C=O stretching vibrations in the range of 1754-1720 cm<sup>-1</sup> and thus at significantly higher wavenumbers [109, 253, 254, 256]. The strong decrease of the C=O stretching frequency in our studies points to a significant weakening of the C=O bond and hence to strong interaction of this group with the Pd surface. Finally it should be noted that the C=O stretching vibration appears at identical frequency as that of acrolein type C on Pd(111).

**propanal at high coverage**

At high propanal coverages, several further IR vibration features are observed. The frequencies of the CH<sub>3</sub> stretching vibrations appear at values closer to that of molecules in the gas-phase. CH<sub>3</sub> asymmetric and symmetric stretching modes are assigned to IR absorption features at 2987 cm<sup>-1</sup> and 2884 cm<sup>-1</sup>. CH<sub>2</sub> asymmetric stretching is observed at 2943 cm<sup>-1</sup> and thus at the same wavenumber as observed for lower propanal coverages. The CH<sub>2</sub> symmetric stretching mode, which could not be detected at lower coverages, is observed at 2904 cm<sup>-1</sup>. Previously, this vibration was observed at 2914-2899 cm<sup>-1</sup> [253, 255]. The features at 2868 cm<sup>-1</sup> and 2752 cm<sup>-1</sup> are both assigned to the aldehyde C-H group. As discussed for acrolein, these two peaks are known to result from strong Fermi resonance between the first overtone of the CH bending and CH stretching fundamental [253, 254, 256, 257].

In the C=O stretching region, we observe two features growing simultaneously at 1728 cm<sup>-1</sup> and 1695 cm<sup>-1</sup>. The vibration at 1728 cm<sup>-1</sup> is close to the frequency reported for propanal in the gas phase and thus points to a mainly unperturbed C=O group. The vibration at 1695 cm<sup>-1</sup>, however, indicates the simultaneous formation of a species with a slightly weakened C=O bond.

CH<sub>3</sub> asymmetric bending and CH<sub>2</sub> scissor bending modes appear at identical frequencies as observed for lower coverages. However, the CH<sub>3</sub> symmetric bend and/or CH bend as well as CH<sub>3</sub> rock vibrations are identified at slightly higher frequencies. The former one is observed at 1392 cm<sup>-1</sup> and the latter one at 1095 cm<sup>-1</sup>. Moreover, IR absorption is observed at 1344 cm<sup>-1</sup>, which we assign to the CH<sub>2</sub> wag mode. Previously, this vibration was observed at 1340 cm<sup>-1</sup> [254].

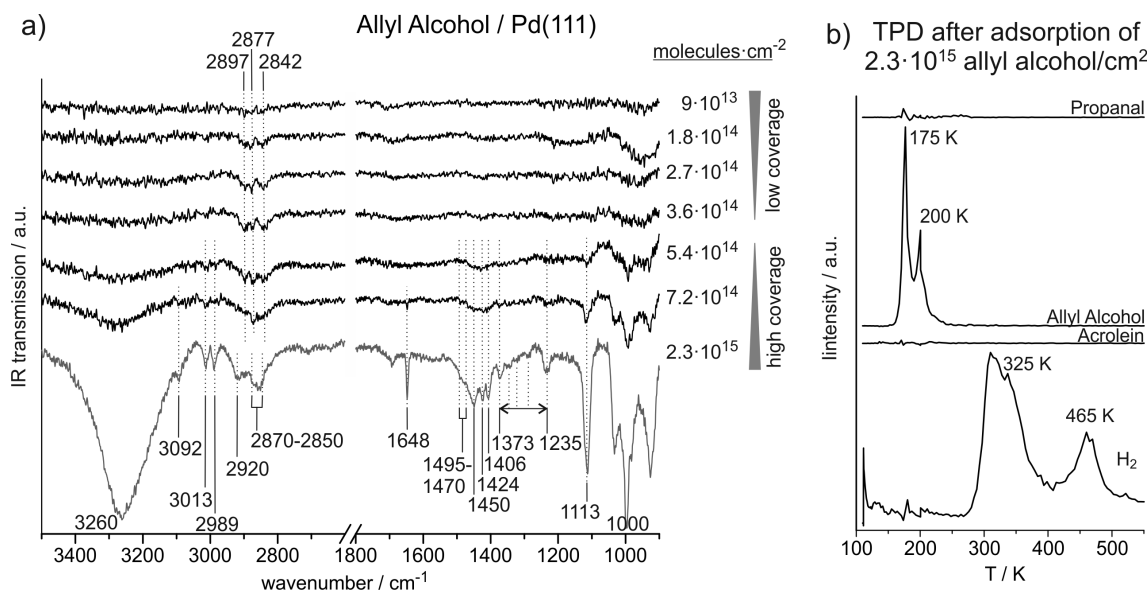


Figure 8.3: a) Coverage-dependent IR spectra of allyl alcohol on Pd(111) recorded at 120 K. b) TPD after deposition of about six layers of allyl alcohol on Pd(111).

#### TPD of propanal at multilayer coverage

Figure 8.2b illustrates a TPD experiment of approximately six layers of propanal on Pd(111). Desorption of acrolein, allyl alcohol, propanal and hydrogen has been studied. Neither acrolein nor allyl alcohol are observed in the gas phase. Propanal, however, appears in a strong and sharp desorption peak at 145 K and in a weak feature at 180 K. Hydrogen desorption is observed near 345 K and 470 K. The two hydrogen peaks point to sequential decomposition resulting in a desorption-limited and a reaction-limited formation of  $\text{H}_2$ . The two propanal desorption peaks indicate a relatively large amount of weakly bound molecules, which desorb near 145 K, and a smaller fraction of molecules from a more strongly bounded state desorbing near 180 K.

#### 8.3.3 Adsorption of Allyl Alcohol

Figure 8.3a illustrates a coverage-dependent IRAS study of allyl alcohol adsorbed on Pd(111) at 120 K. We distinguish between a low coverage range up to of  $3.6 \cdot 10^{14}$  allyl alcohol molecules per  $\text{cm}^2$  and a high coverage regime starting at  $5.4 \cdot 10^{14}$  molecules per  $\text{cm}^2$ . Table 8.3 summarizes the observed IR vibration frequencies for allyl alcohol at low and at high coverages in comparison to previous studies found in literature.

##### allyl alcohol at low coverages

In the low coverage regime, only a small number of IR absorption features in the C–H stretching region are detected. Weak IR vibration features are observed near  $2897 \text{ cm}^{-1}$ ,  $2877 \text{ cm}^{-1}$ , and  $2842 \text{ cm}^{-1}$ . We tentatively assign the two higher wavenumber peaks to  $\text{CH}_2$  asymmetric stretching modes of two different allyl alcohol species and the lower

Table 8.3: Assignment of IR vibrational modes of allyl alcohol on Pd(111) at 120 K.

mode	IRAS vibrations / $\text{cm}^{-1}$		references / $\text{cm}^{-1}$
	low coverage	high coverage	
$\nu(\text{C-O}\dots\text{H})$		3260	3300 [109, 265]
$\nu_a(\text{=CH}_2)$		3092	3124-3099 [260] 3102-3086 [259]
$\nu_s(\text{=CH}_2)$		3013	3034-3010 [260] 2996-2992 [259]
$\nu(\text{CH})$		2989	3033-3011 [260] 3022 [259]
$\nu_a(\text{CH}_2)$	(2897,2877)	2920	2967-2903 [260] 2948-2934 [259]
$\nu_s(\text{CH}_2)$	(2842)	2850-2870	2878-2851 [260] 2880-2854 [259]
$\nu(\text{C=C})$		1648	1655-1644 [260] 1655 [259]
$\delta(\text{CH}_2)$		1470-1495	1500-1482 [260] 1463-1453 [259]
$\delta(\text{=CH}_2)$		1406-1450	1429-1410 [259] 1440-1399 [260] 1450 <sup>1</sup> 1440-1399 [260] 1424 <sup>2</sup> 1440 [260] 1406 <sup>3,4</sup> 1399, 1409 [260]
$\omega(\text{CH}_2)$			1399-1317 [260] 1384-1372 [259]
$\delta(\text{O-H})$		1373-1235	1372-1202 [260] 1328-1321 [259]
$\delta(\text{C-H})$			1281-1272 [260]
$\nu(\text{C-O})$		1113	1111-1033 [260] 1110 [259]
$\omega_T(\text{HC=CH}_2)$		1000	1018-841 [250] 1020-950 [251] 1022-1002 [252] 993 [248] 995-985 [109] 1054-988 [260] 1002-995 [259]

$\nu$ : stretching,  $\nu_a$ : asymmetric stretching,  $\nu_s$ : symmetric stretching,  $\delta$ : bending,  $\omega$ : wagging,  $\omega_t$ : *trans*-wag vibration, <sup>1</sup>: *gauche-trans*, <sup>2</sup>: *gauche-gauche*, <sup>3</sup>: *cis-trans*, <sup>4</sup>: *cis-gauche*

frequency vibration to a CH<sub>2</sub> symmetric stretching vibration. In previous studies on non-adsorbed molecules, the asymmetric stretching was observed at 2967-2903 cm<sup>-1</sup> and the symmetric stretching at 2880-2851 cm<sup>-1</sup> [259, 260].

### allyl alcohol at high coverages

At high coverages, the CH<sub>2</sub> asymmetric and symmetric stretching vibrations are assigned to peaks at 2920 cm<sup>-1</sup> and 2870-2850 cm<sup>-1</sup> and thus at slightly higher wavenumbers than at low coverages. Furthermore, we observe vibrations at 3092 cm<sup>-1</sup>, 3013 cm<sup>-1</sup>, and 2989 cm<sup>-1</sup>. The first one is assigned to the asymmetric stretching of the vinyl-CH<sub>2</sub> group, which was previously observed at 3124-3086 cm<sup>-1</sup> [259, 260]. The latter two are assigned to the vinyl-CH<sub>2</sub> symmetric stretching and CH stretching modes. In literature, the vinyl-CH<sub>2</sub> symmetric stretching was observed at 3034-2992 cm<sup>-1</sup> and the CH stretching was found at 3033-3011 cm<sup>-1</sup> and thus in the same frequency range as in our studies [259, 260]. Finally, the very broad and intense IR absorption near 3260 cm<sup>-1</sup> strongly points to O-H stretching in hydrogen bonded OH groups. It was reported in previous publications near 3300 cm<sup>-1</sup> [109, 265].

The C=C stretching vibration can only be observed at high coverage. It appears at 1648 cm<sup>-1</sup> and thus 30 cm<sup>-1</sup> higher as compared to acrolein. In previous studies on allyl alcohol, the C=C stretching vibration was reported at 1655-1644 cm<sup>-1</sup> [259, 260].

The features from 1495 cm<sup>-1</sup> to 1406 cm<sup>-1</sup> are assigned to CH<sub>2</sub> scissor vibrations. We relate the higher frequencies at 1470-1795 cm<sup>-1</sup> to the alkyl-CH<sub>2</sub> group, while we assign the lower frequencies from 1406-1450 cm<sup>-1</sup> to the vinyl-CH<sub>2</sub> group. In literature, scissor deformations of the alkyl-CH<sub>2</sub> group were found at 1500-1453 cm<sup>-1</sup> and of the vinyl-CH<sub>2</sub> group at 1440-1399 cm<sup>-1</sup> [259, 260]. Durig *et al.* predicted theoretically that the vinyl-CH<sub>2</sub> scissor frequency should strongly depend on the molecular conformation [260]. According to their results, we tentatively assign the vibration at 1406 cm<sup>-1</sup> to the *cis-trans* and *cis-gauche* conformer, the absorptions at 1424 cm<sup>-1</sup> to the *gauche-gauche* and the vibration at 1450 cm<sup>-1</sup> to the *gauche-trans* species. Multiple IR adsorption features are observed between 1373 cm<sup>-1</sup> and 1235 cm<sup>-1</sup>, which we assign to CH<sub>2</sub> wag as well as =C-H and O-H bend vibrations. In previous studies, the exact vibration frequencies were found to depend on the conformation of the molecule [260]. Moreover, the pronounced vibration at 1113 cm<sup>-1</sup> strongly points to C-O stretching vibration, which was reported in literature between 1033 cm<sup>-1</sup> and 1111 cm<sup>-1</sup> [259, 260]. The very strong IR absorption near 1000 cm<sup>-1</sup> is assigned to the CH=CH<sub>2</sub> *trans-wag* vibration, which is discussed in more detail for acrolein.

### TPD of allyl alcohol at multilayer coverage

Figure 8.3b shows the result of a TPD experiment of  $2.3 \cdot 10^{15}$  allyl alcohol molecules / cm<sup>2</sup> on Pd(111), which corresponds to the highest coverage studied by IRAS. Desorption of allyl alcohol, propanal, acrolein, and hydrogen has been investigated. Allyl alcohol is detected at 175 K and 200 K, neither propanal nor acrolein are observed. Similar to our

studies on propanal and acrolein, a significant amount  $\text{H}_2$  appears in the gas-phase in a desorption-limited feature around 325 K and in a reaction-limited process near 465 K.

## 8.4 Discussion

### Acrolein on Pd(111)

The coverage-dependent IRAS studies show the formation of different types of acrolein on Pd(111) with characteristic IR vibration frequencies, especially of the C=O stretching,  $\text{CH}_2$  scissor, and  $\text{HC}=\text{CH}_2$  *trans-wag* vibrational modes. The sub-monolayer species A and B are observed on the surface at coverages below  $3.6 \cdot 10^{14}$  molecules/ $\text{cm}^2$ , which corresponds approximately to one acrolein molecule per four Pd surface atoms. Near  $3.6 \cdot 10^{14}$  molecules/ $\text{cm}^2$ , the formation of a less strongly perturbed adsorbates (species C) indicates the transition from the sub-monolayer regime to the full-monolayer coverage. At higher coverages, the formation of acrolein multilayers is evidenced by the mainly unperturbed molecular structures of species D.

At low coverages, we have identified sub-monolayer species with weak IR absorption of  $\text{CH}_2$  deformation modes; however, there is no signal of the C=O, C=C, or C–C bonds and no IR absorption in the range of C–H stretching vibrations. This intensity ratio is in sharp contrast to the spectra of unperturbed molecules, *e.g.* acrolein type D. The absence of further IR vibration features indicates that the other chemical bonds are either strongly perturbed or cannot be detected because of the MSSR or their IR absorption is too weak due to small dynamic dipole moments and a low surface concentration. Tentatively, we distinguish between two sub-monolayer species, A and B. The  $\text{CH}_2$  scissor vibration frequency of species A appears significantly shifted as compared to unperturbed acrolein molecules, while the same vibrational mode of species B is observed at the identical frequency as in acrolein ice and gas-phase acrolein. The presence of a mainly unperturbed  $\text{CH}_2$  vibration of species B tentatively indicates an intact molecular structure of this adsorbate. The decreased  $\text{CH}_2$  scissor vibration frequency of species A, in contrast, points to a perturbed molecular structure of this adsorbate. However, it should be noted that the IR absorption features of the sub-monolayer species are very weak and a clear identification of the molecular structure of the adsorbates is not possible. Hence, the most reliable information obtained by the IR studies at sub-monolayer coverages may rather be related to the adsorbates' geometry than to their exact molecular structure. The absence of the C=O, C=C, and C–C bond stretching vibration signals reveals a flat-lying molecular plane on the Pd(111) surface.

At the exposure  $3.6 \cdot 10^{14}$  acrolein molecules/ $\text{cm}^2$ , species C appears on the surface. On the one hand, a clearly detectable C=O stretching vibration shows a significant tilting of this group with respect to the metal surface. On the other hand, a significantly lower vibration frequency as compared to acrolein type D points to a weakening of the C=O bond and thus to a strong interaction of this group with the metal surface. Remarkably, the C=O stretching frequency is identical to that of the C=O bond of propanal near the monolayer coverage. This observation indicates that the conjugated  $\pi$  system of acrolein

is strongly distorted by the Pd surface so that the chemical structure of the C=O bond is rather similar to that of a non-conjugated C=O bond. Note that species C is only formed in a very narrow coverage range close to one acrolein molecule per four Pd surface atoms. We relate this coverage to the formation of a complete monolayer. TPD studies of one acrolein on four Pd atoms show decomposition of the entire amount of molecules indicating that the whole layer is in strong contact with the surface. Interestingly, this is exactly the same surface coverage at which we previously observed significant changes in the selectivity and activity of Pd(111) as catalysts in partial selective hydrogenation of acrolein [185] (see Chapter 9. Our previous studies at elevated temperatures showed that the initially adsorbed acrolein is irreversibly adsorbed and converted to a spectator governing the selectivity towards C=O bond hydrogenation. Moreover, previous DFT calculations indicate that acrolein may adsorb on a Pd(111) surface in a way that it blocks four Pd atoms [245]. We conclude that approximately one acrolein molecule per four Pd surface atoms forms a roughly homogeneously distributed and strongly bonded monolayer of flat-lying molecules.

Finally, species D is getting formed on the surface at multilayer coverages. The IR vibrations appear at similar frequencies as reported in literature for gas-phase acrolein. Therefore, the IR spectrum of species D provides a good reference for vibrations of mainly unperturbed adsorbed molecules.

Comparison of the C=O and C=C stretching frequencies of acrolein species D to the C=O and C=C stretching frequencies of propanal and allyl alcohol at multilayer coverages show that both  $\pi$  bond vibration appear at lower wavenumbers in the conjugated  $\pi$  system.

### Propanal on Pd(111)

The strong coverage-dependent vibration frequencies of propanal give detailed insights into molecular structures of propanal on Pd(111). Characteristic vibration frequencies are observed at sub-monolayer coverages pointing to a strong interaction between propanal and Pd while IR vibration frequencies at multilayer coverages indicate mainly unperturbed molecules. Similar to acrolein, we observe the transition from the sub-monolayer to multilayer regime in the range from  $3.6 \cdot 10^{14}$  to  $5.4 \cdot 10^{14}$  molecules/cm<sup>2</sup>.

In contrast to acrolein, a large number of IR vibrational modes are identified already at sub-monolayer coverages providing detailed information on the effect of Pd on CH<sub>3</sub>, CH<sub>2</sub>, CH, C–C, and C=O bonds. On the one hand, the pronounced coverage-dependent changes of the C=O stretching vibration frequency points to a strong interaction of the C=O group by the metal surface. In particular, a very strong binding between propanal and Pd(111) is indicated by a major weakening of the C=O bond at sub-monolayer coverages. However, some uncertainties remain about the interpretation of the absorption at 1560 cm<sup>-1</sup>. Nevertheless, near the full monolayer coverage, a more clearly assigned C=O stretching vibration points to a strong interaction of the Pd surface via a significantly inclined C=O bond. On the other hand, detection of a C=O stretching vibration at sub-monolayer coverage shows that the C=O bond has to be inclined with respect to

the metal surface.

Moreover, significant differences between acrolein and propanal are observed in the region of the C–H stretching vibrations. On the one hand, these vibrations cannot be identified at sub-monolayer coverages of acrolein while C–H stretching modes are clearly identified already at the lowest coverage of propanal. This observation indicates a different ordering of the  $\text{CH}_x$  groups of propanal and acrolein on the Pd surface. On the other hand, the C–H stretching vibrations of propanal appear at significantly higher wavenumbers as compared to acrolein. While all IR absorption features in acrolein appear below  $2860\text{ cm}^{-1}$ , most of the C–H stretching vibrations in propanal are observed clearly above  $2860\text{ cm}^{-1}$ . Both the different intensities as well as the significantly different frequencies of the C–H stretching vibrations in the two compounds can be of advantage in IRAS studies monitoring the surface processes in the course of acrolein hydrogenation on Pd catalysts.

In the coverage range from  $3.6 \cdot 10^{14}$  to  $5.4 \cdot 10^{14}$  molecules/ $\text{cm}^2$ , significant changes of IR absorption features related to C–H and C=O bonds are related to the saturation of the first monolayer of propanal on Pd(111). Vibrational modes that indicate the sub-monolayer regime saturate while new IR vibrations appear at frequencies pointing to more unperturbed chemical bonds. Thus, the formation of a full monolayer of propanal is completed at roughly the same surface concentration as observed for acrolein. At higher coverages, IR vibration frequencies appear close to the values reported for propanal in the gas phase. In the region of the C=O stretching vibrations, however, two IR absorption features appear simultaneously at  $1728\text{ cm}^{-1}$  and  $1695\text{ cm}^{-1}$ , indicating the formation of two different propanal species in the multilayer regime.

TPD experiments of propanal at multilayer coverage show desorption of intact propanal and hydrogen, both in two well-separated peaks. Hydrogen evolution strongly indicates a sequential decomposition of a fraction of the propanal molecules. The desorption-limited  $\text{H}_2$  evolution can be explained by partial dehydrogenation of propanal molecules below 340 K. The high-temperature  $\text{H}_2$  peak, however, must result from further dehydrogenation steps near 470 K. Coverage-dependent TPD data are not available. However, we tentatively relate the  $\text{H}_2$  formation to decomposition of strongly bonded molecules, most likely from the first monolayer. Moreover, the low-temperature propanal desorption is assigned to weakly attached molecules in the multilayer, possibly the multilayer giving rise to the IR absorption near  $1728\text{ cm}^{-1}$ . The higher temperature propanal desorption points to more strongly attached molecules, possibly from the multilayer species with C=O stretching vibration at  $1695\text{ cm}^{-1}$  or the species which is formed near the full-monolayer coverage with C=O stretching at  $1663\text{ cm}^{-1}$ .

### **Allyl Alcohol on Pd(111)**

Identification of allyl alcohol at small concentrations (up to  $3.6 \cdot 10^{14}$  molecules/ $\text{cm}^2$ ) on the Pd(111) surface by IRAS is difficult. Only weak IR absorption features related to C–H stretching vibrations are detected. Weak IR vibration features can have multiple reasons, such as small dynamic dipole moments or dipoles mostly parallel to the metal

surface. While the polarity of C–H and C–C bonds is small, C–O and O–H bonds have a strong dynamic dipole moment. Hence, the absence of IR absorption features related to the C–O and O–H stretching vibrations at low coverages suggests flat-lying C–O–H bonds.

At allyl alcohol coverages higher than  $3.6 \cdot 10^{14}$  molecules/cm<sup>2</sup>, a large number of distinct IR absorption features appear at similar frequencies as reported for allyl alcohol in literature. This observation suggests a transition from the monolayer to multilayer regime in the range of  $3.6 \cdot 10^{14}$  to  $5.4 \cdot 10^{14}$  allyl alcohol molecules per cm<sup>2</sup> and thus approximately at the same surface coverage as determined for acrolein and propanal.

TPD studies on multilayers of allyl alcohol on Pd(111) show desorption of intact allyl alcohol and hydrogen. Both molecules appear in two peaks, as observed for propanal multilayers before. The desorption-limited H<sub>2</sub> evolution indicates partial decomposition of allyl alcohol species at temperatures below 325 K and the reaction-limited H<sub>2</sub> formation points to further dehydrogenation steps near 465 K. Intact allyl alcohol molecules are believed to most likely result from the multilayer regime. However, no coverage dependent TPD data are available.

Interestingly, the high-temperature H<sub>2</sub> desorption in propanal and allyl alcohol TPD experiments appears approximately at the same temperature. This observation indicates that the hydrocarbon fragments staying on the surface up to 470 K might be identical for both molecules propanal and allyl alcohol.

## 8.5 Conclusions

We have investigated the adsorption of acrolein, propanal and allyl alcohol on Pd(111) in detail mainly by IRAS studies with the support of TPD experiments. The coverage-dependent evolution of IR vibrational bands provides deep insights into the adsorbates structure on Pd(111). For all three compounds, we have found mostly unperturbed molecular structures in the multilayer regime and significant effects of the Pd on the chemical bonds of molecules in the first monolayer. A transition from the sub-monolayer to the multilayer regime has been observed in the range from  $3.6 \cdot 10^{14}$  to  $5.4 \cdot 10^{14}$  molecules per cm<sup>2</sup> for all three compounds.

The most detailed assignment of surface species has been achieved for acrolein. We have identified the sub-monolayer species A and B, the monolayer species C, and the multilayer species D. The sub-monolayer species seems to adsorb with C=O, C=C and C–C bonds parallel to the metal surface. Remarkably, only deformation vibrations involving the =CH<sub>2</sub> group have been observed at sub-monolayer coverages. Species C, in contrast, has a strongly inclined C=O bond, which is significantly weakened by the Pd surface as compared to the C=O bond of the multilayer species D. Identical C=O stretching frequencies of acrolein species C and propanal at monolayer coverage points to a strongly distortion of the conjugated  $\pi$  system. At higher coverages, the mainly unperturbed species D is formed. A large number of distinct IR vibration modes have been identified for species D. Further propanal species are observed at multilayer coverages.

The IR studies on propanal point to different surface species in three coverage regimes, at sub-monolayer, full-monolayer, and multilayer coverages. In the sub-monolayer regime, a tentatively assigned C=O stretching vibrations indicates a strong interaction of Pd with the C=O bond as well as a significant inclination of the C=O bond with respect to the surface. Moreover, a large number of C–H stretching and deformation vibrations appear already in the IR spectra obtained at low sub-monolayer coverages. Near the full-monolayer coverage a propanal species with less strongly, but still significantly perturbed C=O bond is observed.

In the case of allyl alcohol, identification of adsorbates at low coverages is difficult due to weak IR absorption. We have been able to identify a few C–H vibration features in the low-coverage regime. With increasing coverage, however, a transition to the multilayer regime has been detected and a large number of distinct IR vibrational modes have been identified.

We found pronounced differences in the adsorbates' structures of acrolein, propanal and allyl alcohol on the Pd(111) surface. While sub-monolayer acrolein species adsorb with the molecular chain parallel to the surface, propanal adsorbs in a tilted geometry with respect to Pd(111) surface plane, interacting with the surface primarily through the C=O group. Propanal at sub-monolayer coverages gives rise to a C=O vibrational peak that points to a considerable weakening and tilting of the C=O bond. In contrast, the C=O bond in acrolein cannot be identified in IRAS studies, most likely because of a parallel orientation with respect to the Pd surface. Moreover, C–H stretching vibrations cannot be observed for the sub-monolayer species of acrolein, while the C–H vibrational peaks of propanal grow roughly monotonically over the whole coverage range, which might point to less perturbed C–H bonds or different geometric ordering of both molecules on the surface. The strong changes of the adsorbates structure from the unsaturated to the saturated aldehyde is expected to play a crucial role in explaining the selectivity of C=C vs. C=O bond hydrogenation in  $\alpha,\beta$ -unsaturated aldehydes. Furthermore, the pronounced differences in the IR spectra of propanal and acrolein can be of advantage to distinguish between both compounds on a Pd catalysts' surface and thus to determine the kinetics of surface processes in the course of acrolein hydrogenation.

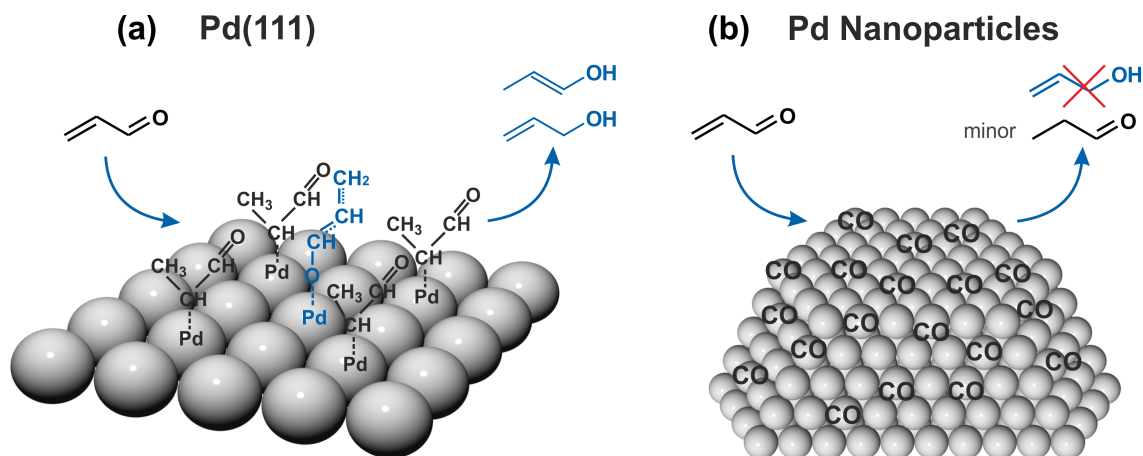
## 9 Spectators control Selectivity in Surface Chemistry: Acrolein partial Hydrogenation over Pd

*Karl-Heinz Dostert<sup>1</sup>, Casey P. O'Brien<sup>1</sup>, Francisco Ivars-Barceló<sup>1</sup>, Swetlana Schauermann<sup>1,2</sup>, and Hans-Joachim Freund<sup>1</sup>*

<sup>1</sup>Fritz-Haber-Institut der Max-Planck-Gesellschaft, Faradayweg 4-6, 14195 Berlin, Germany

<sup>2</sup>Institut für Physikalische Chemie, Christian-Albrechts-Universität zu Kiel, Max-Eyth-Str. 1, 24118 Kiel, Germany

published in *J. Am. Chem. Soc.*, **2015**, *137* (42), 13496-13502

**Abstract**

We present a mechanistic study on selective hydrogenation of acrolein over model Pd surfaces – both single crystal Pd(111) and Pd nanoparticles supported on a model oxide support. We show for the first time that selective hydrogenation of the C=O bond in acrolein to form an unsaturated alcohol is possible over Pd(111) with nearly 100% selectivity. However, this process requires a very distinct modification of the Pd(111) surface with an overlayer of oxopropyl spectator species that are formed from acrolein during the initial stages of reaction and turn the metal surface selective towards propenol formation. By applying pulsed multi-molecular beam experiments and in-situ infrared reflection-absorption spectroscopy we identified the chemical nature of the spectator and the reactive surface intermediate (propenoxy species) and experimentally followed the simultaneous evolution of the reactive intermediate on the surface and formation of the product in the gas phase.

## 9.1 Introduction

Selective partial hydrogenation of multi-unsaturated hydrocarbons, particularly  $\alpha,\beta$ -unsaturated ketones and aldehydes, is of a pivotal importance for numerous applications of heterogeneous catalysis related to fine chemical and pharmaceutical industries. Among the most useful target products in transformations of multi-unsaturated oxygenates are unsaturated alcohols produced by heterogeneous chemoselective hydrogenation of the C=O bond in unsaturated ketones and aldehydes [27, 28]. Generally, thermodynamics favors hydrogenation of the C=C bond in these compounds to form the unwanted product, i.e. saturated aldehydes or ketones. Therefore chemoselective hydrogenation of the C=O bond requires manipulation of kinetic effects by means of a suitable catalyst. This task represents a challenging problem and asks for fundamental studies.

A variety of powdered supported metal catalysts have been already investigated to understand the activity and selectivity of this reaction [27, 28]. As key structural parameters controlling the chemoselectivity, a series of ideas conceiving the amount of steric hindrance to adsorption via the C=C bond [32], presence of surface modifiers [178, 179] or alloying with other metals [47] have been put forward. Complementary, some theoretical work and model studies have been presented in order to understand the chemoselectivity of the underlying elementary processes [52, 60, 180–184]. Despite these efforts, a deep fundamental understanding of this reaction and the parameters governing its activity and selectivity is still missing. Particularly, it remains unclear how the C=O bond is activated on a transition metal surface and what are the structures of the surface intermediates formed under the reaction conditions. To extract this information on the reaction intermediates would be particularly important for approaching a rational design of new catalytic materials for this class of reactions.

In this communication, we present a mechanistic study on selective hydrogenation of the smallest  $\alpha,\beta$ -unsaturated aldehyde acrolein over model Pd surfaces – both single crystal Pd(111) and Pd nanoparticles supported on an planar oxide support – under well-defined ultra high vacuum (UHV) conditions. Previously, acrolein was reported to be hydrogenated almost exclusively on the C=C bond over powdered Pd catalysts forming propanal [28]. In this communication, we show for the first time that selective hydrogenation of the C=O bond in acrolein with nearly 100% selectivity is possible over Pd(111). However, this process requires a very distinct modification of the surface with a spectator species that turns the surface selective towards unsaturated alcohol formation. This densely packed overlayer of spectator species is formed from acrolein during the initial stages of surface reaction. By applying a combination of multi-molecular beam techniques and in-situ infrared reflection-absorption spectroscopy (IRAS) we were able to identify the chemical nature of the spectator and the reactive surface intermediate and for the first time experimentally follow the simultaneous evolution of the reactive intermediate on the surface and formation of the product in the gas phase. With this study it has been possible to directly identify the reaction intermediate that leads to the formation of the unsaturated alcohol as a final product and obtain atomistic-level insights into the chemoselective hydrogenation chemistry of acrolein. Spectator species were found to play

an important role in governing chemoselectivity – the observation that might be of great interest for development of new chemo- and enantio-selective powdered catalysts such as *e.g.* ligand-modified nanoparticles [266].

## 9.2 Experimental

All experiments were performed at the Fritz-Haber-Institut, Berlin, in a UHV-apparatus that has been described in detail previously [100]. Two effusive doubly differentially pumped multi-channel array source operated at room temperature were used to supply acrolein and H<sub>2</sub>. Beam intensities of  $4.8 \cdot 10^{15}$  molecules/(cm<sup>2</sup>s<sup>-1</sup>) for H<sub>2</sub> and  $0.6 \cdot 10^{13}$  or  $1.5 \cdot 10^{13}$  molecules/(cm<sup>2</sup>s<sup>-1</sup>) for acrolein (Fluka, 98% purity) were used in these experiments.

The Pd(111) single crystal was cleaned prior to use by repeated cycles of Ar<sup>+</sup> ion bombardment at room temperature, annealing at 1000 K and oxidation in  $1 \cdot 10^{-6}$  mbar O<sub>2</sub> at 750 K to remove residual carbon.

The supported Pd/Fe<sub>3</sub>O<sub>4</sub> model catalyst was prepared as follows: the thin ( $\approx 100$  Å) Fe<sub>3</sub>O<sub>4</sub> film was grown on a Pt(111) single crystal surface by repeated cycles of Fe (>99.99%, Goodfellow) physical vapor deposition and subsequent oxidation [138, 142]. Pd particles (>99.9%, Goodfellow) were grown by physical vapor deposition using a commercial evaporator (Focus, EFM3, flux calibrated by a quartz microbalance) while keeping the sample temperature fixed at 115 K. During Pd evaporation the sample was biased to 850 V in order to avoid the creation of defects by metal ions. The final Pd coverage used in these experiments was 7 Å. The resulting surfaces were then annealed to 600 K, and stabilized via cycles of oxygen ( $8 \cdot 10^{-7}$  mbar for 1000 s) and CO ( $8 \cdot 10^{-7}$  mbar for 3000 s) exposures at 500 K until the Pd particles reached a stable geometry with an average size of 12 nm [152, 153]. Residual oxygen was removed by heating in CO ( $1 \cdot 10^{-6}$  mbar for 300 s,) followed by flash-annealing in UHV to 485 K. The STM image of the resulting Pd/Fe<sub>3</sub>O<sub>4</sub>/Pt(111) model catalyst is shown in Figure 9.6 in the Supporting Information. That surface displays Pd particles with an average diameter of 12 nm containing approximately 8100 atoms each, and covering the support uniformly with an island density of about  $6 \cdot 10^{11}$  islands/cm<sup>2</sup>. The majority of the particles are well-shaped crystallites grown in the (111) orientation and are predominantly terminated by (111) facets (80%), but a small fraction of (100) facets (20%) is also exposed.

IRAS data were acquired using a vacuum Fourier-Transform Infrared (FT-IR) spectrometer (Bruker IFS 66v/S) with a spectral resolution of 2 cm<sup>-1</sup> and using a mid-infrared (MIR) polarizer and p polarized IR light. An automated quadrupole mass spectrometer (QMS) system (ABB Extrel) was employed for the continuous monitoring of the partial pressures of the reactants and products.

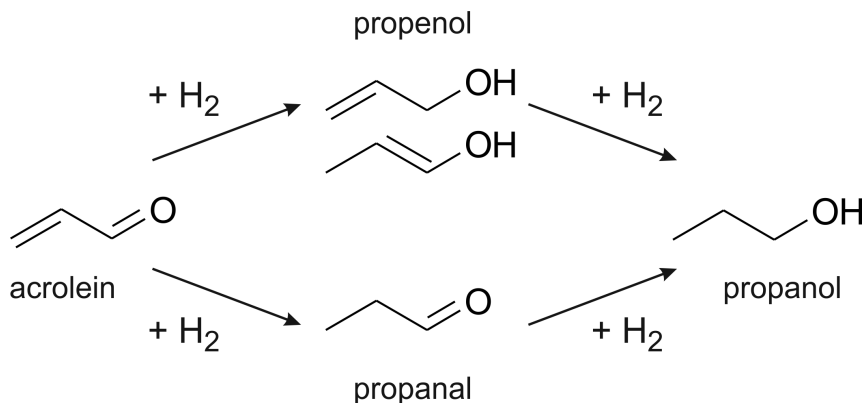


Figure 9.1: Possible reaction pathway of acrolein hydrogenation

### 9.3 Results and Discussion

Selective partial hydrogenation of acrolein was investigated on two well-defined surfaces prepared in-situ under UHV conditions: (i) a single crystal Pd(111) and (ii) 12 nm sized Pd nanoparticles supported on a planar model  $\text{Fe}_3\text{O}_4/\text{Pt}(111)$  oxide support [153]. The catalytic activity of these surfaces was probed under isothermal conditions by using molecular beams [100] with the simultaneous monitoring of the species evolving on the catalytic surface turning over by IRAS. Figure 9.2 shows the possible reaction pathways of acrolein hydrogenation.

The two investigated catalyst systems were found to show very different selectivity in partial acrolein hydrogenation. Figure 9.2 shows the formation rates of competing reaction pathways resulting in selective hydrogenation of either the C=C bond to form propanal (Fig. 9.2a and 9.2b) or the C=O bond to form the unsaturated alcohol (Fig. 9.2c or 9.2d) both on model Pd nanoparticles (left side) and Pd(111) (right side) at different temperatures. For each reported curve, the surface was pre-exposed to a high flux continuous  $\text{H}_2$  beam. At time zero the second molecular beam was opened to give a series of acrolein pulses and the formation rates of reaction products were recorded in the gas phase by quadrupole mass spectrometry. For all investigated catalysts, a short induction period preceded the onset of product formation. On the Pd nanoparticles we observed the only product – propanal – in the first few pulses, after which the reaction rate dropped to zero; no hydrogenation of C=O bond was detected. This behavior is in a good agreement with the results of the earlier studies on powdered Pd catalysts under ambient conditions, showing that essentially only the C=C bond can be hydrogenated [28, 45]. Very surprisingly, Pd(111) showed very high catalytic activity towards the desired reaction product – propenol (Fig. 9.2d). The propenol formation rate exhibits clear temperature dependence with a maximum of conversion at 270 K. To obtain further atomistic-level insight into this catalytic process, we carried out this experiment on the Pd(111) surface using a continuous exposure of both  $\text{H}_2$  and acrolein via molecular beams and simultaneously recorded the evolution of the species on the surface turning over by IRAS.

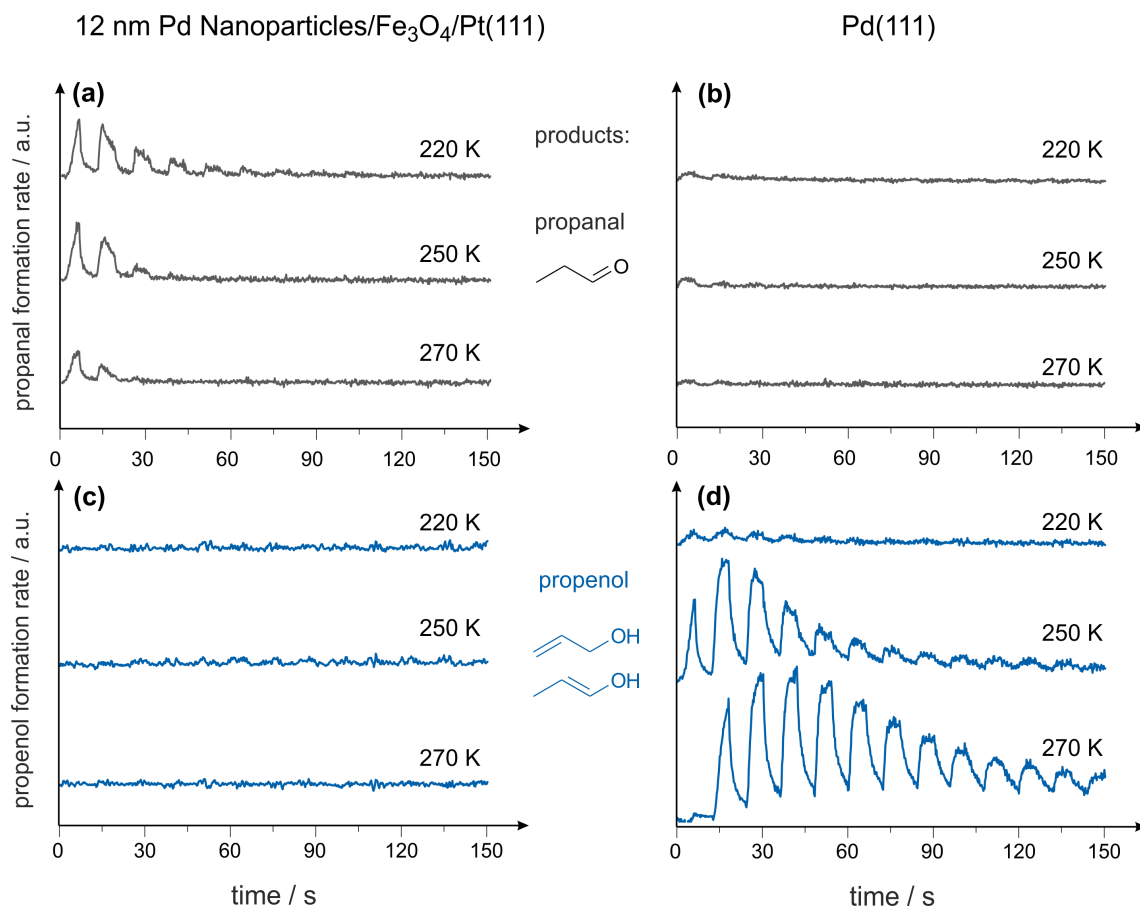


Figure 9.2: Formation rates of the reaction products – propanal (upper row) and propenol (lower row) –on 12 nm-sized supported Pd nanoparticle (a and c) and Pd(111) (b and d) during continuous dosing of H<sub>2</sub> and pulsed dosing of acrolein at different temperatures.

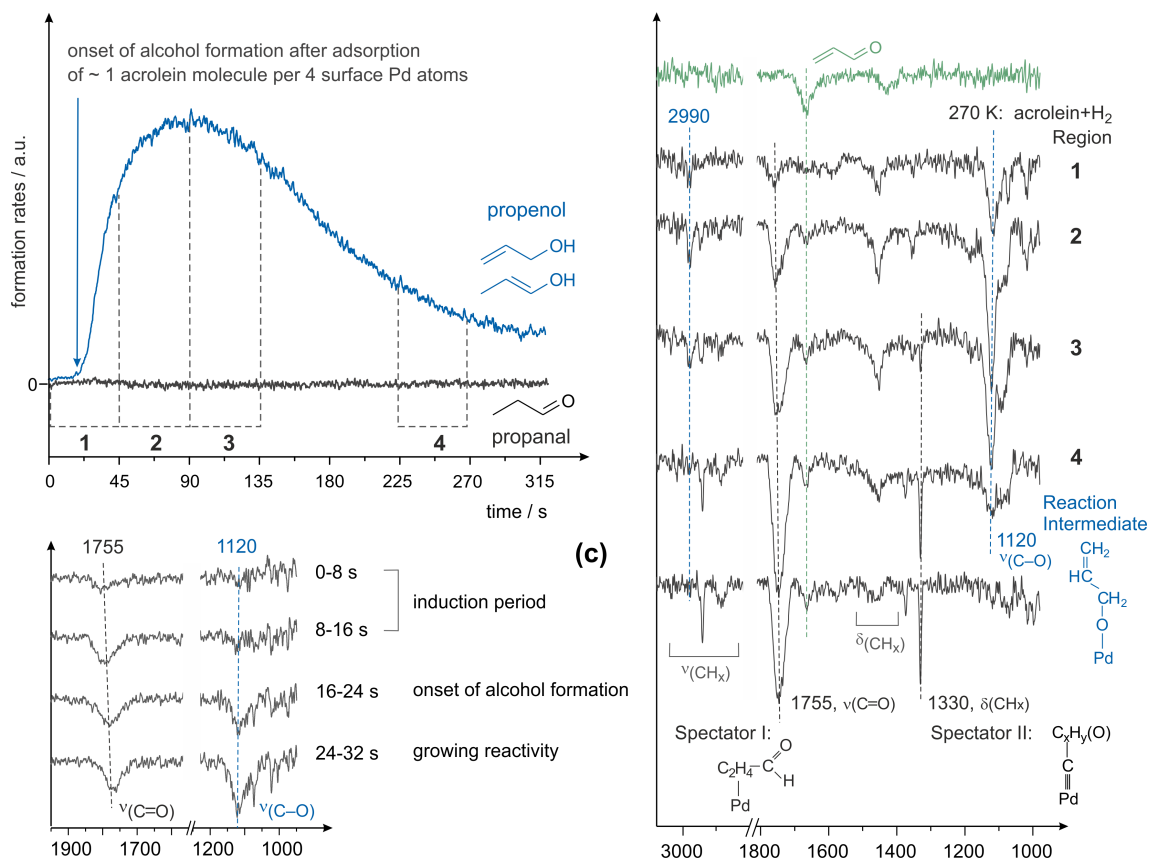


Figure 9.3: (a) Formation rate of propenol (blue line) and propanal (black line) on Pd(111) at 270 K under continuous exposure of H<sub>2</sub> and acrolein. (b) IR spectra obtained for a monolayer of molecularly adsorbed acrolein at 100 K on pristine Pd(111) (green line) and on Pd surface turning over at 270 K during a continuous exposure to acrolein and H<sub>2</sub>. Spectra 1-4 correspond to the regions 1-4 indicated in (a). The lowest spectrum is obtained after 450 s of acrolein exposure after the propenol formation rate has dropped to zero. (c) IR spectra obtained on Pd(111) surface turning over with higher time resolution during the induction period and period of growing reactivity.

Figure 9.3a shows the evolution of the gas phase products – propanal and propenol – over Pd(111) with a continuous reactants exposure at 270 K. Specifically, the surface was pre-exposed with H<sub>2</sub> and then the acrolein beam was switched on at time indicated as zero while the H<sub>2</sub> beam was kept continuously running. Simultaneously, the acquisition of IR spectra started with the time resolution of one spectrum per 45 seconds. Selected IR spectra are shown in Figure 9.3b (labeled 1 to 4), which correspond to the time regions 1-4 indicated in Figure 9.3a. In accordance with the reactivity behavior in a pulsed experiment (Fig. 9.2d), an onset of the propenol formation rate is observed after an induction period of approximately 24 seconds, in which about one acrolein molecule per four Pd atoms on average is irreversibly adsorbed onto the surface. At the end of the induction period the propenol formation rate quickly rises followed by a reactivity decrease after about 95 seconds. The first three IR spectra (1-3) shown in Figure 9.3b are obtained during the initial induction period and the period of the maximal activity, while spectrum 4 was collected during the period of decreasing reactivity. The lowest IR spectrum in Figure 9.3b shows the composition of the surface after its complete deactivation. As a reference for an intact molecule, the IR spectrum of acrolein adsorbed on Pd(111) at 100 K is shown as the uppermost green trace.

Analysis of the IR spectra obtained on the Pd(111) surface under reaction conditions allows us to determine the composition of the active surface turning over and the nature of the reactive intermediate, resulting in formation of propenol. Three major groups of bands corresponding to different surface species can be identified. First, the bands at 1660 cm<sup>-1</sup> and 1755 cm<sup>-1</sup> correspond to the stretching vibration of the C=O bond [181, 182, 213]. While the band at 1660 cm<sup>-1</sup> originates from the adsorbed intact acrolein molecule, in which the C=O bond is still conjugated to the C=C double bond [182, 213] (also see comparison with the uppermost spectrum of intact acrolein), the higher frequency band at 1755 cm<sup>-1</sup> is indicative of the surface species containing the C=O bond not conjugated to the C=C bond anymore [109, 240]. The appearance of this vibration under reaction conditions points to the formation of the oxopropyl surface species, resulting from the partial hydrogenation of acrolein molecule with only one H atom attached to the C=C bond. One of the possible structures of this species is shown in Figure 9.3b next to the vibrational band at 1755 cm<sup>-1</sup>. The present data do not allow us to make a more precise conclusion on whether the original acrolein molecule was partly hydrogenated on the second or third carbon atom to form this species. Remarkably, this band already appears at very early stages of the reaction, grows in intensity and remains intense even after the reaction rate recorded in the gas phase vanishes. This observation strongly suggests that this species is not the reaction intermediate leading to the final gas phase product propenol but is merely a spectator (referred in the following as spectator I).

The second prominent band is the very intense vibration at 1120 cm<sup>-1</sup>. Note that this frequency is present neither in adsorbed intact acrolein on Pd (Fig. 9.3b) nor in acrolein ice [181] and therefore cannot be related to any prominent vibration of the molecularly adsorbed acrolein. Further, this band appears only under the reaction conditions: in presence of H<sub>2</sub> in the temperature range 220-290 K. The most striking observation of this study is that the evolution of this vibrational band shows strong correlation with the evolution

of propenol in the gas phase. Indeed, this band starts to appear in the region 1, which comprises the induction period and the region of growing reaction rate (Fig. 9.3a); then grows in intensity in regions of the highest reactivity 2 and 3. Consecutively, the intensity of this band strongly decreases in region 4 accompanied by the decrease of the propenol formation rate in the gas phase and completely disappears in the lowest spectrum of Figure 9.3b showing the region of zero reactivity. A few other IR bands in the region of  $\text{CH}_x$  stretching and bending vibrations can also be correlated to the gas phase formation rate of propenol.

The observed strong correlation between the gas phase formation rate of propenol and the evolution of the vibrational band at  $1120\text{ cm}^{-1}$  unambiguously shows that the corresponding surface species is the surface intermediate that is directly involved in the selective hydrogenation of the  $\text{C}=\text{O}$  bond. To the best of our knowledge, this is the first direct experimental observation of such a direct correlation between the evolution of the product in the gas phase and the formation of the corresponding reaction intermediate on the surface obtained under the well-defined and isothermal conditions.

The vibrational range  $1050\text{--}1200\text{ cm}^{-1}$  is typical for the stretching vibration of a single  $\text{C}-\text{O}$  bond in an alkoxy group. Previously, a large class of oxygen coordinated surface adsorbates has been observed in this vibrational region [267, 268]. In our case, the most likely species related to the band at  $1120\text{ cm}^{-1}$  is a propenoxy-group  $\text{CH}_2=\text{CH}-\text{CH}-\text{O}-\text{Pd}$ , in which the  $\text{C}-\text{O}$  entity is attached to Pd through the O atom to form a single  $\text{C}-\text{O}$  bond. The high intensity of this band, exceeding even the most intense  $\text{C}=\text{O}$  vibration in acrolein ( $1660\text{ cm}^{-1}$ ) and oxopropyl species ( $1755\text{ cm}^{-1}$ ; regions 2 and 3, Fig. 9.3b), additionally supports formation of a single  $\text{C}-\text{O}$  bond, which has a large dipole moment that can explain very high IR intensity. The vibrational band at  $2990\text{ cm}^{-1}$ , that also can be directly correlated to the evolution of propenol in the gas phase, might be indicative of the stretching vibration of the  $\text{C}-\text{H}$  entity, in which C is involved in the  $\text{C}=\text{C}$  double bond [60], suggesting that the reaction intermediate contains a  $\text{C}=\text{C}$  bond. Please note that the high intensity of the  $\text{C}-\text{O}$  bond vibration indicates that  $\text{C}-\text{O}$  entity is not lying flat on the surface since otherwise this vibration would be not seeing due to the metal surface selection rule [106]. This consideration also implies that the  $\text{C}=\text{C}$  bond cannot be in the very close proximity to Pd and is most likely is not directly involved into the interaction with the surface.

The most likely reaction intermediate consistent with all observed vibrational signatures is shown in Figure 9.3b next to the band at  $1120\text{ cm}^{-1}$ . It contains the  $\text{C}=\text{C}$  bond and is attached to Pd via O forming the  $\text{C}-\text{O}-\text{Pd}$  bond. This intermediate can be formed though adsorption of acrolein via the  $\text{C}=\text{O}$  bond and the addition of one H atom at the C next to O. Only one additional step – the insertion of the second H atom into the  $\text{Pd}-\text{O}$  bond – is required to form propenol.

The third prominent band appears at  $1330\text{ cm}^{-1}$  during the period of highest reactivity and steadily grows in intensity, remaining intense even after the complete stop of the reaction. This band was previously related to formation of ethylidyne and ethylidyne-like

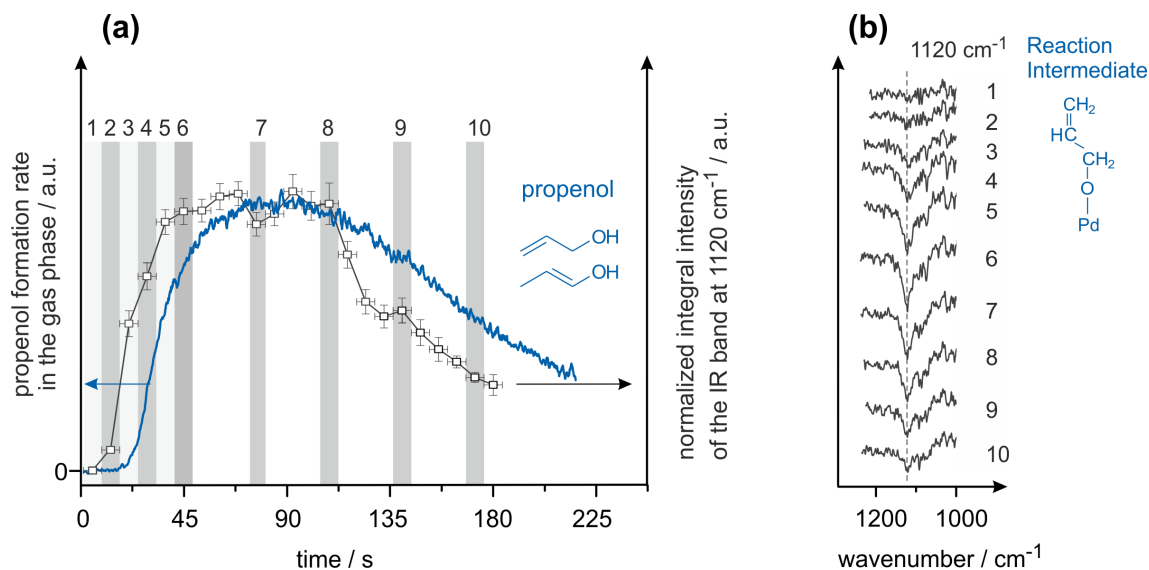


Figure 9.4: (a) Correlation between the formation rate of propenol in the gas phase (blue line) and the evolution of the integral intensity of the band at  $1120\text{ cm}^{-1}$  related to the surface reaction intermediate (black symbols) measured over Pd(111) at 270 K. (b) The corresponding IR spectra obtained on the Pd(111) surface turning over.

species [269]. This species can be considered only as the second type of spectator (spectator II) or a surface poison.

IR spectra obtained with  $\approx 6$  times higher time resolution clearly show that the spectator I is formed on the surface prior the onset of formation of the reaction intermediate (Fig. 9.3c.) The first two spectra, corresponding to the induction period (0-16 s), directly show that first spectator I (band at  $1755\text{--}1790\text{ cm}^{-1}$ ) is formed followed by formation of the propenoxy reaction intermediate ( $1120\text{ cm}^{-1}$ ) close to the onset of propenol evolution in the gas phase. Figure 9.4a shows the gas phase formation rate of propenol (blue line) together with the integral intensity of the vibration band  $1120\text{ cm}^{-1}$  (black squares) of all IR spectra obtained with a high time resolution. The corresponding IR spectra are displayed in Figure 9.4b. As clearly seen, the integral intensity of the vibrational band  $1120\text{ cm}^{-1}$ , related to the proposed reaction intermediate, directly follows the evolution of the product in the gas phase. This strong correlation between the evolution of the reaction rate in the gas phase and the band at  $1120\text{ cm}^{-1}$  is a clear indication for the interrelation of the gas phase product and the proposed reaction intermediate.

It is important to underline that the surface reaction intermediate is formed not on the clean Pd(111) surface but on the surface strongly modified with spectator I (oxopropyl species). Indeed, about one acrolein molecule per four surface Pd atoms was accumulated on the Pd(111) surface to form a dense overlayer of spectator I species prior to the onset of propenol formation. Most likely, such strong geometrical confinement of an adsorption

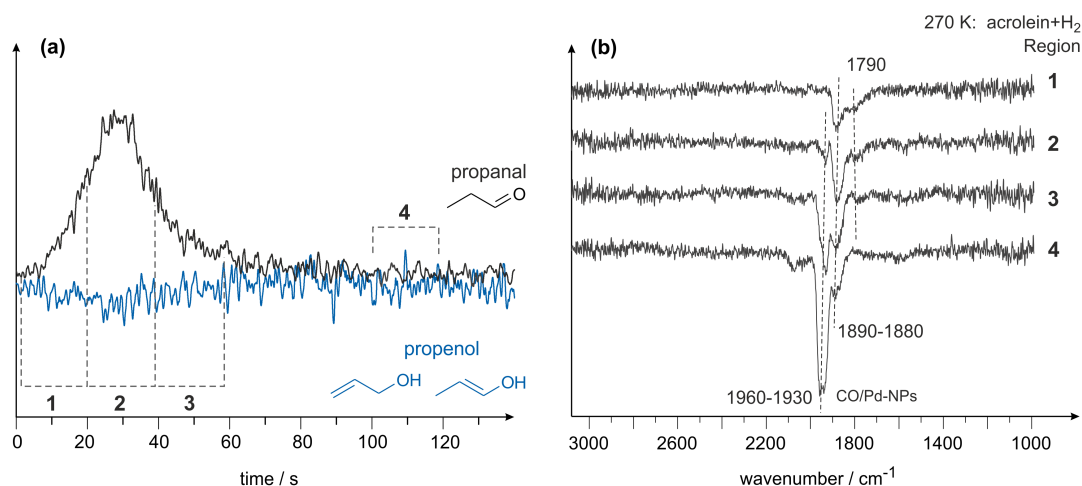


Figure 9.5: (a) Formation rate of propenol (blue line) and propanal (black line) on 12 nm-sized supported Pd nanoparticles at 270 K under continuous exposure of H<sub>2</sub> and acrolein. (b) IR spectra obtained on Pd nanoparticles turning over. Spectra 1-4 correspond to the regions 1-4 indicated in (a).

site for acrolein on the spectator I-covered surface prevents the competing hydrogenation of the C=C bond and allows acrolein to adsorb only via O and to activate the C=O bond. Obviously, the clean Pd surface is not capable of activating the C=O bond towards selective hydrogenation and the strong modification of the surface by spectator I is required to trigger the desired selective chemistry. Formation of the spectator II is correlated with deactivation of the catalytic surface. It might be speculated that it blocks the surface sites that are relevant for the formation of oxopropyl reaction intermediate.

It is important to emphasize that spectroscopic differentiation between the reaction intermediate and the spectator species is possible only if the surface process is carried out in such a way that the reaction intermediate follows a different time dependence than the spectator. Such situation can be achieved *e.g.* in the transient regime applied in this study, in which the spectators were accumulated on the surface, while the concentration of the reaction intermediate was increasing and then decreasing. This fact allowed us to establish the direct correlation between the time evolution of the gas phase product propenol and the surface reaction intermediate propenoxy-group (Fig. 9.4). The more traditional way of carrying out the reaction under the steady state conditions would result in constant concentrations of all surface species and with this prevent their clear assignment to either spectators or reaction intermediates.

To understand the absence of selective acrolein hydrogenation to unsaturated alcohol over Pd nanoparticles, we carried out an identical spectroscopic investigation on the evolution of surface species during the reaction over oxide supported Pd model catalyst with the simultaneous monitoring the gas phase products. Figure 9.5a shows the results of these experiments, for which detailed description we refer the reader to the supporting informa-

tion. The IR spectra obtained on the Pd nanoparticles turning over are dominated by the features in the range 1800-1960  $\text{cm}^{-1}$ , which can be clearly related to an accumulation of CO molecules on the surface that cannot desorb at our low reaction temperatures [270]. This observation suggests that acrolein undergoes decarbonylation on Pd nanoparticles, that was also observed previously on powdered catalysts [181, 182]. Thus, the observed behavior strongly suggests that acrolein decomposes on Pd nanoparticles under the reaction conditions forming CO molecules that block the surface and prevent formation of well-ordered spectator I overlayers required for selective acrolein hydrogenation to propenol. Since the Pd clusters are mostly terminated by (111) facets [153] that are not active in acrolein decomposition as observed for Pd(111), most likely edges, corners, (100) facets and the other low-coordinated surface sites of Pd nanoparticles are responsible for acrolein decarbonylation.

## 9.4 Conclusions

Summarizing, the mechanisms of selective partial hydrogenation of acrolein over two model surfaces – Pd(111) and Pd nanoparticles supported on  $\text{Fe}_3\text{O}_4/\text{Pt}(111)$  film – were investigated using a combination of molecular beam techniques with in situ IRAS under well-defined UHV conditions. The desired reaction pathway – selective hydrogenation of the C=O bond in acrolein to form propenol – was observed over Pd(111) surface with nearly 100% selectivity, while only C=C bond hydrogenation occurred over oxide supported Pd nanoparticles. The selectivity in hydrogenation of the C=O bond was found to critically depend on the presence of an overlayer of spectator species formed at the initial stages of the reaction. Most likely, the spectator, rendering the surface chemoselective, results from the addition of one H atom to the C=C bond of acrolein to form oxopropyl species. After a dense overlayer of the spectator is formed, acrolein adsorbs on this modified surface via the C=O bond and can be selectively hydrogenated to an unsaturated alcohol propenol. The nature of the corresponding surface reaction intermediate was established spectroscopically. By monitoring the surface species during the course of the reaction via IRAS, we were able for the first time to experimentally follow the simultaneous evolution of the reactive intermediate on the surface and formation of the product in the gas phase. With this a direct assignment of one of the surface species to a reaction intermediate was achieved, while the other surface species were identified as spectators. On supported Pd nanoparticles, formation of a spectator overlayer was found to be prevented by strong acrolein decarbonylation and the surface was observed to be active only for hydrogenation of the C=C bond. Obtained atomistic-level insights into chemoselective hydrogenation chemistry of acrolein highlight the exceptional importance of spectator species which are usually formed on the catalytically active surface under reaction conditions. Related effects are expected to play a key role in controlling chemoselectivity in hydrogenation of all types of  $\alpha,\beta$ -unsaturated aldehydes and ketones and hold a great potential for further development of new chemo- and enantio-selective powdered catalysts such as *e.g.*, ligand-modified nanoparticles.

## Author Information

### Corresponding Author

[schauermann@fhi-berlin.mpg.de](mailto:schauermann@fhi-berlin.mpg.de)

**Funding Sources** This work was supported by the European Research Council (ERC Starting Grant ENREMOS, project number 335205)

## Acknowledgement

Support from the European Research Council (ERC Starting Grant ENREMOS, project number 335205) is gratefully acknowledged. S.S. thanks the Fonds der Chemischen Industrie for the Chemiedozentenstipendium.

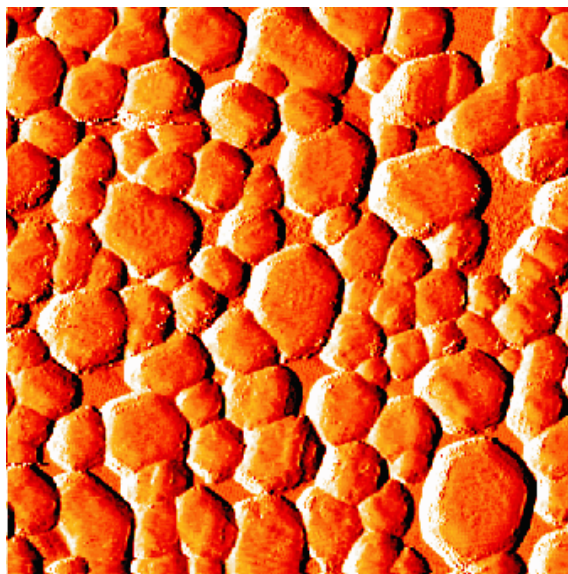


Figure 9.6: STM image of the Pd/Fe<sub>3</sub>O<sub>4</sub>/Pt(111) model catalyst, Pd nominal coverage 7 Å, from [153]

## 9.5 Supporting Information

### Acrolein hydrogenation over model Pd nanoparticles supported on Fe<sub>3</sub>O<sub>4</sub>/Pt(111) oxide film

To understand the absence of selective acrolein hydrogenation to unsaturated alcohol propenol over Pd nanoparticles, we carried out a similar spectroscopic investigation on the evolution of surface species during the reaction over oxide supported Pd model system. The experiments were carried out in the identical way described for Pd(111). Figure 9.7a shows the evolution of both possible reaction products – propanal and propenol – during continuous acrolein and hydrogen exposure. Prior to the reaction, the surface was continuously exposed to hydrogen and at the time indicated as zero the acrolein molecular beam was switched on. Consistent with the data shown in Figure 9.2a and 9.2b of the main manuscript, no formation of propenol was observed on this surface. The onset of propanal formation occurs after a short induction period of about 5 s; however, the reactivity decreases rapidly after passing a small maximum. The evolution of the surface species during acrolein exposure was monitored by IRAS in the way identical to the above described experiments on Pd(111). The IR spectra corresponding to regions 1-4, which are indicated on the kinetic curve of Figure 9.7a, are shown in Figure 9.7b. Obviously, a completely different surface composition is formed during the reaction on the Pd particles compared to that on Pd(111). The spectra are dominated by the features in the range 1800-1960 cm<sup>-1</sup>, which start from the lower wavenumbers and become more intense and red shifted with increasing reaction time. These vibrational features can be clearly related to an accumulation of CO molecules on the surface, which result from acrolein decarbonylation. Very similar evolution of vibrational frequencies was reported previously for consecutive CO adsorption on Pd particles of similar size [270]. It is also well documented

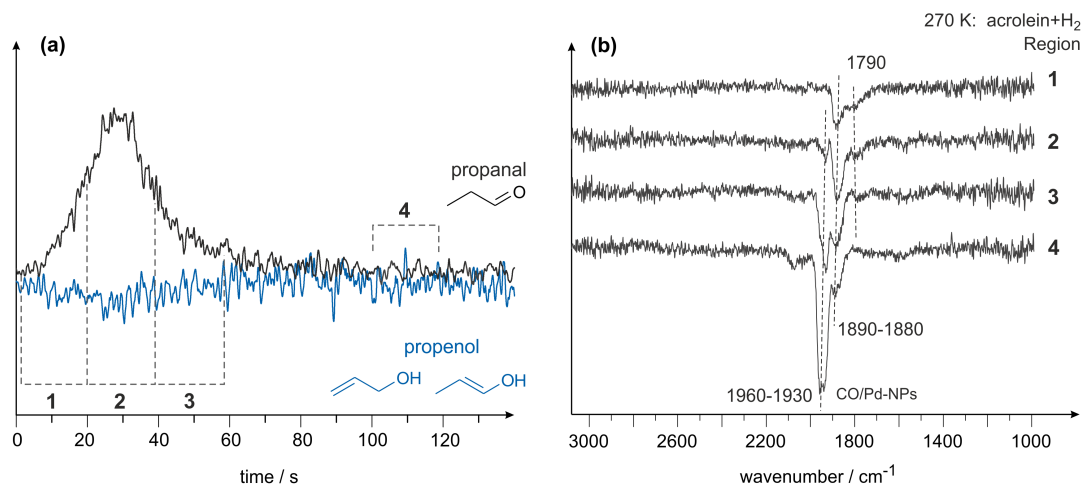


Figure 9.7: (a) Formation rate of propenol (blue line) and propanal (black line) on 12 nm-sized supported Pd nanoparticles at 270 K under continuous exposure of H<sub>2</sub> and acrolein. Prior the experiment, the model catalyst was pre-exposed to H<sub>2</sub>; at time zero acrolein molecular beam was switched on. (b) IR spectra obtained on Pd nanoparticles turning over at 270 K during a continuous exposure to acrolein and hydrogen. Spectra 1-4 correspond to the regions 1-4 indicated in (a).

in the literature that acrolein and the higher  $\alpha,\beta$ -unsaturated ketones and aldehydes can readily undergo decarbonylation over transition metal surfaces [181, 182]. Thus, the observed behavior strongly suggests that acrolein decomposes on Pd nanoparticles under the reaction conditions forming CO molecules that block the surface and prevent formation of well-ordered spectator overlayers required for selective acrolein hydrogenation to unsaturated alcohol. Since the Pd clusters are mostly terminated by (111) facets [153] that are not active in acrolein decomposition as shown by the results obtained on Pd(111), most likely edges, corners, (100) facets and the other low-coordinated surface sites of Pd nanoparticles are responsible for the facile acrolein decomposition and formation of CO. Interestingly, not only alcohol formation but also hydrogenation of the C=C bond, which is discussed to be generally easy even over carbon-containing surfaces, is prevented on the surface covered by CO.

There is a large body of catalytic and surface science literature that could not be cited and discussed in the communication due to the strict size limitations. We refer the interested reader to the following studies: recent reviews and some original studies on powdered materials [27, 28, 45, 179, 248, 271]; surface science studies on model surfaces [52, 60, 180–182, 272–276] and some relevant theoretical work [61, 183, 184, 277–279].



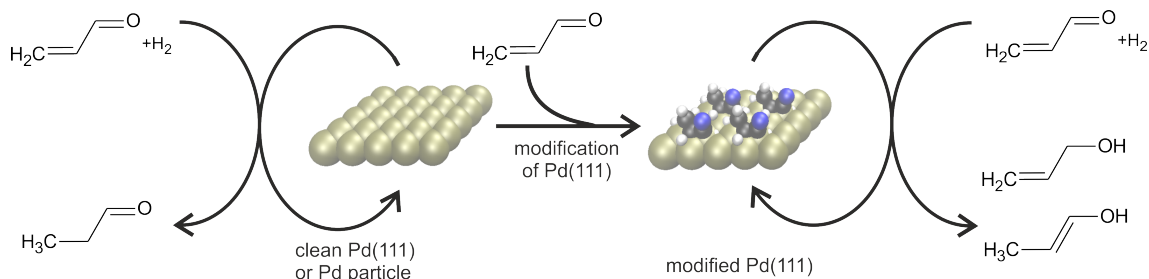
# 10 Selective partial Hydrogenation of Acrolein on Pd: a mechanistic Study

*Karl-Heinz Dostert<sup>1</sup>, Casey P. O'Brien<sup>1</sup>, Svetlana Schauermann<sup>1,2</sup>, and Hans-Joachim Freund<sup>1</sup>*

<sup>1</sup>Fritz-Haber-Institut der Max-Planck-Gesellschaft, Faradayweg 4-6, 14195 Berlin, Germany

<sup>2</sup>Institut für Physikalische Chemie, Christian-Albrechts-Universität zu Kiel, Max-Eyth-Str. 1, 24118 Kiel, Germany

*to be submitted*

**Abstract**

Identifying the surface processes governing the selectivity in hydrogenation of  $\alpha,\beta$ -unsaturated carbonyl compounds on late transition metals is crucial for the rational design of new catalytic materials with the desired selectivity towards C=C or C=O bond conversion. The partial selective hydrogenation of acrolein on a Pd(111) single crystal and  $\text{Fe}_3\text{O}_4$ -supported Pd nanoparticles under well-defined UHV conditions has been investigated in the present study as a prototypical reaction. Molecular beam techniques have been combined with infrared reflection-absorption spectroscopy (IRAS) and quadrupole mass spectrometry (QMS) in order to simultaneously monitor the evolution of surface species and the formation of the final gas-phase products. Over a Pd(111) single crystal, acrolein is hydrogenated at the C=O bond to form propenol with near 100% selectivity, while over Pd/ $\text{Fe}_3\text{O}_4$ , selective conversion of the C=C bond to propenal occurs. We have studied the temperature dependence of both the product formation rates and the evolution of surface species on Pd(111). Moreover, we have investigated the structure dependence of the surface chemistry by comparing the results obtained on Pd(111) and Pd/ $\text{Fe}_3\text{O}_4$ . We found that an initial modification of the Pd(111) surface with a dense monolayer of an oxopropyl species is required for propenol formation. This layer is formed out of the first monolayer of acrolein deposited on the pristine Pd crystal under reaction conditions, most effectively at 270 K. Subsequently deposited acrolein is adsorbed via the C=O bond forming a half-hydrogenated reaction intermediate with saturated C–O bond. The propenol formation rate detected in the gas-phase clearly follows the surface concentration of the reaction intermediate. At higher temperatures or on Pd/ $\text{Fe}_3\text{O}_4$  model catalysts, decarbonylation of acrolein occurs, inhibiting the surface modification required for propenol formation. At lower temperatures, only a small fraction of the initially adsorbed acrolein is converted into the oxopropyl species yielding a partially modified surface and thus rather unselective formation of both products propenal and propenol.

## 10.1 Introduction

Selective partial hydrogenation of multi-unsaturated hydrocarbons, such as  $\alpha,\beta$ -unsaturated aldehydes and ketones is of broad interest for numerous industrial applications. The production of unsaturated alcohols from selective hydrogenation of the C=O bond in unsaturated carbonyl compounds is particularly desired in the field of fine chemicals and pharmaceuticals [27, 28, 30]. Thermodynamics, however, favors the hydrogenation of the C=C bond to the saturated aldehyde by about 35 kJ/mol [28]. Hence, production of unsaturated alcohols requires manipulation of the reaction kinetics by suitable catalysts.

In hydrogenation reactions of  $\alpha,\beta$ -unsaturated aldehydes over Pt group metals, the formation of the saturated aldehydes is strongly favored with close to 100% selectivity. This has been attributed to a strong interaction of the C=C bond with the metals [45]. DFT studies, however, predict a preferential attack at the C=O bond [280], which is in clear contrast to most experimental studies.

Studies over powdered catalyst at ambient or higher pressures point to an improved selectivity to unsaturated alcohols when a second metal (or metal oxide) is added. There are two principally different ways how the second metal may change the selectivity. Either the second compound activates the C=O bond or it poisons the conversion of the C=C bond more than that of the C=O bond [27, 30, 45, 51]. In another approach, partially reducible supports like TiO<sub>2</sub> were used to provide Lewis-acid sites which are believed to coordinate and thus activate the C=O bond. Either strong metal-support interactions create reduced support material on the active metal [47, 54]; or O-vacancies at the TiO<sub>2</sub> support bind the C=O group, which subsequently react with spillover hydrogen from Pt [52]. Other attempts focus on metals which are generally not very active in hydrogenation catalysis. For instance, C=O conversion was observed over silver catalysts under pressures in the range from 100 mbar to 20 bar [34, 35]. The high selectivity to C=C hydrogenation can also be suppressed by using aldehydes or ketones with sterically shielded C=C groups, *e.g.* prenal instead of acrolein. Bulky substituents at the C=C group prevent the attack by the catalyst and thus increase the chance of C=O conversion [31, 32].

In a previous study, we investigated the partial selective hydrogenation of acrolein on a Pd(111) single crystal and on Pd/Fe<sub>3</sub>O<sub>4</sub> model catalysts [185] (see Chapter 9). Acrolein was chosen as a prototypical compound for  $\alpha,\beta$ -unsaturated aldehyde to investigate the selective hydrogenation chemistry at the atomistic level. Over Pd/Fe<sub>3</sub>O<sub>4</sub>, selective conversion of acrolein to propanal occurs, while over a Pd(111) single crystal, propenol is formed with near 100% selectivity.

In the present study, we have investigated key surface reactions that govern the acrolein conversion to propenol over Pd under well-defined ultra high vacuum (UHV) conditions. The combination of molecular beam techniques with time-resolved infrared reflection-absorption spectroscopy (IRAS) and quadrupole mass spectrometry (QMS) has opened up the opportunity to simultaneously monitor the evolution of surface species on Pd and the formation of the gas-phase products. In particular, we have studied the temperature and structure dependence of three surface processes: (i) modification of the Pd surface by a

spectator governing the selectivity towards propenol formation, (ii) C=O bond activation and formation of a half-hydrogenated intermediate, and (iii) formation of spectators that deactivate the Pd surface.

## 10.2 Experimental Details

All experiments have been performed at the Fritz-Haber-Institut, Berlin, in a UHV apparatus that has been described in detail previously [100]. In brief, acrolein and H<sub>2</sub> have been dosed onto the sample through two doubly differentially pumped multi-channel array sources controlled by valves and shutters. The sources have been operated at room temperature, and the beam diameter has been chosen to exceed the sample size. The Pd(111) single crystal was cleaned prior to use by repeated cycles of Ar<sup>+</sup> ion bombardment at room temperature, annealing at 1000 K and oxidation in  $1 \cdot 10^{-6}$  mbar O<sub>2</sub> at 750 K to remove residual carbon. The final cleaning cycle has been stopped after annealing. The flatness and cleanliness of the Pd(111) single crystal surface has been checked by low-energy electron diffraction (LEED) and infrared reflection-absorption spectroscopy (IRAS) of adsorbed CO. The Pd/Fe<sub>3</sub>O<sub>4</sub> model catalysts have been prepared as follows: the thin ( $\approx 100$  Å) Fe<sub>3</sub>O<sub>4</sub> film has been grown on a Pt(111) single crystal surface by repeated cycles of Fe ( $\geq 99.99\%$ , Goodfellow) physical vapor deposition and subsequent oxidation [100, 138, 142]. The quality of the oxide film has been checked by LEED. Pd particles ( $\geq 99.9\%$ , Goodfellow) have been grown by physical vapor deposition using a commercial evaporator (Focus, EFM3, flux calibrated by a quartz microbalance) while keeping the sample temperature fixed at 115 K. The Pd coverage used in these experiments was 7 Å. The quality of the Pd particles has been investigated by IRAS after adsorption of CO. During Fe or Pd evaporation the sample has been biased to the same potential as the evaporant in the evaporator (850 V) in order to avoid the creation of defects by metal ions. The resulting surfaces have been annealed to 600 K, and stabilized via cycles of oxygen ( $1 \cdot 10^{-6}$  mbar for 1000 s) and CO ( $1 \cdot 10^{-6}$  mbar for 3000 s) exposures at 500 K until the Pd particles reached a stable geometry with 12 nm in diameter [152, 153].

IRAS data have been acquired using a vacuum Fourier-Transform Infrared (FT-IR) spectrometer (Bruker IFS 66v/S) with a spectral resolution of  $2 \text{ cm}^{-1}$  and a mid-infrared (MIR) polarizer and p-polarized IR light. An automated quadrupole mass spectrometer (QMS) system (ABB Extrel) has been employed for the continuous monitoring of the partial pressures of the reactants (acrolein: full molecule at 56 amu; H<sub>2</sub>: at 2 amu) and products (propanal: full molecule and main fragment at 58 amu; allyl alcohol: full molecule at 58 amu, main fragment at 57 amu; further fragment at 31 amu; propanol: full molecule 60 amu, main fragment at 31 amu).

Shortly before each experiment the sample has been flashed to 600 K before cooling to the desired temperature. In all experiments, the H<sub>2</sub> exposure rate has been  $4.8 \cdot 10^{15}$  molecules/(cm<sup>2</sup>s). In the reactivity studies presented here with quadrupole mass spectrometry (QMS) the acrolein exposure has been  $1.5 \cdot 10^{13}$  molecules/(cm<sup>2</sup>s). To improve the resolution of IR spectra in the course of acrolein conversion, additional IRAS measurements have been performed with a reduced acrolein flux of  $0.6 \cdot 10^{13}$  molecules/(cm<sup>2</sup>s). Hydrogen exposure has always started 5 min before acrolein exposure. Acrolein (Fluka, 95% purity) has been purified prior to the experiments by repeated freeze-pump-thaw

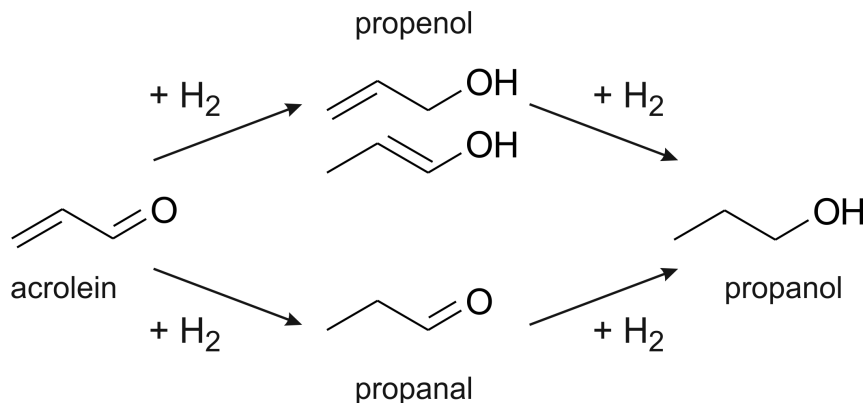


Figure 10.1: Possible reaction pathways of acrolein hydrogenation.

cycles.

The modification of Pd surface sites before the onset of the product formation has been investigated by IRAS measurements after CO exposure. Acrolein has been converted with H<sub>2</sub> until the onset of the product formation after 24 s. The sample has then been cooled to 120 K and exposed to  $9 \cdot 10^{15}$  CO/cm<sup>2</sup>.

### 10.3 Results and Discussion

We have investigated the conversion of acrolein with hydrogen on a Pd(111) single crystal under isothermal conditions at various temperatures in the range from 220 K to 350 K. At each temperature, the Pd(111) surface has been pre-exposed to  $4.8 \cdot 10^{15}$  H<sub>2</sub>/(cm<sup>2</sup>s) for 300 s before the acrolein beam exposing  $1.5 \cdot 10^{13}$  molecules/(cm<sup>2</sup>s) has been switched on additionally. Both beams have been operated in continuous modes.

Figure 10.1 shows the possible reaction pathways of acrolein hydrogenation. Our discussion here is restricted to the formation of the partially hydrogenated products propanal and propenol, since no full hydrogenation to propanol has been observed. It is difficult to unambiguously distinguish between the two possible propenol molecules – allyl alcohol (1-propen-3-ol) and the enol (1-propen-1-ol) – by mass spectrometry. Therefore, we do not specify the propenol species in more detail here.

Our studies on the hydrogenation of acrolein at numerous temperatures show three temperature regimes in which qualitatively similar propanal and propenol formation is observed. We distinguish between reactions at temperatures below 250 K, in the range from 250 K to 300 K, and at temperatures above 300 K. A detailed overview on the product formation rates at various temperatures can be found in Figure 10.9 in the supporting information in Section 10.5. Figure 10.2 illustrates the propanal and propenol formation rates detected in the gas phase by quadrupole mass spectrometry (QMS) at three representative surface temperatures: 220 K, 270 K, and 320 K. The time scale in this figure has been chosen such that acrolein exposure starts at time 0.

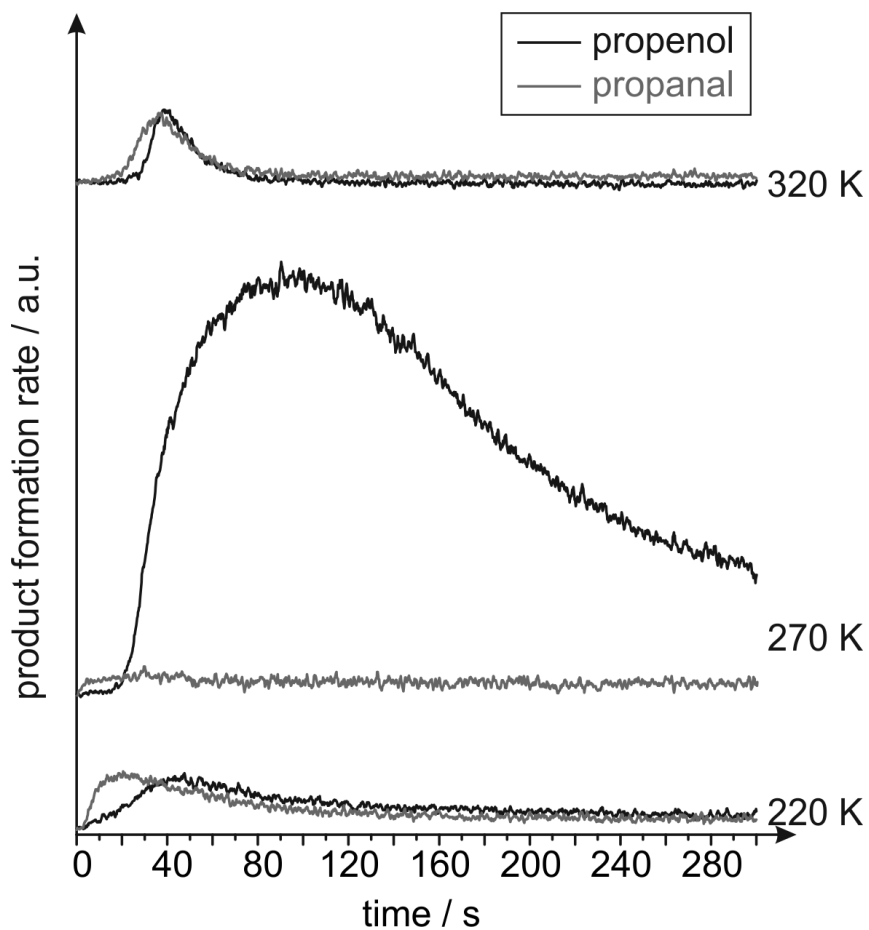


Figure 10.2: Formation rates of propenol (black) and propanal (grey) on Pd(111) during continuous exposure of acrolein and  $\text{H}_2$  at different temperatures. The signals have been corrected for the sensitivity of the QMS.

The amount of propanal detected in the gas phase is rather small at all investigated temperatures. The propenol formation rate, in contrast, exhibits a clear temperature dependence with a strong maximum near 270 K.

In detail, at 220 K, small amounts of both products successively appear. Gas-phase propanal desorbs from the surface shortly after starting the acrolein exposure. The formation rate passes a maximum after about 20 s and subsequently decreases to zero. The propenol production increases more slowly, reaches a maximum after about 50 s and then declines to zero.

At 270 K, three reactivity regimes can be distinguished. Initially, essentially no product formation is observed. Only a very small amount of propanal is indicated by a weak QMS signal. After 24 s, however, the propenol formation rate strongly increases and reaches a maximum after about 100 s, while no further propanal is detected. Finally, the propenol formation slowly declines.

In the whole temperature range from 250 K to 300 K, the Pd(111) surface is highly active for propenol production. The propenol formation always starts after an induction period, then rapidly increases, passes a maximum and finally decreases. At 250 K and 270 K, the induction period takes about 24 s, while it extends to 48 s at 300 K. At 300 K, however, a slightly lower selectivity is evident by a small amount of propanal appearing simultaneously to propenol (see Figure 10.9 in Section 10.5).

Interestingly, acrolein exposure of 24 s corresponds to  $3.6 \cdot 10^{14}$  molecules/cm<sup>2</sup> and thus to approximately one acrolein molecule per four Pd surface atoms. In a separate study, we have found that a full monolayer of acrolein on Pd(111) is formed after exactly the same exposure [176] (see Chapter 8). This observation indicates that under reaction conditions one layer of acrolein is accumulated on the Pd(111) surface prior to the onset of the propenol production.

At 320 K, both products propanal and propenol are formed in small quantities. Propanal starts to appear in the gas phase after about 20 s and propenol desorption is detected after about 30 s. The formation rates of both products increases until about 40 s and then decreases to zero. At higher temperatures, no product formation is observed (see supporting information in Section 10.5).

The temperature and time dependence of the selectivity and activity of the Pd(111) catalyst suggest a quite complex interplay between multiple surface processes, which will be discussed in more detail in the following sections. First, we will focus on the processes on the surface during induction, propenol formation, and poisoning at 270 K. Afterwards, we will present our studies on the reactions at lower and higher temperatures to identify the individual temperature dependencies of the different surface processes. Finally, we will compare the results of acrolein conversion over Pd(111) and Pd particles in order to find the microscopic origin of the different selectivity in acrolein conversion on both surfaces.

### 10.3.1 Acrolein Conversion at 270 K

The time dependence of the propenol formation rate at 270 K illustrated in Figure 10.2 suggests that the course of acrolein conversion can be divided into three steps. First, there is an initial period during which a monolayer of acrolein is adsorbed, but no propenol is formed. Apparently, the Pd(111) surface is getting activated for propenol production. In the second period, high propenol production rates are observed for about 100-200 s. In the final step of the conversion, the activity of the catalyst slowly decreases to zero.

#### Initial Surface Modification

In order to study the change of the single crystal's surface in the course of the induction period, the Pd(111) surface has been exposed to both reactants for 24 s at 270 K. Figure 10.3a illustrates the result of a separate experiment clearly showing that after this exposure the surface is just activated for propenol production. The Pd(111) surface exposed to acrolein for 24 s has subsequently been exposed to CO in order to probe the availability of pristine Pd sites. The corresponding IR spectrum is displayed with the black line in Figure 10.3b. For comparison, an IR spectrum obtained after exposure of pristine Pd(111) to CO is shown with the gray line. In the latter case, a strong IR absorption peak related to the C=O stretching vibration is observed. After exposure of the modified Pd(111) surface to CO, in contrast, no IR absorption feature characteristic for CO is detected, clearly showing that CO does not stick to the surface and thus that no pristine Pd sites are available. Hence, the adsorbed hydrocarbons must be rather homogeneously distributed over the surface than accumulated in islands; otherwise we cannot explain how the exposure of one acrolein per four Pd surface atoms could result in blocking of the entire surface.

#### Surface Species under Reaction Conditions

The chemical structure of the surface species on Pd(111) under reaction conditions at 270 K has been investigated by IRAS. Figure 10.4 shows three IR spectra obtained in the three reactivity regimes on the surface turning over. The second spectrum from top shows the surface during the first 45 s, which include the induction period and the beginning of the propenol formation. The third spectrum has been obtained during high propenol formation rates (45-90 s), and the final spectrum shows the surface with low activity in the final step of the experiment (450-540 s). For comparison, additionally the IR spectrum of a monolayer of acrolein on Pd(111) at 100 K is displayed at the top in Figure 10.4. We distinguish between three spectral regions characteristic for the  $\text{CH}_x$  stretching vibrations ( $3200\text{--}2700\text{ cm}^{-1}$ ), C=O and C=C stretching vibrations ( $1850\text{--}1550\text{ cm}^{-1}$ ), and  $\text{CH}_x$  deformation as well as C–O and C–C stretching vibrations ( $\leq 1500\text{ cm}^{-1}$ ).

**The spectrum of acrolein** The uppermost spectrum in Figure 10.4 shows the IR absorption of  $3.6 \cdot 10^{14}$  acrolein molecules/ $\text{cm}^2$  on Pd(111) at 100 K, which is discussed in detail elsewhere [176] (see Chapter 8). IR absorption features appear at  $1663\text{ cm}^{-1}$  and at  $1430\text{--}1400\text{ cm}^{-1}$ . The pronounced adsorption near  $1663\text{ cm}^{-1}$  is assigned to the stretching

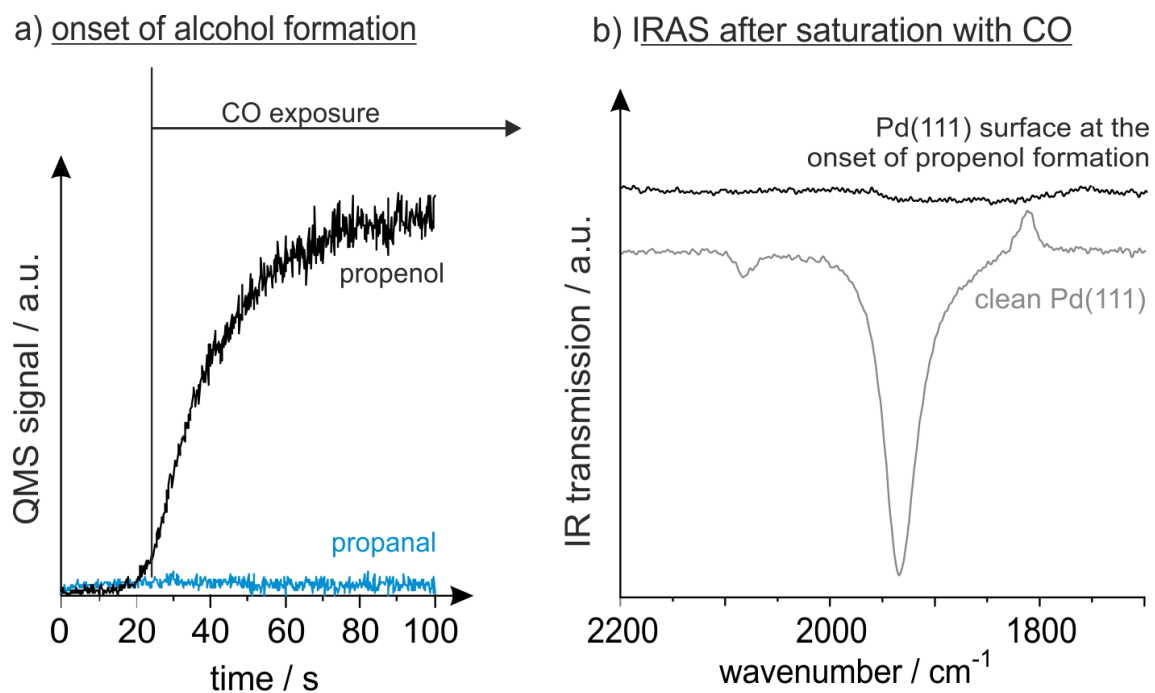


Figure 10.3: Investigation of the Pd(111) surface at the end of the induction period for propenol formation at 270 K: (a) The black and blue curves show the formation rates of propenol and propanal. The propenol formation starts after exposure of both reactants for 24 s. (b) IR spectrum of CO on a pristine Pd(111) single crystal (gray) compared to an IR spectrum after CO adsorption on the Pd(111) crystal exposed to acrolein and H<sub>2</sub> for 24 s under reaction conditions (black).

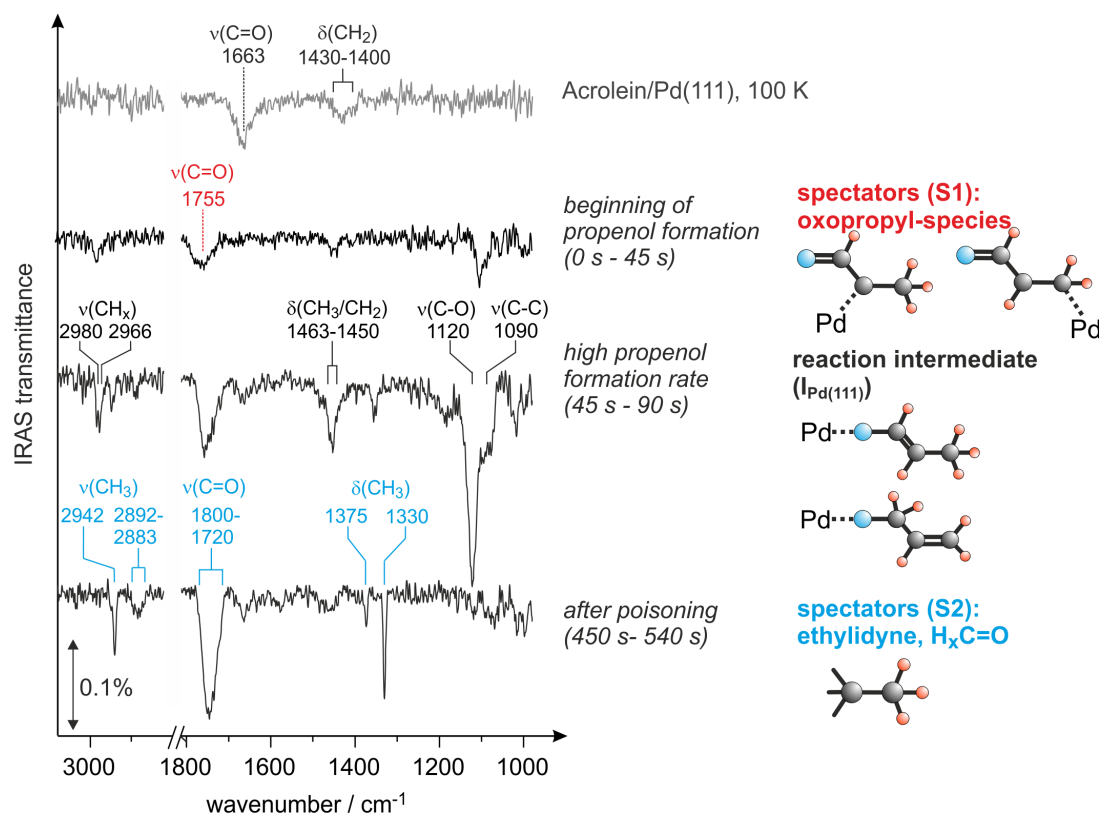


Figure 10.4: IR spectra of a monolayer of molecular adsorbed acrolein on pristine Pd(111) at 100 K (grey line) and of the surface species on Pd(111) turning over at 270 K during continuous exposure to acrolein and  $\text{H}_2$  (black lines). The second spectrum from top has been obtained during the induction period and at the beginning of the propenol formation and mainly shows the IR vibration of spectator S1. The third spectrum has been obtained during high propenol formation rates and shows the additional appearance of the IR vibrations of the reaction intermediate. The fourth spectrum shows spectators S1 and S2 on the inactive surface.

vibration of the carbonyl (C=O) group and the feature at 1430-1400  $\text{cm}^{-1}$  is related to a scissor deformation of the methylene ( $\text{CH}_2$ ) group. Both IR vibrational modes have been discussed in literature before [61, 248–251].

**The initially formed spectator (S1)** The second spectrum in Figure 10.4 has been collected during the first 45 s of acrolein conversion on Pd(111) at 270 K, which corresponds to an exposure of  $6.8 \cdot 10^{14}$  molecules/ $\text{cm}^2$ . It thus includes the induction period and the beginning of the propenol appearance in the gas phase. The obtained IR spectrum is clearly different from that of molecularly adsorbed acrolein. A pronounced IR vibrational mode appears at 1755  $\text{cm}^{-1}$  and a second one near 1120  $\text{cm}^{-1}$ . The vibration at 1755  $\text{cm}^{-1}$  strongly indicates a C=O stretching vibration that is not conjugated to a C=C group anymore. Vibrations near 1755  $\text{cm}^{-1}$  are typical for the carbonyl stretching mode in aldehydes and ketones [109, 240, 244].

The appearance of this IR vibration under reaction conditions points to the formation of an oxopropyl surface species, resulting from partial hydrogenation of acrolein with only one H atom at the C=C group. Our data do not allow to make a more precise conclusion on whether acrolein has been hydrogenated on the  $\alpha$ - or  $\beta$ -C atom to form this species; both products would be consistent with IR vibration at 1755  $\text{cm}^{-1}$ . We will refer to this initially formed adsorbate as spectator 1 (S1). A possible structure of S1 is illustrated on the right hand side of in Figure 10.4. The IR absorption feature at 1120  $\text{cm}^{-1}$  starts to appear during the first 45 s, however, it becomes very pronounced in the spectrum obtained during high propenol formation rates and will therefore be discussed in the following paragraph.

**The reaction intermediate ( $\text{I}_{\text{Pd}(111)}$ )** The third IR spectrum in Figure 10.4 illustrates the surface composition in the period of high propenol formation rates (45 s to 90 s). It clearly shows the formation of a further surface species in the presence of S1 with strong IR absorption features. The newly formed species exhibits pronounced IR vibrations at 1090  $\text{cm}^{-1}$ , 1120  $\text{cm}^{-1}$ , and 1463-1650  $\text{cm}^{-1}$ . Weak IR absorption is detected in the C–H stretching region near 2966  $\text{cm}^{-1}$  and 2980  $\text{cm}^{-1}$ . In the C=O stretching region, however, no IR absorption feature can be assigned to the newly formed species.

The intense IR absorption features at 1090  $\text{cm}^{-1}$  and 1120  $\text{cm}^{-1}$  are present neither in adsorbed molecular acrolein on Pd nor in acrolein ice and therefore cannot be related to any distinctive vibration of intact acrolein molecules. Instead, the IR vibration at 1120  $\text{cm}^{-1}$  is assigned to a stretching mode of a saturated C–O bond. Previously, C–O stretching vibrations have been observed in the range from 1120  $\text{cm}^{-1}$  to 1200  $\text{cm}^{-1}$  when the oxygen is coordinated to a metal surface [61, 267, 275, 281–284]. The IR absorption at 1090  $\text{cm}^{-1}$  is assigned to a stretching vibration of a saturated C–C bond. In literature C–C bond vibrations are reported in the range from about 1000  $\text{cm}^{-1}$  to 1130  $\text{cm}^{-1}$ , depending on their coordination to the surface [61, 180, 250, 284, 285]. The IR absorption at 1450  $\text{cm}^{-1}$  to 1463  $\text{cm}^{-1}$  appear in a typical range for  $\text{CH}_2$  and  $\text{CH}_3$  bending vibrations. Tentatively, we assign it to  $\text{CH}_3$  asymmetric bending modes, which have been reported in the range of 1450-1475  $\text{cm}^{-1}$  [109, 253, 254]. Alternatively, it could also be related to a  $\text{CH}_2$  scissor mode, which, however, typically appear at slightly lower frequency near

1420-1430  $\text{cm}^{-1}$  [61, 248–251]. The vibrations at 2966  $\text{cm}^{-1}$  and 2980  $\text{cm}^{-1}$  clearly show C–H stretching vibrations. The vibration near 2980  $\text{cm}^{-1}$  indicates a C–H bond with a C atom that is part of an unsaturated C=C bond [109].

As no IR vibration characteristic for an alcohol group (O–H) is detected, it is most likely not the final hydrogenation product that is visible in the IR spectrum. However, a new C–H bond vibration appears, which can clearly be assigned to a surface species only formed during high propenol formation rates. We therefore relate this surface species to a the half-hydrogenated reaction intermediate ( $\text{I}_{\text{Pd}(111)}$ ). According to the Horiuti-Polanyi mechanism, first a half-hydrogenated intermediate is formed on the surface by reversible addition of one hydrogen atom to an unsaturated bond. In the following step, the final product is produced by irreversible addition of the second hydrogen atom before it desorbs [286]. Theoretical calculations show that the barrier for addition of an H atom at a C atom is smaller than for addition at the O atom and should therefore occur preferentially [280].

The most likely surface species related to the observed IR absorption features is a propenoxy-group, in which the C–O entity is attached to the Pd through the O atom in an  $\eta^1\text{-(O)}$  configuration ( $\text{CH}_2=\text{CH}-\text{CH}_{(2)}-\text{O}-\text{Pd}$ ). A C–O stretching vibration at similar frequency has been observed in an  $\eta^1\text{-(O)}$  configuration of prenal on a Pt-Sn(111) alloy surface [275]. The high intensity of the 1120  $\text{cm}^{-1}$  band, exceeding even the most intense C=O vibrational band in acrolein and in the oxopropyl species, additionally supports the formation of a C–O bond exhibiting a large dynamic dipole moment and, hence, explains the very high IR intensity. Furthermore, the IR vibration near 2980  $\text{cm}^{-1}$ , which indicates a C–H stretching vibration at a C=C group, suggests that the reaction intermediate  $\text{I}_{\text{Pd}(111)}$  preserves a C=C group. Finally, it should be noted the strong IR absorption related to the C–C stretching at 1090  $\text{cm}^{-1}$  appears relatively intense although the dynamic dipole moment of a C–C bond is rather small. According to the metal surface selection rule (MSSR), the projection of vibrations of the dynamic dipole moment perpendicular to the surface are visible in IRA spectra, while the vibrations parallel to the surface are strongly attenuated due to formation of an image dipole moment in the underlying metal substrate. Based on the MSSR, the high intensity of the C–O and C–C stretching vibration indicates a strongly inclined C–C–C–O–Pd entity.

It is important to note that the surface reaction intermediate is formed not on the pristine Pd(111) surface, but on the surface strongly modified with S1 (oxopropyl species). Indeed, about one acrolein molecule per four Pd surface atoms is accumulated on Pd(111) to form the spectator prior to the onset of the propenol formation. Microscopically, this corresponds to a situation when every fourth Pd atom is covered by S1, forming a dense spectator overlayer structure. Most likely, such strong geometrical confinement of an adsorption site for acrolein on the S1-covered surface prevents the competing pathway of C=C bond hydrogenation and allows acrolein to adsorb only via the O atom to activate the C=O group. Obviously, the clean Pd(111) surface is not capable of activating the C=O group towards selective hydrogenation and the strong modification of the surface by S1 is required to trigger the desired selective chemistry.

**The slowly formed spectator (S2)** The fourth IR spectrum in Figure 10.4 (bottom) has been collected after the formation rate of gas-phase propenol has decreased almost to zero (450 s to 540 s). The features assigned to the half-hydrogenated intermediate  $I_{\text{Pd}(111)}$  have disappeared. Instead vibrations are observed at  $1330\text{ cm}^{-1}$ ,  $1375\text{ cm}^{-1}$ , in the range from  $2883\text{ cm}^{-1}$  to  $2892\text{ cm}^{-1}$ , and at  $2942\text{ cm}^{-1}$ . All these IR absorption features strongly point to vibrations of C–H bonds. The sharp peak at  $1330\text{ cm}^{-1}$  is very characteristic for the umbrella bending mode of the  $-\text{CH}_3$  group in ethylidyne or an ethylidyne-like species, which has been observed in previous studies on Pd(111) and Pt(111) before [287, 288].

This result indicates that a fraction of the acrolein molecules decomposes in a decarbonylation reaction yielding a  $\text{C}_2$  fragment and a carbonyl group which eventually poison the surface. Decarbonylation of acrolein and similar  $\alpha, \beta$ -unsaturated aldehydes on metal surfaces is a well-known phenomenon [181, 289–292]. The decomposition yields a carbonyl fragment and a  $\text{C}_2$  group, such as ethylene. Ethylene formation from acrolein on Pd has been observed in previous studies [181, 289–291]. Moreover, ethylene is known to convert to ethylidyne on metal surfaces such as Pd and Pt [287, 288, 293]. Identification of the carbonyl fragment is most likely not possible, since the C=O stretching vibration of this species may strongly overlap with the C=O vibration of S1. In literature, C=O stretching vibrations of various aldehydes have all been reported near  $1790\text{--}1750\text{ cm}^{-1}$  [109, 244].

### Evolution of the Reaction Intermediate and the Final Product

IRAS studies with higher time resolution have been performed in order to compare the formation of the reaction intermediate on the surface to the appearance of propenol in the gas phase in more detail. Figure 10.5a illustrates a series of IR spectra obtained on the Pd(111) surface turning over at 270 K. During the collection of each spectrum the surface has been exposed to  $1.2 \cdot 10^{13}$  acrolein molecules/ $\text{cm}^2$ , which corresponds to 8 s in the QMS measurement in Figure 10.5b. Note that after the 6<sup>th</sup> spectrum only every fourth spectrum is illustrated in Figure 10.5a. Approximately in the 2<sup>nd</sup> or 3<sup>rd</sup> spectrum, the vibrations indicating  $I_{\text{Pd}(111)}$  start to appear. The intensities of the peaks grow until about the 7<sup>th</sup> or 8<sup>th</sup> spectrum. Finally, all features pointing to  $I_{\text{Pd}(111)}$  disappear again.

Figure 10.5b shows the gas-phase formation rate of propenol (grey line) together with the integral intensity of the most intense IR vibration band of  $I_{\text{Pd}(111)}$  at  $1120\text{ cm}^{-1}$  (black squares). We assume that the intensity of the band at  $1120\text{ cm}^{-1}$  approximately reflects the concentration of  $I_{\text{Pd}(111)}$  on the surface. Thus, the propenol formation rate detected in the gas phase clearly follows the concentration of  $I_{\text{Pd}(111)}$  on the surface. The observed strong correlation unambiguously shows that the corresponding surface species is a reaction intermediate that is directly involved in the selective hydrogenation of acrolein to the propenol.

#### 10.3.2 Acrolein Conversion at lower Temperatures

Figure 10.2 shows that at 220 K small amounts of both partial hydrogenation products are detected in the gas phase. In order to study the surface processes relevant for the lower selectivity and activity as compared to the conversion at 270 K, we have investigated the

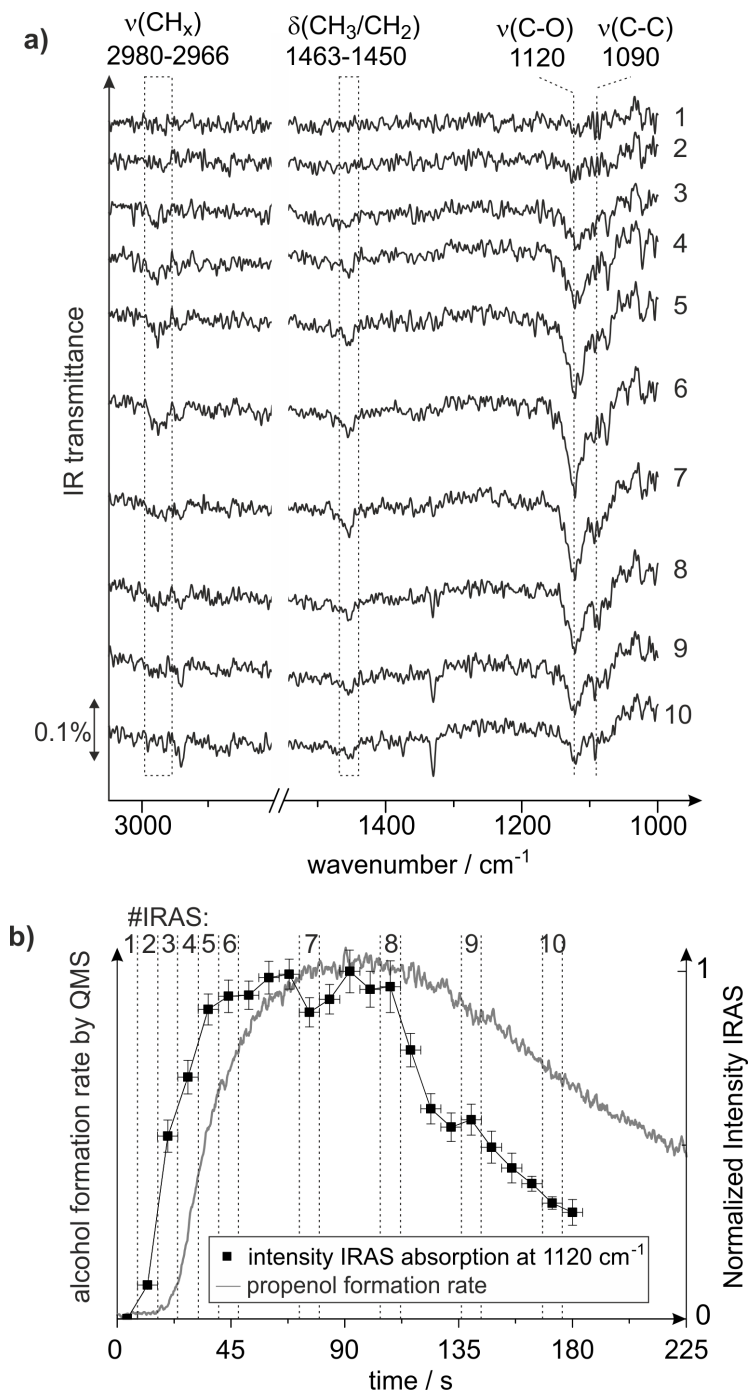


Figure 10.5: The formation of the reaction intermediate  $\text{I}_{\text{Pd}(111)}$  on the surface compared to the evolution of gas-phase propenol. (a) Series of IR spectra with high time resolution taken on the surface turning over. Shown are only the vibrational regions relevant to  $\text{I}_{\text{Pd}(111)}$ . The integral of the most pronounced peak at 1120  $\text{cm}^{-1}$  is plotted in (b) together with the propenol formation rate detected in the gas phase by QMS.

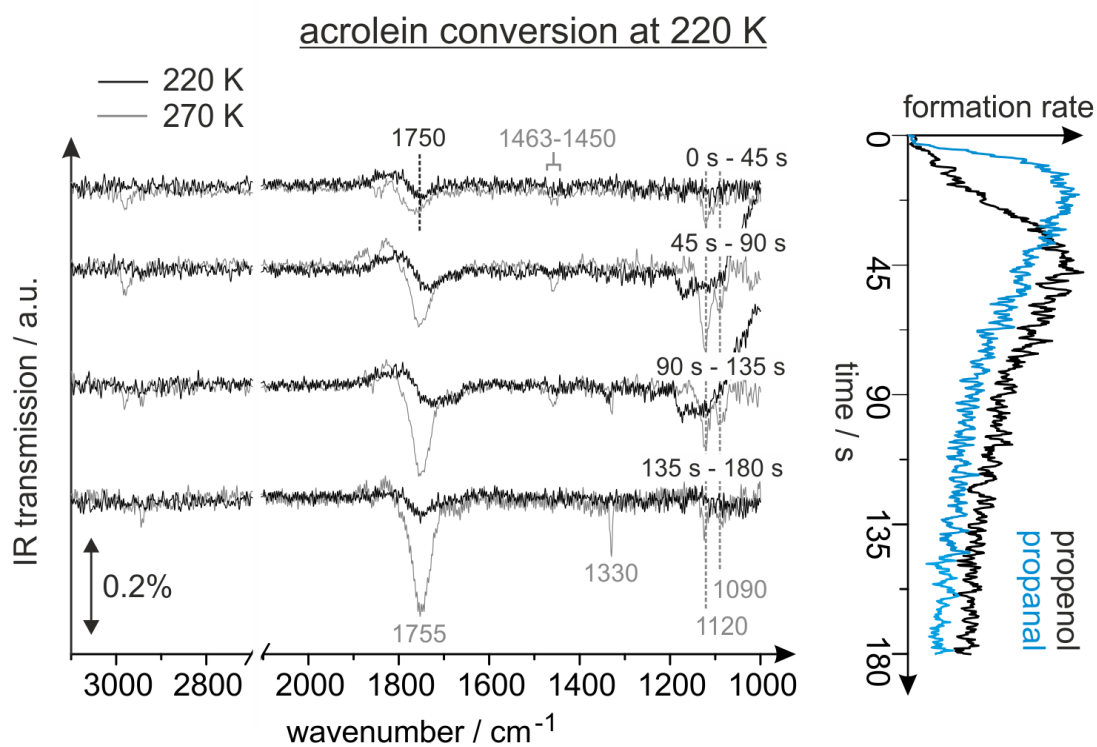


Figure 10.6: Comparison of the propanal and propenol production rates detected in the gas-phase (right) and the formation of surface species on Pd(111) turning over (left) at 220 K.

Pd(111) surface turning over at 220 K by IRAS. Figure 10.6 presents a series of IR spectra taken on the Pd(111) surface under reaction conditions with a time resolution of 45 s (black lines) compared to the IR spectra taken at 270 K (grey line). The simultaneously detected formation of gas-phase propanal and propenol are shown on the right hand side of the IR spectra.

The weak IR absorption feature near  $1750\text{ cm}^{-1}$  is the only IR vibration that appears in the whole series of IR spectra at 220 K. The vibration frequency is almost identical to that of the oxopropyl species (S1) observed at 270 K. The significantly weaker absorption intensity, however, points to a much smaller concentration of this species on the surface. Since we have observed the formation of a monolayer of S1 at 270 K, we can conclude that only a rather small fraction of the Pd(111) surface is getting modified by S1 at 220 K. Moreover, the IR spectra obtained at 220 K do not indicate the formation of the reaction intermediate  $\text{I}_{\text{Pd}(111)}$  absorbing at  $1120\text{ cm}^{-1}$ . The absence of this surface species is, however, not surprising. On the one hand, we found that  $\text{I}_{\text{Pd}(111)}$  only appears on the S1-modified surface – and the concentration of S1 is quite small at 220 K. On the other hand, the small quantity of the final product propenol already points to a small concentration of  $\text{I}_{\text{Pd}(111)}$ . Moreover, it should be pointed out that apparently a large fraction of the Pd(111) surface is not becoming modified by S1, which could be beneficial for C=C bond hydrogenation and thus propanal formation. In fact, the propanal formation rate is significantly larger as determined at 270 K, where the entire Pd(111) surface has been modified by S1.

Our studies at 220 K provide further insights into the relation between specific surface processes and the selectivity in partial selective hydrogenation of acrolein. The IRAS series shows a significantly different surface composition at 220 K as compared to 270 K; at the same time strong changes of the selectivity are evident by the QMS data. While at 270 K the first deposited acrolein monolayer is completely converted to a dense oxopropyl monolayer (S1), only a rather small fraction of the Pd(111) surface is becoming modified by the same species at 220 K. The incomplete modification of the surface and thus the presence of both modified and unmodified Pd(111) may be the reason for the unselective conversion of acrolein to propenol and propanal. In more detail, on the one hand, only a relatively small amount of propenol is formed at 220 K, which seems to be related to the small fraction of the Pd(111) surface modified by S1. On the other hand, a significantly larger amount of propanal is produced at 220 K as compared to 270 K, which may be the result of acrolein conversion on unmodified Pd sites.

### 10.3.3 Acrolein Conversion at higher Temperatures

Figures 10.2 and 10.9 show that also with increasing temperature above 270 K the selectivity and activity of the Pd catalyst in acrolein hydrogenation decreases. In a similar approach as in the previous studies at 220 K and 270 K, we have investigated the Pd(111) surface under reaction conditions at 320 K by simultaneous IRAS and QMS measurements. Figure 10.7 compares a time-resolved series of IR spectra measured on the Pd(111) surface turning over at 320 K (black lines) to the spectra taken at 270 K (grey lines). The formation gas-phase formation rates of both products at 320 K are illustrated on the right

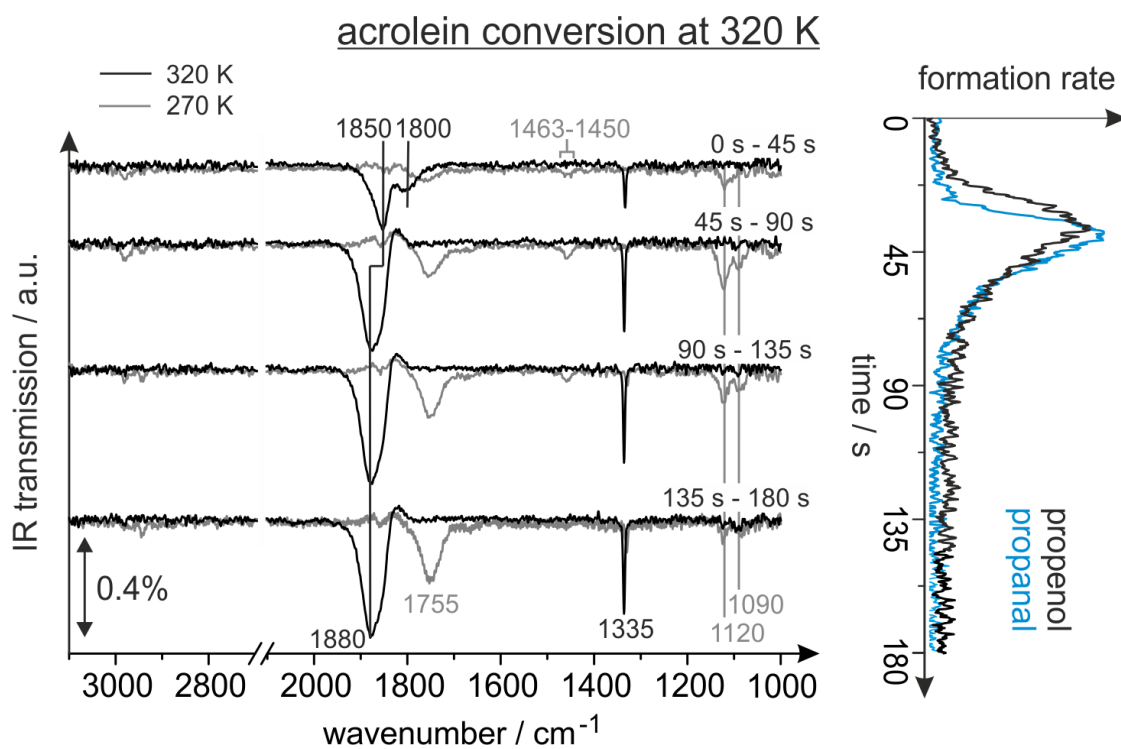


Figure 10.7: Comparison of the propanal and propenol production rates detected in the gas-phase (right) and the formation of surface species on Pd(111) turning over (left) at 320 K.

hand side of the IR spectra.

During the first 45 s of acrolein exposure, two broad IR absorption features appear at  $1850\text{ cm}^{-1}$  and  $1800\text{ cm}^{-1}$  and a sharp peak is observed at  $1335\text{ cm}^{-1}$ . In the same period, the formation rates of both products increase and reach their maxima. In the following time frame from 45 s to 90 s, the peak at  $1800\text{ cm}^{-1}$  vanishes, while the vibration at  $1850\text{ cm}^{-1}$  gains intensity and shifts to  $1880\text{ cm}^{-1}$ . The sharp IR absorption feature at  $1335\text{ cm}^{-1}$  gains intensity as well. In this period, both product formation rates rapidly decrease to zero. Finally, according to the IR spectra taken after 90 s and later, the surface seems to be saturated by the species absorbing at  $1880\text{ cm}^{-1}$  and  $1335\text{ cm}^{-1}$  while the QMS data does not show any further product formation.

The IR vibrations in the  $1800\text{--}1880\text{ cm}^{-1}$  range appear at typical frequencies for stretching vibrations of C=O groups. The initially appearing IR absorption at  $1850\text{ cm}^{-1}$ , which shifts to  $1880\text{ cm}^{-1}$  with increasing coverage, is assigned to molecular CO. The vibration appears in the range of previously observed coverage-dependent shifts of the CO stretching vibrational frequency [113]. The second feature in the carbonyl stretching region at  $1800\text{ cm}^{-1}$  could either result from CO at a very low surface concentration detected at the very beginning of the experiment, or it may point to a carbonyl group in a hydrocarbon species. The IR vibration at  $1335\text{ cm}^{-1}$  strongly indicates ethylidyne, which has already been observed at 270 K.

The IR spectra taken during acrolein conversion over Pd(111) at 320 K show a clearly different surface chemistry from 270 K and 220 K. The IRAS series obtained at 320 K shows strong decomposition of acrolein in a decarbonylation reaction yielding CO and ethylidyne. Only a rather small fraction of acrolein is hydrogenated to propenol or propanal. CO and ethylene accumulate irreversibly on the surface until saturation after 45–90 s of acrolein exposure, which corresponds to  $6.8 \cdot 10^{14}$ – $1.4 \cdot 10^{15}$  molecules/cm<sup>2</sup> and thus to approximately 2–4 ML acrolein. The hydrogenation products propanal and propenol, however, are only formed before the surface is saturated with CO and ethylidyne, indicating that the latter species are responsible for deactivation of the catalyst. Our studies at 270 K already indicated that the products from acrolein decarbonylation irreversibly adsorb on the surface and are responsible for the poisoning of the catalyst. At 270 K, however, the decarbonylation reaction yields ethylene and an aldehyde or ketone fragment instead of molecular CO. Most likely, the further decomposition of the aldehyde or ketone fragment to CO requires a higher surface temperature. Moreover, it should be taken into account that at temperatures near 320 K the hydrogen concentration on the surface is expected to strongly decrease with increasing temperature, since hydrogen typically desorbs from the Pd(111) surface near this temperature [294]. A lower hydrogen concentration on the surface than at 270 K may further promote the decomposition instead of the hydrogenation pathway. In conclusion, our results indicate that the lower activity of the Pd(111) catalyst at higher temperature most likely results from the effective decarbonylation of acrolein yielding irreversibly adsorbed ethylidyne and CO, which poison the catalyst's surface.

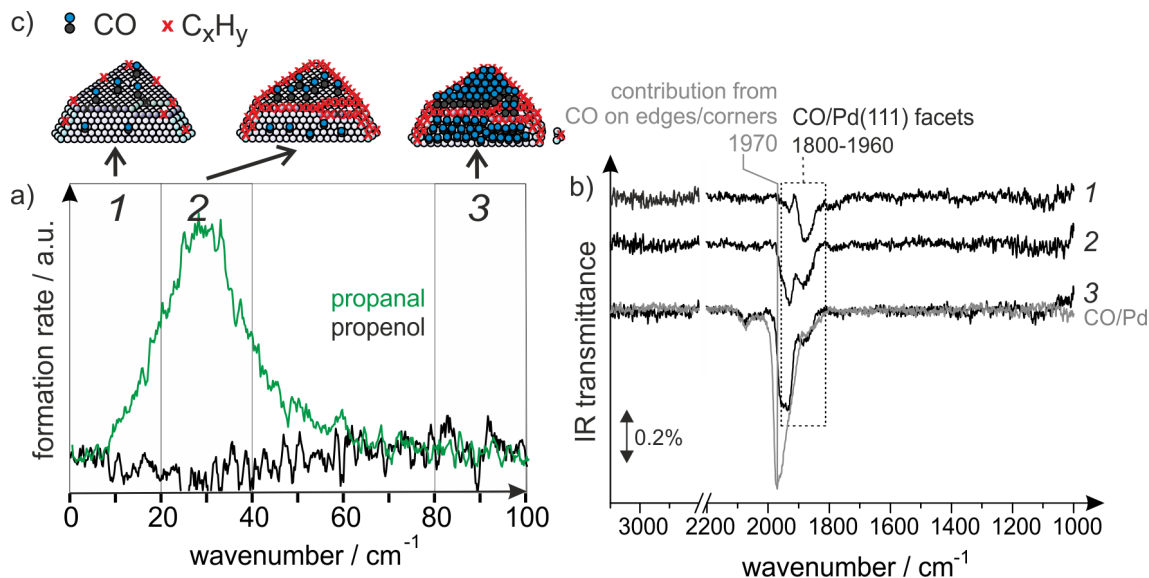


Figure 10.8: (a) Formation rates of the hydrogenation products detected in the gas phase by QMS and (b) simultaneously taken IR spectra of the Pd/Fe<sub>3</sub>O<sub>4</sub> model catalysts turning over at 270 K. The time resolution of the spectra is 20 s and corresponds to the regions 1 to 3 indicated in (a). (c) Model of the accumulation of CO and CH<sub>x</sub> fragments from acrolein decomposition.

#### 10.3.4 Selectivity on Pd(111) and Pd/Fe<sub>3</sub>O<sub>4</sub> at 270 K

The conversion of acrolein over Fe<sub>3</sub>O<sub>4</sub>-supported Pd nanoparticles is presented in detail in a further publication [187] (see Chapter 11). Briefly, over Pd/Fe<sub>3</sub>O<sub>4</sub> model catalysts, a very different selectivity has been observed in partial hydrogenation of acrolein. Propanal is the only gas-phase product formed on the Pd particles, which is most efficient at 220 K. However, also at 270 K, a significant propanal formation rate has been detected. The selective formation of propanal on Pd particles is in good agreement with earlier studies on powdered catalysts under higher pressures showing that essentially only the C=C bond can be hydrogenated [28, 45].

We have spectroscopically investigated the surface reactions occurring on Fe<sub>3</sub>O<sub>4</sub>-supported Pd particles with a diameter of 12 nm to understand the origin of the different selectivity on Pd(111) and Pd/Fe<sub>3</sub>O<sub>4</sub>. Figure 10.8 shows the propanal and propenol formation rates detected in the gas phase (left) and a series of simultaneously detected IR spectra of the Pd/Fe<sub>3</sub>O<sub>4</sub> surface turning over. The first two spectra are taken at 0-20 s and 20-40 s of exposure and thus while the propanal formation rate is relatively high. The final spectrum has been obtained after the surface has become inactive. The IR spectra exhibit strong IR absorption features in the range from 1800-1960 cm<sup>-1</sup>, which can clearly be assigned to CO molecules on Pd. This observation strongly indicates facile decarbonylation of acrolein on the Pd particles at 270 K. In Figure 10.8 the IR spectrum of the surface after becoming inactive (3) is compared to the IR spectrum of CO-saturated Pd/Fe<sub>3</sub>O<sub>4</sub>. The spectra of

the inactive Pd and the CO-saturated Pd particles show similar IR absorption intensities in the range from 1800-1860  $\text{cm}^{-1}$ , indicating saturation of the respective CO species on the inactive particles. The CO species vibrating at 1970  $\text{cm}^{-1}$ , in contrast, has not been formed in the acrolein decarbonylation reaction. Previous studies demonstrated that the stretching frequency of CO on Pd critically depends on the adsorption site [112, 161, 163–167]. The broad IR absorption feature at 1800-1860  $\text{cm}^{-1}$  has been related to CO on Pd(111) facets, while CO attached to the edge sites has been found to contribute to the sharp peak at 1970  $\text{cm}^{-1}$ . Thus, our results strongly indicate CO-saturated (111) facets and CO-free edge sites.

The combination of IRAS and QMS studies indicate that the reversed selectivity of acrolein hydrogenation on Pd/Fe<sub>3</sub>O<sub>4</sub> and Pd(111) is related to significant differences in the surface chemistry under reaction conditions. While decarbonylation of acrolein to CO occurs on Pd particles, an oxopropyl monolayer is formed on the Pd(111) single crystal. Decarbonylation of acrolein forming CO has also been observed in our studies on the Pd(111) single crystal, however, only at higher temperatures. Since CO production on the Pd(111) crystal is not observed at this low temperature, most likely the (100) facets or low-coordinated sites, such as edges and corners, catalyze the decomposition to CO. The formation of a monolayer of CO on the (111) facets, however, indicates that the CO rapidly diffuses there while the CH<sub>x</sub> fragments accumulate elsewhere, *e.g.* at the sites where the decomposition occurs. The decarbonylation of acrolein continues until a saturated monolayer of CO is formed on the (111) facets.

A possible distribution of CO and CH<sub>x</sub> on the Pd particles is illustrated in Figure 10.8c, on top of the QMS data. This comparison allows for two conclusions. On the one hand, propanal is formed as long as the (111) facets are not saturated with CO. On the other hand, the product formation rate reaches a maximum after a fraction of Pd sites is already covered by CO and CH<sub>x</sub>. Most likely, first, highly reactive Pd sites that catalyze the decarbonylation have to be blocked in order to enable the hydrogenation reaction.

## 10.4 Conclusions

The partial hydrogenation of acrolein over Pd has been studied under well-defined UHV conditions by using molecular beam techniques combined with IRAS and QMS. We have found the following key surface processes controlling the selectivity towards propenol formation:

- modification of the Pd(111) surface:  
Under reaction conditions, the first monolayer of acrolein on Pd(111) is converted into an oxopropyl species (S1) forming a dense overlayer which is irreversibly adsorbed on the surface.
- hydrogenation of acrolein to propenol on the modified Pd(111):  
The subsequently deposited acrolein is adsorbed on the S1-modified Pd(111) with the C=O group pointing to the surface activating the C=O bond. This species reacts to the half-hydrogenated intermediate I<sub>Pd(111)</sub> containing a newly formed C–H bond

and a saturated C–O bond, which is attached to the Pd surface. Hence, only one additional step, the insertion of the second H atom into the Pd–O bond, is required to form propenol.

- deactivation of the surface by decarbonylation of acrolein:  
In parallel to the propenol formation, a fraction of the acrolein molecules decomposes in a decarbonylation reaction resulting in ethylidyne and a carbonyl compound (spectators S2). The two species slowly accumulate on the surface while the propenol formation rate decreases. Ethylidyne and the carbonyl compound might be responsible for the deactivation of the surface, *e.g.* by blocking the Pd sites required for acrolein hydrogenation.

The propenol formation rate exhibits a clear temperature dependence with a strong maximum at 270 K, while the propanal formation rate is approximately zero at 270 K and slightly increases towards higher and lower temperatures. In particular, we have found:

- at low temperature (220 K):  
Only a small fraction of the initially adsorbed acrolein is converted to the oxopropyl species (S1). On this partially modified surface, unselective formation of both products propanal and propenol occurs.
- at high temperature (320 K):  
Acrolein almost completely decomposes in a decarbonylation reaction to CO and ethylidyne, which rapidly cover the entire Pd surface. On the one hand, the high reactivity of the surface towards decarbonylation suppresses the modification of the surface by species S1. On the other hand, the fast formation of CO and ethylidyne rapidly blocks and thus poisons the Pd catalyst.

Our studies on acrolein conversion on Pd(111) and Fe<sub>3</sub>O<sub>4</sub>-supported Pd particles at 270 K show that there is strong structure dependence in the selective partial hydrogenation. On Pd particles, we have observed similar surface reactions as on Pd(111) at 320 K: fast acrolein decarbonylation and no formation of species S1 which would be required for propenol production.

The obtained relations between reactions on the Pd surface and the chemoselective hydrogenation of acrolein are expected to be highly relevant for rational design of new catalytic materials to selectively activate the C=O bond in multiple unsaturated hydrocarbons. Particularly, the insights into the role of spectators, governing the selectivity and activity of the catalyst, hold great potential for the development of future industrial catalysts, *e.g.* ligand-modified metal nanoparticles.

## 10.5 Supporting Information

Figure 10.9 shows the propanal and propenol formation rates in acrolein hydrogenation at 220 K, 235 K, 250 K, 270 K, 300 K, 320 K, and 350 K. At each temperature, the Pd(111) surface has been pre-exposed to  $4.8 \cdot 10^{15}$  H<sub>2</sub>/(cm<sup>2</sup>s) for 300 s before the acrolein beam exposing  $1.5 \cdot 10^{13}$  molecules/(cm<sup>2</sup>s) has been switched on additionally. The time scale has been chosen in a ways that acrolein exposure starts at time 0.

As discussed in the main part of this publication, the Pd(111) crystal is most active and selective for propenol formation at 270 K. The propenol formation starts after an induction period of 24 s, rapidly increases until it reaches a maximum after 100 s and finally slowly decreases. Similar product evolution is observed at 250 K and 300 K. However, at both temperatures, a slightly larger amount of propanal is detected, and at 300 K, the induction period is approximately twice as long.

Strong changes of the product formation rates are detected at temperatures below 250 K and above 300 K. From 250 K to 235 K the propenol formation rate rapidly drops while the activity for propanal production stays approximately the same. Further decrease of the temperature to 220 K does not significantly change the product formation rates.

From 300 K to 320 K, the propenol formation drastically drops and the induction period seems to become shorter again while the propanal production rate slightly increases. At 350 K no hydrogenation product can be detected in the gas phase.

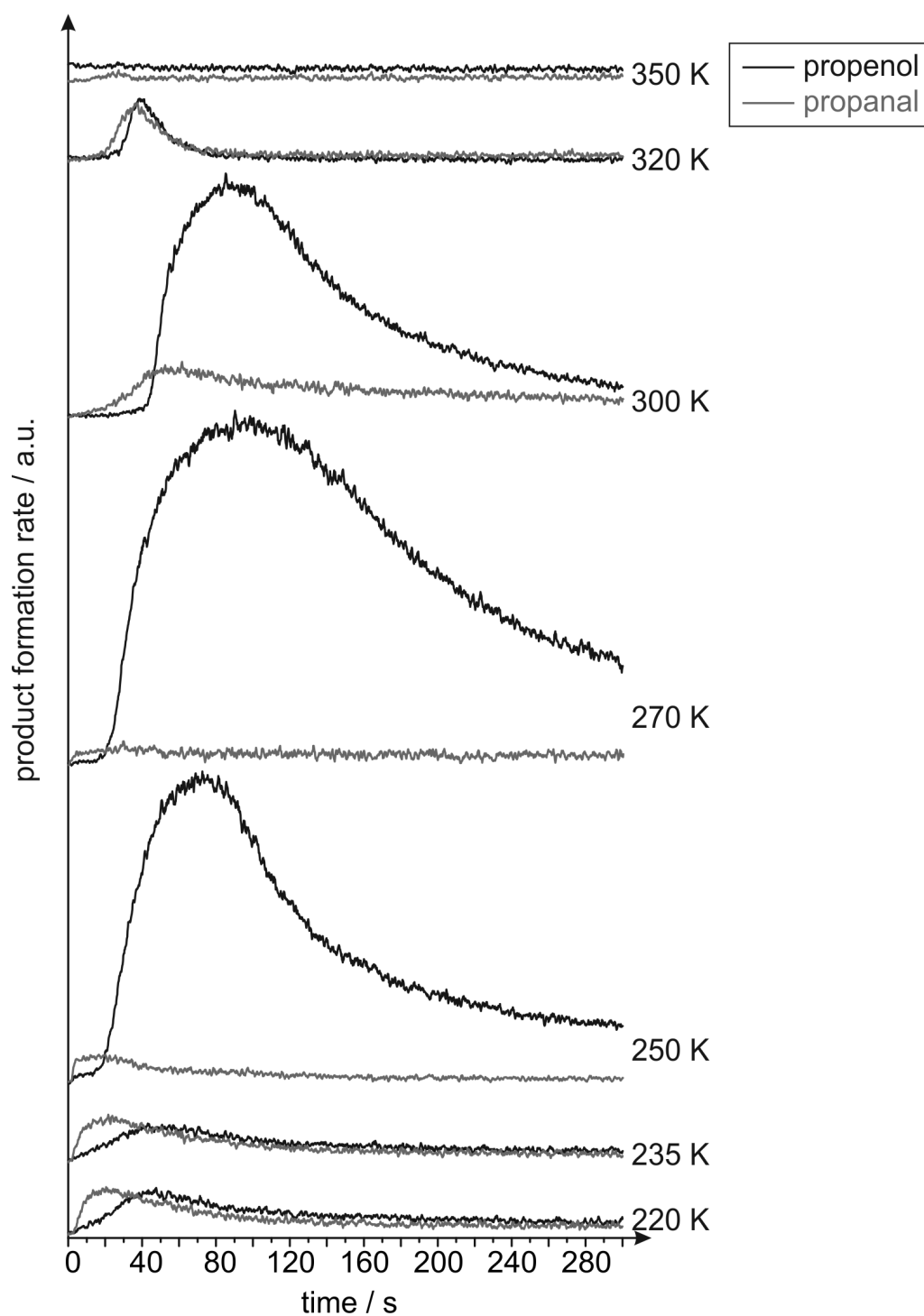


Figure 10.9: Formation rates of propenol (black lines) and propanal (grey lines) on Pd(111) during continuous exposure of acrolein and H<sub>2</sub> at various temperatures.



# 11 Selective Hydrogenation of Acrolein over Pd Model Catalysts: Temperature and Particle Size Effects

*Casey P. O'Brien<sup>1</sup>, Karl-Heinz Dostert<sup>1</sup>, Svetlana Schauermann<sup>1,2</sup>, and Hans-Joachim Freund<sup>1</sup>*

<sup>1</sup>Fritz-Haber-Institut der Max-Planck-Gesellschaft, Faradayweg 4-6, 14195 Berlin, Germany

<sup>2</sup>Institut für Physikalische Chemie, Christian-Albrechts-Universität zu Kiel, Max-Eyth-Str. 1, 24118 Kiel, Germany

*to be submitted*

## Abstract

Selective hydrogenation of either the C=C or the C=O bond in acrolein is a model system for understanding selective surface chemistry. In this work, selective hydrogenation of acrolein is investigated over Pd nanoparticles supported on Fe<sub>3</sub>O<sub>4</sub> as a function of Pd nanoparticle size and temperature. Pd nanoparticles in the 4-12 nm range are in general much less active for C=O bond hydrogenation than Pd(111), which exhibits near 100% selectivity towards the desired product, propenol. The largest Pd nanoparticles in this study (12 nm) produced a significant amount of propenol from selective C=O bond hydrogenation, but only in a narrow temperature range around 250 K. Using in-situ infrared-reflection absorption spectroscopy (IRAS) to detect surface species during the reaction, we were able to understand why the selective hydrogenation of acrolein is so strongly dependent on Pd structure and temperature. We believe that selective hydrogenation of the C=O bond in acrolein requires the formation of a spectator species that is formed on the Pd surface during the beginning of the reaction, and the formation of this activating spectator species is strongly dependent on temperature and Pd structure. At higher temperatures (270 K) acrolein decarbonylates strongly on the Pd nanoparticles, producing CO which covers the facets of the nanoparticles and prevents the formation of the activating spectator species. At lower temperature (220 K), the activating spectator species is formed on the surface of the Pd nanoparticles, but the temperature is too low for significant propenol production. At 250 K, the activating spectator species is formed on the surface of 12 nm Pd nanoparticles, and the temperature is high enough for significant propenol production. Pd nanoparticles smaller than 12 nm did not produce a significant amount of propenol in the 220-270 K range, which suggests that larger Pd nanoparticles favor hydrogenation of the C=O bond in acrolein. It is possible that nanoparticle edges create surface chemistry, such as decarbonylation, that is not favorable for C=O bond hydrogenation.

## 11.1 Introduction

Selective hydrogenation of  $\alpha,\beta$ -unsaturated ketones and aldehydes, a class of compounds which have conjugated C=C and C=O bonds, is a fundamentally interesting problem and an industrially relevant reaction. The propenol produced from selective hydrogenation of the C=O bond is the desired product for the fine chemicals and pharmaceuticals industries, but thermodynamics favors hydrogenation of the C=C bond [30]. Therefore, selective hydrogenation of the C=O bond requires manipulation of kinetic effects by means of a suitable catalyst. However, a lack of fundamental understanding of the parameters governing the selectivity and activity has inhibited the development of practical heterogeneous catalyst systems that can hydrogenate the C=O bond in  $\alpha,\beta$ -unsaturated ketones and aldehydes with high selectivity and activity.

It is generally believed that the adsorption geometry of the reactant on the catalyst surface is an important factor governing the selectivity of  $\alpha,\beta$ -unsaturated ketone hydrogenation [34, 35, 40, 62, 181, 245]. The adsorption geometry of the  $\alpha,\beta$ -unsaturated ketone can be manipulated in favor of C=O bond hydrogenation by adding bulk substituents to the C=C functional group [27, 30, 245]. Acrolein is the most difficult  $\alpha,\beta$ -unsaturated aldehyde to selectively hydrogenate the C=O bond because there are no substituents attached to the C=C group. Higher partial pressures of the reactant have also been shown to enhance the selectivity towards C=O bond hydrogenation [30, 34, 35, 40]. The reason for this has been given that increasing the partial pressure of the reactant, and in effect its surface coverage, causes the C=C group to become more tilted with respect to the surface and less vulnerable to attack by surface hydrogen atoms [27, 34, 62]. The structure of the catalyst also influences the adsorption geometry of the reactant, but how the catalyst structure influences the adsorption geometry is far more subtle, and much less understood, than the effects of molecular structure on adsorption geometry.

Our recent work [185] (Chapter 9) with Pd model catalysts under well-defined ultra-high vacuum conditions has given some new insight into the relationship between catalyst structure and selectivity in partial hydrogenation of acrolein. We showed for the first time that a near 100% selectivity towards hydrogenation of C=O in acrolein is possible over Pd(111). This was a particularly surprising result for a couple of reasons. First, Pd is a very active C=C bond hydrogenation catalyst and has previously showed 100% selectivity towards hydrogenation of C=C in  $\alpha,\beta$ -unsaturated ketones, even when bulky substituents are attached to the C=C bond [246, 247, 295]. Prior to our discovery, Au and Ag were the best known monometallic catalysts for selective hydrogenation of the C=O bond in acrolein, with selectivities of only  $\approx 50\%$  [33, 35, 36, 43, 296]. The second reason that our results were so unexpected is that the acrolein partial pressures at the catalyst surface were in the high-vacuum range. At such low partial pressures, acrolein is expected to have a flat-lying geometry which is not favorable for C=O hydrogenation [245]. In agreement with this expectation, the clean Pd(111) surface was not active for C=O bond hydrogenation. Selective hydrogenation of C=O in acrolein required modification of the Pd(111) surface with a spectator species that formed during the initial stages of the reaction. It is not clear how the spectator species activates the Pd(111) surface

for C=O hydrogenation, but it is possible that the spectator species creates a geometric confinement on the surface and steers the acrolein molecules into an adsorption geometry that is favorable for C=O hydrogenation. Over Pd nanoparticles supported on Fe<sub>3</sub>O<sub>4</sub> (Pd/Fe<sub>3</sub>O<sub>4</sub>), the results were much different than over Pd(111). We observed a near 100% selectivity towards hydrogenation of the C=C bond in acrolein over Pd/Fe<sub>3</sub>O<sub>4</sub>. Therefore, the selective hydrogenation of acrolein is very sensitive to the structure of the Pd catalyst. Further studies are required to understand the strong structure-dependence in the partial hydrogenation of acrolein over Pd.

In this work, we extend our previous study by investigating the influence of Pd nanoparticle size (4-12 nm) and temperature (220-270 K) on the selective hydrogenation of acrolein over Pd/Fe<sub>3</sub>O<sub>4</sub> model catalysts. Gas-phase products of acrolein hydrogenation are detected simultaneously with surface species to gain insight into the mechanism of selective acrolein hydrogenation. We show that selective hydrogenation of acrolein is sensitive to both the temperature and the Pd nanoparticle size. A significant amount of propenol production is observed over 12 nm Pd nanoparticles, but not over 4 or 7 nm Pd nanoparticles, and only in a narrow temperature range around 250 K. Acrolein is more likely to decarbonylate on Pd nanoparticles than on Pd(111), which is possibly due to the edges and corners of the nanoparticles. Therefore, selective hydrogenation of the C=O bond in acrolein is much more difficult over Pd nanoparticles than over Pd(111), but becomes more favorable with increasing Pd particle size.

## 11.2 Experimental

All experiments were performed at the Fritz Haber Institute with an ultra-high vacuum molecular beam machine that has been described in detail previously [100]. Molecular beams of acrolein and H<sub>2</sub> were focused on the sample simultaneously while the sample was held at a constant temperature. The effusive molecular beams were produced by doubly differentially pumped multi-channel array sources. Acrolein (Sigma-Aldrich, 95% purity) was purified prior to each experiment by repeated freeze-pump-thaw cycles. During all reactivity experiments the flux of H<sub>2</sub> on the sample surface was  $4.8 \cdot 10^{15}$  molecules/cm<sup>2</sup>/s. The sample was exposed to H<sub>2</sub> for five minutes prior to acrolein exposure. The flux of acrolein on the sample surface was  $1.5 \cdot 10^{13}$  molecules/cm<sup>2</sup>/s during pulsed reactivity experiments and  $0.6 \cdot 10^{13}$  molecules/cm<sup>2</sup>/s during continuous reactivity experiments. Gas-phase fragments  $m/z = 56, 57$ , and  $58$  were detected with a quadrupole mass spectrometer (ABB Extrel). Surface species were detected simultaneously with gas-phase products using an infrared spectrometer (Bruker IFS 66v) with an MCT detector and a spectral resolution of 2 cm<sup>-1</sup>.

The method for preparing the Pd/Fe<sub>3</sub>O<sub>4</sub> model catalysts has been described in detail previously [153]. Briefly, a well-ordered  $\approx 10$  nm thick Fe<sub>3</sub>O<sub>4</sub> film was grown on a Pt(111) substrate (see [138, 142] for details) followed by Pd deposition onto the Fe<sub>3</sub>O<sub>4</sub> film at 120 K by physical vapor deposition of Pd (Goodfellow, >99.9%) using a commercial evaporator (Focus EFM 3). After depositing Pd, the sample was annealed at 600 K and the Pd nanoparticles were stabilized by repeated cycles of oxidation and reduction at 500 K [152].

The size of the Pd nanoparticles was controlled by the nominal thickness of the Pd film deposited onto the  $\text{Fe}_3\text{O}_4$  substrate at 120 K (see [153] for details). The Pd(111) crystal was cleaned by repeated cycles of  $\text{Ar}^+$  sputtering at room temperature, annealing at 1000 K, and oxidation in  $1 \cdot 10^{-6}$  mbar  $\text{O}_2$  at 750 K. The cleanliness of the Pd/ $\text{Fe}_3\text{O}_4$  and Pd(111) samples was verified prior to every experiment by IRAS of adsorbed CO.

## 11.3 Results and Discussion

### 11.3.1 Influence of Temperature and Particle Size on Gas-Phase Products of Acrolein Hydrogenation

Selective hydrogenation of acrolein over Pd is strongly dependent on the structure of the Pd catalyst [185] (Chapter 9). Here we investigate the effects of temperature and Pd particle size on the partial hydrogenation of acrolein. A continuous beam of  $\text{H}_2$  was focused on the sample surface, which was held at constant temperature, for five minutes prior to the introduction of acrolein. After five minutes of hydrogen exposure, an acrolein molecular beam was exposed to the sample simultaneously in six second pulses while the product gas was analyzed with a mass spectrometer. Figure 11.1 shows the production rate of propenol (left column) and propanal (right column) over Pd(111) and Pd/ $\text{Fe}_3\text{O}_4$  model catalysts with varying Pd particle size (4 nm, 7 nm, and 12 nm) at 220 K (top row), 250 K (middle row), and 270 K (bottom row).

There was no significant production of propenol over all of the (4 nm, 7 nm, and 12 nm) Pd/ $\text{Fe}_3\text{O}_4$  catalysts in the 220-270 K temperature range. Propenol production was only observed over Pd(111), with the rate increasing from almost zero at 220 K to a maximum at 270 K. Neither propenol nor propanal were produced during acrolein hydrogenation over 4 nm Pd particles in the 220-270 K temperature range. Similar propanal production rates were observed over 7 and 12 nm Pd particles at all three temperatures, with a maximum rate at 220 K. There was a small, but significant, amount of propanal produced during acrolein hydrogenation over Pd(111) at all three temperatures. These results show that selective hydrogenation of acrolein is highly sensitive to the structure of the Pd catalyst. Pd nanoparticles, in general, are not active for propenol production under the conditions of these experiments. In the following sections, we will investigate the influence of Pd particle size and temperature on the surface chemistry during acrolein hydrogenation in order to understand the structure-dependent selectivity displayed in Figure 11.1.

### 11.3.2 Comparison of Pd(111) and Pd/ $\text{Fe}_3\text{O}_4$ at 270 K

Simultaneous detection of surface species with IRAS and gas-phase species with mass spectrometry (IRAS-MS) is a useful technique for elucidating reaction mechanisms. Here we use IRAS-MS to understand the mechanisms that are responsible for the high structure sensitivity displayed by Pd catalysts in selective hydrogenation of acrolein. We begin with the conditions that are optimal for propenol production: acrolein hydrogenation over Pd(111) at 270 K. Figure 11.2(a) displays the gas-phase production rate of propenol and propanal over Pd(111) during continuous exposure to acrolein and  $\text{H}_2$  at 270 K. Similar to the results displayed in Figure 11.1, there is a nearly 100% selectivity towards propenol

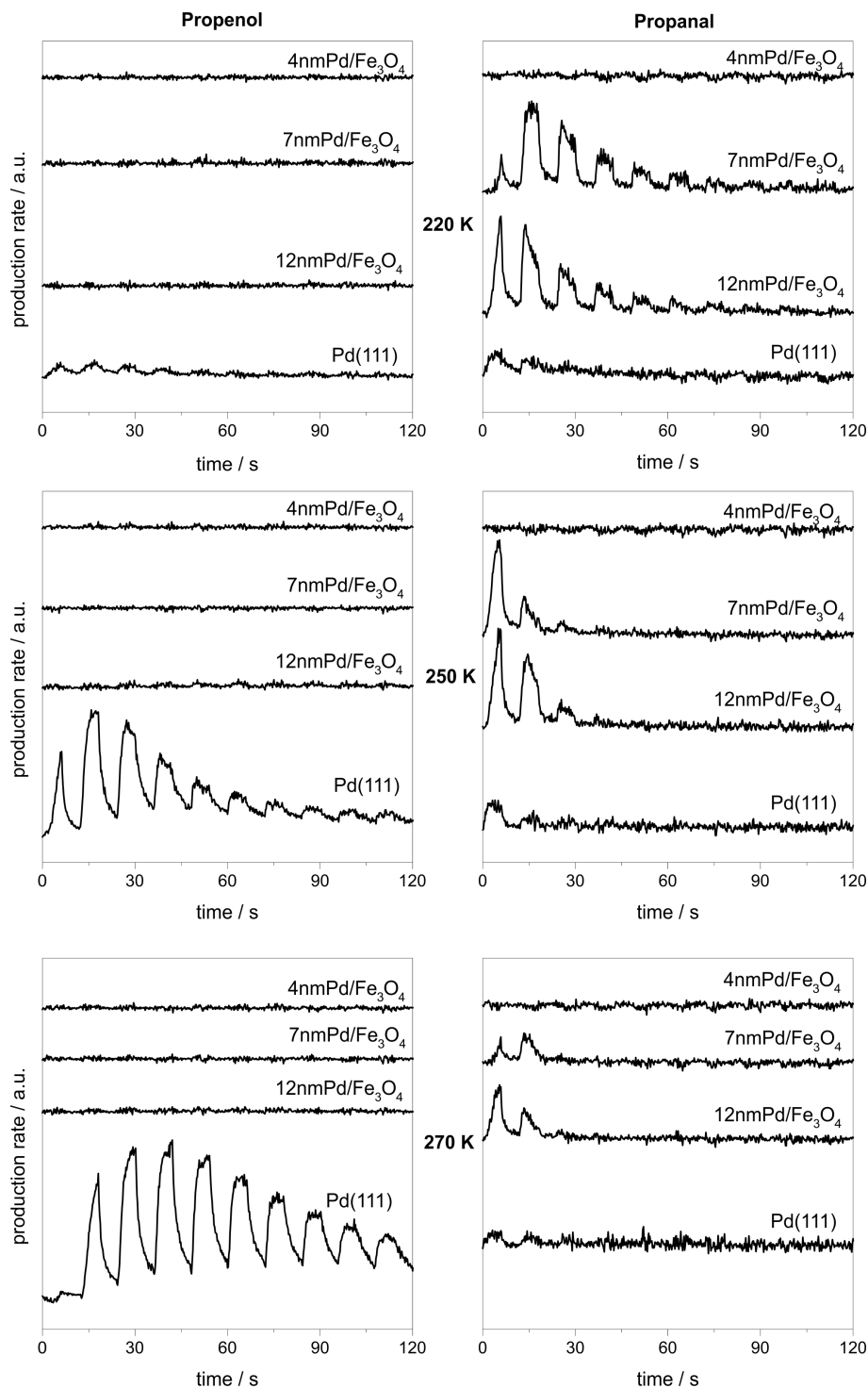


Figure 11.1: Gas-phase production of propenol (left column) and propanal (right column) over  $\text{Pd}(111)$  and  $\text{Pd}/\text{Fe}_3\text{O}_4$  model catalysts with average Pd nanoparticle size 4, 7, and 12 nm at 220 K (top row), 250 K (middle row), and 270 K (bottom row).

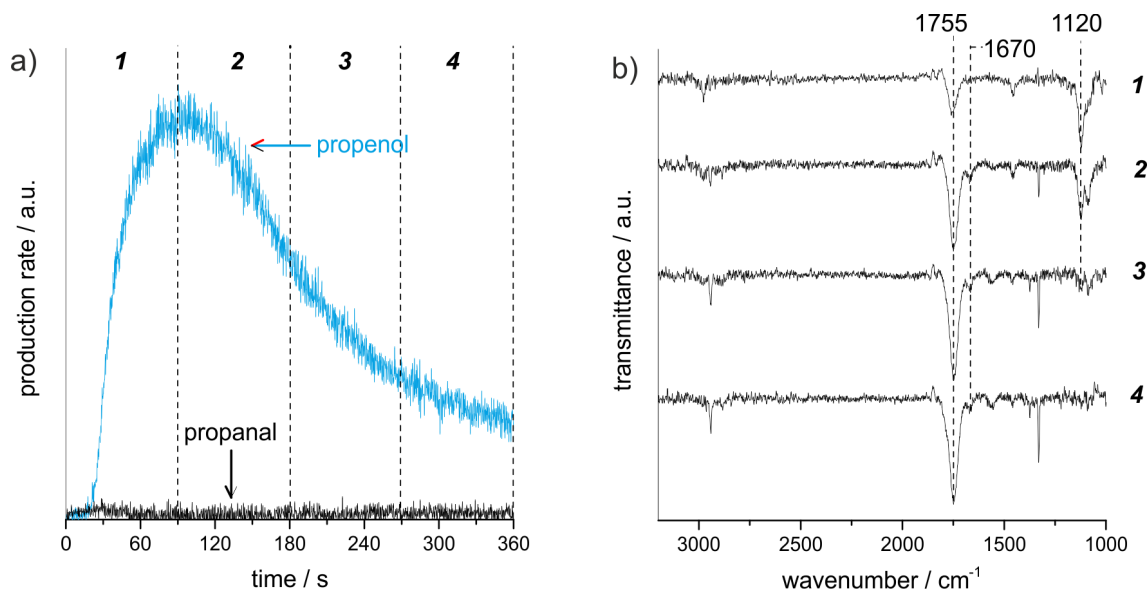


Figure 11.2: Acrolein hydrogenation over Pd(111) at 270 K. (a) Gas-phase production of propanal (black) and propenol (red). (b) Time-resolved IRAS spectra collected during acrolein hydrogenation. Spectra labeled 1-4 were collected during the regions labeled 1-4 in the gas phase products.

production over Pd(111) at 270 K. There is no propenol production during the first  $\approx 20$  seconds of the reaction, which suggests that the Pd(111) surface requires modification by exposure to acrolein and  $\text{H}_2$  to become active for propenol production. The rate of propenol production increases sharply from zero at  $\approx 20$  seconds to a maximum at  $\approx 90$  seconds and then the rate decreases slowly. The corresponding IRAS spectra collected during acrolein hydrogenation over Pd(111) at 270 K are displayed in Figure 11.2(b). There are many peaks in the IR spectra shown in Figure 11.2(b). We will only discuss the peaks at  $1750\text{ cm}^{-1}$ ,  $1670\text{ cm}^{-1}$  and  $1120\text{ cm}^{-1}$ . For a detailed analysis of all the other peaks, refer to [176] (Chapter 8). The band near  $1670\text{ cm}^{-1}$  is associated with the C=O stretching mode of molecular acrolein adsorbed on Pd(111). The band at  $1755\text{ cm}^{-1}$  is most likely associated with a C=O stretching mode, however, the position of this band is blue-shifted by  $\approx 85\text{ cm}^{-1}$  relative to the C=O stretching band in molecular acrolein. We believe that the band at  $1755\text{ cm}^{-1}$  is associated with a spectator species which is the product of partial hydrogenation of the C=C bond in acrolein. Furthermore, we believe that this species/adsorbate may be responsible for activating the Pd(111) surface for propenol production, although further work is required to clarify the mechanism. Finally, the band at  $1120\text{ cm}^{-1}$  is most likely associated with a C–O stretching mode of the reactive intermediate in propenol production [185] (Chapter 9).

In order to understand why Pd nanoparticles are not active for propenol production at 270 K, IRAS was used to detect surface species simultaneously with gas-phase products during acrolein hydrogenation. Figure 11.3(a) shows the production rate of propanal and propenol over 12 nm Pd particles at 270 K during continuous exposure of acrolein and

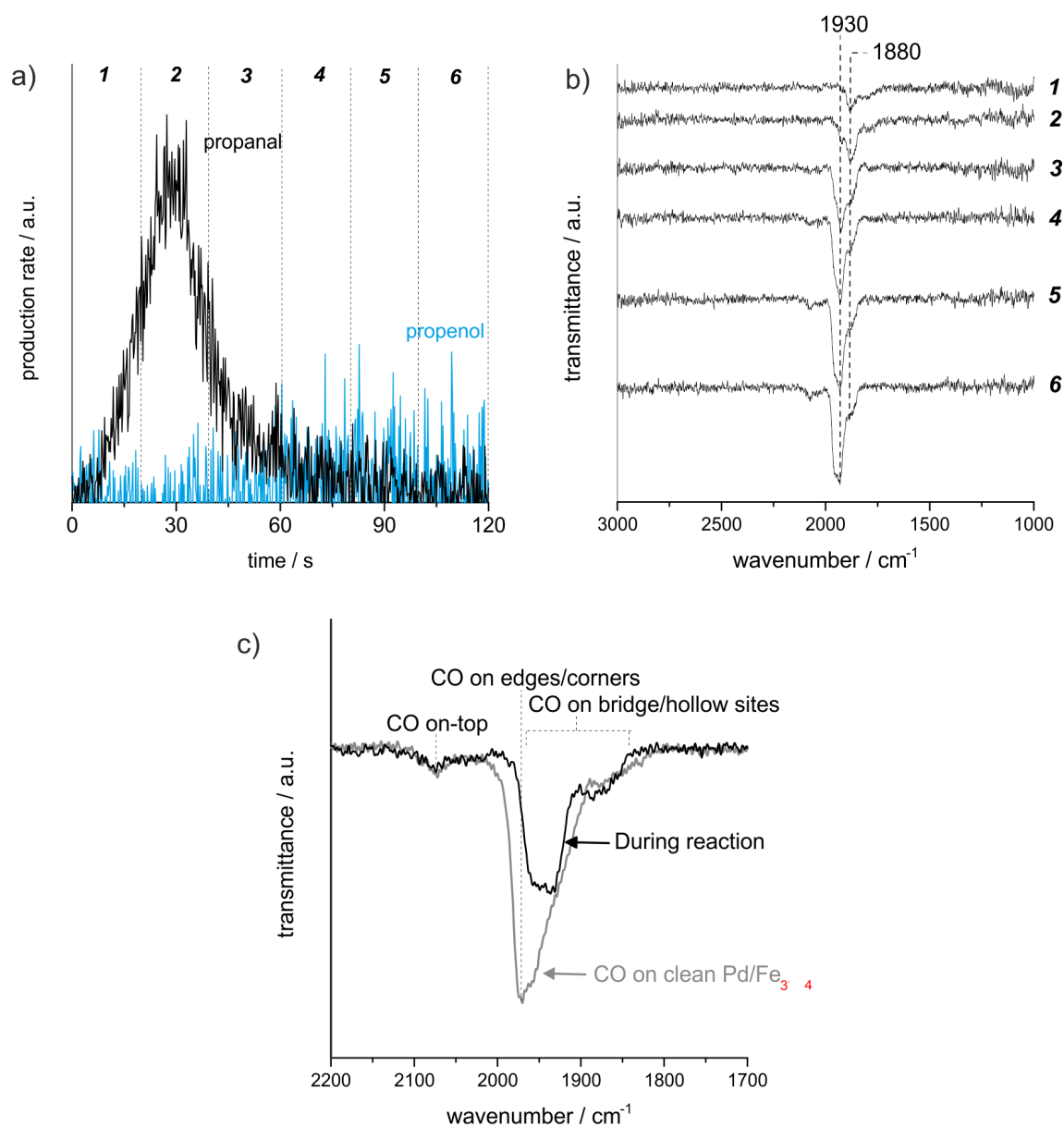


Figure 11.3: Acrolein hydrogenation over  $12\text{nmPd}/\text{Fe}_3\text{O}_4$  at 270 K. (a) Gas-phase production of propanal (black) and propenol (red). (b) Time-resolved IRAS spectra collected during acrolein hydrogenation. Spectra labeled 1-6 were collected during the corresponding regions labeled 1-6 in (a). (c) Comparison of the IRAS spectrum collected during acrolein hydrogenation over  $12\text{nmPd}/\text{Fe}_3\text{O}_4$  at 270 K (region 6 in (a) and (b)) to the IRAS spectrum of CO adsorbed on clean  $12\text{nmPd}/\text{Fe}_3\text{O}_4$ .

H<sub>2</sub>. As expected, there was no significant production of propenol. The rate of propanal production increases from the beginning of the reaction to a maximum at  $\approx 30$  seconds and then decreases to zero after  $\approx 90$  seconds. Figure 11.3(b) shows the IRAS spectra labeled 1-6 collected during the corresponding regions in Figure 11.3(a). The series of IRAS spectra shown in Figure 11.3(b) are significantly different than the series collected during acrolein hydrogenation over Pd(111) at 270 K (Figure 2(b)). Bands at  $1750\text{ cm}^{-1}$  (C=O stretching),  $1670\text{ cm}^{-1}$  (C=O stretching in acrolein), and  $1120\text{ cm}^{-1}$  (C–O stretching) are not present. Instead, there are bands in the  $1800\text{--}1960\text{ cm}^{-1}$  region, which become more intense and red-shifted with increasing reaction time. These bands are characteristic of CO adsorbed on 12 nm Pd particles [153]. To demonstrate that the IR spectra displayed in Figure 11.3(b) are the result of CO adsorbed on Pd nanoparticles, Figure 11.3(c) shows a comparison of the IR spectrum labeled 6 in Figure 11.3(b) to the IR spectrum of a saturation coverage of CO on clean 12 nm Pd particles. The two spectra are similar except the spectrum of CO on clean 12 nm Pd particles is more intense at  $1970\text{ cm}^{-1}$ , which is the position associated with CO adsorbed on edges of Pd particles [153]. These results show that acrolein decomposes on Pd nanoparticles during acrolein hydrogenation at 270 K, producing CO which covers the facets, and some other decomposition products that preferentially adsorb on the edges of the nanoparticles.

### 11.3.3 Influence of Sample Temperature on Pd Nanoparticle Surface Chemistry

During pulsed reactivity experiments (Figure 11.1), reducing the sample temperature from 270 K to 220 K increased the rate of propanal production over both 12 nm and 7 nm Pd particles, but did not significantly change the selectivity. In this section, the influence of sample temperature on the surface chemistry during acrolein hydrogenation over 12 nm Pd particles is investigated by IRAS-MS at sample temperatures of 220 K and 250 K. At 270 K, we saw that acrolein decomposed on 12 nm Pd particles, producing CO which covered the facets of the nanoparticles. At 220 and 250 K, significantly different surface chemistry is observed than at 270 K. Figure 11.4 shows the IRAS-MS results of acrolein hydrogenation over 12 nm Pd particles at 220 K (top row) and 250 K (bottom row).

As expected, there was no propenol detected in the gas phase during acrolein hydrogenation over 12 nm Pd particles at 220 K (Figure 4(a)). The rate of propanal production increased sharply to a maximum  $\approx 30$  seconds after the introduction of acrolein, and then decreased slowly and approached zero after  $\approx 180$  seconds of acrolein hydrogenation. The IR spectra collected during acrolein hydrogenation over 12 nm Pd particles at 220 K are displayed in Figure 11.4(b). There are bands at  $\approx 1750\text{ cm}^{-1}$  and  $\approx 1670\text{ cm}^{-1}$  in the spectrum collected during the first 45 seconds of acrolein hydrogenation (spectrum 1). The band at  $1670\text{ cm}^{-1}$  is most likely associated with C=O stretching in molecular acrolein. The band at  $1755\text{ cm}^{-1}$  is likely associated with C=O stretching that is not conjugated to C=C. A third peak appears at  $1855\text{ cm}^{-1}$  in between 45-90 seconds and the IRAS spectra do not change significantly after 90 seconds of acrolein hydrogenation at 220 K. The peak at  $1855\text{ cm}^{-1}$  is most likely associated with CO adsorbed on facets of the Pd nanoparticles [153]. Interestingly, the band at  $1755\text{ cm}^{-1}$  was also observed

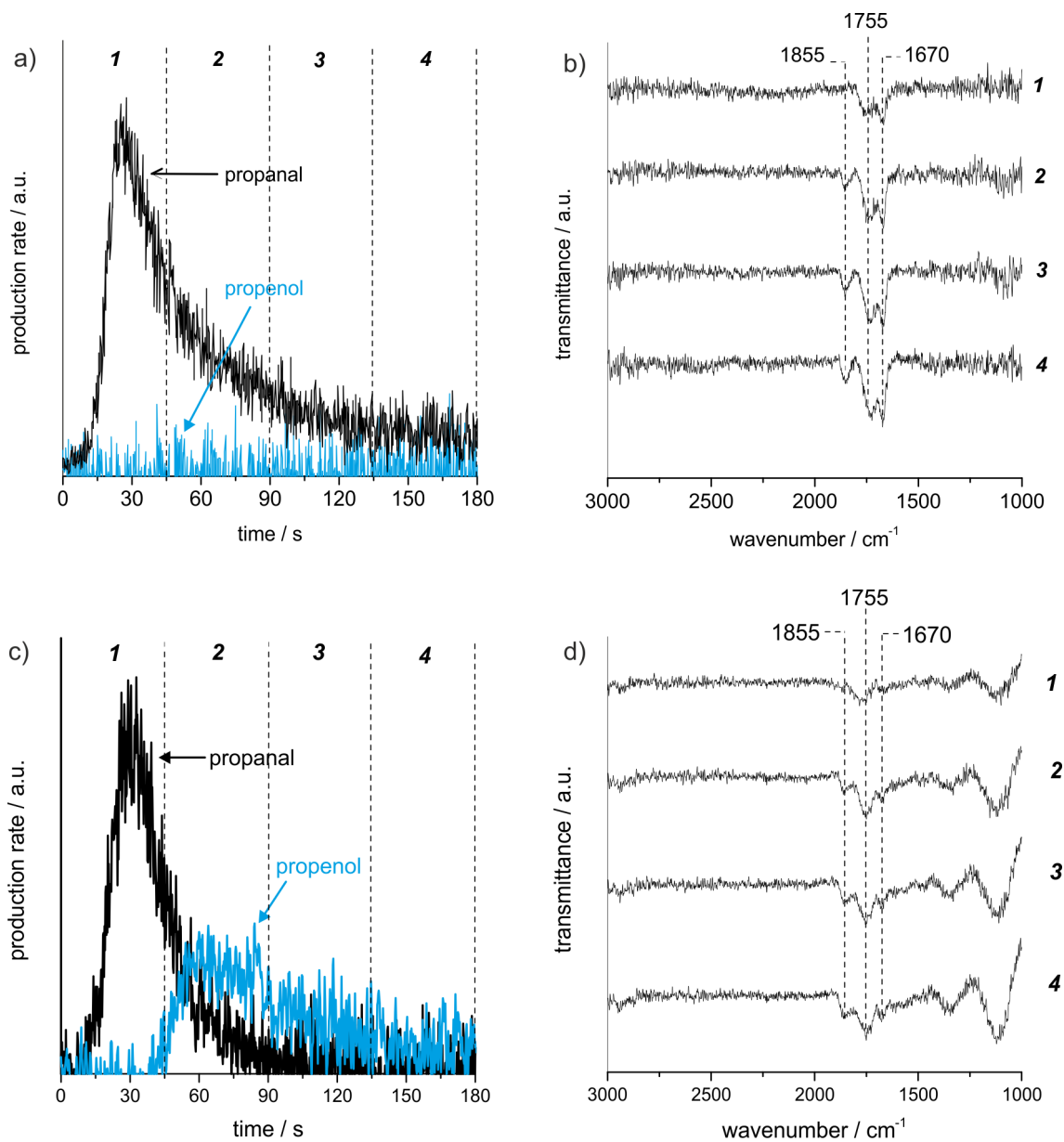


Figure 11.4: Acrolein hydrogenation over  $12\text{nmPd}/\text{Fe}_3\text{O}_4$  at 220 K (top row) and 250 K (bottom row). Gas-phase production of propanal (black) and propenol (red) at (a) 220 K and (c) 250 K. Time-resolved IRAS spectra collected during acrolein hydrogenation at (b) 220 K and (d) 250 K. Spectra labeled 1-4 were collected during the regions labeled 1-4 in the gas phase products.

during acrolein hydrogenation over Pd(111) at 270 K (see Figure 11.2(b)) and we believe that this band might be associated with the species that activates the Pd(111) surface for propenol production. However, the rate of propenol production over Pd(111) is very low at 220 K (see Figure 11.1) and we would not expect to see propenol production over Pd nanoparticles at 220 K, even if the activating surface species is observed.

If the surface species with a characteristic band at  $1755\text{ cm}^{-1}$  is responsible for activating the Pd(111) surface for propenol production, and this band is also observed during acrolein hydrogenation over 12 nm Pd nanoparticles at 220 K, then it could be possible to produce propenol over Pd particles at a slightly higher temperature. In order to test this hypothesis, we performed acrolein hydrogenation over 12 nm Pd particles at 250 K, shown in Figure 11.4, while monitoring (c) gas-phase products and (d) surface species simultaneously. Similar to the results obtained at 220 K, the rate of propanal production (Figure 4(c)) reaches a maximum at  $\approx 30$  seconds and then slowly decays to zero after  $\approx 120$  seconds of acrolein hydrogenation. In contrast to the results at 220 K, however, there is a significant amount of propenol production over 12 nm Pd particles at 250 K following a  $\approx 45$  second induction period at the beginning of the reaction. The rate of propenol production reaches a maximum at  $\approx 60$  seconds and then begins to slowly decay to zero after  $\approx 150$  seconds. The amount of propenol produced over 12 nm Pd particles is much less ( $\approx 1/30^{\text{th}}$ ) than the amount produced over Pd(111) at 270 K, but it is still significant. We did not observe any propenol over 12 nm Pd particles at 250 K during pulsed reactivity experiments (Figure 11.1). It's possible that continuous exposure of acrolein and/or the lower flux of acrolein molecules during IRAS-MS experiments is more favorable for propenol production.

The IR spectra collected during acrolein hydrogenation over 12 nm Pd particles at 250 K (Figure 4(d)) are similar to those collected at 220 K; there are 3 main peaks at  $1855$ ,  $1755$ , and  $1670\text{ cm}^{-1}$  that are associated with CO on particle facets, non-conjugated C=O stretching, and C=O stretching in acrolein, respectively. The waves displayed in all four spectra below  $\approx 1500\text{ cm}^{-1}$  are from an unstable background and are not from infrared absorption by adsorbed chemical species. Due to the waves, and also from the very low rate of propenol production, we are not able to identify the propenol intermediate species at  $1120\text{ cm}^{-1}$ . However, our hypothesis is confirmed and propenol production is possible over 12 nm Pd particles in a narrow temperature range around 250 K.

In this section, we showed that temperature has a significant effect on the surface chemistry during acrolein hydrogenation over 12 nm Pd particles. At higher temperature (270 K), acrolein decarbonylates, producing mainly CO which covers the facets of the Pd nanoparticles. At lower temperature (220 K), acrolein decomposes to a lesser extent than at 270 K, producing some CO, but also some partially hydrogenated surface species. We believe that this partially hydrogenated surface species, which is also observed on the Pd(111) surface during acrolein hydrogenation at 270 K, may be responsible for activating Pd(111) facets of Pd nanoparticles for propenol production. Although this partially hydrogenated species is observed on the 12 nm Pd particles surface during acrolein hydrogenation at 220 K, this temperature is too low for hydrogenating the C=O bond to

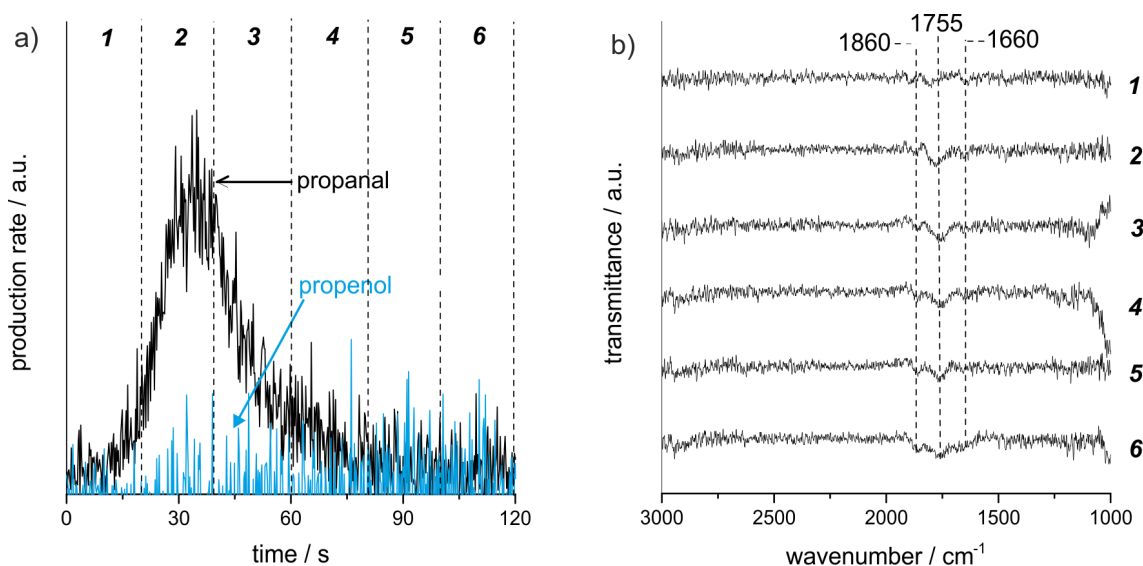


Figure 11.5: Acrolein hydrogenation over 7nmPd/Fe<sub>3</sub>O<sub>4</sub> at 250 K. (a) Gas-phase production of propanal (black) and propenol (red). (b) Time-resolved IRAS spectra collected during acrolein hydrogenation. Spectra labeled 1-6 were collected during the regions labeled 1-6 in the gas phase products.

produce the propenol. At slightly higher temperature, however, the conditions are right for propenol production over 12 nm Pd particles: the partially hydrogenated surface species is formed and propenol production is observed. The amount of propenol produced over 12 nm Pd particles at 250 K is much smaller ( $\approx 1/30^{\text{th}}$ ) than the amount produced over Pd(111) at 270 K, however. In the next section we investigate the effects of Pd particle size on the selective hydrogenation of acrolein.

#### 11.3.4 Particle Size Effects

The influence of Pd particle size on the production of propanal and propenol is evident in Figure 11.1. The 4 nm Pd particles did not produce a significant amount of either propenol or propanal. It is not clear why the 4 nm particles were inactive. There were no species detected on the surface of the 4 nm Pd particles during acrolein hydrogenation in the 220-270 K range, so it is likely that the concentration of Pd atoms is too low to turnover a significant number of acrolein molecules. The amount of Pd in the 4nmPd/Fe<sub>3</sub>O<sub>4</sub> catalyst is more than an order-of-magnitude less than 7-nm-Pd/Fe<sub>3</sub>O<sub>4</sub> and 12-nm-Pd/Fe<sub>3</sub>O<sub>4</sub>. The activity of the 7 nm and 12 nm Pd particles was similar during pulsed acrolein hydrogenation experiments in the 220-270 K temperature range (see Figure 11.1). However, we will show that there is a significant difference in the selectivity of acrolein hydrogenation over 7 nm and 12 nm particles that is not evident in the pulsed reactivity experiments.

In the previous section we showed that propenol production was possible over 12 nm Pd particles, but only in a very narrow temperature range around 250 K. Here we show

that the Pd nanoparticle size also has a significant influence on the selectivity at 250 K. Figure 11.5(a) shows the gas-phase production of propanal and propenol during acrolein hydrogenation over 7 nm Pd particles at 250 K. Unlike the 12 nm particles, there was no significant production of propenol over 7 nm particles at 250 K. IRAS spectra collected during acrolein hydrogenation over 7 nm particles at 250 K are displayed in Figure 11.5(b), with spectra labeled 1-6 collected during the corresponding regions in Figure 11.5(a). Similar to the IRAS spectra collected during acrolein hydrogenation over 12 nm particles at 250 K, there are three main bands at 1860, 1760, and 1660  $\text{cm}^{-1}$  that are associated with CO on particle facets, non-conjugated C=O stretching, and C=O stretching in acrolein, respectively. It is not clear from IRAS-MS why the 12 nm particles are active for propenol, whereas the 7 nm particles aren't. It's possible that the concentration of the surface species which activates the particles for propenol production is much smaller on the 7 nm particles than on the 12 nm particles. It is also possible that larger modified domains are more efficient, or that a minimum domain size is required, for alcohol production.

## 11.4 Discussion

We have shown that there is a strong structure dependence in the selective partial hydrogenation of acrolein over Pd model catalysts. The change in selectivity from nearly 100% towards propenol over Pd(111) to nearly 100% towards propanal over Pd nanoparticles (7 or 12 nm), displayed in Figure 11.1, is the most drastic example of the strong influence of the Pd structure on the selective partial hydrogenation of acrolein. The 12 nm Pd particles were capable of producing a small amount of propenol in a narrow temperature range around 250 K, but no propenol production was observed over 7 or 4 nm Pd particles in the 220-270 K temperature range. Therefore, it appears that the selectivity towards propenol production increases with increasing Pd particle size, from 0% over 4 and 7 nm particles up to nearly 100% over the Pd(111) single crystal, which is essentially an infinitely large particle. It is possible that smaller Pd particles have a higher concentration of edge sites than larger particles, and these edge sites catalyze some surface reactions, for example acrolein decomposition, that prevent propenol production.

Using IRAS we were able to gain insight into the surface chemistry that is responsible for the structure-dependent selectivity in acrolein partial hydrogenation. There were several species observed on the surface of Pd(111) during acrolein hydrogenation at 270 K, including a species which we believe to be an intermediate with a characteristic absorption band near 1120  $\text{cm}^{-1}$ , and a spectator species at 1755  $\text{cm}^{-1}$ . We believe that the spectator surface species, which has a characteristic infrared absorption band near 1755  $\text{cm}^{-1}$  that is associated with a C=O bond that is not conjugated to a C=C bond (i.e. not acrolein), is responsible for controlling the selectivity. The exact structure of this species is not clear from our results, but we believe that it results from the partial hydrogenation of the C=C bond in acrolein, leaving the C=O bond intact. It is not clear how this surface species activates the Pd(111) surface for propenol production. It's possible that a dense overlayer of this partially hydrogenated acrolein surface species forces incoming acrolein molecules to interact with the surface in a geometry that is favorable for C=O bond hydrogenation. This spectator species which activates the Pd(111) surface for propenol production is not

observed on the surface of Pd nanoparticles (7 and 12 nm) during acrolein hydrogenation at 270 K because acrolein decomposes to CO, which covers the facets of the particles. Therefore, it is likely that significant propenol production is not observed over Pd nanoparticles because the edges of Pd nanoparticles catalyze the decomposition of acrolein to CO, instead of forming the spectator species which activates the surface for propenol production.

Temperature also has a significant influence on the selectivity in partial hydrogenation over 12 nm Pd particles. At 270 K acrolein decarbonylates on 7 and 12 nm Pd particles, producing CO which covers the facets. At lower temperature, acrolein decomposes to a lesser extent and other surface species are observed. At 220 K, the spectator species which we believe is responsible for activating the Pd(111) surface for propenol production, with a characteristic absorption band near 1755 cm<sup>-1</sup>, is observed on the surface of 7 and 12 nm Pd particles; however, 220 K is too low for significant production of propenol. At 250 K, the temperature is high enough for propenol production, but not so high that acrolein decomposes to CO, and a small amount of propenol production is observed on 12 nm Pd particles. These results improve our understanding of the structure-dependence in selective hydrogenation of a model multi-unsaturated compound acrolein.

### 11.5 Conclusions

Selective hydrogenation of either the C=C or the C=O bond in acrolein is strongly dependent on temperature and the structure of the Pd catalyst. We believe that selective hydrogenation of the C=O bond in acrolein is related to a spectator species that is formed on the Pd surface during the beginning of the reaction, and the formation of this activating spectator species is strongly dependent on temperature and Pd structure. Pd nanoparticles in general are much less active for C=O bond hydrogenation than single crystal Pd(111). The largest Pd nanoparticles in this study (12 nm) produced a significant amount of propenol from selective C=O bond hydrogenation, but only in a narrow temperature range around 250 K. At higher temperature (270 K), acrolein decarbonylates on Pd nanoparticles producing CO which covers the facets and prevents the formation of the activating spectator species. At lower temperature (220 K), the activating spectator species is formed on the surface of Pd nanoparticles, but the temperature is too low for hydrogenation of the C=O bond, even over Pd(111).

## 12 Insights into the Origin of Selectivity in Acrolein Conversion over Pd/Fe<sub>3</sub>O<sub>4</sub>

*Karl-Heinz Dostert<sup>1</sup>, Svetlana Schauermann<sup>1,2</sup>, and Hans-Joachim Freund<sup>1</sup>*

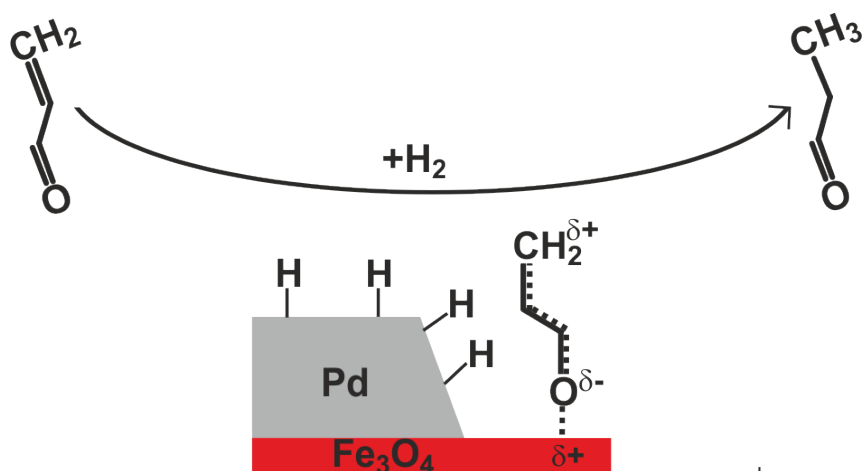
<sup>1</sup>Fritz-Haber-Institut der Max-Planck-Gesellschaft, Faradayweg 4-6, 14195 Berlin, Germany

<sup>2</sup>Institut für Physikalische Chemie, Christian-Albrechts-Universität zu Kiel, Max-Eyth-Str. 1, 24118 Kiel, Germany

*to be submitted*

## Abstract

Atomic-level understanding of kinetic effects that govern the selectivity in partial hydrogenation of  $\alpha,\beta$ -unsaturated aldehydes is of pivotal importance for the rational design of new catalytic materials with the desired selectivity towards C=C or C=O bond conversion. However, in previous studies, the reason for the high selectivity towards C=C bond hydrogenation over Fe<sub>3</sub>O<sub>4</sub>-supported Pd particles remained unclear. In the present study, the binding of acrolein to an Fe<sub>3</sub>O<sub>4</sub> film and to Fe<sub>3</sub>O<sub>4</sub>-supported Pd particles is studied by infrared reflection-absorption spectroscopy (IRAS) at 120 K and temperature-programmed desorption (TPD) experiments to obtain detailed information on the activation of chemical bonds by means of Fe<sub>3</sub>O<sub>4</sub> and Pd. IRAS studies show strongly inclined acrolein molecules on the Fe<sub>3</sub>O<sub>4</sub> support with heavily perturbed chemical bonds. Especially the C=O bond appears significantly weakened in Fe<sub>3</sub>O<sub>4</sub>-adsorbed acrolein. Nevertheless, in TPD experiments, acrolein molecules stay intact on the Fe<sub>3</sub>O<sub>4</sub> film until desorption; on Pd/Fe<sub>3</sub>O<sub>4</sub>, however, decomposition as well as conversion to propanal occurs. Our results indicate that the Fe<sub>3</sub>O<sub>4</sub> support promotes the conversion of the C=C bond by activation of the  $\beta$ -C atom. The polarized form of the C=O bond ( $\text{C}=\text{O} \leftrightarrow \text{C}^+-\text{O}^-$ ) seems to be stabilized by a Lewis acid–base complex between the oxygen atom and electron accepting sites of the support; the electrophilic character of the carbonyl-C atom is transferred along the conjugated  $\pi$  system to the  $\beta$ -C atom.



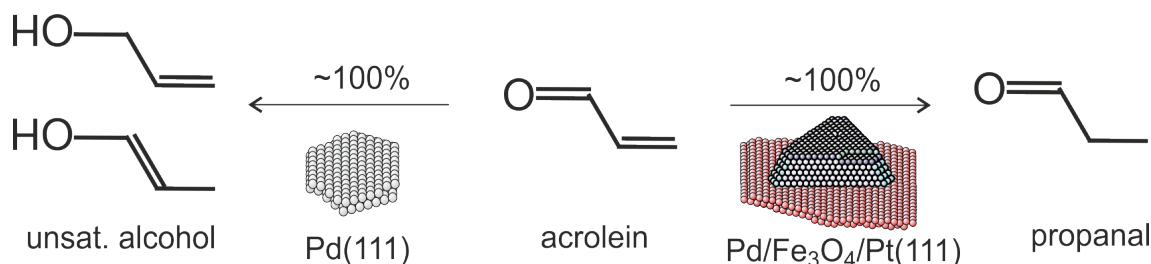


Figure 12.1: Reverse selectivity in hydrogenation of acrolein over Pd/Fe<sub>3</sub>O<sub>4</sub> model catalysts and Pd(111): Over Pd/Fe<sub>3</sub>O<sub>4</sub>, acrolein is converted to propanal with nearly 100% selectivity; while over a Pd(111) single crystal, unsaturated alcohols are formed with nearly 100% selectivity.

## 12.1 Introduction

The catalytic hydrogenation of  $\alpha,\beta$ -unsaturated aldehydes is of broad interest for fundamental understanding as well as for industrial applications [30]. The primary hydrogenation product is either a saturated aldehyde or an unsaturated alcohol. Thermodynamically, the hydrogenation of the C=C bond to the saturated aldehyde is favored [28]. However, fundamental understanding of the parameters governing the selectivity is necessary to avoid the formation of undesired products and thereby an often difficult and cost-intensive separation process.

It is generally believed that the adsorption geometry of the reactant on the catalyst surface is an important factor governing the selectivity of the hydrogenation reaction. The adsorption geometry of an  $\alpha,\beta$ -unsaturated aldehyde or ketone can be manipulated by adding bulky substituents [27, 31, 32]. However, also the structure of the catalyst can have a decisive influence on the selectivity. Enhanced conversion of polar functional groups, such as carbonyl groups, carbon monoxide, and carbon dioxide, over Pt group metals was achieved upon addition of promoters. Studies on the promoting effect of various metal oxides show that the activity of a catalyst for conversion of the C=O bond scales with their Lewis acidity, indicating a critical role of charge transfer between the C=O group and cationic sites of the metal oxide [297, 298]. Particularly TiO<sub>2</sub> supports were found to increase the selectivity of C=O bond hydrogenation in unsaturated aldehydes and ketones over supported Pt catalysts [41, 52, 54].

Figure 12.1 summarizes the previously observed strong dependence of the selectivity in partial hydrogenation of acrolein on the structure of the Pd catalyst. Highly selective formation of unsaturated alcohols was observed over a Pd(111) single crystal, while propanal formation occurred with  $\approx 100\%$  selectivity over Fe<sub>3</sub>O<sub>4</sub>-supported Pd nanoparticles. The formation of unsaturated alcohols was found to critically depend on the presence of an overlayer of spectator species formed on Pd(111) at the initial stages of the reaction. The origin of the high selectivity towards propanal formation by C=C bond hydrogenation over Pd/Fe<sub>3</sub>O<sub>4</sub>, however, remained unclear [185–187] (Chapters 9, 10 and 11).

In a previous publication we reported the molecular structures of acrolein, propanal and allyl alcohol on a Pd(111) single crystal surface. We found mostly unperturbed molecules in the multilayer regime and strongly adsorbed acrolein species in the first monolayer with

C=O and C=C bonds parallel to the Pd(111) surface [176] (Chapter 8).

In order to explore the origin of the selectivity in acrolein hydrogenation over Pd/Fe<sub>3</sub>O<sub>4</sub> model catalysts, we here report a detailed study on the binding of acrolein to an Fe<sub>3</sub>O<sub>4</sub> film and Fe<sub>3</sub>O<sub>4</sub>-supported Pd particles with a diameter of 7 nm by coverage-dependent infrared reflection-absorption spectroscopy (IRAS) and temperature-programmed desorption (TPD) experiments. We particularly focus on the molecular structure of acrolein in the low-coverage limit. The results indicate that the Fe<sub>3</sub>O<sub>4</sub> support promotes the activation of the  $\beta$ -C atom and thus the selective conversion of the C=C bond over Pd/Fe<sub>3</sub>O<sub>4</sub> model catalyst.

## 12.2 Experimental Details

All experiments were performed at the Fritz-Haber-Institut, Berlin, in an ultrahigh vacuum (UHV) apparatus that has been described in detail before [100]. Acrolein was dosed onto the sample through a doubly differentially pumped multi-channel array source controlled by valves and shutters. The source was operated at room temperature, and the beam diameter was chosen to exceed the sample size. The method for preparing the Pd/Fe<sub>3</sub>O<sub>4</sub>/Pt(111) model catalysts has been described in detail previously [153]. A well-ordered 10 nm thick Fe<sub>3</sub>O<sub>4</sub> film was grown on a Pt(111) substrate followed by Pd deposition onto the freshly prepared Fe<sub>3</sub>O<sub>4</sub> film at 120 K by physical vapor deposition of 4 Å Pd (Goodfellow,  $\geq 99.9\%$ ) using a commercial electron-beam evaporator (Focus EFM 3). After depositing Pd, the sample was annealed at 600 K and the Pd particles were stabilized by repeated cycles of oxidation in  $1 \cdot 10^{-6}$  mbar O<sub>2</sub> for 15 min and reduction in  $1 \cdot 10^{-6}$  mbar CO for 45 min at 500 K (see [152]). The stabilization procedure was also used to clean the particles after each experiment. The quality of the particles was checked by infrared reflection-absorption spectroscopy (IRAS) of adsorbed CO prior to every experiment. Shortly before each experiment, the sample was flashed to 600 K before cooling to 120 K.

IRAS data were acquired using a vacuum Fourier-Transform infrared (FT-IR) spectrometer (Bruker IFS 66v/S) with a spectral resolution of  $2 \text{ cm}^{-1}$ , a mid-infrared (MIR) polarizer and p-polarized IR light. Temperature-programmed desorption (TPD) experiments were carried out in the same UHV system by using an automated quadrupole mass spectrometer (QMS) system (Hidden Analytics). In TPD experiments the following masses were detected: 2, 28, 31, 56, 57, 58, and 60.

## 12.3 Results and Discussion

### 12.3.1 Acrolein on Fe<sub>3</sub>O<sub>4</sub>

Figure 12.2a shows a series of coverage-dependent IR spectra of acrolein on an Fe<sub>3</sub>O<sub>4</sub> film at 120 K, ranging from  $9 \cdot 10^{13}$  to  $2.7 \cdot 10^{15}$  molecules/cm<sup>2</sup>. The evolution of characteristic IR absorption features at low, intermediate, and high coverages point to coverage-dependent formation of different surface species, to which we will refer as A, B, C, and D. At the lowest coverage, after exposure of  $9 \cdot 10^{13}$  molecules/cm<sup>2</sup>, species A, B, and C appear. While A and B are saturated, the concentration of C increases until  $3.6 \cdot 10^{14}$  molecules/cm<sup>2</sup>

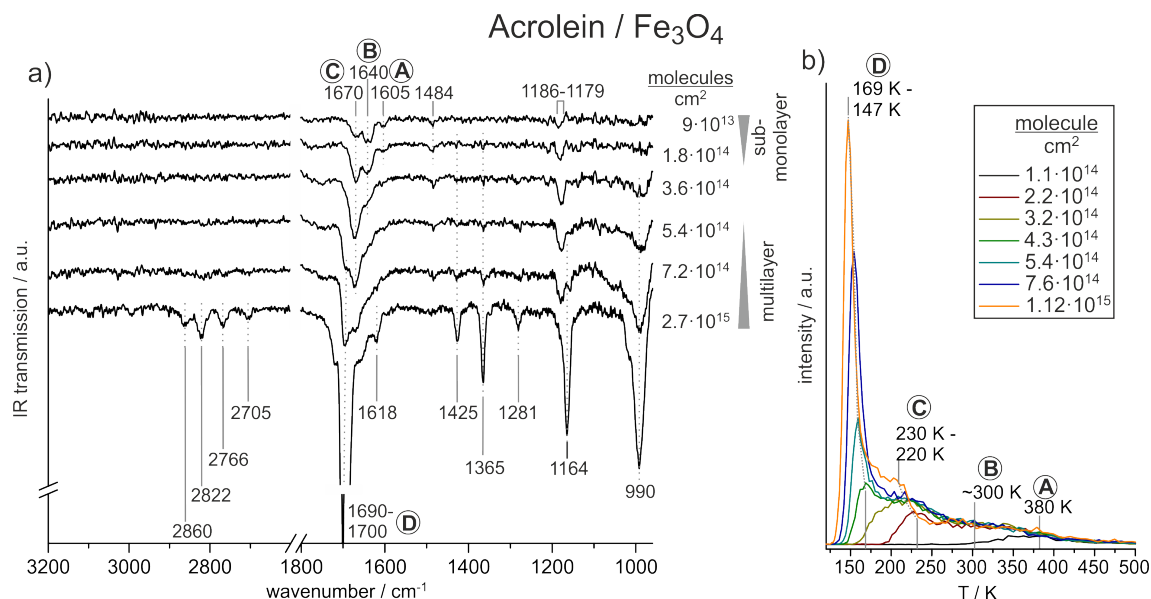


Figure 12.2: (a) IR spectra of acrolein on Fe<sub>3</sub>O<sub>4</sub> from sub-monolayer to multilayer coverages at 120 K; (b) Coverage dependent TPD studies of acrolein on Fe<sub>3</sub>O<sub>4</sub>

have been deposited. Upon further acrolein exposure, D populates the surface; saturation of the latter species was not observed. The vibrational modes of the different types of acrolein are summarized in Table 12.1 and will be discussed below.

Figure 12.2b illustrated a series of TPD experiments of acrolein at coverages from  $1.1 \cdot 10^{14}$  to  $1.12 \cdot 10^{15}$  molecules/cm<sup>2</sup> on an Fe<sub>3</sub>O<sub>4</sub> film. The TPD spectra show up to four acrolein desorption temperatures; desorption of other molecules has not been observed. The different acrolein desorption features point again to the formation of different surface species. At the two lowest coverages ( $1.1 \cdot 10^{14}$  and  $2.2 \cdot 10^{14}$  molecules/cm<sup>2</sup>), acrolein desorbs near 380 K and 300 K. At tentatively higher surface concentration ( $2.2 \cdot 10^{14}$  and  $3.2 \cdot 10^{14}$  molecules/cm<sup>2</sup>), a third peak is observed at 230-220 K. Finally, the last desorption feature grows at 169 K after exposure of  $4.3 \cdot 10^{14}$  molecules/cm<sup>2</sup>. With increasing surface population, the latter peak is gaining intensity and gradually shifts to 147 K.

Both studies, IRAS and TPD, indicate the formation of different acrolein species on the Fe<sub>3</sub>O<sub>4</sub> film at low, intermediate, and high coverages. In the following parts of this section, we will discuss the molecular structure of the adsorbates in these three coverage regimes.

**Multilayer Coverages (Species D)** The IR spectra of acrolein at multilayer coverages provide a reference for mostly unperturbed molecules and are thus independent from the substrate. Table 12.1 shows almost identical IR vibration frequencies of  $2.7 \cdot 10^{15}$  acrolein molecules/cm<sup>2</sup> (species D) on Fe<sub>3</sub>O<sub>4</sub> and Pd(111). For a detailed discussion of the IR vibration modes we therefore refer to our study on Pd(111) [176] (Chapter 8). Here, we

Table 12.1: Assignment of the coverage dependent IR vibration modes of acrolein on Fe<sub>3</sub>O<sub>4</sub>

mode	IR vibrations of acrolein / cm <sup>-1</sup>			on Pd(111) [176] (Ch. 8) multilayer coverage
	species A/B	species C	species D	
$\nu_a(\text{CH}_2)$			2860	2857
$\nu_s(\text{CH}_2)$			2822	2820
$2\delta(\text{CH})_{CO}$			2766	2766
$\nu(\text{CH})_{CO}$			2705	2705
$\nu(\text{C=O})$	1605/1640	1670	1690-1700	1690-1699
$\nu(\text{C=O})$			1618	1618
$\delta(\text{CH}_2)$	1484	1425	1425	1425
$\delta(\text{CH})_{CO}$			1365	1365
$\delta(\text{CH})_{CC}$		1281	1365	
$\nu(\text{C-C})$	1186-1179	1186-1179	1164	1164
$\omega_T(\text{HC=CH}_2)$		990	990	990

$\nu$  = stretch,  $\delta$  = bend,  $\omega_T$  = trans-wag,  $a$  = asymmetric,  $s$  = symmetric  
 $CO$  = aldehyde group,  $CC$  = vinyl group

will briefly summarize the assignment. Asymmetric and symmetric CH<sub>2</sub> stretch modes appear near 2860 cm<sup>-1</sup> and 2822 cm<sup>-1</sup>. The vibrations at 2766 cm<sup>-1</sup> and 2705 cm<sup>-1</sup> have been explained by strong Fermi resonance between the aldehyde-CH deformation overtone and its stretch fundamental. The pronounced C=O stretch mode was found to shift from 1690 cm<sup>-1</sup> to 1700 cm<sup>-1</sup> with increasing coverage. The IR absorption assigned to the C=C stretch vibration is very weak and can only be observed at high acrolein concentrations at 1618 cm<sup>-1</sup>. The CH<sub>2</sub> scissor bend vibration appears at 1425 cm<sup>-1</sup>, the aldehyde-CH and vinyl-CH deformation vibrations at 1365 cm<sup>-1</sup> and 1281 cm<sup>-1</sup>, the C-C stretch mode at 1164 cm<sup>-1</sup>, and a trans-wag vibration of the HC=CH<sub>2</sub> group at 990 cm<sup>-1</sup>.

Despite the fact that species D shows several characteristic vibration frequencies, the strongest indication for its presence on the surface is the pronounced IR absorption of the C=O group. According to this feature, formation of species D requires an exposure of more than  $3.6 \cdot 10^{14}$  molecules/cm<sup>2</sup>. At similar coverage, TPD experiments show the appearance of a relatively weakly attached acrolein species, desorbing at 169 K.

**Near Monolayer Coverage (Species C)** Before the multilayer species (D) appears on the surface, species C saturates after the exposure of  $3.6 \cdot 10^{14}$  molecules/cm<sup>2</sup>. The most pronounced IR vibration of species C appears at 1670 cm<sup>-1</sup>. Very weak IR absorption peaks are indicated at 1425 cm<sup>-1</sup> and 1365 cm<sup>-1</sup> and a stronger one at 1186-1179 cm<sup>-1</sup>. The vibration at 1670 cm<sup>-1</sup> points to a slightly perturbed C=O bond. The vibration frequency is shifted by 20-30 cm<sup>-1</sup> to lower wavenumbers as compared to the unperturbed species D. The very weak IR absorption peaks at 1425 cm<sup>-1</sup> and 1365 cm<sup>-1</sup> have been discussed above and point to CH<sub>2</sub> scissor and aldehyde-CH bend vibrations. The vibration at 1186-1179 cm<sup>-1</sup> indicates a C-C stretch vibration, which is slightly shifted to higher wavenumbers as compared to the multilayer species D (1164 cm<sup>-1</sup>).

Simultaneously to the appearance of species C in the IR spectra, we observe the evolution of an acrolein desorption peak in TPD experiments. The peak appears at 230 K after exposure of  $2.2 \cdot 10^{14}$  molecules/cm<sup>2</sup> and saturates at 220 K after exposure of  $3.2 \cdot 10^{14}$  molecules/cm<sup>2</sup>. The higher desorption temperature as compared to species D indicates a stronger binding of C to the surface.

Both studies, TPD and IRAS, show the formation of the more strongly bound acrolein species C, which is getting formed at surface coverages up to  $3.6 \cdot 10^{14}$  molecules/cm<sup>2</sup>. We assign this species to molecules near the full-monolayer coverage. Since D is not getting formed until C is saturated, we conclude that the surface is first fully wetted by a monolayer of acrolein molecules containing  $\approx 3.6 \cdot 10^{14}$  molecules/cm<sup>2</sup> before the multilayer formation starts. In our previous study on Pd(111), we observed the formation of a full monolayer at the same surface coverage.

**Sub-Monolayer Coverage (Species A and B)** IRAS does not only provide information on the nature of chemical bonds, also their geometry can be deduced based on the metal surface selection rule (MSSR). According to MSSR, only dynamic dipole moments perpendicular to the metal surface can be detected [106, 112, 113]. We took advantage of this effect to determine the preferred geometry of Fe<sub>3</sub>O<sub>4</sub>-adsorbed acrolein.

After exposure of  $9 \cdot 10^{13}$  acrolein molecules/cm<sup>2</sup>, which corresponds to 1/4 of a monolayer, the Fe<sub>3</sub>O<sub>4</sub> surface is saturated with two low-coverage species. The strongest indication for the formation of these species are the IR vibrations at 1605 cm<sup>-1</sup> and 1640 cm<sup>-1</sup>. Further IR absorption features are observed at 1484 cm<sup>-1</sup> and 1186-1179 cm<sup>-1</sup>.

The IR vibrations at 1605 cm<sup>-1</sup> and 1640 cm<sup>-1</sup> appear at relatively low frequencies compared to typical C=O or C=C stretch vibrations. Nevertheless, the relatively intense IR absorption allows for two conclusions. On the one hand, it points to strong dynamic dipole moments and thus rather to C=O than C=C bond vibrations. On the other hand, according to the MSSR, the dipole must be strongly inclined with respect to the metal surface. The relatively low vibration frequencies indicate strong weakened C=O bonds. This effect is most pronounced for the species vibrating at 1605 cm<sup>-1</sup>, which corresponds to a redshift of almost 100 cm<sup>-1</sup>. We refer to this most perturbed adsorbate as type A and to the species absorbing at 1640 cm<sup>-1</sup> as type B. However, both C=O bond appear to be heavily weakened.

The IR absorption at 1484 cm<sup>-1</sup> reveals a scissor bending of a perturbed CH<sub>2</sub> group. The vibration frequency is significantly blueshifted as compared to acrolein at higher coverages (1425 cm<sup>-1</sup>). The strong vibration at 1186-1179 cm<sup>-1</sup> points to a stretch vibration of a strongly inclined C-C bond. It appears at slightly higher frequency as compared to the multilayer regime (1164 cm<sup>-1</sup>), which points to a strengthening of this bond. Although the dynamic dipole moments of C-C and CH<sub>2</sub> bonds are relatively weak, both groups can be detected at low acrolein concentration on the surface, pointing to strongly inclined C-C and C=CH<sub>2</sub> bonds.

In TPD experiments, desorption of acrolein is observed near 380 K and 300 K respectively after the exposure of  $1.1 \cdot 10^{14}$  and  $2.2 \cdot 10^{14}$  molecules/cm<sup>2</sup>. This relatively high

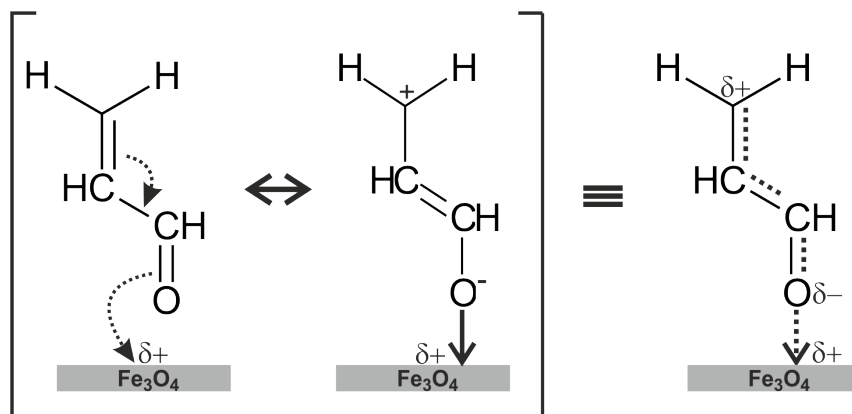


Figure 12.3: Model of the structure of acrolein on Fe<sub>3</sub>O<sub>4</sub> in the low-coverage limit.

desorption temperatures indicate strong binding of the molecules to Fe<sub>3</sub>O<sub>4</sub>.

The characteristic IR absorption features of acrolein in the low-coverage limit give detailed insights into the molecular structure of acrolein on Fe<sub>3</sub>O<sub>4</sub> with regard to the nature of the chemical bonds and their geometry. On the one hand, the relatively strong intensities of C=O, C–C and CH<sub>2</sub> vibrations indicate a strongly inclined molecular chain. On the other hand, heavy perturbation of the C=O bond points to binding of acrolein to Fe<sub>3</sub>O<sub>4</sub> via the C=O group. The perturbation along the whole molecular chain, from the C=O via the C–C to the CH<sub>2</sub> group, can be explained by delocalization of electrons in the conjugated  $\pi$  system. The tendency of the O atom to attract electrons in a carbonyl group is known to result in a weakening of the C=O bond and consequently in a decrease of the C=O stretch vibration frequency [109]. The polarized form of the C=O bond ( $\text{C}=\text{O} \leftrightarrow \text{C}^+-\text{O}^-$ ) might be stabilized by cationic surface sites, which attract the negatively charged O atom. The electrophilic character of the carbonyl-C atom is transferred to the  $\beta$ -C atom via the conjugated  $\pi$  system ( $\text{C}^{\delta+}=\text{C}-\text{C}=\text{O}^{\delta-} \rightarrow \delta^+\text{Fe}_3\text{O}_4$ ), a phenomenon that is well-known as *vinylology* [299–304]. Thereby, the saturated C–C bond gains some  $\pi$  character, which increases the bond order and thus its stretch vibration frequency. The delocalization of electrons away from the terminal CH<sub>2</sub> group might explain the strong blueshift of their scissor vibration frequency. The proposed structure of Fe<sub>3</sub>O<sub>4</sub>-adsorbed acrolein is schematically illustrated in Figure 12.3.

### 12.3.2 Acrolein on Pd/Fe<sub>3</sub>O<sub>4</sub>

Figure 12.4 illustrates coverage-dependent IR spectra of acrolein on Pd/Fe<sub>3</sub>O<sub>4</sub> model catalysts at 120 K. According to our definition of the full-monolayer coverage on pure Fe<sub>3</sub>O<sub>4</sub> and on a Pd(111) single crystal, the spectra in Figure 12.4 correspond to coverages of 1/4, 1/2, 3/4 and 1 monolayer. IR spectra at multilayer coverages are almost identical to those on Fe<sub>3</sub>O<sub>4</sub> and Pd(111) and will not be presented here. Our discussion will be limited to the region of the C=O stretch vibrations.

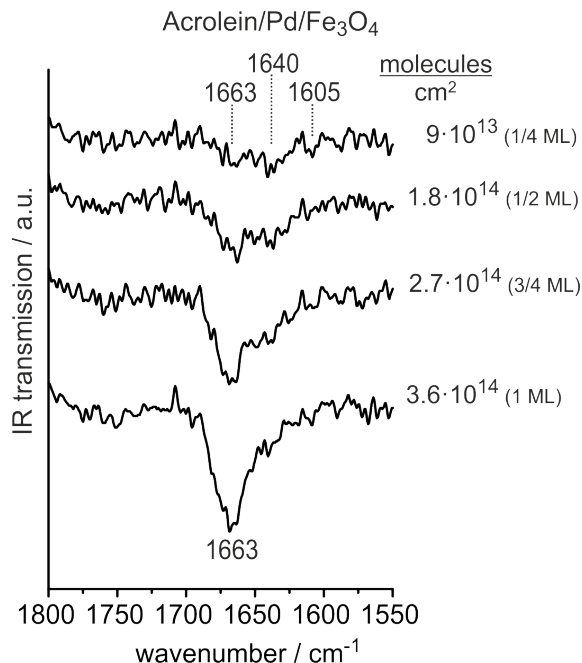


Figure 12.4: IR vibrations of acrolein on Pd/Fe<sub>3</sub>O<sub>4</sub> at 120 K with coverages ranging from  $\approx 1/4$  monolayer to  $\approx 1$  monolayer.

Table 12.2: Characteristic IR vibrations of the C=O bond in adsorbed acrolein

IR vibrations / cm <sup>-1</sup>					
a) saturated at 1/4 ML			b) saturated at 1 ML		
Pd/Fe <sub>3</sub> O <sub>4</sub>	Fe <sub>3</sub> O <sub>4</sub>	Pd(111)	Pd/Fe <sub>3</sub> O <sub>4</sub>	Fe <sub>3</sub> O <sub>4</sub>	Pd(111)
1605,1640	1605,1640	-	1663	1670	1663

The IR spectrum of 1/4 ML acrolein on Pd/Fe<sub>3</sub>O<sub>4</sub> shows two saturated peaks near 1605 cm<sup>-1</sup> and 1640 cm<sup>-1</sup>. A third vibration appears at 1663 cm<sup>-1</sup>, which becomes the most pronounced peak at 1 ML of acrolein on Pd/Fe<sub>3</sub>O<sub>4</sub>. Table 12.2 compares the C=O stretch frequencies of acrolein species that saturate in the low-coverage limit (a) and species that accumulate until full-monolayer coverage (b) on the three surfaces, Pd/Fe<sub>3</sub>O<sub>4</sub>, Fe<sub>3</sub>O<sub>4</sub>, and Pd(111). Almost identical IR spectra of 1/4 ML of acrolein on Pd/Fe<sub>3</sub>O<sub>4</sub> and pure Fe<sub>3</sub>O<sub>4</sub> show that a significant amount of acrolein binds to the Fe<sub>3</sub>O<sub>4</sub> support. Note that identification of acrolein on the Pd particles at low coverage might be very difficult. Previous studies show a flat-lying geometry of acrolein on a Pd(111) surface, which makes them unavailable for IRAS. However, vibrations of molecules attached to the tilted sides of the particles might be detectable. Near the full monolayer coverage, discrimination between molecules attached to Pd and Fe<sub>3</sub>O<sub>4</sub> is not possible due to very similar C=O vibration frequencies on the different surfaces.

Figure 12.5 shows the results of TPD experiments after deposition of  $1.6 \cdot 10^{14}$  acrolein molecules/cm<sup>2</sup> (1/2 ML) and  $7.5 \cdot 10^{14}$  molecules/cm<sup>2</sup> (2 ML) on pristine Pd/Fe<sub>3</sub>O<sub>4</sub> as

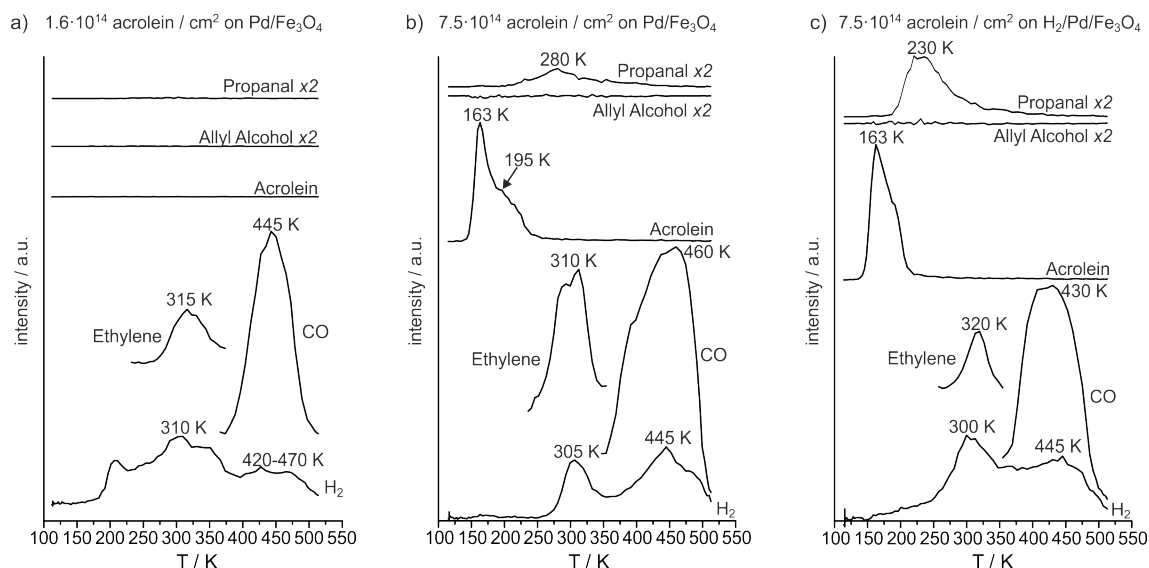


Figure 12.5: TPD studies of acrolein at sub-monolayer coverage (a), at multilayer coverage (b), and at multilayer coverage after hydrogen pre-exposure of Pd/Fe<sub>3</sub>O<sub>4</sub> model catalysts.

well as 2 ML acrolein on H<sub>2</sub> pre-saturated Pd/Fe<sub>3</sub>O<sub>4</sub>. TPD experiments of 1/2 ML of acrolein show decomposition of all molecules to ethylene, CO, and H<sub>2</sub>. TPD spectra show desorption of ethylene near 315 K, carbon monoxide at 445 K, and hydrogen over a broad temperature range with maxima around 310 K and 420-470 K. Ethylene and CO desorption as well as H<sub>2</sub> desorption near 310 K point to desorption limited processes, while H<sub>2</sub> desorption at 420-470 K indicates reaction limited hydrogen evolution. In TPD experiments of 2 ML of acrolein on Pd/Fe<sub>3</sub>O<sub>4</sub>, desorption of acrolein and propanal are observed in addition to the above mentioned decomposition products. The TPD spectra show acrolein desorption in a pronounced peak at 163 K and in a weaker feature near 195 K. The lower-temperature peak points to more weakly adsorbed molecules in the second layer, while the peak at higher temperature indicates desorption of more strongly attached species in the first layer. Propanal appears near 280 K, which shows conversion of the C=C bond of acrolein with hydrogen. TPD studies after deposition of 2 ML acrolein on H<sub>2</sub>/Pd/Fe<sub>3</sub>O<sub>4</sub> show a larger fraction of acrolein being converted to propanal. The desorption peak of the more strongly adsorbed acrolein at 195 K vanishes, while a relatively large amount of propanal appears near 230 K. The decomposition products ethylene, H<sub>2</sub>, and CO are observed at similar temperatures and with similar intensities as compared to pristine Pd/Fe<sub>3</sub>O<sub>4</sub>.

TPD of acrolein provides information on the adsorption of acrolein on Pd/Fe<sub>3</sub>O<sub>4</sub> model catalyst, as well as into the mechanism of its conversion to propanal. On the one hand, TPD experiments of 1/2 ML acrolein do not only show decomposition of acrolein starting below 310 K, they also point to a high mobility of acrolein on the Fe<sub>3</sub>O<sub>4</sub> below 310 K. By IRAS, we found a significant amount of acrolein adsorbed by the Fe<sub>3</sub>O<sub>4</sub> support. How-

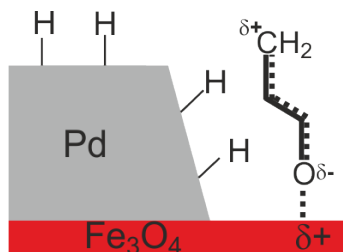


Figure 12.6: Model of a possible configuration of acrolein and hydrogen on Pd/Fe<sub>3</sub>O<sub>4</sub> model catalysts

ever, TPD experiments of acrolein on the pure Fe<sub>3</sub>O<sub>4</sub> film showed no decomposition; in contrast to previous TPD experiments on Pd(111) where complete decomposition of a monolayer of acrolein was observed [176] (Chapter 8). The results indicate that decomposition requires diffusion of acrolein from Fe<sub>3</sub>O<sub>4</sub> to Pd. On the other hand, conversion of acrolein to propanal in TPD experiments as well as in previous studies under isothermal conditions [185, 187] (Chapters 9 and 11) reveal that conversion of the C=C bond requires characteristic kinetic effects of the Pd/Fe<sub>3</sub>O<sub>4</sub> model system and cannot be realized by Pd or Fe<sub>3</sub>O<sub>4</sub> alone.

The combination of IRAS and TPD studies give detailed insights into the mechanism of acrolein conversion over Pd/Fe<sub>3</sub>O<sub>4</sub> model catalysts. Our results point to strong interaction of acrolein with the Fe<sub>3</sub>O<sub>4</sub> support. As discussed before, Fe<sub>3</sub>O<sub>4</sub> seems to activate the  $\beta$ -C atom and thus promote the conversion of the C=C bond with hydrogen. However, hydrogenation requires the presence of atomic hydrogen, which can be provided by Pd. Thus, the characteristic kinetics in hydrogenation over Pd/Fe<sub>3</sub>O<sub>4</sub> model catalysts may arise from the activation of the  $\beta$ -C atom by Fe<sub>3</sub>O<sub>4</sub> combined with the availability of atomic hydrogen on Pd. According to this model, Figure 12.6 illustrates a possible configuration of co-adsorbed hydrogen and acrolein on Pd/Fe<sub>3</sub>O<sub>4</sub> model catalysts for propanal formation.

## 12.4 Conclusion

The interaction of acrolein with an Fe<sub>3</sub>O<sub>4</sub> film and Pd/Fe<sub>3</sub>O<sub>4</sub> model catalyst was studied by combination of coverage-dependent IRAS and TPD experiments. Particularly the studies at low surface concentrations give insights into the perturbation of acrolein by the different surfaces. On Fe<sub>3</sub>O<sub>4</sub>, IRAS results point to strongly inclined acrolein molecules with heavily perturbed chemical bonds. The C=O group is found to be significantly weakened, while the C–C bond seems to slightly gain strength and the also the  $\beta$ -CH<sub>2</sub> group appears to be perturbed. We conclude that positively charged Fe<sub>3</sub>O<sub>4</sub> surface sites might stabilize the polarized form of the C=O group by attracting the negatively charged O atom. According to the effect of vinylogy, the electrophilic character of the carbonyl-C atom can be transferred by the conjugated  $\pi$  system to the  $\beta$ -C atom. Nevertheless, acrolein is not converted in TPD experiments on pure Fe<sub>3</sub>O<sub>4</sub>. In the presence of Pd,

however, we observe decomposition of acrolein at low coverage and conversion to propanal at higher coverage. While decomposition of acrolein was also observed in previous TPD experiments on Pd(111), propanal is only formed on Pd/Fe<sub>3</sub>O<sub>4</sub> model catalysts. The results indicate that selective hydrogenation of the C=C bond in acrolein is achieved by an interplay between the Fe<sub>3</sub>O<sub>4</sub> support, which activates the  $\beta$ -C atom, and Pd, which provides atomic hydrogen. Thus, the addition of the first H atom on acrolein can be seen as 1,4-conjugated addition of Fe<sub>3</sub>O<sub>4</sub> and H.

The enhancement of C=O bond conversion by Lewis-acid–base complexes between the O atom of the CO group and cationic sites, *e.g.* of the support, is well-known from literature. However, promotion of a chemical reaction at the  $\beta$ -C atom using the effect of vinylogy, which is frequently utilized in organic synthesis [299–304], has - to our knowledge - not yet been reported in surface science studies on model catalysts.

The presented atomistic-level insights into the kinetics of acrolein conversion on Pd/Fe<sub>3</sub>O<sub>4</sub> model catalysts highlight the role of the oxide support for the highly selective hydrogenation of the C=C bond. The effect of  $\beta$ -C activation is expected to play a key role in hydrogenation of all  $\alpha,\beta$ -unsaturated carbonyl compounds over catalysts containing Lewis-acidic sites.

# Bibliography

- [1] G. Ertl, H. Knözinger, and J. Weitkamp. *Environmental Catalysis*. Wiley VCH, 1999.
- [2] G. Ertl, H. Knörzinger, F. Schüth, and J. Weitkamp. *Handbook of Heterogeneous Catalysis*, volume 1. Wiley VCH, 2008.
- [3] J. M. Thomas and W. J. Thomas. *Principle and Practice of Heterogeneous Catalysis*. Wiley VCH, second edition, 2015.
- [4] E. K. Rideal. *Concepts in Catalysis*. Academic Press, 1968.
- [5] M. Boudart. Catalysis by supported metals. volume 20 of *Advances in Catalysis*, pages 153 – 166. Academic Press, 1969.
- [6] M. Che and C. O. Bennett. The influence of particle size on the catalytic properties of supported metals. volume 36 of *Advances in Catalysis*, pages 55 – 172. Academic Press, 1989.
- [7] G. C. Bond. The origins of particle size effects in heterogeneous catalysis. *Surface Science*, 156, Part 2(0):966 – 981, 1985.
- [8] J. A. Dumesic, D. F. Rudd, L. M. Aparicio, J. E. Rekoske, and A. A. Trevino. *The Microkinetics of Heterogeneous Catalysis*. American Chemical Society, 1993.
- [9] J. Libuda and H. J. Freund. Molecular beam experiments on model catalysts. *Surface Science Reports*, 57(7-8):157–298, 2005.
- [10] C. R. Henry. Surface studies of supported model catalysts. *Surface Science Reports*, 31(7-8):235–325, 1998.
- [11] G. Ertl. Reactions at surfaces: From atoms to complexity (nobel lecture). *Angewandte Chemie International Edition*, 47(19):3524–3535, 2008.
- [12] M. Bäumer and H. J. Freund. Metal deposits on well-ordered oxide films. *Progress in Surface Science*, 61(7-8):127–198, 1999.
- [13] T. P. St Clair and D. W. Goodman. Metal nanoclusters supported on metal oxide thin films: bridging the materials gap. *Topics in Catalysis*, 13(1-2):5–19, 2000.
- [14] M. Bäumer, J. Libuda, and H. J. Freund. *Metal deposits on thin well ordered oxide films: Morphology, adsorption and reactivity*, volume 331 of *Nato Advanced Science Institutes Series, Series E, Applied Sciences*, pages 61–104. Kluwer Academic Publ, Dordrecht, 1997.

- [15] C. T. Campbell, A. W. Grant, D. E. Starr, S. C. Parker, and V. A. Bondzie. Model oxide-supported metal catalysts: energetics, particle thicknesses, chemisorption and catalytic properties. *Topics in Catalysis*, 14(1-4):43–51, 2001.
- [16] T. Hrncir, V. Matolin, and V. Nehasil. Reactivity of non-continuous rh model catalysts deposited on differently oriented al<sub>2</sub>o<sub>3</sub> substrates. *Surface Science*, 482-485, Part 1:260–265, 2001.
- [17] H.-J. Freund. Clusters and islands on oxides: from catalysis via electronics and magnetism to optics. *Surface Science*, 500(1-3):271 – 299, 2002.
- [18] H.-J. Freund. Adsorption of gases on complex solid surfaces. *Angewandte Chemie International Edition in English*, 36(5):452–475, 1997.
- [19] C. R. Henry. *Adsorption and Reaction at Supported Model Catalysts*, book section 7, pages 239–280. Dekker, 2003. ISBN 0-8247-0879-2.
- [20] C. T. Rettner, D. J. Auerbach, J. C. Tully, and A. W. Kleyn. Chemical dynamics at the gas-surface interface. *The Journal of Physical Chemistry*, 100(31):13021–13033, 1996.
- [21] A. W. Kleyn. Molecular beams and chemical dynamics at surfaces. *Chemical Society Reviews*, 32(2):87–95, 2003.
- [22] R. J. Madix and J. A. Schwarz. Chemical relaxation molecular beam studies of reactive gas-solid scattering: I. reaction of silicon and germanium with molecular chlorine. *Surface Science*, 24(1):264 – 287, 1971.
- [23] T. Enge and H. Kuipers. A molecular-beam investigation of the scattering, adsorption and absorption of {H<sub>2</sub>} and {D<sub>2</sub>} from/on/in pd(111). *Surface Science*, 90(1): 162 – 180, 1979.
- [24] D. F. Padowitz and S. J. Sibener. Kinetics of hydrogen oxidation to water on the rh(111) surface using multiple source modulated molecular beam techniques. *Surface Science*, 254(1-3):125 – 143, 1991.
- [25] M. Bonn, A. W. Kleyn, and G. J. Kroes. Real time chemical dynamics at surfaces. *Surface Science*, 500(1-3):475 – 499, 2002.
- [26] S. Fiechter, I. Dorbandt, P. Bogdanoff, G. Zehl, H. Schulenburg, H. Tributsch, M. Bron, J. Radnik, and M. Fieber-Erdmann. Surface modified ruthenium nanoparticles: Structural investigation and surface analysis of a novel catalyst for oxygen reduction. *The Journal of Physical Chemistry C*, 111(1):477–487, 2007.
- [27] P. Gallezot and D. Richard. Selective hydrogenation of alpha,beta-unsaturated aldehydes. *Catalysis Reviews-Science and Engineering*, 40(1-2):81–126, 1998.
- [28] P. Maki-Arvela, J. Hajek, T. Salmi, and D. Y. Murzin. Chemoselective hydrogenation of carbonyl compounds over heterogeneous catalysts. *Applied Catalysis a-General*, 292:1–49, 2005.

- [29] *Ullmann's Encyclopedia of Industrial Chemistry*. Wiley-VCH Verlag GmbH & Co. KGaA, 2000. ISBN 9783527306732.
- [30] P. Claus. Selective hydrogenation of  $\alpha,\beta$ -unsaturated aldehydes and other  $\text{C}=\text{O}$  and  $\text{C}=\text{C}$  bonds containing compounds. *Topics in Catalysis*, 5(1-4):51–62, 1998.
- [31] C.M. Pradier, T. Birchem, Y. Berthier, and G. Cordier. Hydrogenation of 3-methylbutenal on  $\text{Pt}(110)$ ; comparison with  $\text{Pt}(111)$ . *Catalysis Letters*, 29(3-4):371–378, 1994. ISSN 1011-372X.
- [32] T. Birchem, C. M. Pradier, Y. Berthier, and G. Cordier. Hydrogenation of 3-methylcrotonaldehyde on the  $\text{Pt}(553)$  stepped surface: Influence of the structure and of preadsorbed tin. *Journal of Catalysis*, 161(1):68 – 77, 1996.
- [33] Wolfgang Grünert, Angelika Brückner, Herbert Hofmeister, and Peter Claus. Structural properties of  $\text{Ag}/\text{TiO}_2$  catalysts for acrolein hydrogenation. *The Journal of Physical Chemistry B*, 108(18):5709–5717, 2004.
- [34] M. Bron, D. Teschner, A. Knop-Gericke, A. Scheybal, B. Steinhauer, M. Hävecker, R. Födisch, D. Hönicke, R. Schlögl, and P. Claus. In situ-xas and catalytic study of acrolein hydrogenation over silver catalyst: Control of intramolecular selectivity by the pressure. *Catalysis Communications*, 6(5):371 – 374, 2005.
- [35] M. Bron, D. Teschner, A. Knop-Gericke, F. C. Jentoft, J. Krohnert, J. Hohmeyer, C. Volckmar, B. Steinhauer, R. Schlögl, and P. Claus. Silver as acrolein hydrogenation catalyst: intricate effects of catalyst nature and reactant partial pressures. *Phys. Chem. Chem. Phys.*, 9:3559–3569, 2007.
- [36] Peter Claus, Angelika Brückner, Christian Mohr, and Herbert Hofmeister. Supported gold nanoparticles from quantum dot to mesoscopic size scale: Effect of electronic and structural properties on catalytic hydrogenation of conjugated functional groups. *Journal of the American Chemical Society*, 122(46):11430–11439, 2000.
- [37] C. Mohr, H. Hofmeister, M. Lucas, and P. Claus. Gold catalysts for the partial hydrogenation of acrolein. *Chemical Engineering & Technology*, 23(4):324–328, 2000.
- [38] S. Schimpf, M. Lucas, C. Mohr, U. Rodemerck, A. Brückner, J. Radnik, H. Hofmeister, and P. Claus. Supported gold nanoparticles: in-depth catalyst characterization and application in hydrogenation and oxidation reactions. *Catalysis Today*, 72(1-2): 63–78, 2002.
- [39] C Mohr, H Hofmeister, and P Claus. The influence of real structure of gold catalysts in the partial hydrogenation of acrolein. *Journal of Catalysis*, 213(1):86 – 94, 2003.
- [40] H. Wei, C. Gomez, J. Liu, N. Guo, T. Wu, R. Lobo-Lapidus, C. L. Marshall, J. T. Miller, and R. J. Meyer. Selective hydrogenation of acrolein on supported silver catalysts: A kinetics study of particle size effects. *Journal of Catalysis*, 298(0):18 – 26, 2013.

- [41] M. Englisch, A. Jentys, and J. A. Lercher. Structure sensitivity of the hydrogenation of crotonaldehyde over pt/sio<sub>2</sub> and pt/tio<sub>2</sub>. *Journal of Catalysis*, 166(1):25 – 35, 1997.
- [42] Yuriko Nitta, Kenji Ueno, and Toshinobu Imanaka. Selective hydrogenation of  $\alpha, \beta$ -unsaturated aldehydes on cobalt-silica catalysts obtained from cobalt chrysotile. *Applied Catalysis*, 56(1):9 – 22, 1989.
- [43] Christian Mohr, Herbert Hofmeister, Jörg Radnik, and Peter Claus. Identification of active sites in gold-catalyzed hydrogenation of acrolein. *Journal of the American Chemical Society*, 125(7):1905–1911, 2003.
- [44] Paul N. Rylander. *Catalytic hydrogenation over platinum metals*. Academic Press, 1967.
- [45] V. Ponec. On the role of promoters in hydrogenations on metals;  $\alpha, \beta$ -unsaturated aldehydes and ketones. *Applied Catalysis A: General*, 149(1):27 – 48, 1997.
- [46] P. Beccat, J.C. Bertolini, Y. Gauthier, J. Massardier, and P. Ruiz. Crotonaldehyde and methylcrotonaldehyde hydrogenation over pt(111) and pt<sub>80</sub>fe<sub>20</sub>(111) single crystals. *Journal of Catalysis*, 126(2):451 – 456, 1990.
- [47] M. Englisch, V. S. Ranade, and J. A. Lercher. Hydrogenation of crotonaldehyde over pt based bimetallic catalysts. *Journal of Molecular Catalysis A: Chemical*, 121(1):69–80, 1997.
- [48] D. Richard, J. Ockelford, A. Giroir-Fendler, and P. Gallezot. Composition and catalytic properties in cinnamaldehyde hydrogenation of charcoal-supported, platinum catalysts modified by fecl<sub>2</sub> additives. *Catalysis Letters*, 3(1):53–58, 1989.
- [49] S. Galvagno, A. Donato, G. Neri, R. Pietropaolo, and D. Pietropaolo. Hydrogenation of cinnamaldehyde over platinum catalysts: influence of addition of metal chlorides. *Journal of Molecular Catalysis*, 49(2):223 – 232, 1989.
- [50] C.G. Raab, M. Englisch, T.B.L.W. Marinelli, and J.A. Lercher. Selective hydrogenation of crotonaldehyde over pt derived catalysts. In M. Guisnet, J. Barbier, J. Barrault, C. Bouchoule, D. Duprez, G. Perot, and C. Montassier, editors, *Heterogeneous Catalysis and Fine Chemicals III Proceedings of the 3rd International Symposium*, volume 78 of *Studies in Surface Science and Catalysis*, pages 211 – 218. Elsevier, 1993.
- [51] T.B.L.W. Marinelli and V. Ponec. A study in the selectivity in acrolein hydrogenation on platinum catalysts: A model for hydrogenation of  $\alpha, \beta$ -unsaturated aldehydes. *Journal of Catalysis*, 156(1):51–59, 1995.
- [52] G. Kennedy, L. R. Baker, and G. A. Somorjai. Selective amplification of c=O bond hydrogenation on pt/tio<sub>2</sub>: Catalytic reaction and sum-frequency generation vibrational spectroscopy studies of crotonaldehyde hydrogenation. *Angewandte Chemie International Edition*, 53(13):3405–3408, 2014.

- [53] M. Albert Vannice and B. Sen. Metal-support effects on the intramolecular selectivity of crotonaldehyde hydrogenation over platinum. *Journal of Catalysis*, 115(1):65 – 78, 1989.
- [54] M. A. Vannice. The influence of msi (metal–support interactions) on activity and selectivity in the hydrogenation of aldehydes and ketones. *Topics in Catalysis*, 4 (3-4):241–248, 1997.
- [55] Hideaki Yoshitake, Kiyotaka Asakura, and Yasuhiro Iwasawa. Chemical environments around active sites and reaction mechanisms for deuterium-acrolein reaction over ir/nb<sub>2</sub>o<sub>5</sub> in normal and smsi states. *J. Chem. Soc., Faraday Trans. 1*, 85: 2021–2034, 1989.
- [56] Hideaki Yoshitake and Yasuhiro Iwasawa. Cooperative behavior of two kinds of reaction sites and reaction mechanisms for deuteration of acrolein on smsi-pt/nb<sub>2</sub>o<sub>5</sub> catalyst. *Journal of Catalysis*, 125(1):227 – 242, 1990.
- [57] J. Greeley and M. Mavrikakis. Surface and subsurface hydrogen: Adsorption properties on transition metals and near-surface alloys. *The Journal of Physical Chemistry B*, 109(8):3460–3471, 2005.
- [58] J. Hohmeyer, E.V. Kondratenko, M. Bron, J. Kröhnert, F.C. Jentoft, R. Schlögl, and P. Claus. Activation of dihydrogen on supported and unsupported silver catalysts. *Journal of Catalysis*, 269(1):5 – 14, 2010.
- [59] V. Zhukov, K. D. Rendulic, and A. Winkler. Coadsorption of hydrogen and potassium on silver single crystal surfaces. *Vacuum*, 47(1):5 – 11, 1996.
- [60] C. J. Kliewer, M. Bieri, and G. A. Somorjai. Hydrogenation of the alpha,beta-unsaturated aldehydes acrolein, crotonaldehyde, and prenal over pt single crystals: A kinetic and sum-frequency generation vibrational spectroscopy study. *Journal of the American Chemical Society*, 131(29):9958–9966, 2009.
- [61] D. Loffreda, Y. Jugnet, F. Delbecq, J. C. Bertolini, and P. Sautet. Coverage dependent adsorption of acrolein on pt(111) from a combination of first principle theory and hreels study. *The Journal of Physical Chemistry B*, 108(26):9085–9093, 2004.
- [62] K. Brandt, M. E. Chiu, D. J. Watson, M. S. Tikhov, and R. M. Lambert. Chemoselective catalytic hydrogenation of acrolein on ag(111): Effect of molecular orientation on reaction selectivity. *Journal of the American Chemical Society*, 131(47):17286–17290, 2009.
- [63] S. K. Beaumont, G. Kyriakou, D. J. Watson, O. P. H. Vaughan, A. C. Papageorgiou, and R. M. Lambert. Influence of adsorption geometry in the heterogeneous enantioselective catalytic hydrogenation of a prototypical enone. *Journal of Physical Chemistry C*, 114(35):15075–15077, 2010.
- [64] Luis E. Murillo, Amit M. Goda, , and Jingguang G. Chen. Selective hydrogenation of the co bond in acrolein through the architecture of bimetallic surface structures. *Journal of the American Chemical Society*, 129(22):7101–7105, 2007.

- [65] Jens R. Rostrup-Nielsen. Industrial relevance of coking. *Catalysis Today*, 37(3):225 – 232, 1997.
- [66] Peter Albers, Jörg Pietsch, and Stewart F Parker. Poisoning and deactivation of palladium catalysts. *Journal of Molecular Catalysis A: Chemical*, 173(1-2):275 – 286, 2001.
- [67] K. M. Neyman and S. Schauermaun. Hydrogen diffusion into palladium nanoparticles: Pivotal promotion by carbon. *Angewandte Chemie International Edition*, 49: 4743–4746, 2010.
- [68] W. Ludwig, A. Savara, R. J. Madix, S. Schauermaun, and H.-J. Freund. Subsurface hydrogen diffusion into pd nanoparticles: Role of low-coordinated surface sites and facilitation by carbon. *The Journal of Physical Chemistry C*, 116(5):3539–3544, 2012.
- [69] M. Wilde, K. Fukutani, W. Ludwig, B. Brandt, J.-H. Fischer, S. Schauermaun, and H.-J. Freund. Influence of carbon deposition on the hydrogen distribution in pd nanoparticles and their reactivity in olefin hydrogenation. *Angewandte Chemie International Edition*, 47(48):9289–9293, 2008.
- [70] M. Wilde, K. Fukutani, M. Naschitzki, and H.-J. Freund. Hydrogen absorption in oxide-supported palladium nanocrystals. *Phys. Rev. B*, 77:113412, 2008.
- [71] D. Teschner, J. Borsodi, A. Woosch, Z. RÄ©vay, M. Hävecker, A. Knop-Gericke, S. D. Jackson, and R. Schlögl. The roles of subsurface carbon and hydrogen in palladium-catalyzed alkyne hydrogenation. *Science*, 320(5872):86–89, 2008.
- [72] G.E. Gdowski, T.E. Felter, and R.H. Stulen. Effect of surface temperature on the sorption of hydrogen by pd(111). *Surface Science*, 181(3):L147 – L155, 1987.
- [73] M. Wilde, K. Fukutani, W. Ludwig, B. Brandt, J.-H. Fischer, S. Schauermaun, and H.-J. Freund. Influence of carbon deposition on the hydrogen distribution in pd nanoparticles and their reactivity in olefin hydrogenation. *Angewandte Chemie International Edition*, 47(48):9289–9293, 2008.
- [74] Markus Wilde, Katsuyuki Fukutani, Wiebke Ludwig, Björn Brandt, Jan-Henrik Fischer, Svetlana Schauermaun, and Hans-Joachim Freund. Influence of carbon deposition on the hydrogen distribution in pd nanoparticles and their reactivity in olefin hydrogenation. *Angewandte Chemie International Edition*, 47:9289–9293, 2008.
- [75] K.W. Kolasinski. *Surface Science: Foundations of Catalysis and Nanoscience*. Wiley, 2008. ISBN 9780470997819.
- [76] M. Bowker. The role of precursor states in adsorption, surface reactions and catalysis. *Journal of Physics-Condensed Matter*, 22(26):14, 2010.

- [77] A. Cassuto and D. A. King. Rate expressions for adsorption and desorption-kinetics with precursor states and lateral interactions. *Surface Science*, 102(2-3):388–404, 1981.
- [78] W. H. Weinberg and R. P. Merrill. Simple classical model for trapping in gas-surface interactions. *Journal of Vacuum Science & Technology*, 8(6):718, 1971.
- [79] P. Kisliuk. The sticking probabilities of gases chemisorbed on the surfaces of solids. *Journal of Physics and Chemistry of Solids*, 3(1-2):95–101, 1957. ISSN 0022-3697.
- [80] D. R. Rainer and D. W. Goodman. Metal clusters on ultrathin oxide films: model catalysts for surface science studies. *Journal of Molecular Catalysis a-Chemical*, 131(1-3):259–283, 1998.
- [81] N. Takahashi, H. Shinjoh, T. Iijima, T. Suzuki, K. Yamazaki, K. Yokota, H. Suzuki, N. Miyoshi, S. Matsumoto, T. Tanizawa, T. Tanaka, S. Tateishi, and K. Kasahara. The new concept 3-way catalyst for automotive lean-burn engine: Nox storage and reduction catalyst. *Catalysis Today*, 27(1-2):63–69, 1996.
- [82] E. Fridell, H. Persson, L. Olsson, B. Westerberg, A. Amberntsson, and M. Skoglundh. Model studies of nox storage and sulphur deactivation of nox storage catalysts. *Topics in Catalysis*, 16(1-4):133–137, 2001.
- [83] C. Sedlmair, K. Seshan, A. Jentys, and J. A. Lercher. Elementary steps of nox adsorption and surface reaction on a commercial storage-reduction catalyst. *Journal of Catalysis*, 214(2):308–316, 2003.
- [84] I. Stara, V. Nehasil, and V. Matolin. Influence of substrate structure on activity of alumina supported pd particles: Co adsorption and oxidation. *Surface Science*, 365(1):69–77, 1996.
- [85] E. Gillet, S. Channakhone, V. Matolin, and M. Gillet. Chemisorptional behavior of pd small supported particles depending on size and structure - tds, ssims and tem investigation. *Surface Science*, 152(APR):603–614, 1985.
- [86] C. Becker and C. R. Henry. Cluster size dependent kinetics for the oxidation of co on a pd/mgo(100) model catalyst. *Surface Science*, 352:457–462, 1996.
- [87] W. C. Conner and J. L. Falconer. Spillover in heterogeneous catalysis. *Chemical Reviews*, 95(3):759–788, 1995.
- [88] U. Diebold. The surface science of titanium dioxide. *Surface Science Reports*, 48(5-8):53–229, 2003.
- [89] J. Libuda and H. J. Freund. Reaction kinetics on complex model catalysts under single scattering conditions. *Journal of Physical Chemistry B*, 106(19):4901–4915, 2002.
- [90] V. P. Zhdanov and B. Kasemo. Kinetics of rapid heterogeneous reactions on the nanometer scale. *Journal of Catalysis*, 170(2):377–389, 1997.

## Bibliography

- [91] V. P. Zhdanov and B. Kasemo. Kinetics of rapid reactions on nanometer catalyst particles. *Physical Review B*, 55(7):4105–4108, 1997.
- [92] K. Fichthorn, E. Gulari, and R. Ziff. Noise-induced bistability in a monte-carlo surface-reaction model. *Physical Review Letters*, 63(14):1527–1530, 1989.
- [93] Y. Suchorski, J. Beben, E. W. James, J. W. Evans, and R. Imbihl. Fluctuation-induced transitions in a bistable surface reaction: Catalytic co oxidation on a pt field emitter tip. *Physical Review Letters*, 82(9):1907–1910, 1999.
- [94] V. P. Zhdanov and B. Kasemo. Bistability in catalytic reactions on the nm scale. *Surface Science*, 496(3):251–263, 2002.
- [95] A. Berko and F. Solymosi. Adsorption-induced structural changes of rh supported by tio<sub>2</sub>(110)-(1x2): An stm study. *Journal of Catalysis*, 183(1):91–101, 1999.
- [96] G. Scoles, editor. *Atomic and molecular beam methods*, volume 1. Oxford University Press New York, 1988.
- [97] G. Scoles, editor. *Atomic and molecular beam methods*, volume 2. Oxford University Press New York, 1992.
- [98] R. (Ed.) Campargue. *Atomic and Molecular Beams*. Springer Berlin Heidelberg, 2001. ISBN 978-3-642-63150-4.
- [99] R. D. Levine and R. B. Bernstein. *Molecular Reaction Dynamics and Chemical Reactivity*. Oxform University Press, 1987. ISBN 0-19-504139-9.
- [100] J. Libuda, I. Meusel, J. Hartmann, and H. J. Freund. A molecular beam/surface spectroscopy apparatus for the study of reactions on complex model catalysts. *Review of Scientific Instruments*, 71(12):4395–4408, 2000.
- [101] J. A. Barker and D. J. Auerbach. Gas-surface interactions and dynamics; thermal energy atomic and molecular beam studies. *Surface Science Reports*, 4(1-2):1–99, 1984.
- [102] M. P. D'Evelyn and R. J. Madix. Reactive scattering from solid surfaces. *Surface Science Reports*, 3(8):413–495, 1983.
- [103] M. L. Yu and L. A. DeLouise. Surface chemistry on semiconductors studied by molecular-beam reactive scattering. *Surface Science Reports*, 19(7-8):285–380, 1994.
- [104] H. Pauly. *Other Low-energy beam sources*, volume 1, book section 4, pages 83–123. Oxford University Press, 1988.
- [105] P. Hollins. The influence of surface-defects on the infrared-spectra of adsorbed species. *Surface Science Reports*, 16(2):51–94, 1992.
- [106] F. M. Hoffmann. Infrared reflection-absorption spectroscopy of adsorbed molecules. *Surface Science Reports*, 3(2-3):107–192, 1983.

- [107] B. E. Hayden. *Reflection Absorption Infrared Spectroscopy*, volume 1 of *Methods of Surface Characterization*, book section 7, pages 267–344. Springer US, 1987. ISBN 978-1-4684-8761-9.
- [108] H. Günzler and H.-U. Gremlich. *IR-Spektroskopie*. Wiley-VCH, 2003.
- [109] N. B. Colthup, L. H. Daly, and S. E. Wiberley. *Introduction to Infrared and Raman Spectroscopy*. Academic Press, San Diego and London, 3rd edition, 1990.
- [110] J. J. J. Sakurai. *Modern Quantum Mechanics*. ADDISON WESLEY Publishing Company Incorporated, 1994.
- [111] P. W. Atkins and R. S. Friedman. *Molecular Quantum Mechanics*. Oxford University Press, third edition edition, 1983. ISBN 0 19 855947 X (Pbk).
- [112] S. A. Francis and A. H. Ellison. Infrared spectra of monolayers on metal mirrors. *Journal of the Optical Society of America*, 49(2):131–138, 1959.
- [113] P. Hollins and J. Pritchard. Infrared studies of chemisorbed layers on single crystals. *Progress in Surface Science*, 19(4):275–349, 1985. ISSN 0079-6816.
- [114] T. B. Grimley. Normal mode frequencies of chemisorbed atoms and molecules. *Proceedings of the Physical Society of London*, 79(512):1203, 1962.
- [115] G. Blyholder. Molecular orbital view of chemisorbed carbon monoxide. *Journal of Physical Chemistry*, 68(10):2772, 1964.
- [116] G. Blyholder. Cnd model of carbon-monoxide chemisorbed on nickel. *Journal of Physical Chemistry*, 79(7):756–761, 1975.
- [117] S. Efrima and H. Metiu. The role of the electrostatic interaction in shifting the vibrational frequencies for 2 adsorbed molecules. *Surface Science*, 109(1):109–126, 1981.
- [118] R. M. Hammaker, S. A. Francis, and R. P. Eischens. Infrared study of intermolecular interactions for carbon monoxide chemisorbed on platinum. *Spectrochimica Acta*, 21(7):1295–1309, 1965. ISSN 0371-1951.
- [119] C. M. Mate, C. T. Kao, and G. A. Somorjai. Carbon-monoxide induced ordering of adsorbates on the rh(111) crystal-surface - importance of surface dipole-moments. *Surface Science*, 206(1-2):145–168, 1988.
- [120] P. R. Griffiths and J. A. de Haseth. *Fourier Transform Infrared Spectrometry*. John Wiley & Sons, Inc., 2006. ISBN 9780470106310.
- [121] H. Budzikiewicz and M. Schaefer. *Massenspektrometrie*. Wiley-VCH, 2005. ISBN 3-527-30822-9.
- [122] P. H. Dawson, W. E. Austin, R. F. Herzog, J. F. J. Todd, G. Lawson, R. F. Bonner, and M. S. Story. *Quadrupole Mass Spectrometry and its applications*. Elsevier Scientific Publishing Company, 1976. ISBN 0-444-41345-6.

## Bibliography

- [123] J. H. Gross. *Massenspektrometer*, book section 4, pages 129–244. Springer Berlin Heidelberg, 2013. ISBN 978-3-8274-2980-3.
- [124] Joachim Stöhr. *NEXAFS Spectroscopy*, volume 25. Springer Berlin Heidelberg, 1992. ISBN 978-3-642-08113-2.
- [125] G. Hähner. Near edge x-ray absorption fine structure spectroscopy as a tool to probe electronic and structural properties of thin organic films and liquids. *Chemical Society Reviews*, 35(12):1244–1255, 2006.
- [126] J. Stohr and D. A. Outka. Determination of molecular orientations on surfaces from the angular dependence of near edge x-ray absorption fine-structure spectra. *Physical Review B*, 36(15):7891–7905, 1987.
- [127] D. A. Outka and J. Stohr. Curve fitting analysis of near-edge core excitation spectra of free, adsorbed, and polymeric molecules. *Journal of Chemical Physics*, 88(6):3539–3554, 1988.
- [128] J. A. Horsley, J. Stohr, A. P. Hitchcock, D. C. Newbury, A. L. Johnson, and F. Sette. Resonance in the k shell excitation spectra of benzene and pyridine: Gas phase, solid, and chemisorbed states. *Journal of Chemical Physics*, 83(12):6099–6107, 1985.
- [129] G. Ertl. Elementary steps in heterogeneous catalysis. *Angewandte Chemie International Edition in English*, 29(11):1219–1227, 1990.
- [130] T. Engel and G. Ertl. A molecular beam investigation of the catalytic oxidation of co on pd (111). *The Journal of Chemical Physics*, 69(3):1267–1281, 1978.
- [131] V.P. Zhdanov and B. Kasemo. Simulations of the reaction kinetics on nanometer supported catalyst particles. *Surface Science Reports*, 39(2-4):25 – 104, 2000.
- [132] R.M. Jaeger, H. Kuhlenbeck, H.-J. Freund, M. Wuttig, W. Hoffmann, R. Franchy, and H. Ibach. Formation of a well-ordered aluminium oxide overlayer by oxidation of nial(110). *Surface Science*, 259(3):235 – 252, 1991.
- [133] H.-J. Freund, B. Dillmann, D. Ehrlich, M. Haßel, R.M. Jaeger, H. Kuhlenbeck, C.A. Ventrice Jr, F. Winkelmann, S. Wohlrab, C. Xu, Th. Bertrams, A. Brodde, and H. Neddermeyer. Adsorption and reaction of molecules on surfaces of metal-metal oxide systems. *Journal of Molecular Catalysis*, 82(2-3):143 – 169, 1993. A Special Issue containing the Proceedings of the Fourth International Symposium on the Theoretical Approach to Catalysis at Interfaces.
- [134] C. G. Chen, J. E. Crowell, and J.T. Yates Jr. The metal-metal oxide interface: A study of thermally-activated diffusion at the ni/al<sub>2</sub>o<sub>3</sub> interface using electron spectroscopies. *Surface Science*, 185(3):373–393, 1987.
- [135] D. N. Belton and S. J. Schmieg. Interaction of rh(co)<sub>2</sub>cl<sub>2</sub> with {O<sub>2</sub>} oxidized al(100): Effect of al<sub>2</sub>o<sub>3</sub> preparation on rh(co)<sub>2</sub>cl<sub>2</sub> decomposition. *Surface Science*, 199(3):518 – 536, 1988.

- [136] X. Xu, W. S. Oh, and D. W. Goodman. Interfacial reactions between oxide films and refractory metal substrates. *Langmuir*, 12(20):4877–4881, 1996.
- [137] T. Schroeder, M. Adelt, B. Richter, M. Naschitzki, M. Bömer, and H.-J. FREUND. Epitaxial growth of  $\text{SiO}_2$  on  $\text{Mo}(112)$ . *Surface Review and Letters*, 07(01n02):7–14, 2000.
- [138] W. Weiss and W. Ranke. Surface chemistry and catalysis on well-defined epitaxial iron-oxide layers. *Prog. Surf. Sci.*, 70(1-3):1, 2002.
- [139] G. H. Vurens, V. Maurice, M. Salmeron, and G. A. Somorjai. Growth, structure and chemical properties of  $\text{FeO}$  overlayers on  $\text{Pt}(100)$  and  $\text{Pt}(111)$ . *Surf. Sci.*, 268(1-3):170, 1992.
- [140] W. Weiss, A. Barbieri, M. A. van Hove, and G. A. Somorjai. Surface-structure determination of an oxide film grown on a foreign substrate -  $\text{Fe}_3\text{O}_4$  multilayer on  $\text{Pt}(111)$  identified by low-energy-electron-diffraction. *Phys. Rev. Lett.*, 71(12):1848, 1993.
- [141] Sh. K. Shaikhutdinov, M. Ritter, X.-G. Wang, H. Over, and W. Weiss. Defect structures on epitaxial  $\text{Fe}_3\text{O}_4(111)$  films. *Phys. Rev. B*, 60:11062–11069, 1999.
- [142] C. Lemire, R. Meyer, V. E. Henrich, Sh. K. Shaikhutdinov, and H.-J. Freund. The surface structure of  $\text{Fe}_3\text{O}_4(111)$  films as studied by  $\text{CO}$  adsorption. *Surf. Sci.*, 572(1):103, 2004.
- [143] A. Sala, H. Marchetto, Z.-H. Qin, S. Shaikhutdinov, Th. Schmidt, and H.-J. Freund. Defects and inhomogeneities in  $\text{Fe}_3\text{O}_4(111)$  thin film growth on  $\text{Pt}(111)$ . *Phys. Rev. B*, 86:155430, 2012.
- [144] A. Barbieri, W. Weiss, M.A. Van Hove, and G.A. Somorjai. Magnetite  $\text{Fe}_3\text{O}_4(111)$ : surface structure by {LEED} crystallography and energetics. *Surface Science*, 302(3):259 – 279, 1994.
- [145] Y. Joseph, G. Ketteler, C. Kuhrs, W. Ranke, W. Weiss, and R. Schlogl. On the preparation and composition of potassium promoted iron oxide model catalyst films. *Phys. Chem. Chem. Phys.*, 3:4141–4153, 2001.
- [146] Y.J. Kim, C. Westphal, R.X. Ynzunza, Z. Wang, H.C. Galloway, M. Salmeron, M.A. Van Hove, and C.S. Fadley. The growth of iron oxide films on  $\text{Pt}(111)$ : a combined xpd, stm, and {LEED} study. *Surface Science*, 416(1-2):68 – 111, 1998.
- [147] W. Weiss and M. Ritter. Metal oxide heteroepitaxy: Stranski-krastanov growth for iron oxides on  $\text{Pt}(111)$ . *Phys. Rev. B*, 59:5201–5213, 1999.
- [148] Y.J. Kim, Y. Gao, and S.A. Chambers. Selective growth and characterization of pure, epitaxial  $\alpha\text{-Fe}_2\text{O}_3(0001)$  and  $\text{Fe}_3\text{O}_4(001)$  films by plasma-assisted molecular beam epitaxy. *Surface Science*, 371(2-3):358 – 370, 1997.

- [149] M. Ritter and W. Weiss. Fe<sub>3</sub>O<sub>4</sub>(111) surface structure determined by {LEED} crystallography. *Surface Science*, 432(1-2):81 – 94, 1999.
- [150] Y. Joseph, W. Ranke, and W. Weiss. Water on feo(111) and fe<sub>3</sub>O<sub>4</sub>(111): Adsorption behavior on different surface terminations. *The Journal of Physical Chemistry B*, 104(14):3224–3236, 2000.
- [151] T. Schalow, M. Laurin, B. Brandt, S. Schauermaun, S. Guimond, H. Kuhlenbeck, D. E. Starr, S. K. Shaikhutdinov, J. Libuda, and H.-J. Freund. Oxygen storage at the metal/oxide interface of catalyst nanoparticles. *Angewandte Chemie International Edition*, 44(46):7601–7605, 2005.
- [152] T. Schalow, B. Brandt, D.E. Starr, M. Laurin, S. Schauermaun, Sh.K. Shaikhutdinov, J. Libuda, and H.-J. Freund. Oxygen-induced restructuring of a pd/fe<sub>3</sub>O<sub>4</sub> model catalyst. *Catalysis Letters*, 107(3-4):189–196, 2006. ISSN 1011-372X.
- [153] T. Schalow, B. Brandt, D. E. Starr, M. Laurin, S. K. Shaikhutdinov, S. Schauermaun, J. Libuda, and H.-J. Freund. Particle size dependent adsorption and reaction kinetics on reduced and partially oxidized pd nanoparticles. *Phys. Chem. Chem. Phys.*, 9:1347–1361, 2007.
- [154] A. M. Bradshaw and F. M. Hoffmann. The chemisorption of carbon monoxide on palladium single crystal surfaces: IR spectroscopic evidence for localised site adsorption. *Surf. Sci.*, 72:513, 1978.
- [155] M. K. Rose, T. Mitsui, J.C. Dunphy, A. Borg, D. F. Ogletree, M. Salmeron, and P. Sautet. Ordered structures of CO on Pd(111) studied by STM. *Surf. Sci.*, 512(1-2):48, 2002.
- [156] H. Othani, M. A. van Hove, and G. Somorjai. LEED intensity analysis of the surface-structures of Pd(111) and of CO adsorbed on Pd(111) in a  $(\sqrt{3} \times \sqrt{3}) R30^\circ$  arrangement. *Surf. Sci.*, 187(2-3):372, 1988.
- [157] D. Loffreda, D. Simon, and P. Sautet. Dependence of stretching frequency on surface coverage and adsorbate-adsorbate interactions: A density-functional theory approach of CO on Pd(111). *Surf. Sci.*, 425(1):68, 1999.
- [158] S. Surnev, M. Sock, G. M. Ramsey, F. P. Netzer, M. Wiklund, M. Borg, and J. N. Andersen. CO adsorption on Pd(111): A high-resolution core level photoemission and electron energy loss spectroscopy study. *Surf. Sci.*, 470(1-2):171, 2000.
- [159] T. Giebel, O. Schaff, C. J. Hirschmugl, V. Fernandez, K.-M. Schindler, A. Theobald, S. Bao, R. Lindsay, W. Berndt, A. M. Bradshaw, C. Baddeley, A. F. Lee, R. M. Lambert, and D. P. Woodruff. A photoelectron diffraction study of ordered structures in the chemisorption system Pd(111)-CO. *Surf. Sci.*, 406(1-3):90, 1998.
- [160] W. K. Kuhn, J. Szanyi, and D. W. Goodman. CO adsorption on Pd(111) - the effects of temperature and pressure. *Surf. Sci. Lett.*, 274(3):L611, 1992.

- [161] H. Unterhalt, G. Rupprechter, and H.-J. Freund. Vibrational sum frequency spectroscopy on Pd(111) and supported Pd nanoparticles: CO adsorption from ultrahigh vacuum to atmospheric pressure. *J. Phys. Chem. B*, 106(2):356, 2002.
- [162] A. Ortega, F. M. Hoffman, and A. M. Bradshaw. The adsorption of CO on Pd(100) studied by IR reflection absorption-spectroscopy. *Surf. Sci.*, 119(1):79, 1982.
- [163] X. P. Xu and D. W. Goodman. An infrared and kinetic-study of CO oxidation on model silica-supported palladium catalysts from  $10^{-9}$  to 15 torr. *J. Phys. Chem.*, 97(29):7711, 1993.
- [164] C. Goyhenex, M. Croci, C. Claeys, and C. R. Henry. FTIR studies of the adsorption of CO on supported metallic clusters Pd/MgO(100). *Surf. Sci.*, 352:475, 1996.
- [165] K. Wolter, O. Seiferth, H. Kuhlenbeck, M. Bäumer, and H.-J. Freund. Infrared spectroscopic investigation of CO adsorbed on Pd aggregates deposited on an alumina model support. *Surf. Sci.*, 399(2-3):190, 1998.
- [166] S. Bertarione, D. Scarano, A. Zecchina, V. Johnnek, J. Hoffmann, S. Schauer mann, M. M. Frank, J. Libuda, G. Rupprechter, and H.-J. Freund. Surface reactivity of Pd nanoparticles supported on polycrystalline substrates as compared to thin film model catalysts: Infrared study of CO adsorption. *Surf. Sci.*, 108(11):3603, 2004.
- [167] M. Morkel, H. Unterhalt, M. Salmeron, G. Rupprechter, and H.-J. Freund. SFG spectroscopy from  $10^{-8}$  to 1000 mbar: less ordered CO structures and coadsorption on Pd(111). *Surf. Sci.*, 532:103, 2003.
- [168] H. K. Lee, J. H. Han, K. J. Kim, T. H. Kang, and B. Kim. Configuration of pentacene (c22h14) films on si(100)-2 x 1 studied by nexafs. *Surface Science*, 601(6):1456–1460, 2007.
- [169] J. Taborski, P. Vaterlein, H. Dietz, U. Zimmermann, and E. Umbach. Nexafs investigations on ordered adsorbate layers of large aromatic molecules. *Journal of Electron Spectroscopy and Related Phenomena*, 75:129–147, 1995.
- [170] P. Yannoulis, K. H. Frank, and E. E. Koch. Electronic-structure and orientation of anthracene on ag(111). *Surface Science*, 241(3):325–334, 1991.
- [171] G. Hähner, R. Hofer, and I. Klingenfuss. Order and orientation in self-assembled long chain alkanephosphate monolayers adsorbed on metal oxide surfaces. *Langmuir*, 17(22):7047–7052, 2001.
- [172] A. Schoell, Y. Zou, D. Huebner, S. G. Urquhart, Th. Schmidt, R. Fink, and E. Umbach. A comparison of fine structures in high-resolution x-ray-absorption spectra of various condensed organic molecules. *The Journal of Chemical Physics*, 123(4), 2005.
- [173] A. J. Urquhart, F. J. Williams, O. P. H. Vaughan, R. L. Cropley, and R. M. Lambert. Adsorbate conformation determines catalytic chemoselectivity: crotonaldehyde on the pt(111) surface. *Chemical Communications*, -(15):1977–1979, 2005.

- [174] K.-H. Dostert, C. P. O'Brien, W. Riedel, A. Savara, W. Liu, M. Oehzelt, A. Tkatchenko, and S. Schauermann. Interaction of isophorone with pd(111): A combination of infrared reflection-absorption spectroscopy, near-edge x-ray absorption fine structure, and density functional theory studies. *The Journal of Physical Chemistry C*, 118(48):27833–27842, 2014.
- [175] K.-H. Dostert, C. P. O'Brien, W. Liu, W. Riedel, A. Savara, A. Tkatchenko, S. Schauermann, and H.-J. Freund. Adsorption of isophorone and trimethyl-cyclohexanone on pd(111): A combination of infrared reflection absorption spectroscopy and density functional theory studies. *submitted to Surf. Sci.*, 2015.
- [176] K.-H. Dostert, C. P. O'Brien, F. Mirabella, F. Ivars-Barcelo, S. Schauermann, and H.-J. Freund. Adsorption of acrolein, propanal, and allyl alcohol on pd(111): A combination of infrared reflection absorption spectroscopy and temperature programmed desorption studies. *to be submitted*, 2015.
- [177] K.-H. Dostert, S. Schauermann, and H.-J. Freund. Insights into the origin of selectivity in acrolein conversion over pd/fe<sub>3</sub>o<sub>4</sub>. *to be submitted*, 2015.
- [178] T.B.L.W. Marinelli, S. Nabuurs, and V. Ponec. Activity and selectivity in the reactions of substituted  $\alpha,\beta$ -unsaturated aldehydes. *Journal of Catalysis*, 151(2): 431 – 438, 1995.
- [179] G.J. Hutchings, F. King, I.P. Okoye, M.B. Padley, and C.H. Rochester. Selectivity enhancement in the hydrogenation of  $\alpha,\beta$ -unsaturated aldehydes and ketones using thiophene-modified catalysts. *Journal of Catalysis*, 148(2):453 – 463, 1994.
- [180] J. Haubrich, D. Loffreda, F. Delbecq, P. Sautet, A. Krupski, C. Becker, and K. Wandelt. Adsorption of  $\alpha,\beta$ -unsaturated aldehydes on pt(111) and pt-sn alloys: Ii. crotonaldehyde. *Journal of Physical Chemistry C*, 113(31):13947–13967, 2009.
- [181] J. C. de Jesus and F. Zaera. Adsorption and thermal chemistry of acrolein and crotonaldehyde on pt(111) surfaces. *Surface Science*, 430(1-3):99 – 115, 1999.
- [182] Luis E. Murillo and Jingguang G. Chen. A comparative study of the adsorption and hydrogenation of acrolein on pt(1 1 1), ni(1 1 1) film and pt-n-pt(1 1 1) bimetallic surfaces. *Surface Science*, 602(4):919 – 931, 2008.
- [183] David Loffreda, Françoise Delbecq, Fabienne Vignat, and Philippe Sautet. Cover picture: Catalytic hydrogenation of unsaturated aldehydes on pt(111): Understanding the selectivity from first-principles calculations (angew. chem. int. ed. 33/2005). *Angewandte Chemie International Edition*, 44(33):5151–5151, 2005.
- [184] Matthew S. Ide, Bing Hao, Matthew Neurock, and Robert J. Davis. Mechanistic insights on the hydrogenation of  $\alpha,\beta$ -unsaturated ketones and aldehydes to unsaturated alcohols over metal catalysts. *ACS Catalysis*, 2(4):671–683, 2012.
- [185] K.-H. Dostert, O'Brien C. P., F. Ivars-Barcelo, S. Schauermann, and H.-J. Freund. Spectators control selectivity in surface chemistry: Acrolein partial hydrogenation over pd. *J. Am. Chem. Soc.*, 137(42):13496–13502, 2015.

- [186] K.-H. Dostert, C. P. O'Brien, S. Schauermaun, and H.-J. Freund. Partial selective hydrogenation of acrolein on pd: a mechanistic study. *to be submitted*, 2015.
- [187] C. P. O'Brien, K.-H. Dostert, S. Schauermaun, and H.-J. Freund. Selective hydrogenation of acrolein over pd model catalysts: Temperature and particle size effects. *to be submitted*, 2015.
- [188] M. T. Pirnot, D. A. Rankic, D. B. C. Martin, and D. W. C. MacMillan. Photoredox activation for the direct beta-arylation of ketones and aldehydes. *Science*, 339(6127): 1593–1596, 2013.
- [189] Y. Zhu, H. F. Qian, B. A. Drake, and R. C. Jin. Atomically precise au-25(sr)(18) nanoparticles as catalysts for the selective hydrogenation of alpha,beta-unsaturated ketones and aldehydes. *Angewandte Chemie-International Edition*, 49(7):1295–1298, 2010.
- [190] S. Fleischer, S. L. Zhou, K. Junge, and M. Beller. General and highly efficient iron-catalyzed hydrogenation of aldehydes, ketones, and ,alpha,beta-unsaturated aldehydes. *Angewandte Chemie-International Edition*, 52(19):5120–5124, 2013.
- [191] M. G. Hitzler, F. R. Smail, S. K. Ross, and M. Poliakoff. Selective catalytic hydrogenation of organic compounds in supercritical fluids as a continuous process. *Organic Process Research and Development*, 2(3):137–146, 1998.
- [192] T. Sato, C. V. Rode, O. Sato, and M. Shirai. Hydrogenation of isophorone with noble metal catalysts in supercritical carbon dioxide. *Applied Catalysis B-Environmental*, 49(3):181–185, 2004.
- [193] Dan I. Enache, Graham J. Hutchings, Stuart H. Taylor, and E. Hugh Stitt. The hydrogenation of isophorone to trimethyl cyclohexanone using the downflow single capillary reactor. *Catalysis Today*, 105(3-4):569–573, 2005.
- [194] Antal Tungler, Karina Fodor, Tibor Mathe, and Roger A. Sheldon. Enantioselective hydrogenation of ethyl pyruvate and isophorone over modified pt and pd catalysts. In A. Baiker H.U. Blaser and R. Prins, editors, *Heterogeneous Catalysis and Fine Chemicals IV Proceedings of the 4th International Symposium on Heterogeneous Catalysis and Fine Chemicals*, volume 108 of *Studies in Surface Science and Catalysis*, pages 157 – 165. Elsevier, 1997.
- [195] M. Studer, H. U. Blaser, and C. Exner. Enantioselective hydrogenation using heterogeneous modified catalysts: An update. *Advanced Synthesis & Catalysis*, 345(1-2):45–65, 2003.
- [196] H. U. Blaser, B. Pugin, and F. Spindler. Progress in enantioselective catalysis assessed from an industrial point of view. *Journal of Molecular Catalysis a-Chemical*, 231(1-2):1–20, 2005.
- [197] A. Tungler and G. Fogassy. Catalysis with supported palladium metal, selectivity in the hydrogenation of c=c, c=o and c=n bonds, from chemo- to enantioselectivity. *Journal of Molecular Catalysis a-Chemical*, 173(1-2):231–247, 2001.

- [198] T. Tarnai, A. Tungler, T. Mathe, J. Petro, R. A. Sheldon, and G. Toth. A new chiral auxiliary in enantioselective hydrogenations - (-)-dihydrovinpocetine 1. hydrogenation of isophorone. *Journal of Molecular Catalysis a-Chemical*, 102(1):41–47, 1995.
- [199] G. Farkas, K. Fodor, A. Tungler, T. Mathe, G. Toth, and R. A. Sheldon. New chiral auxiliaries in enantioselective heterogeneous catalytic hydrogenations: (-) and (+)-dihydro-apovincaminic acid. comparison with (-)-dihydro-apovincaminic acid ethyl ester. iii. *Journal of Molecular Catalysis a-Chemical*, 138(2-3):123–127, 1999.
- [200] A. Tungler, Y. Nitta, K. Fodor, G. Farkas, and T. Mathe. Comparison of chiral modifiers in the pd catalysed hydrogenation of phenylcinnamic acid and isophorone. *Journal of Molecular Catalysis a-Chemical*, 149(1-2):135–140, 1999.
- [201] E. Sipos and A. Tungler. Effect of pretreatment of the catalyst and catalyst-modifier system in the enantioselective hydrogenation of isophorone. *Reaction Kinetics and Catalysis Letters*, 80(2):365–373, 2003.
- [202] E. Sipos, A. Tungler, and G. Fogassy. New substrates and modifiers in the enantioselective heterogeneous catalytic hydrogenation of the c=c double bond. *Journal of Molecular Catalysis a-Chemical*, 216(2):171–180, 2004.
- [203] M. Fodor, A. Tungler, and L. Vida. Heterogeneous catalytic asymmetric hydrogenations with modifiers of axial chirality. *Reaction Kinetics and Catalysis Letters*, 90(2):413–418, 2007.
- [204] S. Li, E. S. Zhan, Y. Li, Y. D. Xu, and W. J. Shen. Enantio selective hydrogenation of isophorone and kinetic resolution of 3,3,5-trimethylcyclohexanone over pd catalysts in the presence of (s)-proline. *Catalysis Today*, 131(1-4):347–352, 2008.
- [205] V. G. Ruiz, W. Liu, E. Zojer, M. Scheffler, and A. Tkatchenko. Density-functional theory with screened van der waals interactions for the modeling of hybrid inorganic-organic systems. *Physical Review Letters*, 108(14), 2012.
- [206] V. Blum, R. Gehrke, F. Hanke, P. Havu, V. Havu, X. G. Ren, K. Reuter, and M. Scheffler. Ab initio molecular simulations with numeric atom-centered orbitals. *Computer Physics Communications*, 180(11):2175–2196, 2009.
- [207] A. Tkatchenko and M. Scheffler. Accurate molecular van der waals interactions from ground-state electron density and free-atom reference data. *Physical Review Letters*, 102(7), 2009.
- [208] E. M. Lifshitz. The theory of molecular attractive forces between solids. *Soviet Physics JETP-USSR*, 2(1):73–83, 1956.
- [209] E. Zaremba and W. Kohn. Van-der-waals interactions between an atom and a solid-surface. *Physical Review B*, 13(6):2270–2285, 1976.
- [210] E. van Lenthe, E. J. Baerends, and J. G. Snijders. Relativistic total energy using regular approximations. *The Journal of Chemical Physics*, 101(11):11, 1994.

- [211] M. B. Casu, A. Scholl, K. R. Bauchspiess, D. Hubner, T. Schmidt, C. Heske, and E. Umbach. Nucleation in organic thin film growth: Perylene on  $\text{Al}_2\text{O}_3/\text{Ni}_3\text{Al}(111)$ . *Journal of Physical Chemistry C*, 113(25):10990–10996, 2009.
- [212] I. Ishii and A. P. Hitchcock. The oscillator-strength for c1s and o1s excitation of some saturated and unsaturated organic alcohols, acids and esters. *Journal of Electron Spectroscopy and Related Phenomena*, 46(1):55–84, 1988.
- [213] F. Bournel, C. Laffon, P. Parent, and G. Tourillon. Adsorption of some substituted ethylene molecules on  $\text{Pt}(111)$  at 95 K. 1. NEXAFS, XPS and UPS studies. *Surface Science*, 350(1-3):60–78, 1996.
- [214] J. P. Perdew, K. Burke, and M. Ernzerhof. Generalized gradient approximation made simple. *Physical Review Letters*, 77(18):3865–3868, 1996.
- [215] C. Burkner, N. Ferri, A. Tkatchenko, A. Gerlach, J. Niederhausen, T. Hosokai, S. Duhm, J. Zegenhagen, N. Koch, and F. Schreiber. Exploring the bonding of large hydrocarbons on noble metals: Diindoperylene on  $\text{Cu}(111)$ ,  $\text{Ag}(111)$ , and  $\text{Au}(111)$ . *Physical Review B*, 87(16), 2013.
- [216] W. Liu, J. Carrasco, B. Santra, A. Michaelides, M. Scheffler, and A. Tkatchenko. Benzene adsorbed on metals: Concerted effect of covalency and van der Waals bonding. *Physical Review B*, 86(24), 2012.
- [217] D. A. Egger, V. G. Ruiz, W. A. Said, T. Bucko, A. Tkatchenko, and E. Zojer. Understanding structure and bonding of multilayered metal-organic nanostructures. *Journal of Physical Chemistry C*, 117(6):3055–3061, 2013.
- [218] W. Liu, A. Savara, X. G. Ren, W. Ludwig, K. H. Dostert, S. Schauerermann, A. Tkatchenko, H. J. Freund, and M. Scheffler. Toward low-temperature dehydrogenation catalysis: Isophorone adsorbed on  $\text{Pd}(111)$ . *Journal of Physical Chemistry Letters*, 3(5):582–586, 2012.
- [219] M. P. Gaigeot, M. Martinez, and R. Vuilleumier. Infrared spectroscopy in the gas and liquid phase from first principle molecular dynamics simulations: application to small peptides. *Molecular Physics*, 105(19-22):2857–2878, 2007.
- [220] K. Christmann. Interaction of hydrogen with solid-surfaces. *Surface Science Reports*, 9(1-3):1–163, 1988.
- [221] T. Mallat, E. Orglmeister, and A. Baiker. Asymmetric catalysis at chiral metal surfaces. *Chemical Reviews*, 107(11):4863–4890, 2007.
- [222] D. J. Watson, R. J. Jesudason, S. K. Beaumont, G. Kyriakou, J. W. Burton, and R. M. Lambert. Heterogeneously catalyzed asymmetric hydrogenation of  $\text{C}=\text{C}$  bonds directed by surface-tethered chiral modifiers. *Journal of the American Chemical Society*, 131(40):14584–14589, 2009.

## Bibliography

- [223] Wei Liu, Alexandre Tkatchenko, and Matthias Scheffler. Modeling adsorption and reactions of organic molecules at metal surfaces. *Accounts of Chemical Research*, 47(11):3369–3377, 2014.
- [224] Wei Liu, Sergey N. Filimonov, Javier Carrasco, and Alexandre Tkatchenko. Molecular switches from benzene derivatives adsorbed on metal surfaces. *Nature Communication*, 4(11):2569, 2013.
- [225] J. J. Fox and A. E. Martin. Investigations of infra-red spectra. absorption of the  $\text{CH}_2$  group in the region of  $3\ \mu$ . *Proceedings of the Royal Society of London Series A-Mathematical and Physical Sciences*, 167(A929):0257–0281, 1938.
- [226] J. J. Fox and A. E. Martin. Investigations of infra-red spectra. determination of  $\text{C-H}$  frequencies ( $\sim 3000\ \text{cm}^{-1}$ ) in paraffins and olefins, with some observations on "polythenes". *Proceedings of the Royal Society of London Series A-Mathematical and Physical Sciences*, 175(A961):0208–0233, 1940.
- [227] J. C. Lavalley and N. Sheppard. Anharmonicity of  $\text{CH}_3$  deformation vibrations and fermi resonance between the symmetrical  $\text{CH}_3$  stretching mode and overtones of  $\text{CH}_3$  deformation vibrations. *Spectrochimica Acta Part A: Molecular Spectroscopy*, 28(11):2091–2101, 1972.
- [228] Norman Sheppard and Delia M. Simpson. The infra-red and raman spectra of hydrocarbons. part ii. paraffins. *Quarterly Reviews, Chemical Society*, 7(1):19–55, 1953.
- [229] R. A. Macphail, H. L. Strauss, R. G. Snyder, and C. A. Elliger.  $\text{C-H}$  stretching modes and the structure of normal-alkyl chains .2. long, all-trans chains. *Journal of Physical Chemistry*, 88(3):334–341, 1984.
- [230] J. H. Schachtschneider and R. G. Snyder. Vibrational analysis of the n-paraffins .2. normal co-ordinate calculations. *Spectrochimica Acta*, 19(1):117–168, 1963.
- [231] R. G. Snyder and J. H. Schachtschneider. Vibrational analysis of the n-paraffins .1. assignments of infrared bands in the spectra of  $\text{C}_3\text{H}_8$  through  $\text{n-C}_{19}\text{H}_{40}$ . *Spectrochimica Acta*, 19(1):85–116, 1963.
- [232] N. B. Colthup. Molecular-orbitals and  $\text{CH}_3$ ,  $\text{CH}_2$ , and  $\text{CH}$  deformation group frequencies. *Applied Spectroscopy*, 34(1):1–6, 1980.
- [233] R. G. Snyder, M. C. Goh, V. J. P. Srivatsavoy, H. L. Strauss, and D. L. Dorset. Measurement of the growth-kinetics of microdomains in binary n-alkane solid-solutions by infrared-spectroscopy. *Journal of Physical Chemistry*, 96(24):10008–10019, 1992.
- [234] M. Shimomura, K. Song, and J. F. Rabolt. Spectroscopic determination of diffusion in langmuir-blodgett-films .1. interlayer diffusion of cadmium arachidate and its deuterated analog through a polymer interface. *Langmuir*, 8(3):887–893, 1992.
- [235] H. L. McMurtry and V. Thornton. Correlation of infrared spectra - paraffins, olefins, and aromatics with structural groups. *Analytical Chemistry*, 24(2):318–334, 1952.

- [236] B. Nolin and R. N. Jones. The infrared absorption spectra of diethyl ketone and its deuterium substitution products. *Journal of the American Chemical Society*, 75(22):5626–5628, 1953.
- [237] N. B. Colthup. Spectra-structure correlations in the infra-red region. *Journal of the Optical Society of America*, 40(6):397–400, 1950.
- [238] R. S. Rasmussen. Vibrational frequency assignments for paraffin hydrocarbons - infra-red absorption spectra of the butanes and pentanes. *Journal of Chemical Physics*, 16(7):712–727, 1948.
- [239] R. A. Meiklejohn, R. J. Meyer, S. M. Aronovic, H. A. Schuette, and V. W. Meloch. Characterization of long-chain fatty acids by infrared spectroscopy. *Analytical Chemistry*, 29(3):329–334, 1957.
- [240] R. Mecke and K. Noack. Untersuchungen über die beeinflussung der frequenz und intensität der  $\nu$ -C=O-banden und  $\nu$ -C=C-banden im ir-spektrum ungesättigter ketone durch konjugation und sterische hinderung. *Spectrochimica Acta*, 12(4):391–393, 1958.
- [241] R. Barlet, M. Montagne, and P. Arnaud. Infrared spectroscopy of carbonyl compounds .2. effect of alkyl substitution and stereochemistry on  $\nu$ (C=O) and  $\nu$ (C=C) stretching frequencies of aliphatic and alicyclic alpha-ethylene ketones with 6-membered and higher-membered chains. *Spectrochimica Acta Part a-Molecular Spectroscopy*, A 25(6):1081, 1969.
- [242] E. G. Hoffmann. Infrarotspektroskopische untersuchungen definiert an der doppelbindung deuterierter olefine. *Annalen Der Chemie-Justus Liebig*, 618(1-3):276–291, 1958.
- [243] Marie L. Laury, Matthew J. Carlson, and Angela K. Wilson. Vibrational frequency scale factors for density functional theory and the polarization consistent basis sets. *Journal of Computational Chemistry*, 33(30):2380–2387, 2012.
- [244] S.E. Stein. book section Infrared Spectra by NIST Mass Spec Data Center. National Institute of Standards and Technology, Gaithersburg MD, August 1, 2014. URL <http://webbook.nist.gov>.
- [245] F. Delbecq and P. Sautet. Competitive C=C and C=O adsorption of  $\alpha$ - $\beta$ -unsaturated aldehydes on Pt and Pd surfaces in relation with the selectivity of hydrogenation reactions: A theoretical approach. *Journal of Catalysis*, 152(2):217 – 236, 1995.
- [246] R. A. Karakhanov, T. I. Odintsova, V. B. Yakovlev, and A. P. Rodin. Selective catalytic-hydrogenation of double-bonds in unsaturated furan ketones. *Reaction Kinetics and Catalysis Letters*, 33(1):219–221, 1987.
- [247] M. L. A. Vonholleben, M. Zucolotto, C. A. Zini, and E. R. Oliveira. A selective reduction of alpha,beta-unsaturated ketones. *Tetrahedron*, 50(4):973–978, 1994.

## Bibliography

- [248] Y. Hamada, Y. Nishimura, and M. Tsuboi. Infrared-spectrum of trans-acrolein. *Chemical Physics*, 100(3):365–375, 1985.
- [249] C. Puzzarini, E. Penocchio, M. Biczysko, and V. Barone. Molecular structure and spectroscopic signatures of acrolein: Theory meets experiment. *Journal of Physical Chemistry A*, 118(33):6648–6656, 2014.
- [250] S. Fujii, N. Osaka, M. Akita, and K. Itoh. Infrared reflection-absorption spectroscopic study on the adsorption structures of acrolein on an evaporated silver film. *Journal of Physical Chemistry*, 99(18):6994–7001, 1995.
- [251] M. Akita, N. Osaka, and K. Itoh. Infra-red reflection absorption spectroscopic study on adsorption structures of acrolein on polycrystalline gold and au(111) surfaces under ultra-high vacuum conditions. *Surface Science*, 405(2-3):172–181, 1998.
- [252] N. Osaka, M. Akita, and K. Itoh. Infrared reflection-absorption spectroscopic study on the adsorption structures of 1,3-butadiene at au(111) and ag(111) surfaces. *Journal of Physical Chemistry B*, 102(35):6817–6824, 1998.
- [253] G. A. Guirgis, B. R. Drew, T. K. Gounev, and J. R. Durig. Conformational stability and vibrational assignment of propanal. *Spectrochimica Acta Part a-Molecular and Biomolecular Spectroscopy*, 54(1):123–143, 1998.
- [254] S. G. Frankiss and W. Kynaston. Vibrational-spectra of propanal, 1-deuteropropanal and 2,2-dideuteropropanal. *Spectrochimica Acta Part a-Molecular Spectroscopy*, A 28(11):2149, 1972.
- [255] G. Sbrana and V. Schettin. Vibrational spectra and isomerism in propyl- and butylaldehydes. *Journal of Molecular Spectroscopy*, 33(1):100, 1970.
- [256] J. S. Byrne, K. J. Morgan, and P. F. Jackson. Carbonyl group frequency .4. aliphatic aldehydes. *Journal of the Chemical Society-Perkin Transactions 2*, (10):1291, 1972.
- [257] S. Pinchas. Infrared absorption of the aldehydic c-h group. *Analytical Chemistry*, 27(1):2–6, 1955.
- [258] D. F. Eggers and W. E. Lingren. C-h vibrations in aldehydes. *Analytical Chemistry*, 28(8):1328–1329, 1956.
- [259] B. Silvi and J. P. Perchard. Vibration-spectra and normal coordinates of 4 isotopic allyl alcohol species. *Spectrochimica Acta Part a-Molecular and Biomolecular Spectroscopy*, 32(1):11–22, 1976.
- [260] J. R. Durig, A. Ganguly, A. M. El Defrawy, C. Zheng, H. M. Badawi, W. A. Herrebout, B. J. van der Veken, G. A. Guirgis, and T. K. Gounev. Conformational stability of allyl alcohol from temperature dependent infrared spectra of rare gas solutions, ab initio calculations, r(0) structural parameters, and vibrational assignment. *Journal of Molecular Structure*, 922(1-3), 2009.

- [261] Luis E. Murillo, Amit M. Goda, and Jingguang G. Chen. Selective hydrogenation of the co bond in acrolein through the architecture of bimetallic surface structures. *Journal of the American Chemical Society*, 129(22):7101–7105, 2007.
- [262] L. J. Bellamy and R. F. Branch. The infra-red spectra of chelate compounds. part ii. metal chelate compounds of [small beta]-diketones and of salicylaldehyde. *Journal of the Chemical Society (Resumed)*, pages 4491–4494, 1954.
- [263] Elisabetta Finocchio, Guido Busca, Vincenzo Lorenzelli, and Ronald J. Willey. Ftir studies on the selective oxidation and combustion of light hydrocarbons at metal oxide surfaces. propane and propene oxidation on mgcr2o4. *Journal of the Chemical Society, Faraday Transactions*, 90(21):3347–3356, 1994.
- [264] J. E. Bailie, C. H. Rochester, and G. J. Hutchings. Ir study of acrolein hydrogenation over co/sio2 catalysts. *Journal of the Chemical Society-Faraday Transactions*, 93(24):4389–4394, 1997.
- [265] A. V. Stuart and Gbbm Sutherland. Effect of hydrogen bonding on the deformation frequencies of the hydroxyl group in alcohols. *Journal of Chemical Physics*, 24(3):559–570, 1956.
- [266] E. Gross, H.-C. LiuJack, F. D. Toste, and G. A. Somorjai. Control of selectivity in heterogeneous catalysis by tuning nanoparticle properties and reactor residence time. *Nature Chemistry*, 4:947–952, 2012.
- [267] W. J. Mitchell, J. Xie, T. A. Jachimowski, and W. H. Weinberg. Carbon-monoxide hydrogenation on the ru(001) surface at low-temperature using gas-phase atomic-hydrogen - spectroscopic evidence for the carbonyl insertion mechanism on a transition-metal surface. *Journal of the American Chemical Society*, 117(9):2606–2617, 1995.
- [268] Marcus K. Weldon, , and Cynthia M. Friend. Probing surface reaction mechanisms using chemical and vibrational methods: Alkyl oxidation and reactivity of alcohols on transition metal surfaces. *Chemical Reviews*, 96(4):1391–1412, 1996.
- [269] Francisco Zaera. On the mechanism for the hydrogenation of olefins on transition-metal surfaces: The chemistry of ethylene on pt(111). *Langmuir*, 12(1):88–94, 1996.
- [270] A. Sandell, J. Libuda, P. A. Brühwiler, S. Andersson, A. J. Maxwell, M. Bäumer, N. Martensson, and H. J. Freund. Interaction of co with pd clusters supported on a thin alumina film. *Journal of Vacuum Science and Technology A*, 14(3):1546–1551, 1996.
- [271] Takato Mitsudome, Motoshi Matoba, Tomoo Mizugaki, Koichiro Jitsukawa, and Kiyotomi Kaneda. Core-shell agnp@ceo2 nanocomposite catalyst for highly chemoselective reductions of unsaturated aldehydes. *Chemistry - A European Journal*, 19(17):5255–5258, 2013. ISSN 1521-3765.

- [272] May E. Chiu, Georgios Kyriakou, Federico J. Williams, David J. Watson, Mintcho S. Tikhov, and Richard M. Lambert. Sulfur, normally a poison, strongly promotes chemoselective catalytic hydrogenation: stereochemistry and reactivity of crotonaldehyde on clean and s-modified cu(111). *Chem. Commun.*, pages 1283–1285, 2006.
- [273] May E. Chiu, David J. Watson, Georgios Kyriakou, Mintcho S. Tikhov, and Richard M. Lambert. Tilt the molecule and change the chemistry: Mechanism of s-promoted chemoselective catalytic hydrogenation of crotonaldehyde on cu(111). *Angewandte Chemie International Edition*, 45(45):7530–7534, 2006.
- [274] J. C. Serrano-Ruiz, A. Lopez-Cudero, J. Solla-Gullon, A. Sepulveda-Escribano, A. Aldaz, and F. Rodr  guez-Reinoso. Hydrogenation of  $\alpha,\beta$  unsaturated aldehydes over polycrystalline, (111) and (100) preferentially oriented pt nanoparticles supported on carbon. *Journal of Catalysis*, 253(1):159 – 166, 2008.
- [275] J. Haubrich, D. Loffreda, F. Delbecq, P. Sautet, Y. Jugnet, A. Krupski, C. Becker, and K. Wandelt. Adsorption and vibrations of  $\alpha,\beta$ -unsaturated aldehydes on pure pt and pt-sn alloy (111) surfaces i. prenatal. *Journal of Physical Chemistry C*, 112(10):3701–3718, 2008.
- [276] Francisco Zaera. An organometallic guide to the chemistry of hydrocarbon moieties on transition metal surfaces. *Chemical Reviews*, 95(8):2651–2693, 1995.
- [277] F. Delbecq and P. Sautet. A density functional study of adsorption structures of unsaturated aldehydes on pt(111): A key factor for hydrogenation selectivity. *Journal of Catalysis*, 211(2):398 – 406, 2002.
- [278] Xiao-Ming Cao, Robbie Burch, Christopher Hardacre, and P. Hu. Reaction mechanisms of crotonaldehyde hydrogenation on pt(111): Density functional theory and microkinetic modeling. *The Journal of Physical Chemistry C*, 115(40):19819–19827, 2011.
- [279] Kok Hwa Lim, Amjad B. Mohammad, Ilya V. Yudanov, Konstantin M. Neyman, Michael Bron, Peter Claus, and Notker R  sch. Mechanism of selective hydrogenation of  $\alpha,\beta$ -unsaturated aldehydes on silver catalysts: A density functional study. *The Journal of Physical Chemistry C*, 113(30):13231–13240, 2009.
- [280] D. Loffreda, F. Delbecq, F. Vigne, and P. Sautet. Chemo-regioselectivity in heterogeneous catalysis: Competitive routes for co and cc hydrogenations from a theoretical approach. *Journal of the American Chemical Society*, 128(4):1316–1323, 2006.
- [281] M. Borasio, O. R. de la Fuente, G. Rupprechter, and H. J. Freund. In situ studies of methanol decomposition and oxidation on pd(111) by pm-iras and xps spectroscopy. *Journal of Physical Chemistry B*, 109(38):17791–17794, 2005.
- [282] S. Schauer mann, J. Hoffmann, V. Johanek, J. Hartmann, and J. Libuda. Adsorption, decomposition and oxidation of methanol on alumina supported palladium particles. *Physical Chemistry Chemical Physics*, 4(15):3909–3918, 2002.

- [283] B. A. Sexton. Methanol decomposition on platinum (111). *Surface Science*, 102(1): 271–281, 1981.
- [284] JL Davis and MA Barteau. Polymerization and decarbonylation reactions of aldehydes on the pd (111) surface. *Journal of the American Chemical Society*, 111(5): 1782–1792, 1989.
- [285] H. C. Hollein and W. H. Snyder. The dipropenyl ethers - vibrational and c-13 nmr-spectra. *Journal of Molecular Structure*, 82(3-4):187–204, 1982.
- [286] Iuro Horiuti and M. Polanyi. Exchange reactions of hydrogen on metallic catalysts. *Transactions of the Faraday Society*, 30(0):1164–1172, 1934.
- [287] S. B. Mohsin, M. Trenary, and H. J. Robota. Kinetics of ethylidyne formation on pt(111) from time-dependent infrared-spectroscopy. *Chemical Physics Letters*, 154 (6):511–515, 1989.
- [288] J. M. Hill, J. Y. Shen, R. M. Watwe, and J. A. Dumesic. Microcalorimetric, infrared spectroscopic, and dft studies of ethylene adsorption on pd and pd/sn catalysts. *Langmuir*, 16(5):2213–2219, 2000.
- [289] N. F. Brown and M. A. Barteau. Reactions of unsaturated oxygenates on rhodium(111) as probes of multiple coordination of adsorbates. *Journal of the American Chemical Society*, 114(11):4258–4265, 1992.
- [290] J. L. Davis and M. A. Barteau. Vinyl substituent effects on the reactions of higher oxygenates on pd(111). *Journal of Molecular Catalysis*, 77(1):109–124, 1992.
- [291] J. C. de Jesus and F. Zaera. Double-bond activation in unsaturated aldehydes: conversion of acrolein to propene and ketene on pt(111) surfaces. *Journal of Molecular Catalysis a-Chemical*, 138(2-3):237–240, 1999.
- [292] J. Haubrich, D. Loffreda, F. Delbecq, P. Sautet, Y. Jugnet, A. Krupski, C. Becker, and K. Wandelt. Mechanistic and spectroscopic identification of initial reaction intermediates for prenal decomposition on a platinum model catalyst. *Physical Chemistry Chemical Physics*, 13(13):6000–6009, 2011.
- [293] L. V. Moskaleva, H. A. Aleksandrov, D. Basaran, Z. J. Zhao, and N. Rosch. Ethylidyne formation from ethylene over pd(111): Alternative routes from a density functional study. *Journal of Physical Chemistry C*, 113(34):15373–15379, 2009.
- [294] H. Conrad, G. Ertl, and E.E. Latta. Adsorption of hydrogen on palladium single crystal surfaces. *Surface Science*, 41(2):435 – 446, 1974.
- [295] A. Giroir-Fendler, D. Richard, and P. Gallezot. Selectivity in cinnamaldehyde hydrogenation of group-viii metals supported on graphite and carbon. In M. Guisnet, J. Barrault, C. Bouchoule, D. Duprez, C. Montassier, and G. PÃ©rot, editors, *Heterogeneous Catalysis and Fine Chemicals Proceedings of an International Symposium*, volume 41 of *Studies in Surface Science and Catalysis*, pages 171 – 178. Elsevier, 1988.

## Bibliography

- [296] Claudia E. Volckmar, Michael Bron, Ursula Bentrup, Andreas Martin, and Peter Claus. Influence of the support composition on the hydrogenation of acrolein over ag/sio<sub>2</sub>-al<sub>2</sub>o<sub>3</sub> catalysts. *Journal of Catalysis*, 261(1):1 – 8, 2009.
- [297] A. Boffa, C. Lin, A.T. Bell, and G.A. Somorjai. Promotion of CO and CO<sub>2</sub> hydrogenation over Rh by metal oxides: The influence of oxide lewis acidity and reducibility. *Journal of Catalysis*, 149(1):149 – 158, 1994.
- [298] A.B. Boffa, C. Lin, A.T. Bell, and G.A. Somorjai. Lewis acidity as an explanation for oxide promotion of metals: implications of its importance and limits for catalytic reactions. *Catalysis Letters*, 27(3-4):243–249, 1994.
- [299] R. Beckert, E. Fanghänse, W. D. Habicher, P. Metz, D. Pavel, and K. Schwetlick. *Reaktionen vinyloger Carbonylverbindungen und anderer vinyloger Systeme*, volume 22, book section 7.4. Wiley-VCH, Weinheim, 2009. ISBN 3-527-31148-3.
- [300] R. C. Fuson. The principle of vinylogy. *Chemical Reviews*, 16(1):1–27, 1935.
- [301] Subrahmanya Krishnamurthy. The principle of vinylogy. *Journal of Chemical Education*, 59(7):543, 1982.
- [302] P. Bruneau, P. J. Taylor, and A. J. Wilkinson. The tautomerism of indazolinone in aqueous solution. a note on the 'principle of vinylogy'. *J. Chem. Soc., Perkin Trans. 2*, pages 2263–2269, 1996.
- [303] G. Casiraghi, F. Zanardi, G. Appendino, and G. Rassu. The vinylogous aldol reaction: A valuable, yet understated carbon-carbon bond-forming maneuver. *Chemical Reviews*, 100(6):1929–1972, 2000.
- [304] J. Clayden, N. Greeves, S. Warren, and P. Wothers. *Conjugated Addition*, volume 1, book section 10, pages 227–240. Oxford University Press, 2005. ISBN 0-19-850346-6.



## Abbreviations

AES	Auger electron spectroscopy
CEM	channeltron electron multiplier
BOA	Born-Oppenheimer approximation
DFT	density functional theory
EB	effusive beam
ER	Eley-Rideal
FT	Fourier transform
HOMO	highest occupied molecular orbital
HREELS	high-resolution electron energy loss
I <sub>Pd(111)</sub>	reaction intermediate on Pd(111)
IR	infrared
IRAS	infrared reflection-absorption spectroscopy
LEED	low energy electron diffraction
LH	Langmuir-Hinshelwood
LUMO	lowest unoccupied molecular orbital
MB	molecular beam
MBRS	molecular beam relaxation spectroscopy
MCA	multi-channel arrays
ML	monolayer
MO	molecular orbital
MS	mass spectrometry
MSSR	metal surface selection rule
NEXAFS	near-edge X-ray absorption fine structure
PES	photoelectron spectroscopy
PES	photoelectron spectroscopy
PVD	physical vapor deposition
QMS	quadrupole mass spectrometry
SI/S1	spectator 1 (oxopropyl species)
SII/S2	spectator 2
SFG-VS	sum-frequency generation vibrational spectroscopy
SMSI	strong metal-support interactions
SSB	supersonic beam
STM	scanning tunneling microscopy
TEM	transmission electron microscopy
TMCH	3,3,5-trimethyl-cyclohexanone
TDS	thermal desorption spectroscopy
TPD	temperature programmed desorption
TPR	temperature programmed reaction
TR	time-resolved
UHV	ultra-high vacuum
XPD	X-ray photoelectron diffraction
XPS	X-ray photoelectron spectroscopy
XRD	X-ray diffraction

# Publikationsverzeichnis

## *Supports and Modified Nano-particles in Designing Model Catalysts*

K.-H. Dostert, M. Hollerer, C. Stiehler, C. P. O'Brien, F. Calaza, S. Schauer-  
mann, S. Shaikhutdinov, M. Sterrer, H.-J. Freund, *Faraday Discuss.*, **2015**, DOI: 10.1039/C5FD00143A

## *Spectators Control Selectivity in Surface Chemistry: Acrolein Partial Hydrogenation over Pd*

K.-H. Dostert, C. P. O'Brien, F. Ivars-Barceló, S. Schauer-  
mann, H.-J. Freund, *J. Am. Chem. Soc.*, **2015**, *137* (42), 13496-13502

## *Water Interaction with Iron Oxides*

P. Dementyev, K.-H. Dostert, F. Ivars-Barceló, C. P. O'Brien, F. Mirabella, S. Schauer-  
mann, X. Li, J. Paier, J. Sauer, H.-J. Freund, *Angew. Chem. Int. Ed.*, **2015**, DOI:  
10.1002/anie.201506439R1

## *Adsorption of Isophorone and Trimethyl-Cyclohexanone on Pd(111): A Combination of Infrared Reflection Absorption Spectroscopy and Density Functional Theory Studies*

K.-H. Dostert, C. P. O'Brien, W. Riedel, A. Savara, W. Liu, A. Tkatchenko, S. Schauer-  
mann, *submitted to Surf. Sci.*, **2015**

## *Selective partial Hydrogenation of Acrolein on Pd: a mechanistic Study*

K.-H. Dostert, C. P. O'Brien, S. Schauer-  
mann, H.-J. Freund, *to be submitted*, **2015**

## *Adsorption of Acrolein, Propanal, and Allyl Alcohol on Pd(111): A combination of Infrared Reflection-Absorption Spectroscopy and Temperature Programmed Desorption Studies*

K.-H. Dostert, C. P. O'Brien, F. Mirabella, F. Ivars-Barceló, S. Schauer-  
mann, H.-J. Freund, *to be submitted*, **2015**

## *Catalysis beyond frontier molecular orbitals: Origin of selectivity in partial hydrogenation of multi-unsaturated hydrocarbons on Pd catalysts*

W. Liu, K.-H. Dostert, A. Savara, C. P. O'Brien, W. Riedel, S. Schauer-  
mann, A. Tkatchenko, *to be submitted*, **2015**

## *Selective Hydrogenation of Acrolein over Pd Model Catalysts: Temperature and Particle Size Effects*

C. P. O'Brien, K.-H. Dostert, S. Schauer-  
mann, H.-J. Freund, *to be submitted*, **2015**

## *Acrolein Hydrogenation on clean and modified Pd(111): Isothermal and temperature-*

## Bibliography

### *programmed Reactivity Studies*

C. P. O'Brien, K.-H. Dostert, S. Schauermann, H.-J. Freund, *to be submitted*, **2015**

### *Insights into the Origin of Selectivity in Acrolein Conversion over Pd/Fe<sub>3</sub>O<sub>4</sub>*

K.-H. Dostert, S. Schauermann, H.-J. Freund, *to be submitted*, **2015**

### *Interaction of Isophorone with Pd(111): A Combination of IRAS, NEXAFS and DFT Studies*

K.-H. Dostert, C. P. O'Brien, W. Riedel, A. Savara, W. Liu, M. Oehzelt, A. Tkatchenko, S. Schauermann, *J. Phys. Chem. C*, **2014**, *118* (48), 27833-27842

### *Temperature dependence of the 2-butene hydrogenation over supported Pd nanoparticles and Pd(111)*

A. Savara, W. Ludwig, K.-H. Dostert, S. Schauermann, *J. Mol. Catal. A: Chem.*, **2013**, *377*, 137-142

### *Trends in the Binding Strength of Surface Species on Nanoparticles: How Does the Adsorption Energy Scale with the Particle Size?*

M. Peter, J. M. Flores Camacho, S. Adamovski, L. K. Ono, K.-H. Dostert, C. P. O'Brien, B. Roldan Cuenya, S. Schauermann, H.-J. Freund, *Angew. Chem. Int. Ed.*, **2013**, *52* (19), 5175-5179

### *Towards Low-Temperature Dehydrogenation Catalysis: Isophorone on Pd(111)*

W. Liu, A. Savara, X. Ren, W. Ludwig, K.-H. Dostert, S. Schauermann, A. Tkatchenko, H.-J. Freund, M. Scheffler, *J. Phys. Chem. Lett.*, 2012, **3**, 582-586

### *Near Field Guided Chemical Nanopatterning*

K.-H. Dostert, Marta Álvarez, Kaloian Koynov, Aránzazu del Campo, Hans-Jürgen Butt, Maximilian Kreiter, *Langmuir*, **2012**, *28* (8), 3699-3703

### *Olefin Hydrogenation on Pd Model Supported Catalysts: New Mechanistic Insights*

W. Ludwig, A. Savara, K.-H. Dostert, S. Schauermann, *J. Catal.*, **2011**, *284* (2), 148-156

### *Template-free structuring of colloidal hetero-monolayers by inkjet printing and particle floating*

M. Retsch, K.-H. Dostert, S. K. Nett, N. Vogel, J. S. Gutmann, U. Jonas, *Soft Matter*, **2010**, *6*, 2403-2412

# Selbstständigkeitserklärung

Ich erkläre, dass ich die Dissertation selbständig und nur unter Verwendung der von mir gemäß § 7 Abs. 3 der Promotionsordnung der Mathematisch-Naturwissenschaftlichen Fakultät, veröffentlicht im Amtlichen Mitteilungsblatt der Humboldt-Universität zu Berlin Nr. 126/2014 am 18.11.2014 angegebenen Hilfsmittel angefertigt habe.

Ich habe mich nicht anderwärts um einen Doktorgrad im Promotionsfach Chemie beworben und besitze keinen Doktorgrad im Promotionsfach Chemie. Die Promotionsordnung der Mathematisch-Naturwissenschaftlichen Fakultät, veröffentlicht im Amtlichen Mitteilungsblatt der Humboldt-Universität zu Berlin Nr. 126/2014 am 18.11.2014 habe ich zur Kenntnis genommen.